NASA/TM-2002-21004/Rev3-Vol2

James L. Mueller[1] and Giulietta S. Fargion[2]
Editors

[1] *CHORS, San Diego State University, San Diego, California*
[2]*Science Applications International Corporation, Beltsville, Maryland*

Ocean Optics Protocols For Satellite Ocean Color Sensor Validation, Revision 3, Part II

J. L. Mueller, C. Pietras, S. B. Hooker, D. K. Clark, A. Morel, R. Frouin, B.G. Mitchell, R. R. Bidigare, C. Trees, J. Werdell, G. S. Fargion, R. Arnone, R. W. Austin, S. Bailey, W. Broenkow, S. W. Brown, K. Carder, C. Davis, J. Dore, M. Feinholz, S. Flora, Z.P. Lee, B. Holben, B. C. Johnson, M. Kahru, D. M. Karl, Y. S Kim, K. D. Knobelspiesse, C. R. McClain, S. McLean, M. Miller, C. D. Mobley , J. Porter, R.G. Steward, M. Stramska, L. Van Heukelem, K. Voss, J. Wieland, M. A.Yarbrough and M. Yuen.

National Aeronautical and
Space administration

Goddard Space Flight Space Center
Greenbelt, Maryland 20771

February 2002

NASA/TM-2002-

James L. Mueller[1] and Giulietta S. Fargion[2]
Editors

[1] *CHORS, San Diego State University, San Diego, California*
[2]*Science Applications International Corporation, Beltsville, Maryland*

Ocean Optics Protocols For Satellite Ocean Color Sensor Validation, Revision 3, Part II

J. L. Mueller, C. Trees and R. W. Austin
CHORS, San Diego State University, San Diego, California
C. Pietras and G. S. Fargion
Science Applications International Corporation, Maryland
S. Hooker, B. Holben and C. R. McClain
NASA, Goddard Space Flight Center, Greenbelt, Maryland
D. K. Clark and M. Yuen
NOAA National Environmental Satellite Data Information Service, Suitland, Maryland
A. Morel
Laboratoire d'Oceanographie, Universite Pierre et Marie Curie, France
R. Frouin, B. Greg Mitchell, M. Kahru, J. Wieland and M. Stramska
Scripps Institution of Oceanography, University of California, California
R. R. Bidigare, D. M. Karl and J. Dore
Department of Oceanography, University of Hawaii, Hawaii
P. J. Werdell and K. D. Knobelspiesse
Science Systems & Applications Inc.,Maryland
R. Arnone
Naval Research Laboratory, Stennis Space Center, Mississippi
S. Bailey
Futuretech Corporation, Greenbelt, Maryland
W. Broenkow, M. Feinholz, S. Flora and M. A. Yarbrough,
Moss Landing Marine Laboratory, California
K. Carder, Z.P. Lee and R.G. Steward
University of South Florida, Florida
C. Davis
Naval Research Laboratory, Washington DC
B. C. Johnson and S. W. Brown
National Institute of Standards and Technology, Maryland
Y. S. Kim
Data Systems Technologies, Inc., Maryland
S. McLean
Satlantic Inc., Halifax, Nova Scotia, Canada
M. Miller
Department of Applied Science, Brookhaven National Laboratory, New York
C. D. Mobley
Sequoia Scientific Inc., Redmond, Washington
J. Porter
School of Ocean & Earth Science and Technology, University of Hawaii, Hawaii
L. Van Heukelem
University of Maryland Center for Environmental Science, Maryland
K. Voss
Physics Department, University of Miami, Florida

National Aeronautical and
Space administration

Goddard Space Flight Space Center
Greenbelt, Maryland 20771

February 2002

Preface

This document stipulates protocols for measuring bio-optical and radiometric data for the Sensor Intercomparison and Merger for Biological and Interdisciplinary Oceanic Studies (SIMBIOS) Project activities and algorithm development. This document supersedes the earlier version (Fargion and Mueller 2000) and is organized into four parts:

- *Introductory Background*: The initial part covers perspectives on ocean color research and validation (Chapter 1), fundamental definitions, terminology, relationships and conventions used throughout the protocol document (Chapter 2), and requirements for specific *in situ* observations (Chapter 3).
- *Instrument Characteristics*: This group of chapters begins with a review of instrument performance characteristics required for *in situ* observations to support validation (Chapter 4), and the subsequent chapters cover detailed instrument specifications and underlying rationale (Chapter 5) and protocols for instrument calibration and characterization standards and methods (Chapters 6 through 8).
- *Field Measurements and Data Analysis*: The methods used in the field to make the *in situ* measurements needed for ocean color validation, together with methods of analyzing the data, are briefly, but comprehensively, reviewed in Chapter 9. The remaining chapters of this part provide detailed measurement and data analysis protocols for in-water radiometric profiles (Chapter 10), the Marine Optical Buoy (MOBY) radiometric observatory for vicarious calibration of satellite ocean color sensors (Chapter 11), above water measurements of remote sensing reflectance (Chapter 12), determinations of exact normalized water-leaving radiance (Chapter 13), atmospheric radiometric measurements to determine aerosol optical thickness and sky radiance distributions (Chapter 14), determination of absorption spectra from water samples (Chapter 15), and determination of phytoplankton pigment concentrations using HPLC (Chapter 16) and fluorometric (Chapter 17) methods.
- *Data Reporting and Archival*: Chapter 18 describes the methods and procedures for data archival, data synthesis and merging, and quality control applicable to the SeaWiFS Bio-optical Archive and Storage System (SeaBASS), which is maintained to support ocean color validation for the SeaWiFS, SIMBIOS and other cooperating satellite sensor projects. Current SeaBASS file content and formatting requirements are given in Appendix B.

What is new in Revision 3 to the ocean optics protocol document, as compared to Revision 2 (Fargion and Mueller 2000). The most obvious changes are the insertion of 3 new chapters into the document, and the renumbering of the other chapters to accommodate them. The new chapters are:

1. Chapter 2, *Fundamental Definitions, Relationships and Conventions*, introduces the radiometric quantities, inherent optical properties, fundamental concepts and terminology underlying the *in situ* measurement and analysis protocols discussed throughout the document. The chapter also discusses the scales adopted in these protocols for such quantities as extraterrestrial solar irradiance, and the absorption and scattering coefficients of pure water.
2. Chapter 11, *MOBY, A Radiometric Buoy for Performance Monitoring and Vicarious Calibration of Satellite Ocean Color Sensors: Measurement and Data Analysis Protocols*, documents the specific measurement and data analysis protocols used in the operation of this critical radiometric observatory. The MOBY normalized water-leaving radiance time series has provided the principal, common basis for vicarious calibration of every satellite ocean color sensor in operation since 1996.
3. Chapter 13, *Normalized Water-Leaving Radiance and Remote Sensing Reflectance: Bidirectional Reflectance and Other Factors*, develops the physical basis underlying the bidirectional aspects of the ocean's reflectance, and presents methods for removing this effect to determine *exact normalized water-leaving radiance*, the only form of water-leaving radiance suitable for comparisons between determinations based on satellite and *in situ* measurements.

Aside from renumbering, several of the chapters carried over from Revision 2 have been revisited and significantly revised, while others have been modified only slightly. The two chapters providing overviews

of Instrument Characteristics (Chapter 4) and Field Measurements and Data Analysis (Chapter 9) have been revised to reflect the changed content of those two major parts of the document. Chapter 15, covering protocols for laboratory spectrophotometric determinations of absorption by particles and dissolved materials in seawater samples, has been significantly revised to condense the workshop results reported in the Revision 2 version into more focused descriptions of measurement and analysis protocols; the more detailed workshop results and background in the original version of this chapter (as cited in the present version) comprise the single case where material presented in Revision 2 is not completely superceded by the present document. Protocols for HPLC measurements of concentrations of phytoplankton pigments (Chapter 16) and fluorometric measurements of chlorophyll a concentration (Chapter 17) have been significantly updated and revised. Protocols for characterization of radiometers (Chapter 6) and for calibration of, and measurements using, sun photometers and sky radiance instruments (Chapters 7 and 14) have been updated significantly, but modestly, and modifications to the remaining chapters are all relatively minor.

Although the present document represents another significant, incremental improvement in the ocean optics protocols, there are several protocols that have either been overtaken by recent technological progress, or have been otherwise identified as inadequate. Some of the deficiencies and corrective steps that will be taken in Revision 4, scheduled for completion in 2002, include:

- The present state of the art in instruments and methods for determining *inherent optical properties* (IOP) is described only via abstract-level summaries in Chapters 4 and 9. A new chapter will provide more complete and up-to-date IOP related protocols.
- Another new chapter will address methods for *radiometric and bio-optical measurements from moored and drifting buoys*. These methods have much in common with, but also differ in many important respects from, those implemented for the highly specialized MOBY vicarious calibration observatory (Chapter 11).
- *Radiometric measurements from aircraft* are discussed at several points in the present protocols, but detailed methods are nowhere discussed. A third new chapter will be included in Revision 4 to rectify this omission.
- Recent advances, at the National Institute of Standards and Technology (NIST), in radiometric standards, methods of calibration, and stray light characterization have outdated much of the material in the current protocols for characterization of radiometers (Chapter 6). Key improvements relate to the *NIST 2000 detector based scale of spectral irradiance*, and the *NIST Spectral Irradiance and Radiance responsivity Calibrations with Uniform Sources (SIRCUS)* facility. An important goal for Revision 4 is to update the characterization protocols of Chapter 6 to reflect these state-of-the-art methods.

This technical report is not meant as a substitute for scientific literature. Instead, it will provide a ready and responsive vehicle for the multitude of technical reports issued by an operational Project. The contributions are published as submitted, after only minor editing to correct obvious grammatical or clerical errors.

Table of Contents and Author List

CHAPTER 11 ..... **138**

MOBY, A RADIOMETRIC BUOY FOR PERFORMANCE MONITORING AND VICARIOUS CALIBRATION OF SATELLITE OCEAN COLOR SENSORS: MEASUREMENT AND DATA ANALYSIS PROTOCOLS
Dennis K. Clark, Mark A. Yarbrough, Mike Feinholz, Stephanie Flora, William Broenkow, Yong Sung Kim, B. Carol Johnson, Steven W. Brown, Marilyn Yuen and James L. Mueller

CHAPTER 12 ..... **171**

ABOVE-WATER RADIANCE AND REMOTE SENSING REFLECTANCE MEASUREMENT AND ANALYSIS PROTOCOLS
James L. Mueller, Curtiss Davis, Robert Arnone, Robert Frouin, Kendall Carder, Z.P. Lee, R.G. Steward, Stanford Hooker, Curtis D. Mobley and Scott McLean

CHAPTER 13 ..... **183**

NORMALIZED WATER-LEAVING RADIANCE AND REMOTE SENSING REFLECTANCE: BIDIRECTIONAL REFLECTANCE AND OTHER FACTORS
Andre Morel and James L. Mueller

CHAPTER 14 ..... **211**

SUN AND SKY RADIANCE MEASUREMENTS AND DATA ANALYSIS PROTOCOLS
Robert Frouin, Brent Holben, Mark Miller, Christophe Pietras, Kirk D. Knobelspiesse, Giulietta S. Fargion, John Porter and Ken Voss

CHAPTER 15 ..... **231**

DETERMINATION OF SPECTRAL ABSORPTION COEFFICIENTS OF PARTICLES, DISSOLVED MATERIAL AND PHYTOPLANKTON FOR DISCRETE WATER SAMPLES
B. Greg Mitchell, Mati Kahru, John Wieland and Malgorzata Stramska

CHAPTER 16 ..... **258**

HPLC PHYTOPLANKTON PIGMENTS: SAMPLING, LABORATORY METHODS, AND QUALITY ASSURANCE PROCEDURES
Robert R. Bidigare, Laurie Van Heukelem and Charles C. Trees

CHAPTER 17 ..... **269**

FLUOROMETRIC CHLOROPHYLL A: SAMPLING, LABORATORY METHODS, AND DATA ANALYSIS PROTOCOLS
Charles C. Trees, Robert R. Bidigare, David M. Karl Laurie Van Heukelem and John Dore

CHAPTER 18 ..... **284**

SEABASS DATA PROTOCOLS AND POLICY
P. Jeremy Werdell, Sean Bailey and Giulietta S. Fargion

APPENDIX A **288**

CHARACTERISTICS OF SATELLITE OCEAN COLOR SENSORS: PAST, PRESENT AND FUTURE
Giulietta S. Fargion

APPENDIX B **292**

SEABASS FILE FORMAT.
P. Jeremy Werdell, Sean Bailey and Giulietta S. Fargion

APPENDIX C **299**

LIST OF ACRONYMS
James L. Mueller

APPENDIX D 303

FREQUENTLY USED SYMBOLS
James L. Mueller

Chapter 11

MOBY, A Radiometric Buoy for Performance Monitoring and Vicarious Calibration of Satellite Ocean Color Sensors: Measurement and Data Analysis Protocols

Dennis K. Clark[1], Mark A. Yarbrough[2], Mike Feinholz[2], Stephanie Flora[2], William Broenkow[2], Yong Sung Kim[3], B. Carol Johnson[4], Steven W. Brown[4], Marilyn Yuen[1], and James L. Mueller[5]

[1]*NOAA National Environmental Satellite Data Information Service, Suitland, Maryland*
[2]*Moss Landing Marine Laboratory, California*
[3]*Data Systems Technologies, Inc., Rockville, Maryland*
[4]*National Institute of Standards and Technology, Gaithersburg, Maryland*
[5]*Center for Hydro-Optics and Remote Sensing, San Diego State University, California*

11.1 INTRODUCTION

The Marine Optical Buoy (MOBY) (Clark *et al.* 1997) is the centerpiece of the primary ocean measurement site for calibration of satellite ocean color sensors based on independent *in situ* measurements. Since late 1996, the time series of normalized water-leaving radiances $L_{WN}(\lambda)$ determined from the array of radiometric sensors attached to MOBY are the primary basis for the on-orbit calibrations of the USA Sea-viewing Wide Field-of-view Sensor (SeaWiFS), the Japanese Ocean Color and Temperature Sensor (OCTS), the French Polarization Detection Environmental Radiometer (POLDER), the German Modular Optoelectronic Scanner on the Indian Research Satellite (IRS1-MOS), and the USA Moderate Resolution Imaging Spectrometer (MODIS). The MOBY vicarious calibration $L_{WN}(\lambda)$ reference is an essential element in the international effort to develop a global, multi-year time series of consistently calibrated ocean color products using data from a wide variety of independent satellite sensors.

A longstanding goal of the SeaWiFS and MODIS (Ocean) Science Teams is to determine satellite-derived $L_{WN}(\lambda)$ with a relative combined standard uncertainty[1] of 5 % (Chapter 1). Other satellite ocean color projects and the Sensor Intercomparison for Marine Biology and Interdisciplinary Oceanic Studies (SIMBIOS) project have also adopted this goal, at least implicitly. Because water-leaving radiance contributes at most 10 % of the total radiance measured by a satellite sensor above the atmosphere (Gordon 1997), a 5 % uncertainty in $L_{WN}(\lambda)$ implies a 0.5 % uncertainty in the above-atmosphere radiance measurements. This level of uncertainty can only be approached using "vicarious-calibration" approaches as described below. In practice, this means that the satellite radiance responsivity is adjusted to achieve the best agreement, in a least-squares sense, for the $L_{WN}(\lambda)$ results determined using the satellite and the independent optical sensors (*e.g.* MOBY). The end result of this approach is to implicitly absorb unquantified, but systematic, errors in the atmospheric correction, incident solar flux, and satellite sensor calibration into a single correction factor to produce consistency with the *in situ* data (see *e.g.* Gordon 1981, 1987, 1988).

Clearly, the combined standard uncertainty of the *in situ* $L_{WN}(\lambda)$ determinations must be less than 5 % if the stated uncertainty goal is to be approached. The uncertainty budget of MOBY $L_{WN}(\lambda)$ determinations may be divided into environmental and radiometric factors. Environmental factors include uncertainties

[1] All uncertainties in this document are standard uncertainties, unless noted otherwise. Standard uncertainty is the uncertainty of the result of a measurement expressed as a standard deviation (Taylor and Kuyatt 1994).

due to radiance and irradiance fluctuations associated with surface waves and platform motions during the radiometric measurements, and with extrapolation of upwelling radiance measurements from depths of 1 m or more to, and through, the sea surface. The uncertainties associated with these ambient conditions have been shown to be less than, but approaching, 5 % for upwelled radiance (Siegel *et al.* , 1995; Hooker and Maritorena, 2000). Radiometric uncertainty components associated with instrument characterization, calibration and stability, *i.e.* the radiance measurements *per se*, must be summed in quadrature to yield the combined standard uncertainty of the MOBY $L_{WN}(\lambda)$ determinations.

The estimated combined standard uncertainty of MOBY radiance measurements is between 4 % and 8 % (Clark *et al.* 2001). This estimate is based on uncertainties of MOBY calibrations at less than 3 %, changes in pre- and post-deployment calibrations ranging from 1 % to 6 %, radiometric stability tests during deployments using internal reference sources that show changes less than 1 %, and diver-deployed external reference lamp responses that are stable within less than 3 % (the estimated uncertainty of the method) (Clark *et al.* 2001). The 8 % upper limit on the combined standard uncertainty estimate does not include preliminary results of recently undertaken stray light characterization of the MOBY spectrographs, which indicate systematic stray light offsets in $L_{WN}(\lambda)$ may have approximate magnitudes of +5 % and -3 % at blue and green wavelengths respectively (Sects. 11.4 and 11.8 below, and Clark *et al.* 2001). Once the stray light characterization is completed on all MOBY spectrographs, the entire MOBY $L_{WN}(\lambda)$ time series will be reprocessed with an expected combined standard uncertainty of less than 5 %. Variations in the measurement environment may add additional uncertainty.

The nature of, and data requirements for, vicarious calibration of a satellite ocean color sensor are briefly described in Chapter 1 (Sect. 1.5), and in more detail by Gordon (1981, 1987, 1988, 1997), Gordon *et al.* (1983), Evans and Gordon (1994), and Clark *et al.* (1997). A critical element of the procedure is the ability to monitor a satellite sensor's performance at daily to weekly intervals by comparing its derived $L_{WN}(\lambda)$ with concurrently derived *in situ* $L_{WN}(\lambda)$ meeting the uncertainty criteria described above. The most direct way of measuring $L_{WN}(\lambda)$ on a continuing daily basis over periods of several years is to utilize a specially designed array of radiometers mounted on a moored buoy. This buoy must be designed to mount the optical collectors well away from platform shading and reflections, artifacts similar to ship shadow, as discussed in Chapter 10 (Sect. 10.2). To minimize uncertainties due to extrapolation of upwelling radiance $L_u(z,\lambda)$ to the sea surface, the buoy must be moored at a location with consistently transparent case 1 waters and with negligible mesoscale to sub-mesoscale spatial variability. To assure frequent occurrences of matched satellite and buoy measurements, the site must be cloud free throughout most of the year. The mooring must be located close to an island based sun photometer and sky radiance sensor to allow concurrent determinations of aerosol optical thickness and sky radiance distribution. On the other hand, the atmospheric conditions at the mooring location must not be significantly influenced by the island's wake. Extraordinary calibration maintenance procedures are needed to assure low uncertainties in the buoy's radiometric measurements. In addition, comparative shipboard measurements must be made near the buoy to check the radiometric stability of its instrumentation, to determine spatial variability surrounding the buoy location, and to develop and validate bio-optical algorithms. Some of these measurements can be made during cruises staged to replace the mooring at 3 to 4 month intervals, but dedicated cruises of 1 to 2 week duration are also required. The logistical demands of buoy maintenance, calibration activities, deployment and relief, and ship support operations strongly argue for placing the buoy conveniently near a permanent support facility. The locations of the MOBY mooring, near the island of Lanai, and the associated support facilities in Honolulu, Hawaii closely satisfy all of the above conditions.

The radiometric measurements at a primary reference site for vicarious calibration of satellite ocean color sensors differ in several aspects from the radiometric in-water profiling methods described in the Chapter 10. A primary reference data set must consist of *in situ* determinations of band-averaged $L_{WN}(\lambda)$'s that reproduce the spectral response functions of each satellite sensor's bands with more accuracy than can be realized using off the shelf radiometers. The need for flexibility in the choice of spectral response weighting functions used to determine band-averaged $L_{WN}(\lambda)$ imposes a requirement for full-spectrum measurements with resolutions <1 nm. Instead of measuring radiometric profiles resolved at several samples per m (Chapter 10, Sect. 10.2), downwelling irradiance $E_d(z,\lambda)$ and upwelling radiance $L_u(z,\lambda)$ can be measured on a buoy at only a few fixed depths, which complicates the problem of accurately determining $L_u(0^-,\lambda)$ (just below the sea surface).

To be affordable, a moored array must typically be deployed and operated semi-autonomously for periods of 3 to 4 months. Provisions to assure radiometric stability through these extended period operations should include, as a minimum, pre- and post-deployment calibrations of all radiometers, combined with continuous monitoring of on-board light sources of known stability. Moreover, instruments suspended in seawater for periods of this duration experience fouling by biological organisms that, if not countered effectively using antifouling methods and frequent cleaning by divers, seriously degrade the performance of optical sensors. Affordable servicing and maintenance during each deployment is limited to *circa* monthly visits by divers to clean instruments, check sensor calibrations against portable underwater lamp sources, and perform minimal maintenance.

Because of these uniquely different measurement requirements, platform related geometry, instrument characteristics, and operational conditions, the protocols applying to the MOBY instruments and methods of measurement and data analysis are presented separately in the present chapter. Where appropriate, certain protocols will be defined and described by reference to other chapters. This chapter documents the protocols used by the MOBY Operations Team to measure and derive the MOBY data sets that consist of the $L_{WN}(\lambda)$ time series. The information is intended as background for those wishing to apply this data to validate water-leaving radiances from one or more satellite ocean color sensors.

11.2 THE MOBY PRIMARY VICARIOUS CALIBRATION SITE

The primary components of the MOBY vicarious calibration site are located as shown in Fig. 11.1. A MOBY is continuously moored approximately 20 km west of the island of Lanai in 1200 m of water. During prevailing trade wind conditions, this location is sheltered in the lee of the island, yet it is far enough offshore to minimize atmospheric perturbations associated with the island's wake. CIMEL[2] sun photometers on Lanai and Oahu, operated by the Aerosol Robotic Network (AERONET) Project (Chapters 7 and 14), provide time series measurements of aerosol optical thickness and sky radiance distributions that are required to reduce the uncertainty budgets of atmospheric correction models used during vicarious calibration analyses. The MOBY Operation Site, located at the University of Hawaii (UH) Marine Facility in Honolulu, is staffed full time by personnel from the Moss Landing Marine Laboratory (MLML) for buoy maintenance, instrument maintenance and calibration, and for staging buoy relief and bio-optical sampling cruises. The UH's research vessels are used for cruises to support buoy deployments (L-series cruises identified in Table 11.1), Marine Optical Characterization Experiments (MOCE-series), and interim maintenance and quality control operations. During the MOCE and some L-series cruises (Table 11.1), *in situ* bio-optical measurements are made to validate MOBY $L_{WN}(\lambda)$ determinations, to characterize spatial variability near the mooring, and to develop and validate bio-optical algorithms. A subset of the MOBY data is transmitted, in real time via cellular telephone, to the MLML in California. The MOBY data are processed at MLML to produce and extract appropriately weighted band-averaged $L_{WN}(\lambda)$'s for SIMBIOS and SeaWiFS Project Offices at the National Aeronautics and Space Administration (NASA) Goddard Space Flight Center (GSFC), and/or to the MODIS Team at the University of Miami.

MOBY and the Marine Optical System (MOS)

MOBY is a 12 m spar buoy (including the lower instrument bay) uniquely designed as an optical bench for measurements of $E_d(z,\lambda)$ and $L_u(z,\lambda)$ at depths of 1 m, 5 m, 9 m, and 12 m (Fig. 11.2). The features of MOBY are summarized in Table 11.2. Fig. 11.3 is a schematic illustration of the MOBY system's sensors, operations and communications, while the mechanical layouts of the upper and lower instrument bays are illustrated in Fig. 11.4 and Fig. 11.5, respectively. The MOBY spar is tethered to a second surface buoy, which is slack moored, *i.e.* isolated by subsurface floats, to an anchor on the sea floor (Fig. 11.6). Sensors for wind speed, wind direction, air temperature, relative humidity, and barometric pressure are mounted on the main mooring buoy.

[2] Certain commercial equipment, instruments, or materials are identified in this document to foster understanding. Such identification does not imply recommendation or endorsement by the National Institute of Standards and Technology, nor does it imply that the materials or equipment identified are necessarily the best available for the purpose.

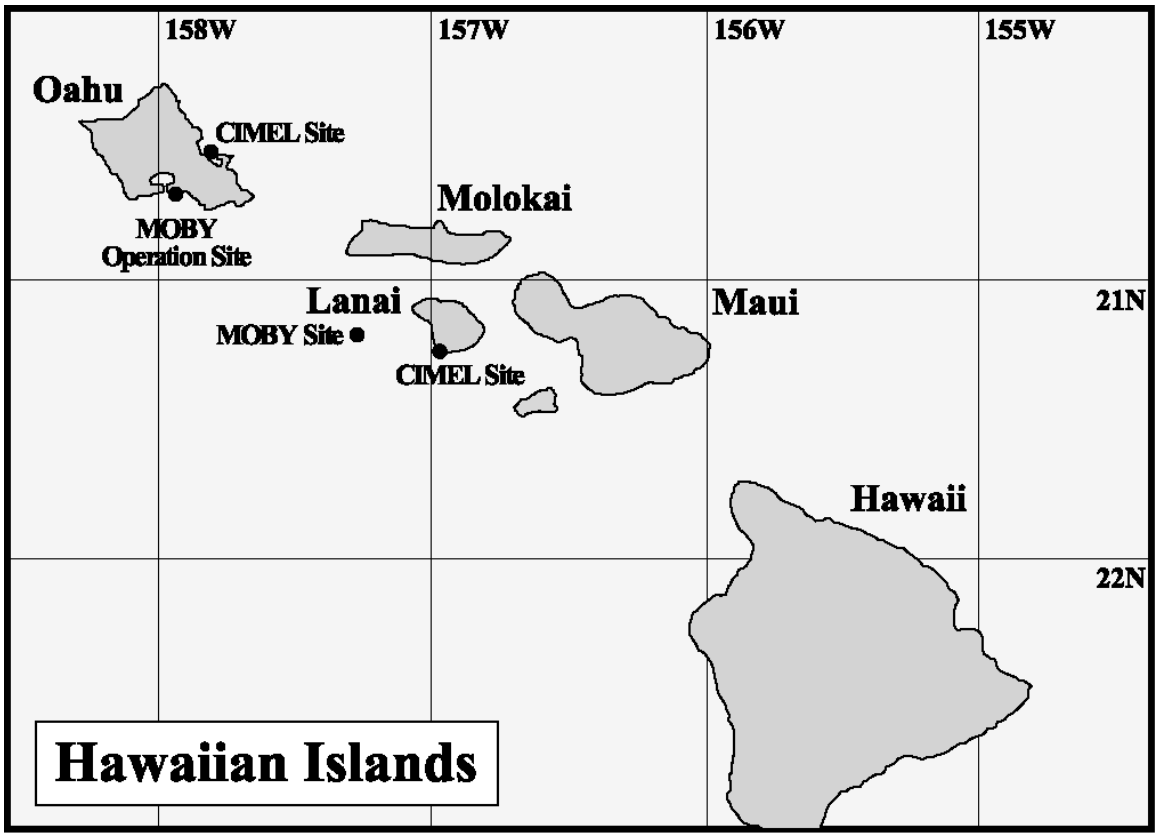

Figure 11.1: Chart showing locations of the MOBY mooring, the two CIMEL robotic sun photometers on Oahu and Lanai, cell phone relay stations used for data communications, and the MOBY Operations Site in Honolulu, Hawaii.

The Marine Optical System (MOS), the heart of MOBY, consists of two single-grating CCD spectrographs connected via an optical multiplexer and fiber optic cables to the $E_d(z,\lambda)$ and $L_u(z,\lambda)$ optical heads mounted at the ends of the buoy's 3 standoff arms (Fig. 11.2 and Fig. 11.3). To provide low-loss transmission at ultraviolet wavelengths, 1 mm diameter silica fiber-optic cables are used to connect the optical heads to MOS. $L_u(12,\lambda)$, at z = 12 m, is measured through a window in the bottom of the MOS housing itself. A seventh fiber optic cable connects a surface irradiance $E_s(\lambda)$ cosine collector, mounted at the top of the MOBY above-water mast, to the spectrographs. Each pair of in-water optical heads is mounted on a standoff arm to minimize radiometric artifacts due to shadows or reflections from the buoy. To minimize self-shading by the $L_u(z,\lambda)$ radiometer (Chapter 10, Sect. 10.4; Gordon and Ding 1992), the underwater housings for the optical heads are very small in diameter (7 cm).

The principal characteristics of MOS are summarized in Table 11.3. The MOS system elements and optical layout are illustrated schematically in Fig. 11.7 and Fig. 11.8, respectively. Light from an $L_u(z,\lambda)$, $E_d(z,\lambda)$, or $E_s(\lambda)$ head enters the spectrograph package via its fiber optic cable and the multiplexer, is directed to a dichroic mirror that reflects light at wavelengths between 350 nm and 630 nm into one (blue) grating spectrograph, and transmits wavelengths greater than 630 nm to the other (red) spectrograph. The MOS spectrograph package is mounted in MOBY's lower instrument bay (Fig. 11.5), at a depth of approximately 12 m, primarily to isolate the package from the shock and vibration that surface waves inflict on the upper instrument bay. The deeper location also facilitates heat dissipation from the thermoelectric coolers used to maintain the operating temperature of the CCD arrays, and $L_u(12,\lambda)$ may be measured through the MOS optical window at the very bottom of the MOBY spar. Even more critically,

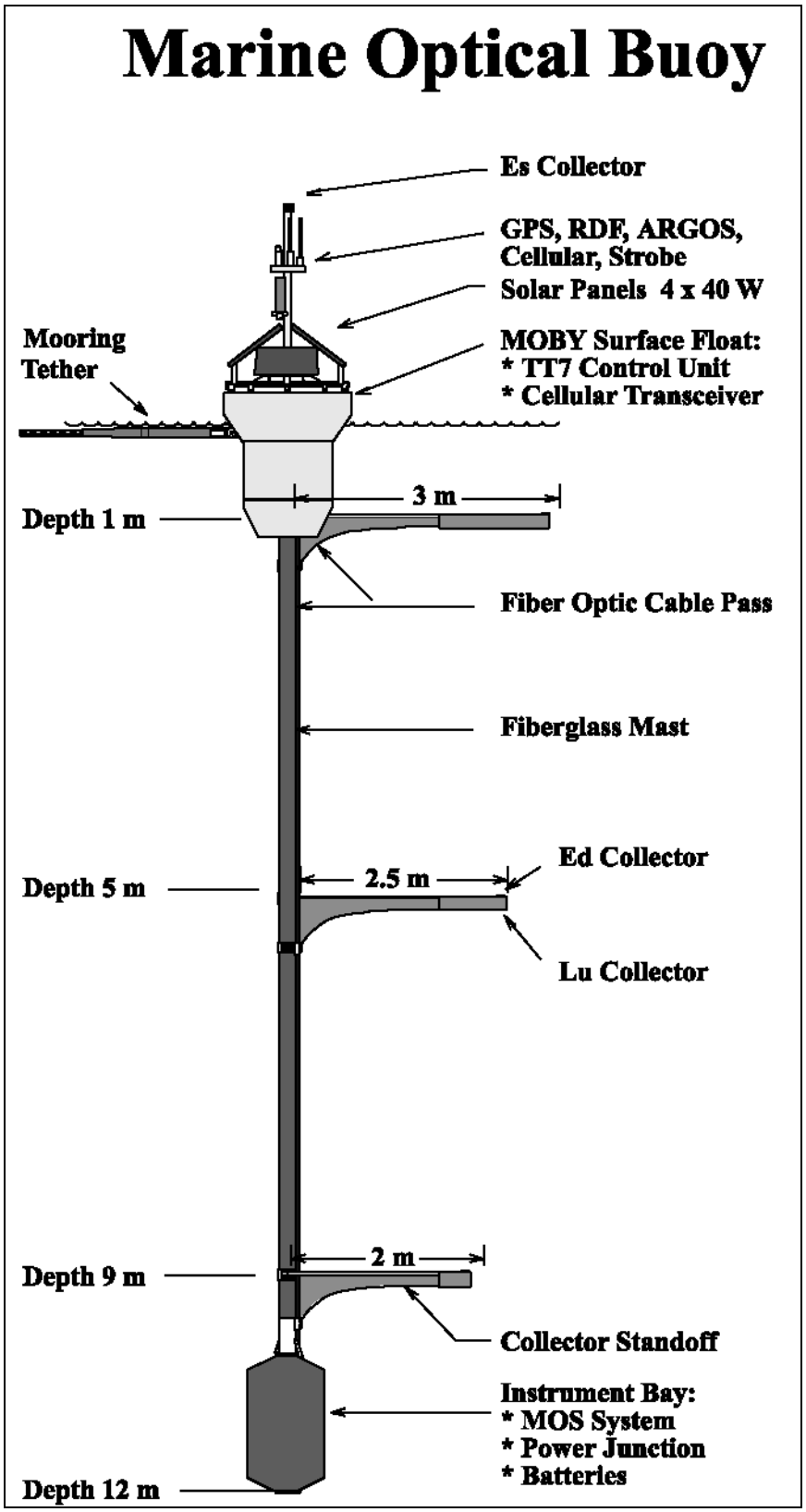

Figure 11.2: The Marine Optical Buoy (MOBY).

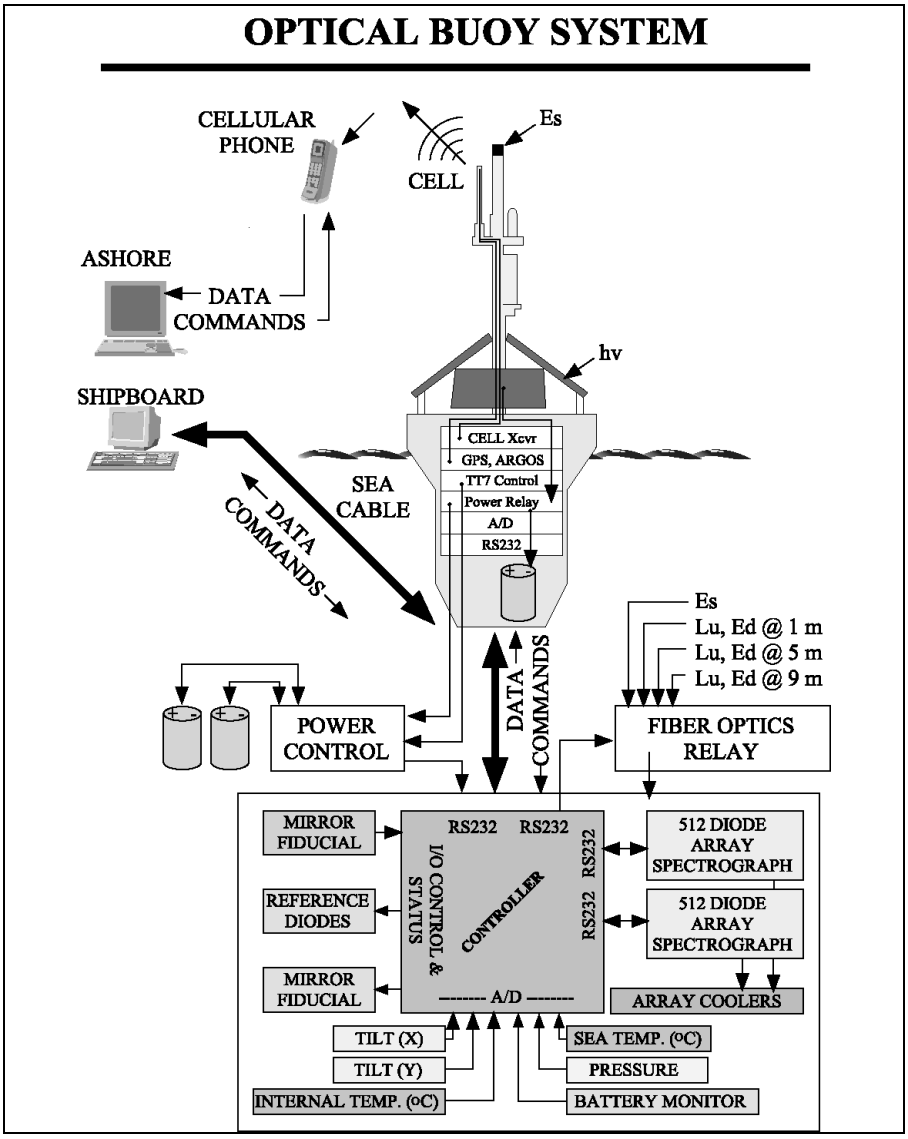

Figure 11.3: A schematic overview of the MOBY system elements.

the high current draw of the MOS requires that it be located close to the batteries, which themselves must be placed at the bottom of the spar to act as stabilizing ballast.

The elements defining the spectral radiometric characteristics of each of the spectrographs are the entrance slit, holographic grating, and cooled CCD detector array (Fig. 11.8). For the blue spectrograph (350 nm to 630 nm), the full-width at half-maximum (FWHM) bandpass of the spectral slit response function centered at any given wavelength is approximately 2 nm, and the 512 element detector array is designed to sample at approximately a 0.6 nm interval. The MOS was designed with such high spectral resolution to support vicarious calibrations of a variety of different satellite ocean color sensors (Appendix A). By measuring *in situ* spectra of $L_u(\lambda,z)$ at this resolution, it is practical to compute band-averaged values of $L_{WN}(\lambda)$ that are appropriately weighted for any of these satellite ocean color sensors.

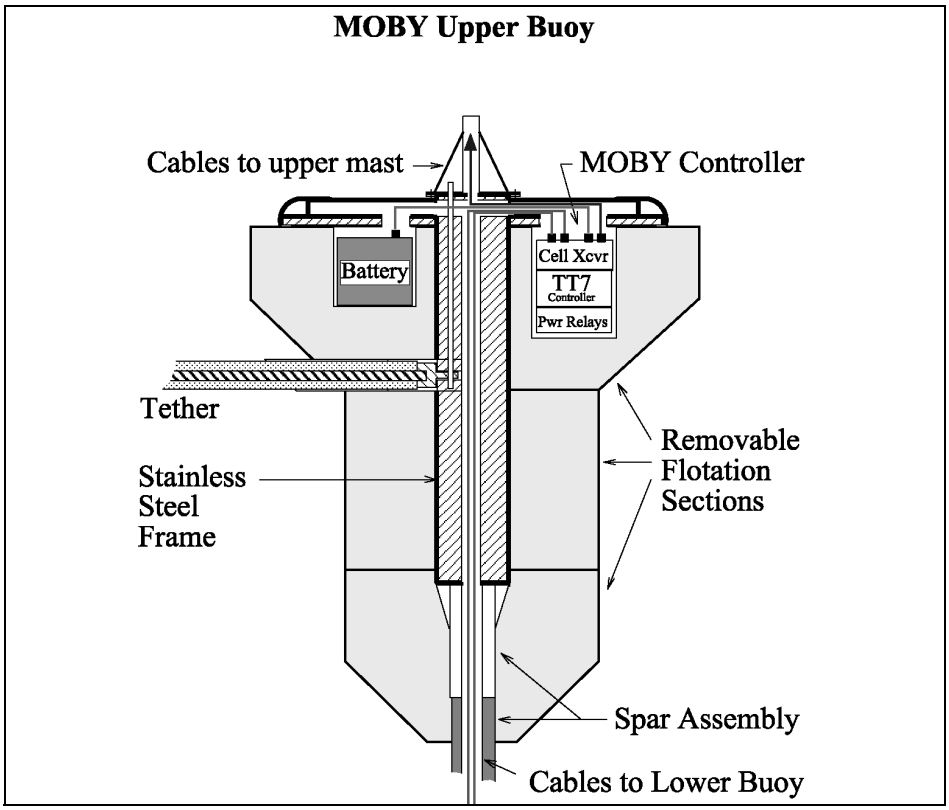

Figure 11.4: The MOBY flotation and upper instrument bay assembly.

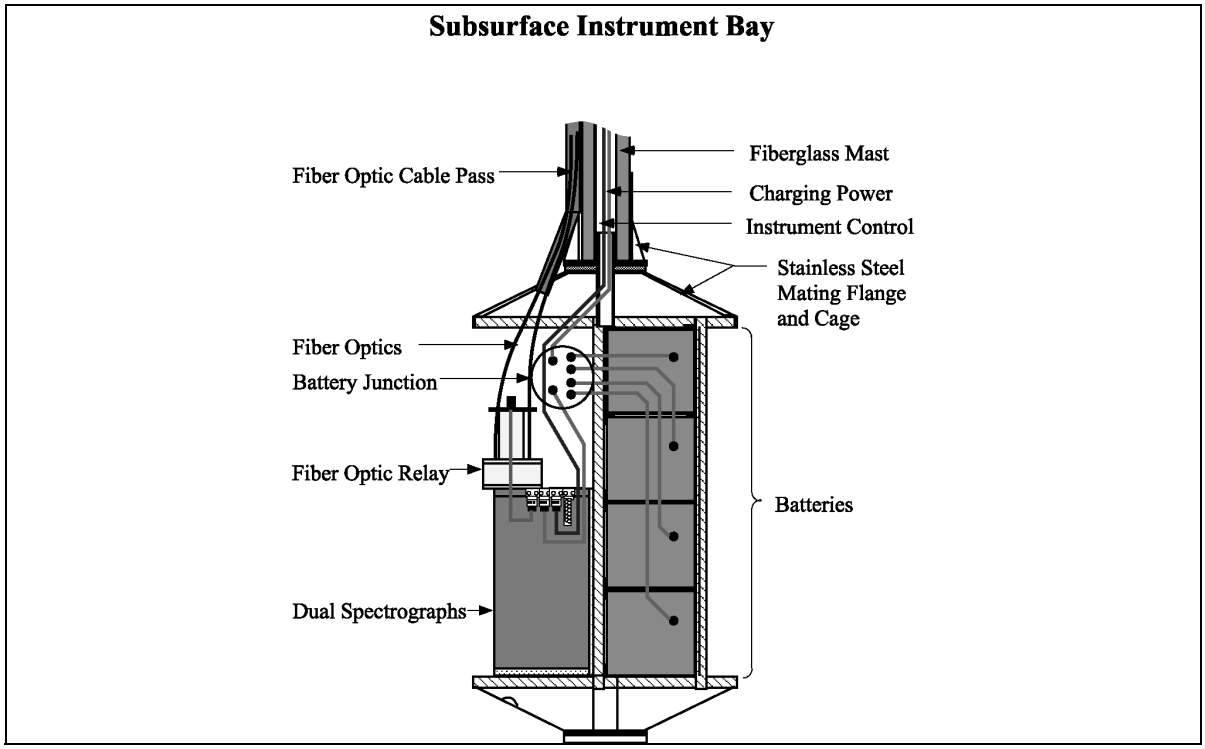

Figure 11.5: A schematic diagram illustrating the mechanical layout of the subsurface instrument and battery bay on MOBY.

Ancillary Measurements on MOBY

The principal navigation (latitude and longitude) and UTC (Universal Time, Coordinated) clock reference are determined from the Global Positioning System (GPS) receiver mounted in the MOBY upper instrument bay (Fig. 11.3 and Table 11.2). A secondary navigational position is provided by the System ARGOS transmitter, which is also installed in the upper bay (Fig. 11.3) and provides frequent MOBY position updates as a precaution against losing the buoy should the mooring fail. On two occasions, in fact, the MOBY array did break away from its moorings and was recovered safely thanks to the ARGOS tracking capability. Additional ancillary sensors are installed in the MOS package:

- Internal housing and CCD array temperatures are measured as indicators of performance quality, and may be used in applying radiometric calibration factors to the data.
- A high precision pressure transducer is installed on the top radiometric arm (Fig. 11.2) to determine depth variations [$z(t)$ - z_P] about its nominal reference depth z_P (fixed by its location on the spar) during each radiometric measurement sequence. A separate temperature sensor monitors the temperature of the pressure transducer, to minimize uncertainties in the depth determinations.
- Tilt sensors within the MOS package are used to determine the 2-axis orientation (pitch and yaw) of the MOBY spar relative to the local vertical. A flux gate compass, also installed within the MOS package, is used to determine the direction (magnetic) in which the radiometric sensor arms extend out from the spar. The relative angle between the spar pointing azimuth and the solar azimuth are used to detect measurement geometries in which the irradiance and radiance collectors may be influenced by shadows, or reflections, from the main MOBY structure.

Mooring Buoy Measurements

Sensors mounted on the mast of the mooring buoy measure wind velocity, surface barometric pressure, air temperature, and relative humidity (Fig. 11.6). Also, near surface sensors on this buoy measure water temperature and conductivity, and chlorophyll *a* fluorescence.

Data Communications

Data from the MOS and other sensors mounted on MOBY are assembled into data records, and annotated with time, latitude and longitude as based on GPS input, by the Tattletale[2] (Model TT7) microcomputer installed in the upper instrument bay (Table 11.2, Fig. 11.3 and Fig. 11.4). Data records are stored on hard disk for download when the MOBY is recovered and replaced at the end of a deployment. The microcomputer also transmits the data records over the cellular phone link to MLML in California. Normally, 99 % of the data are recovered via telemetry. Data from the meteorological sensors on the mooring buoy are similarly processed autonomously by a microcomputer. All data records are stored on hard disk and are downloaded once daily.

11.3 MOBY OPERATIONS AND MEASUREMENT METHODS

Deployment Schedule and Methods

There are two complete MOBY systems, one of which is moored and operational at any given time. The history of MOBY deployments, and key events associated with each, are summarized in Table 11.4. The typical duration of a single mooring deployment is between 3 and 4 months. During this period, the other MOBY is maintained and refurbished and its MOS recalibrated. At approximately monthly intervals during a deployment, the Operations Team visits the MOBY mooring site using a small boat launched from the island of Maui. During these interim visits, divers clean the optical collectors and use a specially designed underwater lamp reference source to check the radiometric stability of the deployed MOS (Sect. 11.4). During these “interim-servicing” cruises, water samples are filtered for phytoplankton pigment analyses, for comparison with pigment concentration determinations using the MOBY radiometric measurements. These pigment concentration comparisons are made to validate the pigment algorithms associated with the various satellite ocean color sensors.

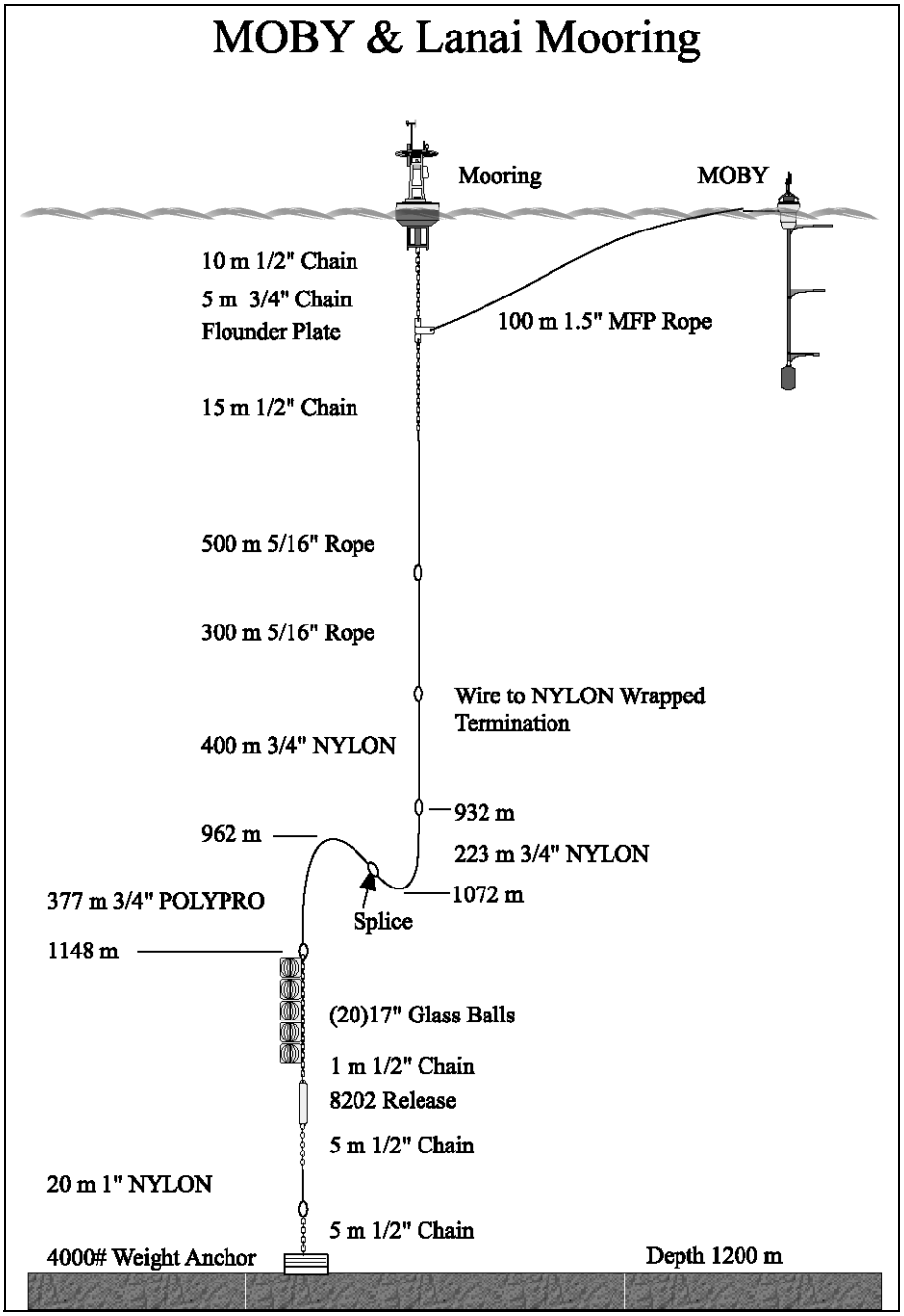

Figure 11.6: The MOBY mooring configuration.

When the time comes to exchange the MOBY systems, the replacement buoy is loaded aboard a research vessel and transported to the mooring site. On arriving at the site, the recalibrated and refurbished replacement MOBY is first deployed and set adrift (Fig. 11.9). Divers release the tether connecting the moored MOBY to the mooring buoy. The replacement buoy is then towed into position by the divers

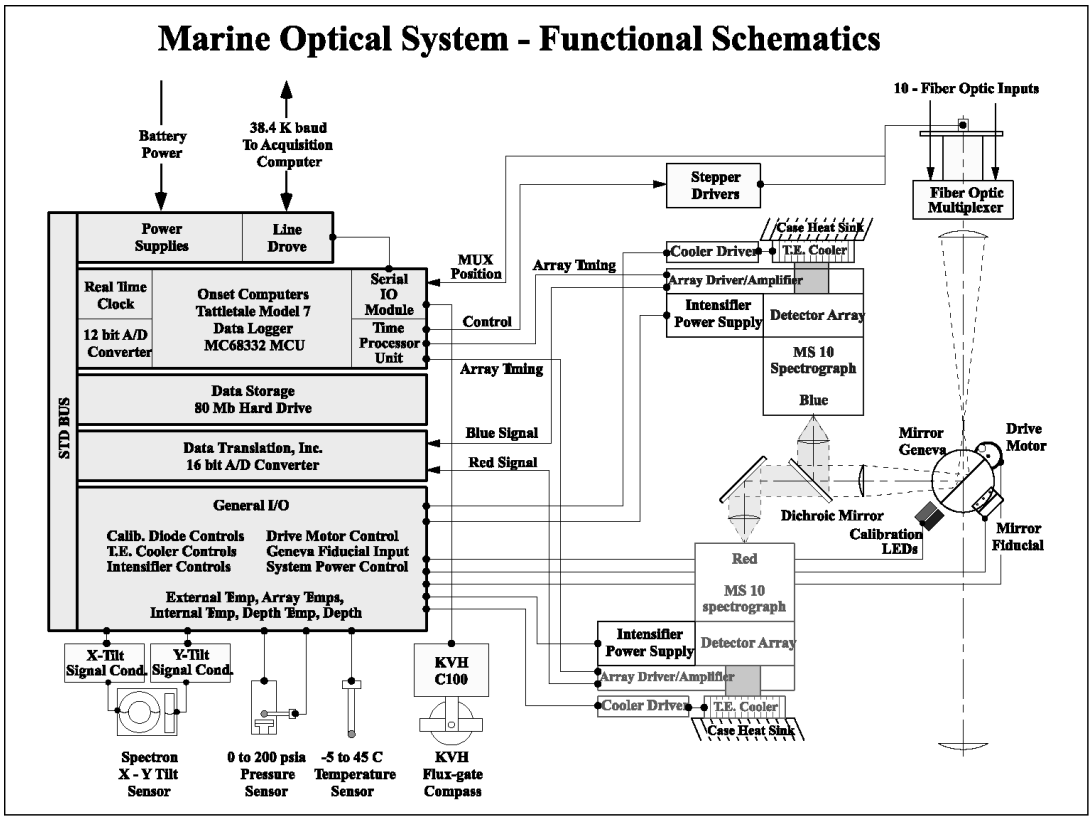

Figure 11.7: A schematic diagram of the MOS functional elements.

(operating from a support boat) and connected to the mooring. When possible, in-water radiometric measurements are made with both MOBY systems as a final check on the stability of the recovered system. Finally, the recovered MOBY is secured aboard the ship for its return to the MOBY Operations Site in Honolulu. The entire mooring (Fig. 11.6) is replaced at approximately 1-year intervals (Table 11.4). On these occasions, the acoustic release (Fig. 11.6) is activated to free the mooring line and its flotation from its anchor. A new anchor and surface mooring buoy are deployed, and a MOBY is tethered to it.

MOCE and Other Validation Shipboard Operations

On some of the MOBY replacement cruises ("L-cruises" in Table 11.1), additional ship time is used to make "Required" and "Highly Desired" radiometric and bio-optical measurements (Chapter 3, Table 3.1), both for radiometric validation of the MOBY and satellite ocean color sensor measurements, and for algorithm development and validation.

Complementing the MOBY project are the MOCE cruises, which are carried out primarily to support vicarious calibration and validation of satellite ocean color sensors. The MOCE team is comprised of scientists from the National Oceanic and Atmospheric Administration/National Environmental Satellite Data Information Service (NOAA/NESDIS), MLML, San Diego State University, and the University of Miami (Florida). MOCE cruises, which are typically between 10 and 30 days in duration, have been conducted in the general vicinity of the MOBY site and off the west coast of North America (Table 11.1).

Measurements acquired during the MOCE cruises are generally more extensive than those made during the "L-cruises". As an example, measurements made during MOCE-5 are listed in Table 11.5, which includes all of the "Required", nearly all of the "Highly Desired" and some of the "Specialized Measurements" categories of variables listed in Table 3.1 (Chapter 3). Protocols for most of these measurements and analyses conform to those described elsewhere in this document. However, protocols

are not provided elsewhere for two of the specialized measurements listed in Table 11.5, “Instrument Self-Shading” and “Particle Size Distribution”, nor are measurements of these variables identified in Chapter 3.

The effects of instrument self-shading on upwelling radiance and irradiance measurements are discussed briefly in Chapter 4 (Sect. 4.2), and provisional protocols (based on Gordon and Ding 1992) for removing self-shading effects from measurements are described in Chapter 10 (Sect. 10.4). Direct measurements of the self-shading phenomenon are made during MOCE cruises (Table 11.5) to test the predictions of Gordon and Ding (1992) and determine relative uncertainties under a variety of ambient illumination conditions. A Fiber Optic Spectrometer (FOS) was developed using two modified American Holographic AH4000 series dual-beam spectrometers, one configured for radiometric measurements spanning the wavelength range from 375 nm to 725 nm at 5 nm resolution, and the other from 600 nm to 1100 nm at 10 nm resolution. The spectrometers are placed in a pressure housing and are coupled by fiber-optic leads to upwelling radiance and downwelling irradiance collectors that are located approximately 1 m away to minimize shading and reflection effects. The upwelling radiance probe is ~5 cm in diameter, and the self-shading effect is varied by attaching discs of increasing diameter to it.

Particle size distributions are measured using a commercial (Spectrex) laser particle counter. Particle counts, binned by size, are determined by measuring the magnitude of reflections from particles in a small working volume of water illuminated by a Helium-Neon diode (670.8 nm) LASER. The working volume, which is embedded in a 100 ml water sample, and its geometry are defined by the optical elements of the instrument. The water sample is agitated with a magnetic stirrer to keep particles in suspension during the measurements. The protocols used for determining particle size distributions are those provided by the manufacturer of the Spectrex, which claim to resolve particle sizes as small as 1 μm. On the other hand, the assumptions underlying the method are that the individual particles are separated by distances large compared to the wavelength of illumination, and that particle diameters are at least 5 times larger than the wavelength, so that particle reflection is governed by geometric optics. Other investigators have used the Spectrex instrument to measure particle size distributions, but a community consensus has yet to be developed for protocols related to this measurement and its interpretation.

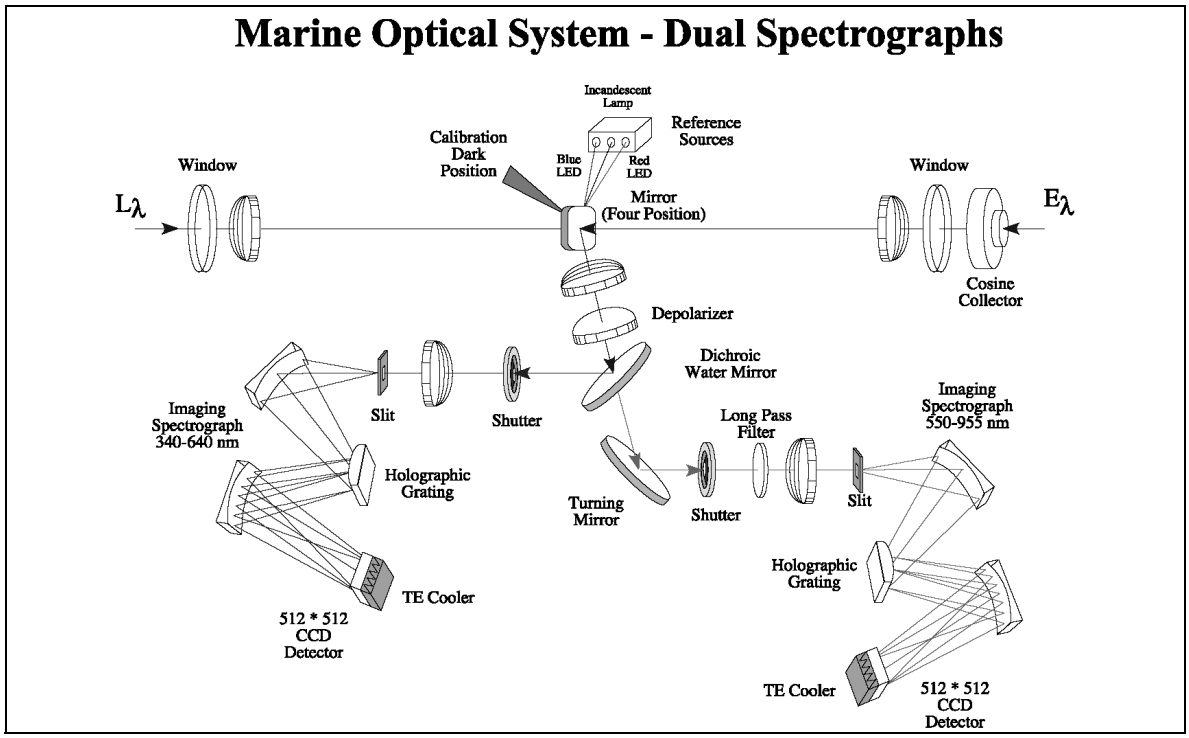

Figure 11.8: A schematic diagram showing the optical design of the MOS spectrographs.

Figure 11.9: Deployment of a MOBY.

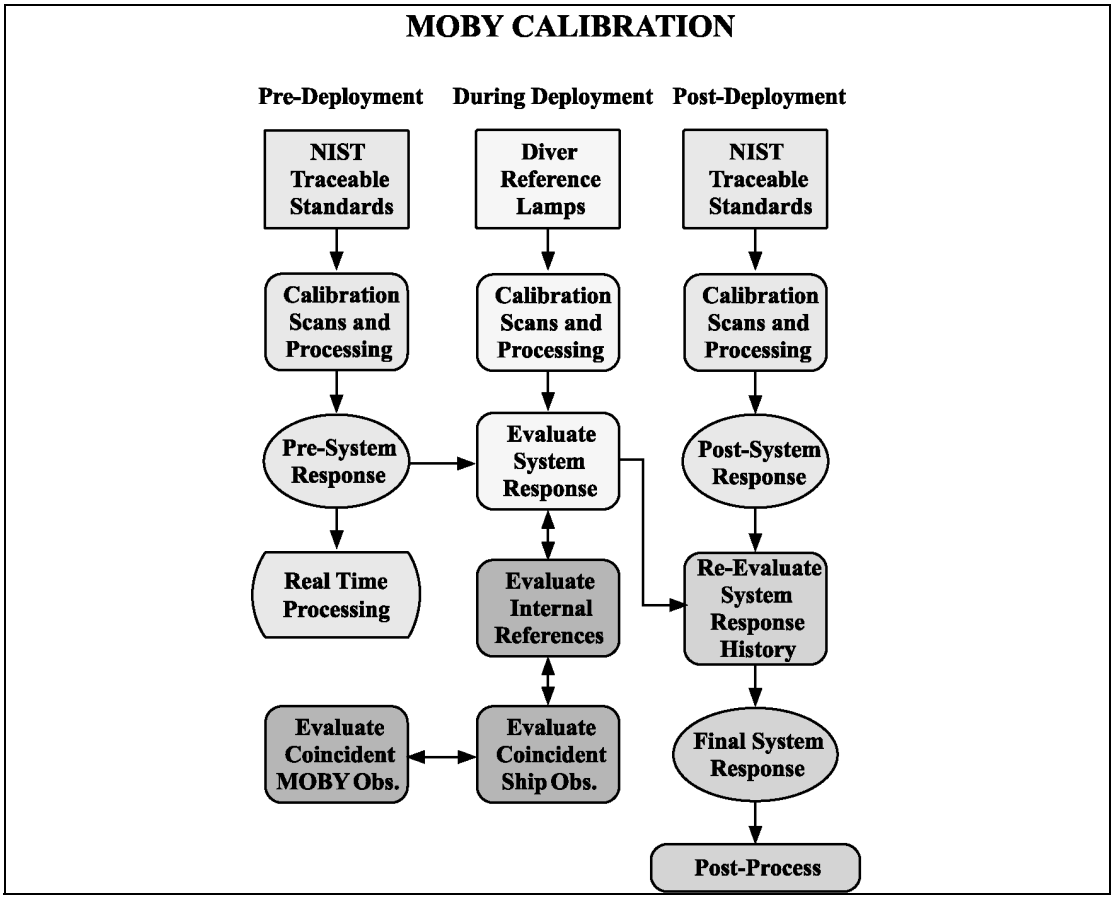

Figure 11.10: MOBY radiometric calibration and system stability check flow chart.

Figure 11.11: The diver-deployed underwater radiometric stability reference unit attached to an upwelling radiance collector on MOBY.

MOBY System Operations Scheduling

MOBY data collection is programmed at the MOBY Operations Site in Honolulu, prior to each deployment. After the buoy has been deployed, any necessary program changes are made using a direct connection to the buoy's on-board computer. The on-board computer is programmed to acquire data during each event when the mooring site is in view of a satellite ocean color sensor. Currently, the MOBY radiometric measurement sequence, described below, is executed twice daily, coincident with the predicted overpasses of SeaWiFS and MODIS.

Radiometric Measurements

The MOS measures radiation input from one $L_u(z,\lambda)$, $E_d(z,\lambda)$ or $E_s(\lambda)$ head at a time. The desired channel is selected by the optical multiplexer. A rotating mirror within the MOS selects alternatively the input from the multiplexer, a dark reference calibration, light emitting diodes (LEDs), or a tungsten halogen incandescent lamp (Table 11.3). Integration times for the radiance collector on the top arm, at 1 m, typically range from 1 s to 4 s for the blue spectrograph and 10 s to 30 s for the red spectrograph. A typical sequence would be to measure $L_u(\lambda,z)$ from a depth, preceded and followed by $E_s(\lambda)$ surface reference spectra and associated dark spectra. Then this sequence is repeated at the 2nd and 3rd depths to complete the profile for $L_u(\lambda,z)$, as summarized in the example of Table 11.6. Note that there are a total of 35 measurements for radiances at the 3 depths, surface irradiance $E_s(\lambda)$ and sensor dark spectra. The 35 measurements are grouped into overlapping subsets of 15 measurements, representing the cycle associated with upwelled radiance measurements at each depth. Not included in the example are measurements from the base of the MOS itself, because these data are not currently used to determine water-leaving radiance. This entire procedure requires between 30 min and 1 hr to complete.

Methods for Mitigating Bio-Fouling

Marine organisms, including algae and barnacles, typically attach themselves to any surface that is immersed in seawater for an extended period. This "bio-fouling" process changes the transmittance of the radiance windows and irradiance cosine diffusers. The radiance windows are placed at the base of copper tubes, and small amounts of bromide are slowly released near the windows throughout the deployment. Both of these substances are poisons for most marine life. It is not practical to use this approach with the irradiance collectors, so a combination of Teflon collector material, copper bezels and less effective anti-fouling compounds is used here. Divers clean the optical collectors and recharge the bromide dispensers at monthly intervals during each deployment.

Ancillary Measurements

Aboard the mooring buoy, the meteorological state variables (wind velocity, surface pressure, air temperature and humidity), sea surface temperature and conductivity, and near-surface *in situ* chlorophyll *a* fluorescence, are sampled as 5 min averages at 15 min intervals, and recorded continuously on the system disk. The data records are downloaded once daily.

Sun Photometer and Sky Radiance Measurements (on Lanai and Oahu)

The AERONET Project at NASA GSFC operates the CIMEL[1] sun photometers on Lanai and Oahu, and retrieves the data, remotely. The aerosol optical thickness and sky radiance distribution data measured at these sites are needed as input to atmospheric correction models when the MOBY water leaving radiances are used for vicarious calibration of the satellite ocean color sensor. The data are archived by, and may be obtained from, the AERONET Project at NASA GSFC. MOBY support personnel visit the photometer sites at monthly intervals to check and clean the instruments.

11.4 CALIBRATION AND QUALITY CONTROL

The MOBY radiometers are characterized and calibrated using procedures that conform to the protocols described in Chapter 6. The unique role of MOBY as a primary, long term, and daily reference for vicarious calibration of satellite ocean color sensors requires radiometric measurements of the highest possible quality, and this in turn places stringent demands on the methods of traceability to NIST radiometric standards. For example, the MOBY team uses exclusively irradiance standards acquired directly from NIST, NIST recalibrates these sources frequently (see below), and NIST investigators validate the team's radiometric sources at annual intervals.

The MOS radiometers are calibrated before and after each deployment, and stability tests are made during deployments using both on-board and diver-deployed sources. These calibrations, tests and comparative measurements are illustrated schematically in Figure 11.10. The special aspects of the MOBY radiometric calibration, characterization and stability test procedures are described in this section.

Radiometric Calibration and Characterization of MOS

The spectral irradiance responsivities of the MOS $E_d(z,\lambda)$ and $E_s(\lambda)$ channels are calibrated using FEL-type lamp standards of spectral irradiance, and the $L_u(z,\lambda)$ channels are calibrated using lamp-illuminated integrating sphere sources. The wavelength calibration is performed using spectral line emission lamps, and every calibration cycle includes a measure of three internal sources (see below). Each instrument, whether for a MOCE or for a MOBY deployment, is calibrated at the support facility site in Honolulu before and after the in-water deployment. The standards of spectral irradiance and radiance are recalibrated every 50 h of operation. The irradiance standards, 1000 W quartz-halogen lamps (model number FEL), are calibrated by NIST. The integrating sphere source radiance standards are calibrated by their manufacturer, Optronic Laboratories, Inc. The MOS irradiance responsivity assignments are NIST-traceable using the NIST-issued FEL lamps. During the MOS irradiance calibration, the lamps are operated at the correct current using a calibrated shunt resistor in series with the lamp. The lamp is operated in an enclosed

housing at the same distance and with the same collection area as at NIST (50 cm and 1 cm^2, respectively). A reference mounting plate ensures the alignment of the lamp to the irradiance collector. The validity of this approach was verified by NIST (Mueller *et al.* 1996).

The radiance assignment is NIST-traceable via the commercial standards laboratory's calibration of integrating sphere sources (ISSs). Two ISSs are used: model OL420 and model OL425. They are externally illuminated, with an aperture wheel to vary the radiant output in discrete amounts. However, the two ISS units differ in the designs of their internal baffles, and in the method used by each to continuously vary the output. The ISSs are operated at constant current. The OL425 has, additionally, an internal illuminance monitor detector that is used to relate the output to that during the calibration measurements at Optronic Laboratories. The ISSs are re-lamped by Optronic Laboratories, and calibrated before and after this procedure, so for each sphere and lamp configuration, there is an initial and a final radiometric calibration; to date, only the initial calibration values have been used for the MOBY calibrations.

In addition to the routine calibration of the MOBY radiometric standards, two single-channel, dual-mode radiometers were designed and built by NIST to verify the calibrations of the FELs and ISSs and to monitor their stability at the support facility site in Honolulu. These Standard Lamp Monitors (SLMs) (Clark *et al.* 2001) have interchangeable foreoptics for operation in either radiance or irradiance mode. The narrowband (approximately 10 nm bandwidth) interference filters are centered at 412 nm and 872 nm. During every radiometric calibration at the support site, the SLMs are used to record the output of the radiometric standards. The absolute radiometric response of the SLMs is determined by measurements at NIST, both during the initial development and subsequently on an interval of 12 months to 18 months.

Finally, site visits by NIST personnel are done at regular intervals, and radiance comparisons are performed. Initially, the SeaWiFS Transfer Radiometer (SXR), a multichannel filter radiometer (Johnson *et al.* 1998) that is calibrated at NIST, was used. At the present time, a later version of the SXR, the Visible Transfer Radiometer (VXR) (Johnson *et al.* 2002) is used, along with a stable, portable, NIST-calibrated ISS, the NIST Portable Radiance Source (NPR) (Brown and Johnson 2002). The VXR and the NPR were developed by NIST in support of the calibration program for the Earth Observing System (EOS) (Butler *et al.* 1999).

MOS Internal Reference Sources

An internal reference system was incorporated into the MOS design to monitor the stability of the radiometric detectors, electronics, and internal optics. These measurements are critical for establishing confidence in the observations acquired during a deployment cycle. One of the viewing positions on the main relay mirror mechanism reflects light from a Spectralon[1] diffuser plate into the blue and red spectrograph optical relays. The diffuser is illuminated in sequence by an incandescent lamp, a blue light emitting diode (LED), and a red LED. The blue and red diodes are centered at 465 nm and 705 nm, respectively, with approximately 100 nm bandwidths. The lamps are run with current controlled circuitry and the temperature of the lamp holder block is monitored. These lamps are observed at the end of each MOBY data acquisition set (Sect. 11.3). Time histories of reference lamp responses for each deployment period show the MOS spectrograph responses to be stable at the 1 % level.

Field Tests of Radiometric Stability Using Diver Deployed Sources

The internal reference lamp and diodes responses (above) do not reflect changes in the throughput of the MOS irradiance and radiance collectors due to bio-fouling. During the nominal three-month duration of a MOBY system deployment period, a team of divers conducts inspections, external reference lamp stability tests, and cleaning monthly. During these maintenance operations, the near-surface components of the moored buoy and MOBY are inspected for damage, deterioration, and bio-fouling. The condition of the buoy is documented with underwater photography. To document these effects on MOBY radiometry, external underwater reference lamp stability baseline measurements are conducted on each irradiance, or radiance, collector immediately after the MOBY is deployed (Fig. 11.11). The underwater reference lamp radiometric stability tests are repeated during each monthly service visit, before and after each collector is cleaned. The reference lamp system is a modified commercial underwater unit using a 35 W incandescent lamp. The lamp is powered by a submersible, 12 V, 6.5 A h battery-pack. Modifications to the

commercial lamp system included the addition of constant current circuitry to the battery pack, and construction of lamp housings that fit over the radiance and irradiance collectors to block ambient light, while maintaining a fixed distance between the lamp source and collector. The radiance reference lamp system has a translucent diffuser placed between the lamp and collector window. Laboratory stability tests of the reference lamp systems show the output to be repeatable within 1 % if the battery voltage remains within 25 % of full charge. In the field, batteries are replaced and recharged when voltage decreases to 50 % of full charge.

Examples of the diver reference lamp responses for a few wavelengths at one upwelling radiance collector are illustrated in Fig. 11.12. Data shown at each wavelength represent the difference between the MOS responses on 3 August 2000, when the MOBY was deployed, and the responses before and after cleaning on 4 October 2000. The vertical bars illustrate the standard uncertainty in the diver reference lamp comparisons. Because all the response measurements fall within this uncertainty, the diver lamp response data have not been used to correct for trends during a deployment.

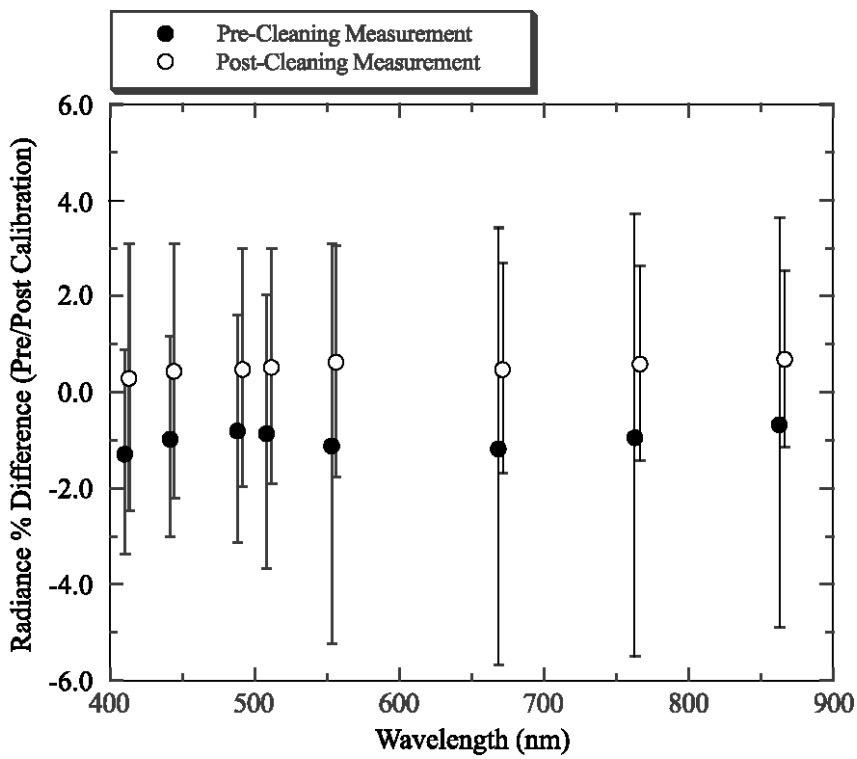

Figure 11.12: An example showing results of diver-deployed underwater radiometric stability source tests for several wavelengths and one radiance collector. The measurements were made immediately before, and after, the diver cleaned the radiance collector. The data are charted as percent differences from the similar test done on the day the buoy was deployed, approximately 2 months earlier.

Wavelength Stability Tests Using Fraunhofer Lines

Solar Fraunhofer lines and the atmosphere's oxygen A band absorption near 762 nm are resolved in the MOS $E_S(\lambda)$ spectra. The MOS detector array pixel locations of these lines are used to monitor the wavelength stability of the system throughout each deployment. Within the spectral resolution of the MOS spectrographs, no changes in the locations of any of these bands have occurred since the first MOBY deployment.

Stray Light Characterization

A critical issue in ocean color measurements arises because of the large difference in the relative spectral shape of the lamp-illuminated ISS (radiance mode), or the FEL lamp (irradiance mode), when compared to the relative spectral shape of $L_u(z,\lambda)$, or $E_d(z,\lambda)$, measured in the ocean. Radiometric sensors

do not have an ideal spectral selectivity, *i.e.*, the response at a wavelength of interest to flux at other wavelengths is small but finite (Chapter 5, Sect. 5.2 and Chapter 6, Sect. 6.4). As a result, measurements at the wavelength of interest include both a component that is proportional to the flux at that wavelength (*e.g.*, the "in-band" component) plus a component that sums the product of the sensor response and the spectrum of flux at wavelengths outside the in-band region. The latter sum, representing the out-of-band component, must be evaluated for all wavelengths for which the detector has finite responsivity. For MOS, the out-of-band response is largely determined by the scattering properties of the grating and unwanted reflections of flux diffracted in second order. We refer to the effect as "stray light".

Stray light considerations for MOS motivated dividing the spectrum into two regions using a dichroic beamsplitter and two spectrographs. As seen by the blue spectrograph, this division results in a better match between the spectral shapes of the FEL-type spectral irradiance sources and $E_d(z,\lambda)$, or the ISSs and $L_u(z,\lambda)$, and minimizes stray light effects in the critical ocean color wavelength bands. At 412 nm and 440 nm, for example, comparisons of $L_u(z,\lambda)$ for MOCE or MOBY deployments agree with measurements using independent filter radiometers to within ±5 %.

The effect of stray light in MOS is most evident in the region of overlap between the two spectrographs, from 545 nm to 650 nm. For the red spectrograph, the decreased transmittance of the dichroic beamsplitter in this region, where it goes from zero to nearly unity transmittance, means that the ratio of the in-band to the out-of-band components is unfavorable. Indeed, for some MOS wavelengths (CCD columns) at the blue side of the red spectrograph, the recorded signals can be dominated by the out-of-band component. At the present time, the processing algorithms use the results from the blue spectrograph up to 620 nm, and those from the red spectrograph beyond 620 nm. The differences are generally stable in time and depend on depth, another indication that the effect is related to source spectral shape.

To correct for stray light, the function that describes the sensitivity to flux at wavelengths other than the desired wavelength must be determined. This requires a tunable, monochromatic source that fills the entrance pupil of the sensor. Improvements in technology and the recent addition of new facilities at NIST have made it possible to fully characterize sensors such as CCD spectrographs using fully tunable laser-illuminated, integrating sphere sources (Brown, Eppeldauer, and Lykke 2000). The facility is called Spectral Irradiance and Radiance responsivity Calibrations with Uniform Sources (SIRCUS).

A thorough stray light characterization study for the MOBY project was begun in early 2000. Work started on SIRCUS with a MOS bench unit (Habauzit *et al.* 2002), and continued with the full characterization of MOS202 (which is used as a profiler instrument). Measurements are ongoing for the MOBY MOS units. The SIRCUS measurements yield the absolute radiance response of the sensors. Examples of the response of a single column in the blue spectrograph (column 380), and of the red spectrograph (column 277), are shown in Fig. 11.13 and Fig. 11.14 for the MOS profiler. The small peak near 510 nm for the blue spectrograph is caused by flux diffracted in second order and reflected onto the CCD by the grating and the second spherical mirror.

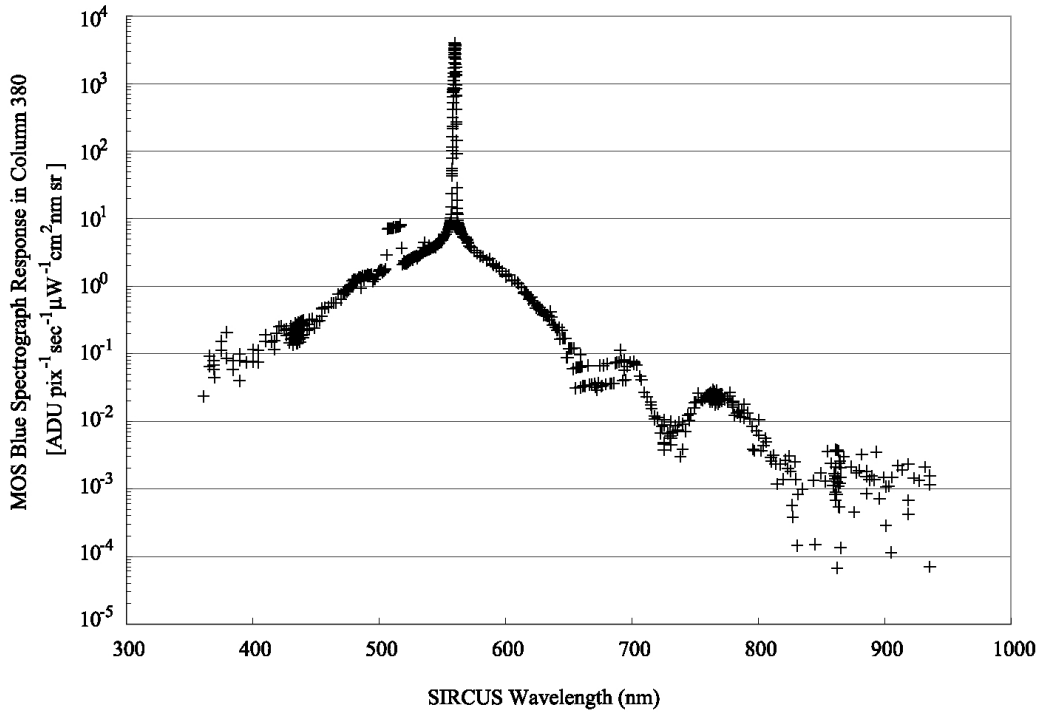

Figure 11.13: An example of the wavelength dependent spectral stray light responsivity of one CCD pixel location (wavelength) for the MOS blue spectrograph.

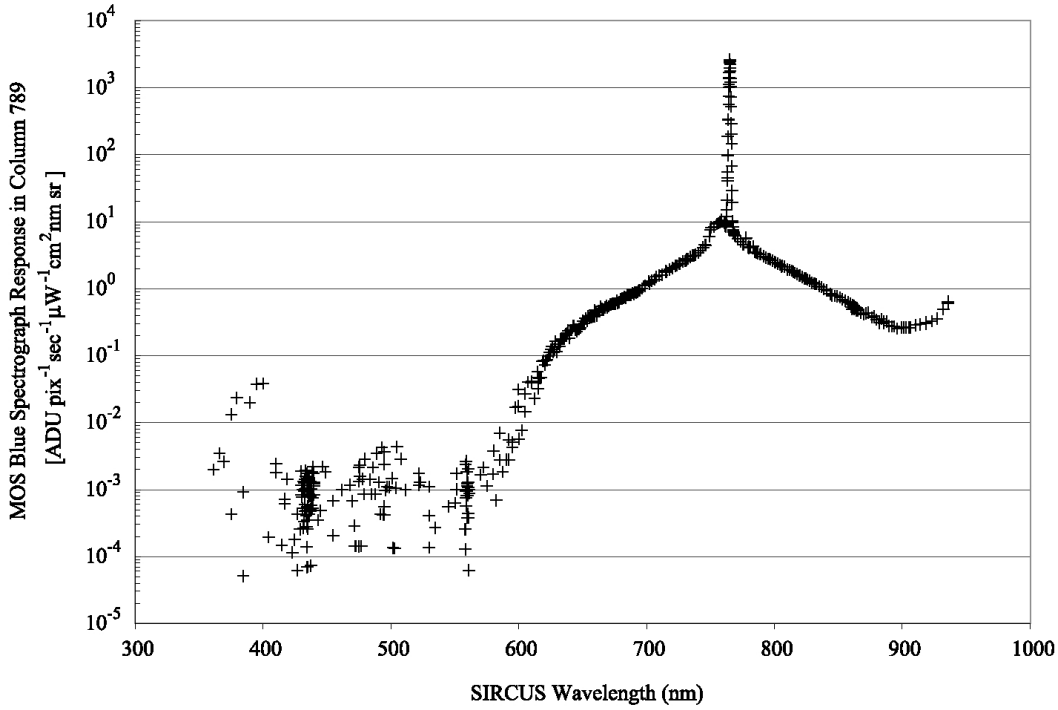

Figure 11.14: Same as Figure 11.13, but for one CCD pixel of the MOS red spectrograph.

A stray light correction algorithm was developed that is based on determination of the in-band region for one column on each CCD spectrograph, a description of the shape of the out-of-band response, and a model to account for the effects of the second order "reflection peak" (Brown *et al* 2002). To date, the SIRCUS results for the MOS profiler have been used to implement a preliminary version of the stray light correction algorithm, and test applications to the MOCE5 data sets are extremely encouraging. These preliminary results indicate that stray light affected the MOS Profiler results during MOCE 5 by up to +5 % at 412 nm (the uncorrected radiances are too small) and up to -1.5 % at 546 nm (the uncorrected radiances are too large).

Validation of the stray light correction algorithm is accomplished using an ISS that is made to simulate the spectral shape of in-water radiances using colored glass filters. The radiance of this colored source is determined independently by a NIST calibrated double grating monochromator. The results are compared to the corrected and uncorrected MOBY values and used to estimate the uncertainty of the stray-light correction.

CIMEL Sun Photometer and Sky Radiance Sensor Calibrations

The CIMEL instruments deployed at the stations on Oahu and Lanai are calibrated and maintained at NASA GSFC by the SIMBIOS Project Office, in collaboration with AERONET Project, following the procedures described in Chapter 7.

11.5 DATA ANALYSIS METHODS

As described above in Sect. 11.3, a single MOBY observation comprises a sequence of four to seven spectral radiance and irradiance measurement cycles for optical collectors located at the different depths on the spar (Table 11.6). The portion of the data record for an individual measurement cycle, *e.g.* for the upwelling radiance collector on a MOBY arm at depth z_i, is recorded as 3 arrays of digital counts $C_{Li}(\tau,N_p,z_i,t_m,\lambda)$ [m = 7, 8, 9 in an $L_u(z_i,\lambda)$ cycle of Table 11.6], where t_m is the time of the $m^{\underline{th}}$ measurement and τ is integration time. The "bin factor" N_p is expressed as the number of CCD rows read into the output register during each read step. Preceding and following each set of 3 radiance count arrays $C_{Li}(\tau,z_i,t_m,\lambda)$, the data record for one measurement cycle contains digital count arrays for incident surface irradiance (above water on the MOBY mast) $C_s(\tau_{sm},t_m,N_{pdm},\lambda)$, [m = 2, 3 4 (pre) and m = 12, 13, 14 (post) (Table 11.6)], and the MOS system dark response $D(\tau_{dm},t_m,N_{pdm},\lambda)$, for E_s [m = 1 and 5 (pre) and m = 11 and 15 (post)] and L_u [m = 6 and 10]. The central time, t_{Li} [or t_{Ei}], associated with a single radiance [or irradiance] measurement cycle (Table 11.6) is calculated as, *e.g.*

$$t_{Li} = \frac{1}{15}\sum_{i=1}^{15} t_i. \tag{11.1}$$

Temporal Averaging

The first step in processing the data is to scale each digital count array to unit integration time and average the individual measurements. Average counts for surface irradiance, normalized to unit integration time and bin factor, are computed as

$$\bar{C}_s\left(t_{Li},\lambda\right) = \frac{1}{6}\sum_m \left[\frac{C_s\left(\tau_{s,i},t_m,\lambda\right)}{N_{p,s,i}\tau_{s,i}}\right], m = 2,3,4,12,13,14 \text{ (Table 11.6)} \tag{11.2}$$

Average counts for MOS L_u Dark response, normalized to unit integration time and bin factor, are computed as (L_u cycle indices as in Table 11.6)

$$\bar{D}\left(t_{Li},\lambda\right) = \frac{1}{2}\left[\frac{D\left(\tau_{d,6},t_6,\lambda\right)}{N_{p,d,6}\tau_{d,6}} + \frac{D\left(\tau_{d,10},t_{10},\lambda\right)}{N_{p,d,10}\tau_{d,10}}\right]. \tag{11.3}$$

The 4 E_S Darks for the associated surface reference are averaged similarly. Finally, the average counts for the cycle of upwelled radiance measurements, normalized to unit integration time and bin factor, are computed as

$$\bar{C}_{\mathrm{L}i}\left(z_i, t_{\mathrm{L}i}, \lambda\right) = \frac{1}{3N_{\mathrm{p}}\tau}\sum_{m=7}^{9} C_{\mathrm{L}i}\left(\tau, z_i, t_m, \lambda\right). \tag{11.4}$$

With appropriate changes in subscripts (*i.e.* "E*i*" in place of "L*i*"), equations (11.1) through (11.4) apply also to a spectral downwelling irradiance measurement cycle at depth z_i.

System Spectral Response Functions

The MOS system spectral radiance (or irradiance) responsivity functions $R_j(\lambda, \tau)$, for optical collector j and unit integration time (*i.e.* $\tau = 1$), are determined following procedures described in Chapter 6 (Sect. 6.2), with extensions described above in Sect. 11.4. Following the example cycle of M upwelling radiance scans for the MOBY arm at depth z_i, bracketed by surface irradiance and dark response records, incident spectral irradiances $E_S(t_{\mathrm{L}i},\lambda)$ [μW cm^{-2}nm^{-1}] and average upwelling spectral radiance $L_u(z_i,t_{\mathrm{L}i},\lambda)$ [μW cm^{-2}nm^{-1}sr^{-1}]

$$E_{\mathrm{s}}\left(t_{\mathrm{L}i}, \lambda\right) = R_{\mathrm{Es}}\left(\lambda\right)\left[\bar{C}_s\left(t_{\mathrm{L}i}, \lambda\right) - \bar{D}\left(t_{\mathrm{L}i}, \lambda\right)\right], \tag{11.5}$$

and

$$L_{\mathrm{u}}\left(z_i, t_{\mathrm{L}i}, \lambda\right) = R_{\mathrm{L}i}\left(\lambda\right) F_{\mathrm{imm}}^{\mathrm{L}i}\left(\lambda\right)\left[\bar{C}_{\mathrm{L}i}\left(z_i, t_{\mathrm{L}i}, \lambda\right) - \bar{D}\left(t_{\mathrm{L}i}, \lambda\right)\right], \tag{11.6}$$

where $F_{\mathrm{imm}}^{\mathrm{L}i}\left(\lambda\right)$ is the immersion factor for the $i^{\underline{\mathrm{th}}}$ radiance collector as determined during the sensor's characterization (Chapter 6, Sect. 6.5 and Sect. 11.4). In equation (11.6), "L*i*" indicates that the subscripted (or superscripted) quantity applies to the spectral radiance collector mounted at depth z_i on the MOBY frame. Equation (11.6), substituting appropriate variables and subscripts, applies also to downwelling spectral irradiance $E_d(z_i,t_{\mathrm{E}i},\lambda)$ [μW cm^{-2}nm^{-1}] measurements using the irradiance collector mounted on MOBY at depth z_i.

Measurement Depths

On MOBY, $L_u(z,\lambda)$ is measured at 4 depths that are rigidly separated at fixed intervals on the buoy. These depths are nominally z_1 = 1 m, z_2 = 5 m, z_3 = 9 m, and z_4 = 11.5 m. The radiance measurement at 11.5 m is not currently used to determine water-leaving radiance. $E_d(z,\lambda)$ is measured only at nominal depths z_1, z_2, and z_3.

K(λ) Analysis

Following the above processing through equation (11.6), the attenuation coefficient for $L_u(z,\lambda)$ is computed from measurements at two discrete depths z_i and z_j as

$$K_{\mathrm{L}}\left(\bar{z}_{ij}, \lambda\right) = \frac{1}{z_j - z_i}\ln\left(\frac{L_{\mathrm{u}}\left(z_i, \lambda\right)E_{\mathrm{s}}\left(t_j, \lambda\right)}{L_{\mathrm{u}}\left(z_j, \lambda\right)E_{\mathrm{s}}\left(t_i, \lambda\right)}\right),\ z_{\mathrm{j}} > z_{\mathrm{i}},\ i = 1,2,3,\ j = 2,3,4, \tag{11.7}$$

where t_i and t_j are the times of radiance measurements at depths z_i and z_j, respectively. The ratio of incident surface irradiances appears in (11.7) to account for changes in illumination, *e.g.* due to clouds, between the times of the two radiance measurements. The mean depth in the interval between z_i and z_j is

$$\overline{z}_{ij} = \frac{z_i + z_j}{2}. \tag{11.8}$$

The diffuse attenuation coefficient for $E_d(z,\lambda)$ is computed similarly to (11.7) as

$$K_d\left(\overline{z}_{ij},\lambda\right) = \frac{1}{z_j - z_i}\ln\left(\frac{E_d\left(z_i,\lambda\right)E_s\left(t_j,\lambda\right)}{E_d\left(z_j,\lambda\right)E_s\left(t_i,\lambda\right)}\right),\ z_j > z_i,\ i = 1,2,\ j = 2,3. \tag{11.9}$$

For computing $K_L\left(\overline{z}_{ij},\lambda\right)$ and $K_d\left(\overline{z}_{ij},\lambda\right)$ from data measured with the shipboard MOS instrument, the actual depths z_i are determined to the nearest cm using data from its high precision depth transducer.

Determining $L_W(\lambda)$ by Upward Extrapolation

To determine $L_W(\lambda)$, the measurement of upwelling radiance from a selected depth z_i is propagated to the surface as

$$L_u\left(0^-,\lambda\right) = L_u\left(z_i,\lambda\right)e^{K_L\left(\overline{z}_{ij},\lambda\right)z_i}. \tag{11.10}$$

The depth z_i is selected according to the following hierarchical rules:

1. If the data from the top arm are valid, then that depth is selected.
2. Else, the data from the middle arm, if valid, are selected.
3. Else, the data sequence is rejected entirely.

Water-leaving radiance is calculated by propagating $L_u(0^-,\lambda)$ through the interface as

$$L_W\left(\lambda\right) = \frac{1-\rho}{n^2}L_u\left(0^-,\lambda\right), \tag{11.11}$$

where the upward transmittance through the interface, for nadir viewing radiance, is approximately constant, with value

$$\frac{1-\rho}{n^2} = 0.543, \tag{11.12}$$

being only weakly dependent on wavelength and insensitive to wind speed (Austin 1974; see also Chapters 2, 10 and 13).

Normalized Water-Leaving Radiance

Since the water-leaving radiances are apparent optical properties and are dependent upon the effects of the atmosphere, variations in solar zenith angle θ_o, and the earth-sun distance d, it is necessary to normalize the data to remove these effects for some applications. The normalizing approach used with MOBY water-leaving radiances follows the procedures that were defined by Gordon and Clark (1981) to compute *solar-normalized water leaving radiances* as

$$L_{WN}\left(\lambda\right) = \frac{L_W\left(\lambda\right)}{t\left(\lambda,\theta_o\right)\cos\theta_o\left(\frac{d_o}{d}\right)^2}, \tag{11.13}$$

where d_o is the mean earth-sun distance, and $t(\lambda, \theta_o)$ is the diffuse atmospheric transmittance computed as

$$t\left(\lambda,\theta_o\right) = e^{-\frac{\frac{1}{2}\tau_R(\lambda)+\tau_{O_3}(\lambda)}{\cos\theta_o}}. \tag{11.14}$$

The Rayleigh optical thickness $\tau_R(\lambda)$ is taken for mean atmospheric pressure (Penndorf 1957), and the ozone optical thickness $\tau_{O_3}(\lambda)$ is computed for an atmospheric ozone concentration of 350 Dobson units. The ratio of average to actual earth sun distances is approximated as

$$\frac{d_o}{d} = 1 + 0.0167\cos\left[\frac{2\pi(J-3)}{365}\right], \tag{11.15}$$

where J is the sequential day of the year.

The *normalized water-leaving radiances* $L_{WN}(\lambda)$ computed with Equations (11.13) through (11.15) are still dependent on the bidirectionality of the ocean's reflectance, as determined by the local inherent optical properties of the water and the solar zenith angle θ_o (Morel and Gentili 1996). To remove the bidirectional reflectance effects, it is necessary to convert the above $L_{WN}(\lambda)$ to *exact normalized water-leaving radiance* $L_{WN}^{ex}(\lambda)$ following the protocols in Chapter 13.

Spectral Band Averaging

The water leaving radiance corresponding to each wavelength band of a satellite ocean color sensor is determined from the MOBY solar-normalized water leaving radiances $L_{WN}(\lambda)$ as

$$L_{WN}^{MS}(\bar{\lambda}_i) = \frac{\int_0^\infty r_n^S(\lambda, \bar{\lambda}_i) L_{WN}(\lambda)\, d\lambda}{\int_0^\infty r_n^S(\lambda, \bar{\lambda}_i)\, d\lambda}, \tag{11.16}$$

where the superscripts S and MS denote a particular satellite ocean color sensor and a MOBY derived estimate for that satellite, respectively, $\bar{\lambda}_i$ is the effective wavelength of the ith band of that sensor, and $r_n^S(\lambda, \bar{\lambda}_i)$ is the normalized relative spectral response function of that channel. In practice, (11.16) is approximated numerically.

An example MOBY water-leaving radiance spectrum is compared to the shapes of the spectral response function of MODIS ocean bands in Fig. 11.15. Note that $L_{WN}(\lambda)$ must be transformed to $L_{WN}^{ex}(\lambda)$ (Chapter 13) prior to match-up comparisons between MOBY and satellite water-leaving radiances.

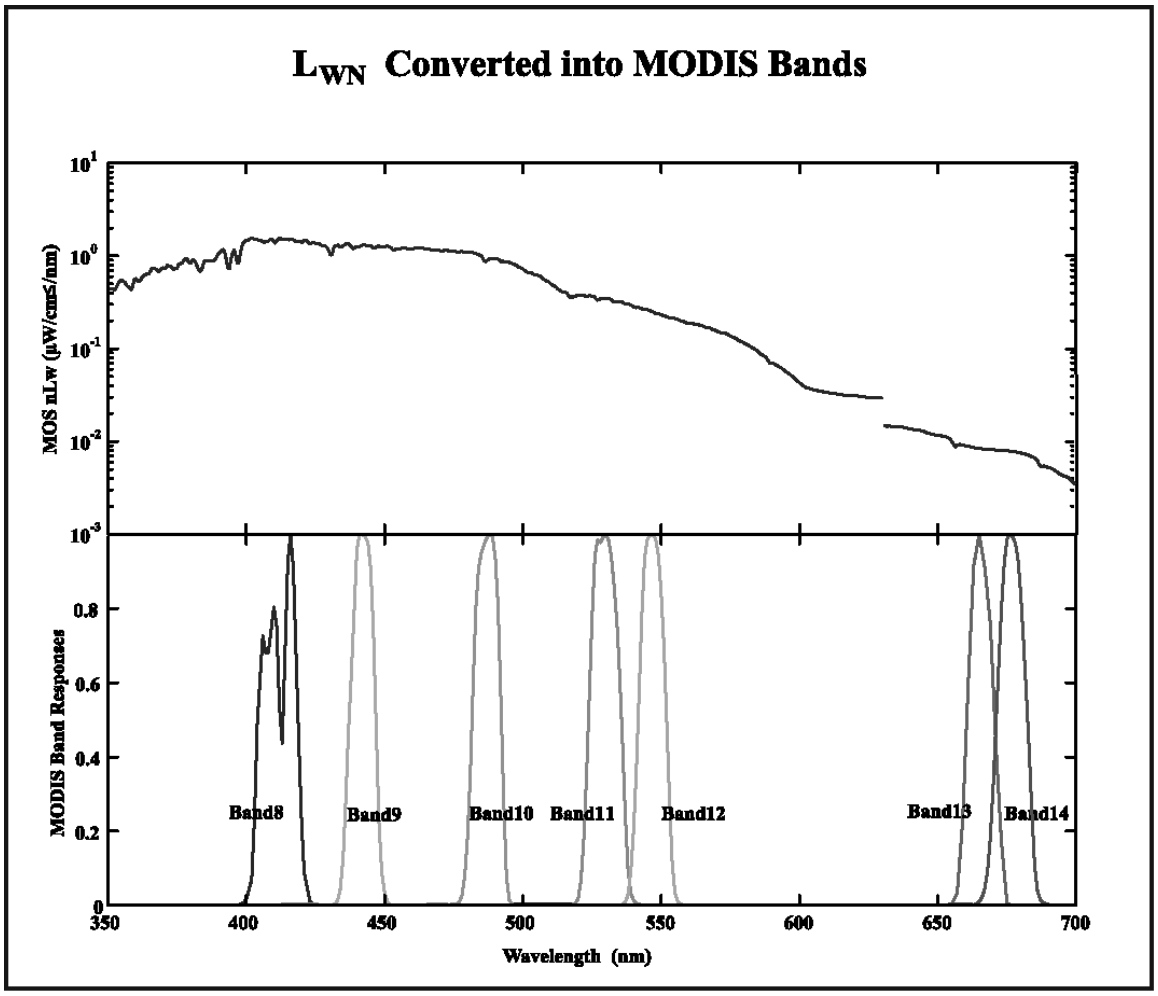

Figure 11.15: Comparison of a normalized water-leaving radiance spectrum measured by MOBY with the spectral band response functions of the MODIS ocean channels. The MOBY radiances have not been corrected for stray light, as is obvious from the large offset between the blue and red spectrographs at 630 nm.

11.6 DATA ARCHIVAL AND RECORDKEEPING

Band averaged water-leaving radiances for SeaWiFS and MODIS are transmitted to the SeaWiFS and SIMBIOS Project Offices, where they are archived in SeaBASS (Chapter 18). These data are also transmitted to and archived by the MODIS Team at the University of Miami. All data recorded by the MOBY system and on MOCE and other cruises are archived at MLML in Moss Landing, California and at NOAA NESDIS in Camp Springs, Maryland.

11.7 FUTURE DIRECTIONS

Temperature Characterizations

Although the MOS CCDs are temperature-controlled, the temperatures of the optical components in the spectrographs, the electronics, the MOBY fiber optics, and other system components are subject to environmental conditions. These ancillary instrument temperatures are recorded and archived, but are not used in the present data processing algorithms. Because the ambient temperature and degree of thermal equilibrium depends on the measurement purpose (calibration vs. in-water radiometry) and type of deployment (MOBY vs. MOS), the radiometric responsivities of MOBY and MOS are being studied as a

function of temperature. Various temperature-controlled baths are used, including one large enough for MOS.

Stray Light Characterizations

The MOBY Project includes a suite of instruments, requiring multiple field deployments to address the stray light issues. Once the required data are in hand, the stray light algorithm for all of the required instruments will be optimized. This may require separate model parameters for each input collector on MOBY. Then, the MOCE and MOBY data sets will be reprocessed, leading to an improvement in the accuracy of the derived $L_{WN}(\lambda)$'s that are used for vicarious calibration of MODIS, SeaWiFS, and other ocean color satellite sensors. It is anticipated that the uncertainty in the correction will be about 10 % of the effect, *e.g.* the uncertainty in the corrected values from stray light would be 0.5 % for a 5 % correction.

ACKNOWLEDGMENTS

The NIST efforts are supported by NOAA under contract NA00AANEG0072. Additional support for the NIST participation in this project has been provided under contracts S-41365-F (EOS Project Science Office) and S-64096-E (SeaWiFS Project). The Electro-optics Calibration Coordination Group, U.S. Air Force section, provided funding for SIRCUS (CCG98-439).

REFERENCES

Austin, R.W., 1974: The remote sensing of spectral radiance from below the ocean surface. In: Optical Aspects of Oceanography, N.G. Jerlov and E.S. Nielson, Eds., pp 317-344.

Brown, S.W., G.P. Eppeldauer, and K.R. Lykke, 2000: NIST facility for spectral irradiance and radiance responsivity calibrations with uniform sources. *Metrologia*, **37**, 579-582.

Brown, S.W., and B.C. Johnson, 2002: Development of a portable integrating sphere source for the Earth Observing System's Calibration Validation Program. To appear in *International Journal of Remote Sensing*.

Brown, S.W., C. Habauzit, B.C. Johnson, and K.R. Lykke, 2002: Tunable-laser based calibration of a CCD spectrograph. In preparation.

Butler, et al. 1999: J.J. Butler J.J., B.L. Markham, B.C. Johnson, S.W. Brown, H.W. Yoon, R.A.Barnes, S.F. Biggar, E.F. Zalewski, P.R. Spyak, F. Sakuma, and J.W. Cooper, 1999: Radiometric measurement comparisons using transfer radiometers in support of the calibration of NASA's Earth Observing System (EOS) Snesors, in Sensors, Systems, and Next Generation Satellites III, Proc. SPIE Vol. 3870, Ed. P.L. Slater, (Bellingham, Washington: Society of Photo-Optical Instrumentation Engineers), 180-192.

Clark, D.K, H.R. Gordon, K.J. Voss, Y. Ge, W. Broenkow, and C.C. Trees, 1997: Validation of atmospheric corrections over oceans. *J. Geophs. Res*., **102**: 17209-17217.

Clark, D.K., M.E. Feinholz, M.A. Yarbrough, B.C. Johnson, S. W. Brown, Y.-S. Kim, and R.A. Barnes, 2001: Overview of the radiometric calibration of MOBY. *Proc. SPIE, Earth Observing Systems VI*, **4483**, xxx—yyy.

Clark, D.K, H.R. Gordon, K.J. Voss, Y. Ge, W. Broenkow, and C.C. Trees, 1997: Validation of atmospheric corrections over oceans. *J. Geophs. Res*., **102**: 17209-17217.

Evans, R.H. and H.R. Gordon, 1994: Coastal Zone Color Scanner system calibration: a retrospective examination. *J. Geophys. Res.*, **99**:7293-7307.

Fargion, G.S. and J.L. Mueller, 2000: *Ocean Optics Protocols for Satellite Ocean Color Sensor Validation, Revision 2*, NASA TM 2001-209955, NASA Goddard Space Flight Center, Greenbelt, Maryland, 184 pp.

Gordon, H.R., 1981: Reduction of error introduced in the processing of Coastal Zone Color Scanner-type imagery resulting from sensor calibration and solar irradiance uncertainty. *Appl. Opt.*, **20**: 207-210.

Gordon, H.R., 1987: Calibration requirements and methodology for remote sensors viewing the ocean in the visible. *Remote Sens. Environ*., **22**:103-126.

Gordon, H.R., 1988: Ocean color remote sensing systems: radiometric requirements. *Recent Advances in Sensors, Radiometry, and Data Processing for Remote Sensing*, P.N. Slater, Ed., SPIE, **924**: 151-157.

Gordon, H.R., J.W. Brown, O.B. Brown, R.H. Evans, and D.K. Clark, 1983: Nimbus-7 CZCS: reduction of its radiometric sensitivity with time. *Appl. Opt*., **24**:3929-3931.

Gordon, H.R. and D.K. Clark, 1981: Clear water radiances for atmospheric correction of Coastal Zone Color Scanner imagery. *Appl. Opt.*, **20:** 4174-4180.

Gordon, H.R., D.K. Clark, J.W. Brown, O.B. Brown, R.H. Evans, and W.W. Broenkow, 1983: Phytoplankton pigment concentrations in the middle Atlantic bight: comparison of ship determinations and CZCS estimates. *Appl. Opt*. **22:** 20-36.

Gordon, H.R. and K. Ding, 1992: Self shading of in-water optical instruments. *Limnol. Oceanogr*., **37**: 491-500.

Hooker, S.B. and S. Maritorena, 2000: An evaluation of oceanographic radiometers and deployment methodologies. *J. Atmos. Oceanic Technol*. **17**: 811-830.

Habauzit, C., S.W. Brown, K.R. Lykke, B.C. Johnson, M.E. Feinholz, M.A. Yarbrough, and D.K. Clark, 2002: Radiometric characterization and absolute calibration of the Marine Optical System (MOS) bench unit. Submitted to the Journal of Atmospheric and Oceanic Technology.

Johnson, B.C., J.B. Fowler, and C.L. Cromer, 1998: The SeaWiFS Transfer Radiometer (SXR). *NASA Tech. Memo. 1998-206892, Vol. 1*, S.B. Hooker and E.R. Firestone, Eds., NASA Goddard Space Flight Center, Greenbelt, Maryland, 58 pp.

Johnson, B.C., S.W. Brown, G.P. Eppeldauer, and K.R. Lykke, 2002: System-level calibration of a transfer radiometer used to validate EOS radiance scales. To appear in International Journal of Remote Sensing.

Morel, A. and B. Gentili, 1996: Diffuse reflectance of oceanic waters. III. Implication of bidirectionality for the remote-sensing problem. *Applied Optics*, **35**: 4850-4862.

Mueller, J.L. and R.W. Austin, 1992: Ocean Optics Protocols for SeaWiFS Validation. *NASA Tech. Memo. 104566, Vol. 5*, S.B. Hooker and E.R. Firestone, Eds., NASA Goddard Space flight center, Greenbelt, Maryland, 45 pp.

Mueller, J.L. and R.W. Austin, 1995: Ocean Optics Protocols for SeaWiFS Validation, Revision 1. *NASA Tech. Memo. 104566, Vol.* ***25***, S.B. Hooker and E.R. Firestone, Eds., NASA Goddard Space flight center, Greenbelt, Maryland, 66 pp.

Mueller, J.L., B.C. Johnson, C.L. Cromer, S.B. Hooker, J.T. McLean, and S.F. Biggar, 1996: The Third SeaWiFS Intercalibration Round-Robin Experiment, SIRREX-3, September 1994. *NASA Tech. Memo 104566, Vol. 34*, S. B. Hooker, E. R. Firestone, and J. G. Acker, Eds., NASA Goddard Space Flight Center, Greenbelt, Maryland, 78 pp.

Penndorf R., 1957: Tables of the refractive index for standard air and the Rayleigh scattering coefficient for the spectral region between 0.2 and 20.0 microns and their application to atmospheric optics, *J. Opt. Soc. Am.*, **47**, 176-182.

Siegel, D.A., M.C. O'Brien, J.C. Sorenson, D.A. Konnoff, E.A. Brody, J.L. Mueller, C.O. Davis, W.J. Rhea, and S.B. Hooker, 1995: Results of the SeaWiFS Data Analysis Round Robin, July 1994 (DARR-94). *NASA Tech Memo. 104566, Vol.* ***26***, S.B. Hooker and E.R. Firestone, Eds., NASA Goddard Space Flight Center, Greenbelt, Maryland, 58p.

Taylor, B.N., and C.E. Kuyatt, 1994: Guidelines for Evaluating and Expressing the Uncertainty of NIST Measurement Results. *NIST Tech. Note 1297*, U.S. Department of Commerce, National Institute of Standards and Technology, Washington, DC, 20 pp.

Table 11.1: Summary of MOCE data collection cruises. Cruises dedicated to the collection of bio-optical data are indicated with "MOCE". Cruises where data were collected in conjunction with MOBY operations are indicated with "MOBY".

Cruise	Cruise Dates	Cruise Location	No. of Stns	Satellite(s) Supported
MOCE-1	28 Aug-11 Sep 1992	Monterey Bay	7	
MOCE-2	27 Mar-14 Apr 1993	Gulf of California	13	
MOCE-3	27 Oct-15 Nov 1994	Hawaiian Archipelago	16	
MOBY-L14	14-22 Sep 1996	Hawaii-Lanai	6	
MOBY-L15	14-22 Nov 1996	Hawaii-Lanai	5	OCTS Initialization
MOBY-L16	23 -28 Feb 1997	Hawaii-Lanai	8	OCTS Initialization
MOBY-L20	19-27 Jul 1997	Hawaii-Lanai	5	
MOBY-L22	22 Sep-4 Oct 1997	Hawaii-Lanai	7	
MOBY-L25	7-15 Dec 1997	Hawaii-Lanai	3	
MOCE-4	26 Jan-12 Feb 1998	Hawaiian Islands	17	SeaWiFS Initialization
MOBY-L28	30 Mar-1 Apr 1998	Hawaii-Lanai	2	
MOBY-L35	23-26 Jul 1998	Hawaii-Lanai	5	
MOBY-L38	25-30 Oct 1998	Hawaii-Lanai	5	
MOBY-L43	6-11 Feb 1999	Hawaii-Lanai	3	
MOBY-L45	1-6 May 1999	Hawaii-Lanai	4	
MOCE-5	1-21 Oct 1999	Gulf of California	20	
MOBY-L54	10-15 Feb 2000	Hawaii-Lanai	2	
MOCE-6	9-16 Apr 2000	Hawaiian Islands	8	MODIS Initialization-Side A
MOBY-L56	15-19 May 2000	Hawaii-Lanai	3	
MOBY-L59	24 Jul-11 Aug 2000	Hawaii-Lanai	3	MODIS Initialization-Side A
MOCE-7	3-10 Dec 2000	Hawaiian Islands	7	MODIS Initialization-Side B
MOCE-8	28 Feb-9 Mar 2001	Hawaiian Islands	9	MODIS Initialization-Side B
MOBY-L69	1-4 Jun 2001	Hawaiian Islands	2	

Table 11.2a: MOBY Specifications

Physical Specifications:	
Dimensions D x L (m)	1.7 x 15
Collector standoff length (m)	3.0 max
Weight in air (kg)	955
Height above waterline (m)	3
Reserve buoyancy (kg)	816
Flotation material	Isomer foam
Undamped period (sec)	2.5
Damping	Suspended drag device
Surface float frame	Welded stainless steel (T316L)

Spar	Stainless steel reinforced fiberglass		
Instrument Bay	Welded stainless steel (T316L)		
Collector standoff depths	Variable		
Optical:			
Spectrograph	MOS		
MOS optical interface	Fiber optic multiplexer, 10 ports		
Fiber optics	1mm silica/silica		
Fiber optic Interface	O-ring sealed SMAS		
Collectors:			
	E_s:	**E_d:**	**L_u:**
Dimensions	5 cm x 18 cm	5 cm x 17 cm	5 cm x 17 cm
Collector dimensions	3 cm	7 cm	2.8 cm
FOV	Cosine response	Cosine response	Max 5 °
f#	-	-	2
Electrical:			
Power source	4 x 40 W solar panels		
Charge control	Trace C12		
Battery monitoring	Individual monitor and charge control		
Average daily power production (W)	640		
Reserve battery capacity (W)	9600		
Instrument Bay battery type	4 x 200 A h, 12 v, Sealed Marine Gel Cell		
GPS	Raytheon RS112LP		
Argos	Seimac GPSMML		
R.F. beacon/locator strobe	Novatec, RF700C5		
Cellular antenna	Cellwave		
Controller battery type	80 A h, 12 v Sealed Marine Gel Cell		
Controller battery capacity	960		
Buoy power consumption, Sleep (uW)	3		
Buoy power consumption, Active (W)	9.6		
Buoy power consumption, Telemetry mode(W)	42		
Buoy power consumption, Acquisition mode (W)	132		
Surface Buoy Controller:			
Processor	MC68332		
Operating system	MLML Forth		
Modem	Zyxel, U-1496P		
Cellular transceiver	Motorola, S1765A		
Host serial interface	RS232, 9600 baud		
MOS serial interface	RS485, 9600 baud		
Subsurface power controller serial interface	RS485, 19.2k baud		
GPS serial interface	RS232, 4800 baud		
Internal power control	Latching relays		
A/D System:	**High resolution**	**Low resolution**	
Resolution	16 bit	12 bit	
Gains	1,10,100,500		
Channels	16	4	
Throughput	33 kHz, max	>100 kHz	
Accuracy	0.0024%, max	0.01%	
Subsurface Instrument bay Power Controller			
Operating system	TTBasic		
Status functions	Instrument bay power monitor		
	MOS power monitor		
	Battery charge monitor		
Control functions	Battery charge control		
	MOS power control		

Table 11.2b: MOBY Ancillary measurements

Parameter	Sensor Type	Range	Precision	Accuracy
Surface controller battery voltage (V)	Voltage monitor	0-25	0.006	0.02
Humidity	Monolithic capacitive	0-100 %	0.01%	2%
Case internal temperature (°C)	Thermistor	-10-50	0.05	0.1
Upper arm pressure (depth)	Strain gauge	0-25 meters	1.0 mm	5mm
Controller current (A)	Shunt	0-25	0.04	0.25
Controller battery charge current (A)	Shunt	0-25	0.04	0.25
Solar panel 1 current (A)	Shunt	0-25	0.04	0.25
Solar panel 2 current (A)	Shunt	0-25	0.04	0.25
Solar panel 3 current (A)	Shunt	0-25	0.04	0.25
Solar panel 4 current (A)	Shunt	0-25	0.04	0.25
Subsurface power controller voltage (V)	Voltage monitor	0-25	0.006	0.02
MOS voltage	Voltage monitor	0-25	0.006	0.02
MOS Battery current (A)	Shunt	0-25	0.04	0.25
MOS Battery #1	Voltage monitor	0-25	0.006	0.02
MOS Battery #2	Voltage monitor	0-25	0.006	0.02
MOS Battery #3	Voltage monitor	0-25	0.006	0.02
MOS Battery #4	Voltage monitor	0-25	0.006	0.02

Table 11.3a: MOS Spectrograph Characteristics

Dimensions:	
MOS only, D x L, (mm)	330 x 660
Weight in air (Kg)	64
Weight in sea water (Kg)	4
MOS with profiling rack and battery, D x L, (mm)	673 x787
Weight in air (Kg)	143
Weight in sea water (Kg)	122
Construction	O-ring sealed aluminum
Depth rating (meters)	100
Electrical:	
Profiler Lead-acid battery capacity (W)	600
MOS Power consumption (W)	120 W @ 10.5 – 14.5
Optics:	
Material (windows, lenses)	Fused Silica
Input optics f#	2
Diameter (mm)	43
FOV (deg)	Max 5 °
Input telescope ports	2 (up & down)
Polarization filter (option)	Quartz wedges
Input selection	4 positions
Input mirror settings	Up, Down, Reference, Dark
Spectrographs	2
Spectral separation optics	45° dichroic mirror
Separation wavelength, 50% pass (nm)	635
Full spectral range (nm)	340-955

Spectral resolution (nm)	<1
Polarization sensitivity	<1% (with depolarizing optics option)
Spectrographs:	
Dimensions, L x W x H (mm)	178 x 152 x 100
Type	Offner variant
Construction	Stainless steel (T316) bench Aluminum fixtures
Optics	SiO protected, Al coated glass (Blue) Au coated, black glass (Red)
Grating	Convex holographic
Wavelength Range (nm)	340 - 640 (Blue) 550 - 955 (Red)
Focal length (mm)	100
f#	3.8
Slit dimension (um)	12 (h) * 25 (w) * 40 (t)
Slit material	Electroformed Nickel
Resolution (nm)	0.6 (Blue) / 0.8 (Red)
Bandpass, FWHM, over spectrograph range, (nm)	1.0 - 1.2 (Blue) / 1.28 - 1.5 (red)
Fore optics	Ø25 mm, Cylindrical
Out of band rejection filters	580 nm High Pass (Red)

Table 11.3b: MOS Ancillary Measurements

Parameter	Sensor Type	Range	Precision	Accuracy
Mains (Battery) voltage	Voltage monitor	0-25 V	0.006 V	0.02 V
Humidity	Monolithic capacitive	0-100 %	0.01%	2%
Case internal temperature	Thermistor	-10-50°C	0.05	0.1
Water Temperature	Thermistor	-10 to 50 °C	0.005	0.05
Pressure (depth)	Strain gauge	0-200 meters	1.0 cm	4.0 cm
Tilt-X	Electrolytic	±60°	0.0026 °	0.03 °
Tilt-Y	Electrolytic	±60°	0.0026 °	0.03 °
Blue Array Temperature	Thermistor	-50 to 40°C	0.005 °C	0.05 °C
Red Array Temperature	Thermistor	-50 to 40°C	0.005 °C	0.05 °C
Blue Calib diode monitor	Photodiode	NA	15-bit	0.001%
Red Calib diode monitor	Photodiode	NA	15-bit	0.001%
Calib. Source block temp	Thermistor	-10 to 50 °C	0.005	0.05 °C
Coolant Flow	Pelton Wheel	20-2000 ml/min	1.5 ml/min	0.01 ml/min
Depth Sensor Temperature	Thermistor	-10 to 50 °C	0.005	0.05 °C
System Current	Hall effect	0 - 20 A	.01 A	0.05 A
Blue CCD Heater Monitor	Voltage monitor	NA	15-bit	0.001%
Red CCD Heater Monitor	Voltage monitor	NA	15-bit	0.001%
Internal Temperature at TT7	Thermistor	-10-50°C	0.05	0.1
Blue CCD Head Temperature	Thermistor	-10 to 50 °C	0.005	0.05 °C
Red CCD Head Temperature	Thermistor	-10 to 50 °C	0.005	0.05 °C
Heading	Flux gate compass	0 to 360 °	0.1°	0.5 °

Table 11.4: Summary of MOBY Deployment and Interim Servicing Cruises.

Cruise Name	Cruise Dates	Mooring	Diver Cals	MOBY	CIMEL
MOBY-L1	3-7 Oct 93	deployed			
MOBY-L2	6-10 Feb 94			aborted deploy	
MOBY-L3	21-25 Feb 94			deployed	
MOBY-L4	24-29 Mar 94		X		
MOBY-L5	5-9 May 94			check-up	
MOBY-L6	24-27 May 94		cancelled-bad weather		
MOBY-L7	25-30 Jun 94	retrieved		recovered	
MOBY-L8	9-12 Sep 94			testing	
MOBY-L9	8-27 Mar 95			testing	
MOBY-L10	15-30 Aug 95			testing	
MOBY-L11	3-8 Nov 95	deployed			
MOBY-L12	21 Feb-6 Mar 96			testing	
MOBY-L13	24 Jul-15 Aug 96			testing	X
MOBY-L14	14-21 Sep 96			deployed	
MOBY-L15	2-4, 14-22 Nov 96			exchanged	
MOBY-L16	23 Feb-2 Mar 97			recovered	
MOBY-L17	1-17 Apr 97			assembly	
MOBY-L18	9-23 May 97			testing	
MOBY-L19	9-23 Jun 97			testing	
MOBY-L20	19-27 Jul 97			deployed	
MOBY-L21	31-Aug-97		X		
MOBY-L22	22 Sep-4 Oct 97		X		
MOBY-L23	30-31 Oct 97			retrieved/reattached	
MOBY-L24	10-11 Nov 97		X		
MOBY-L25	7-14 Dec 97	exchanged	X	exchanged	
MOBY-L26	13-14 Jan 98		X		
MOBY-L27	9-10 Mar 98		X		
MOBY-L28	29 Mar-2 Apr 98			aborted-bad weather	
MOBY-L29	21-24 Apr 98			exchanged	X
MOBY-L30	4-May-98		cancelled-bad weather		X
MOBY-L31	15-May-98			maintenance	X
MOBY-L32	2-3 Jun 98		X		
MOBY-L33	21-Jun-98			repair	X
MOBY-L34	2-3 Jul 98		X		X
MOBY-L35	22-26 Jul 98			exchanged	

MOBY-L36	25, 28-29 Aug 98		cancelled-bad weather		X
MOBY-L37	17, 19-20 Sep 98		X	maintenance	
MOBY-L38	24-30 Oct 98		X	exchanged	X
MOBY-L39	7-10 Dec 98		X	maintenance	
MOBY-L40	5-Jan-99			maintenance	
MOBY-L41	10-12 Jan 99		X		X
MOBY-L42	21-Jan-99			maintenance	
MOBY-L43	6-11 Feb 99	exchanged	X	exchanged	
MOBY-L44	9-11 Mar 99		X	maintenance	X
MOBY-L45	1-6 May 99		X	exchanged	
MOBY-L46	2-3 Jun 99		X	maintenance	X
MOBY-L47	29 Jun-1 Jul 99		X	maintenance	X
MOBY-L48	29 Jul-1 Aug 99		X	exchanged	
MOBY-L49	5-Sep-99			check-up	
MOBY-L50	10-Oct-99			check-up	
MOBY-L51	15-18 Nov 99		X	exchanged	
MOBY-L52	16-19 Dec 99		X		X
MOBY-L53	25-Jan-00			maintenance	X
MOBY-L54	10-15 Feb 00	exchanged	X	exchanged	
MOBY-L55	29-31 Mar 00		X	maintenance	
MOBY-L56	15-19 May 00		X	exchanged	
MOBY-L57	19 -21 Jun 00		X		X
MOBY-L58	17-19 Jul 00		X		
MOBY-L59	3-6 Aug 00		X	exchanged	
MOBY-L60	12-14 Sep 00		X		X
MOBY-L61	23-Sep-00			maintenance	
MOBY-L62	5-6 Oct 00		X		X
MOBY-L63	9-11 Jan 01		X		X
MOBY-L64	28-Jan-01			maintenance	
MOBY-L65	7-8 Feb 01		X		
MOBY-L66	18-Mar-01			check-up	
MOBY-L67	7-9 Apr 01		X		X
MOBY-L68	22-23 May 01			maintenance	X
MOBY-L69	1-4 Jun 01		X	exchanged	
MOBY-L70	4-6 Jul 01		X	maintenance	X

Table 11.5: *In situ* observations collected during a MOCE cruise in support of vicarious calibration/validation of satellite ocean color systems. Measurement subcategories follow those shown in Chapter 3, Table 3.1.

MOCE Cruise Data Acquisition	Institution	Instrumentation System
Required Measurements		
Downwelled Irradiance	MLML	MOS, SPMR
Upwelled Radiance	MLML	MOS, SPMR
Incident Irradiance	MLML	SIS, SMSR
Aerosol Optical Depth	NOAA/NESDIS, U of Miami	HHCRM, MicroTops
Phytoplankton Pigment Composition	CHORS	HPLC
Chlorophyll a and Phaeopigment Concentration	CHORS	Fluorometric
Latitude and Longitude	NOAA/NESDIS	Trimble GPS
Date and Time (UTC)	NOAA/NESDIS	Trak
Wind Speed and Direction	NOAA/NESDIS	Young
Surface Barometric Pressure	NOAA/NESDIS	Setra
Air Temperature/Relative Humidity	NOAA/NESDIS	Vaisala
Cloud Cover	NOAA/NESDIS	Sky Camera
Secchi Depth	MLML	Secchi Disk
Highly Desired Measurements		
Beam Attenuation	NOAA/NESDIS	VLST
Beam Attenuation Profiles	MLML	WETLabs C-Star
Particle Absorption	NOAA/NESDIS	Diode Array Spectrophotometer
Dissolved Material (CDOM) Absorption	NOAA/NESDIS	Diode Array Spectrophotometer
Non-Pigmented Particle Absorption	NOAA/NESDIS	Diode Array Spectrophotometer
Phytoplankton Absorption	NOAA/NESDIS	Diode Array Spectrophotometer
Fluorometric Profiles	MLML	Chelsea
Whitecap Conditions	U of Miami	
Conductivity and Temperature Profiles	MLML	SeaBird CTD
Conductivity and Temperature - Alongtrack	NOAA/NESDIS	Falmouth TSG
Specialized Measurements		
Instrument Self-Shading	NOAA/NESDIS	FOS
Upwelled Radiance Distribution	U of Miami	RADS
Particle Size Data	NOAA/NESDIS	Laser Particle Counter
Total Suspended Particulate Matter (TSM)	MLML	
Particulate Organic Carbon/Nitrogen (POC/PON)	MLML	

Table 11.6: An example of a MOBY MOS upwelled radiance measurement cycle. The cumulative index is the order in which measurements are made. The $L_u(z_i,\lambda)$ Cycle Indices group the measurements at depth z_i with bracketing $E_s(\lambda)$ measurements and associated dark measurements; these indices are used in Equations (11.1) through (11.4) to average the individual measurements within each cycle.

Cumulative Index	**Variable Measured**	**Depth z (m)**	$L_u(z_1,\lambda)$ **Cycle Index**	$L_u(z_2,\lambda)$ **Cycle Index**	$L_u(z_3,\lambda)$ **Cycle Index**
1	$E_s(\lambda)$ Dark	--		1	
2 – 4	$E_s(\lambda)$	0^+		2 – 4	
5	$E_s(\lambda)$ Dark	--		5	
6	$L_u(\lambda)$ Dark	--		6	
7 – 9	$L_u(z_2,\lambda)$	5		7 – 9	
10	$L_u(\lambda)$ Dark	--		10	
11	$E_s(\lambda)$ Dark	--	1	11	
12 – 14	$E_s(\lambda)$	0^+	2 – 4	12 – 14	
15	$E_s(\lambda)$ Dark	--	5	15	
16	$L_u(\lambda)$ Dark	--	6		
17 – 19	$L_u(z_1,\lambda)$	1	7 – 9		
20	$L_u(\lambda)$ Dark	--	10		
21	$E_s(\lambda)$ Dark	--	11		1
22 – 24	$E_s(\lambda)$	0^+	12 – 14		2 – 4
25	$E_s(\lambda)$ Dark	--	15		5
26	$L_u(\lambda)$ Dark	--			6
27 – 29	$L_u(z_3,\lambda)$	9			7 – 9
30	$L_u(\lambda)$ Dark	--			10
31	$E_s(\lambda)$ Dark	--			11
32 – 34	$E_s(\lambda)$	0^+			12 – 14
35	$E_s(\lambda)$ Dark	--			15

Chapter 12

Above-Water Radiance and Remote Sensing Reflectance Measurement and Analysis Protocols

James L. Mueller[1], Curtiss Davis[2], Robert Arnone[3], Robert Frouin[4], Kendall Carder[5], Z.P. Lee[5], R.G. Steward[5], Stanford Hooker[6], Curtis D. Mobley[7] and Scott McLean[8]

[1]*Center for Hydro-Optics and Remote Sensing, San Diego State University, California*
[2]*Naval Research Laboratory, Washington, District of Columbia*
[3]*Naval Research Laboratory, Stennis Space Center, Mississippi*
[4]*Scripps Institution of Oceanography, University of California, San Diego, California*
[5]*University of South Florida, St. Petersburg, Florida*
[6]*NASA, Goddard Space Flight Center, Greenbelt, Maryland*
[7]*Sequoia Scientific Inc., Redmond, Washington*
[8]*Satlantic Inc., Halifax, Nova Scotia, Canada*

12.1 INTRODUCTION

As an alternative to the in-water methods of Chapters 10 and 11, water-leaving radiance can be measured from the deck of a ship. A shipboard radiometer is used to measure radiance $L_{\mathrm{sfc}}\left(\lambda,\theta,\phi\in\Omega_{\mathrm{FOV}};\theta_{\mathrm{o}}\right)$ emanating from the sea surface at zenith angle θ (usually chosen between 30° and 50°) and azimuth angle ϕ (usually chosen between 90° and 180° away the sun's azimuth ϕ_{o}). In the convention used here, azimuth angles ϕ are measured relative to the sun's azimuth, *i.e.* $\phi_{\mathrm{o}} = 0$.

The surface radiance measured with a radiometer having a solid-angle field of view (FOV) of Ω_{FOV} sr may be expressed, following Mobley (1999), as

$$L_{\mathrm{sfc}}\left(\lambda,\theta,\phi\in\Omega_{\mathrm{FOV}};\theta_{\mathrm{o}}\right)=L_{\mathrm{W}}\left(\lambda,\theta,\phi\in\Omega_{\mathrm{FOV}};\theta_{\mathrm{o}}\right)+\rho L_{\mathrm{sky}}\left(\lambda,\theta_{\mathrm{sky}},\phi_{\mathrm{sky}}\in\Omega'_{\mathrm{FOV}};\theta_{\mathrm{o}}\right). \quad (12.1)$$

$L_{\mathrm{W}}\left(\lambda,\theta,\phi\in\Omega_{\mathrm{FOV}};\theta_{\mathrm{o}}\right)$ is water-leaving radiance centered at angles (θ, ϕ) and averaged over Ω_{FOV} [as weighted by the radiometer's directional response function (see Chapter 5)]. $L_{\mathrm{sky}}\left(\lambda,\theta_{\mathrm{sky}},\phi_{\mathrm{sky}}\in\Omega'_{\mathrm{FOV}};\theta_{\mathrm{o}}\right)$ is sky radiance measured with the radiometer looking upward at angles (θ_{sky}, ϕ_{sky}). In practice, θ and θ_{sky} are numerically equal angles in the nadir and zenith directions, respectively, and the sea and sky viewing azimuths $\phi = \phi_{\mathrm{sky}}$. The reflectance factor ρ is operationally defined as the total skylight actually reflected from the wave-roughened sea surface into direction (θ,ϕ) divided by sky radiance measured with the radiometer from direction (θ_{sky},ϕ_{sky}), both quantities being averaged over Ω_{FOV} (Mobley 1999). Remote sensing reflectance is then determined, using water-leaving radiance calculated from (12.1), as

$$R_{\mathrm{RS}}\left(\lambda,\theta,\phi\in\Omega_{\mathrm{FOV}};\theta_{o}\right)=\frac{L_{\mathrm{W}}\left(\lambda,\theta,\phi\in\Omega_{\mathrm{FOV}};\theta_{\mathrm{o}}\right)}{E_{\mathrm{S}}\left(\lambda;\theta_{\mathrm{o}}\right)}, \quad (12.2)$$

where $E_S(\lambda;\theta_o)$ is incident spectral irradiance measured above the sea surface. All of the above variables vary with solar zenith angle θ_o.

A simplified notation is used in Chapters 10 and 11 (and elsewhere in the protocols) when discussing water leaving radiance $L_W(\lambda)$ and remote sensing reflectance $R_{RS}(\lambda)$ derived from in-water profile measurements of $L_u(z,\lambda)$. Because $L_u(z,\lambda)$ is measured viewing the nadir direction, $L_W(\lambda)$ represents

radiance leaving the surface in the zenith direction $(\theta, \phi) = (0^o, 0^o)$. Therefore, $L_W(\lambda)$ in Chapter 11 corresponds to $L_W(\lambda, 0, 0 \in \Omega_{FOV}; \theta_o)$, and $R_{RS}(\lambda)$ to $R_{RS}(\lambda, 0, 0 \in \Omega_{FOV}; \theta_o)$, in the present notation .

12.2 PROPOSED MEASUREMENT CONCEPTS

Proposed protocols for measuring remote sensing reflectance group essentially into three basic categories of measurement concepts, each of which is described briefly in this section. Remote sensing reflectance determination by some, but not all three, of the proposed above-water methods have been compared to each other (Hooker et al. 1999, 2000). Comparisons have also been made between each method and $R_{RS}(\lambda)$ determined from in-water $L_u(z,\lambda)$ and above-water $E_s(\lambda;\theta_o)$ measurements (*e.g.* Rhea and Davis, 1997; Mueller *et al*. 1997; Fougnie *et al*. 1999; Hooker *et al*. 1999), finding root-mean-square differences generally larger than 20 % for any sample spanning a reasonably large range of environmental conditions. Some of these investigators have normalized the measurements, using the method of Morel and Gentili (1996) to account for variations in viewing and solar zenith angles and in the ocean Bidirectional Reflectance Distribution Function (BRDF), prior to making the comparisons (*e.g.* Mueller *et al.* 1997; Toole *et al*. 2000), and some have not (*e.g.* Rhea and Davis 1997; Fougnie et al. 1999).

Method 1: Calibrated radiance and irradiance measurements.

Radiometers which have been fully characterized and calibrated, following the methods of Chapter 6, are used to measure $L_{sfc}(\lambda, \theta, \phi \in \Omega_{FOV}; \theta_o)$, $L_{sky}(\lambda, \theta_{sky}, \phi_{sky} \in \Omega'_{FOV}; \theta_o)$ and $E_s(\lambda;\theta_o)$. Assumptions are chosen to estimate surface reflectance ρ, and $L_W(\lambda, \theta, \phi \in \Omega_{FOV}; \theta_o)$ and $R_{RS}(\lambda, \theta, \phi \in \Omega_{FOV}; \theta_o)$ are calculated using equations (12.1) and (12.2). Example implementations of this straightforward instrumental approach, and comparisons with remote sensing reflectance determined from in-water measurements, are described in Rhea and Davis (1997), Mueller et al. (1997), Hooker et al. (1998), Hooker and Lazin (2000), and Toole et al. (2000).

Method 2: Uncalibrated radiance and reflectance plaque measurements

In this approach, a radiance sensor that has not been calibrated is used to measure signals proportional to $L_{sfc}(\lambda, \theta, \phi \in \Omega_{FOV}; \theta_o)$, $L_{sky}(\lambda, \theta_{sky}, \phi_{sky} \in \Omega'_{FOV}; \theta_o)$ and radiance reflected from a horizontal plaque, or "grey-card", having a known bi-directional reflectance (often assumed to be near-Lambertian) for the solar and viewing directions. The raw uncalibrated radiance signals are substituted in (12.1) to express $L_W(\lambda, \theta, \phi \in \Omega_{FOV}; \theta_o)$ as

$$L_W(\lambda, \theta, \phi \in \Omega_{FOV}; \theta_o) = F_L(\lambda)\left[S_{sfc}(\lambda, \theta, \phi \in \Omega_{FOV}; \theta_o) - \rho S_{sky}(\lambda, \theta_{sky}, \phi_{sky} \in \Omega'_{FOV}; \theta_o)\right], \quad (12.3)$$

where $F_L(\lambda)$ is the instrument's unknown radiance response calibration factor, and $S_{sfc}(\lambda, \theta, \phi \in \Omega_{FOV}; \theta_o)$ and $S_{sky}(\lambda, \theta_{sky}, \phi_{sky} \in \Omega'_{FOV}; \theta_o)$ are the radiometer's measured responses. The radiance reflected from the plaque is scaled to estimate $E_s(\lambda;\theta_o)$ as

$$E_S(\lambda;\theta_o) = \frac{\pi F_L(\lambda) S_g(\lambda, \theta_g, \phi_g \in \Omega_{FOV}; \theta_o, \phi_o)}{R_g(\lambda, \theta_g, \phi_g \in \Omega_{FOV}; \theta_o, \phi_o)}, \quad (12.4)$$

where $S_g(\lambda, \theta_g, \phi_g \in \Omega_{FOV}; \theta_o, \phi_o)$ is the sensor response signal when the plaque (grey-card) is viewed at angles (θ_g, ϕ_g) with the sun at (θ_o, ϕ_o), and $R_g(\lambda, \theta_g, \phi_g \in \Omega_{FOV}; \theta_o, \phi_o)$ is the plaque's bi-directional reflectance function (BRDF) for that sun and viewing geometry [including whatever is assumed regarding the contribution of sky irradiance to $E_s(\lambda;\theta_o)$]. The most straightforward BRDF geometry is for the sensor to view the center of the plaque normal to its surface (*i.e.* $\theta_g = 0$), allowing the BRDF to be determined for illumination angles between normal and 90° at, *e.g.* 5° increments. When expressions (12.3) and (12.4) are

substituted into (12.2) to calculate $R_{\mathrm{RS}}\left(\lambda,\theta,\phi\in\Omega_{\mathrm{FOV}};\theta_{\mathrm{o}}\right)$, the unknown radiance response calibration factor $F_L(\lambda)$ cancels. As with the other methods, the reflectance of the sea surface ρ is estimated using one of several possible sets of assumptions and approximations.

For quantitative determinations of $E_s(\lambda;\theta_o)$ and $L_{\mathrm{W}}\left(\lambda,\theta,\phi\in\Omega_{\mathrm{FOV}};\theta_{\mathrm{o}}\right)$ by this method, the radiometer must be calibrated to determine the coefficients $F_L(\lambda)$.

This method was adapted for ocean color applications, initially by Carder and Steward (1985), from an approach used widely in the LANDSAT remote sensing community to measure reflectance spectra of terrestial surfaces. Carder et al. (1993) used the method with a vertical polarizer to minimize reflected skylight, and Lee et al. (1997b) compared measurements with and without the polarizer (and found little difference – a result subsequently explained by Fougnie et al. 1999). Other aspects and applications of this approach are described in Lee *et al*. (1997a). In particular, they spectrally deconvolve the Rayleigh from aerosol skylight reflected from the sea surface using a Fresnel value for the Rayleigh, and a variable reflectance value for wave-modulated aerosol radiance. When sunglint is not an issue, the $(\theta, \phi) = (30^{o},90^{o})$ angle provides less uncertainty due to wave modulation in the Fresnel reflectance using the Lee et al. (1997a) method. Rhea and Davis (1997), Toole et al. (2000), and Hooker et al. (1999) compared reflectances determinations by this method with determinations from in-water measurements.

Method 3: Calibrated surface polarized radiance measurements with modeled irradiance and sky radiance

A radiance sensor is fitted with a polarizing filter set to pass only vertically polarized component of viewed radiance. The polarizer minimizes the skylight reflectance term in (12.1) when the surface is viewed near the Brewster angle. The instrument is calibrated using the methods of Chapter 6, and is used to measure only $L_{\mathrm{sfc}}\left(\lambda,\theta,\phi\in\Omega_{\mathrm{FOV}};\theta_{\mathrm{o}}\right)$. A sun photometer is used to determine aerosol optical thicknesses at each wavelength (Chapter 14). A radiative transfer model is then used to calculate $E_s(\lambda;\theta_o)$ and $L_{\mathrm{sky}}\left(\lambda,\theta_{\mathrm{sky}},\phi_{\mathrm{sky}}\in\Omega'_{\mathrm{FOV}};\theta_{\mathrm{o}}\right)$ so that (12.1) and (12.2) may be solved for $R_{\mathrm{RS}}\left(\lambda,\theta,\phi\in\Omega_{\mathrm{FOV}};\theta_{\mathrm{o}}\right)$. The details of this method, which is the protocol recommended for use with the SIMBAD radiometer (see also Chapters 7 and 14), are described by Fougnie *et al*. (1999).

Exact Normalized Remote Sensing Reflectance

The remote sensing reflectances determined by any of the above methods are not comparable with each other for different days or viewing angles, with satellite ocean color determinations of $R_{\mathrm{RS}}(\lambda)$, or with $R_{\mathrm{RS}}(\lambda)$ determined from in-water measurements. For these purposes, measured $R_{\mathrm{RS}}\left(\lambda,\theta,\phi\in\Omega_{\mathrm{FOV}};\theta_{\mathrm{o}}\right)$ must be converted to *exact normalized remote sensing reflectance*, defined as

$$R_{\mathrm{RS}}^{\mathrm{ex}}(\lambda)\equiv\frac{L_{\mathrm{WN}}^{\mathrm{ex}}(\lambda)}{\bar{F}_{\mathrm{o}}(\lambda)}, \tag{12.5}$$

where $\bar{F}_{\mathrm{o}}(\lambda)$ is mean solar irradiance above the atmosphere (Neckel and Labs, 1984), and the *exact normalized water-leaving radiance* $L_{\mathrm{WN}}^{\mathrm{ex}}(\lambda)$ is defined Chapter 13, together with protocols for determining it from $R_{\mathrm{RS}}\left(\lambda,\theta,\phi\in\Omega_{\mathrm{FOV}};\theta_{\mathrm{o}}\right)$.

12.3 RADIOMETRIC MEASUREMENT METHODS

Field of View Considerations

In the protocols for determining $L_W(\lambda)$ from in-water measurements of radiance profiles (Chapters 10 and 11), the radiance sensor's angular FOV is not critical, because the upwelling radiance distribution varies relatively little over zenith angles up to 30°. When measuring $L_{\mathrm{sfc}}\left(\lambda,\theta,\phi\in\Omega_{\mathrm{FOV}};\theta_{\mathrm{o}}\right)$, however, the size of an instrument's solid angle FOV Ω_{FOV} affects its sensitivity to variability in the skylight reflection

term of (12.1) (Lee *et al*. 1997a; Fougnie et al. 1999; Mobley 1999). This situation arises because the slope of the wind roughened sea surface varies spatially and temporally on scales small compared to the typical area subtended by Ω_{FOV} and sensor integration time, respectively. The surface slope distribution varies strongly as a function of, and may be estimated from, local wind speed (Cox and Munk 1954). For a small area of sea surface at a fixed location, wind gustiness may cause variations in the slope distribution (visible as "cat's paws") on time scales from seconds to minutes. The surface slope distribution is also systematically varied on time scales of order 10 sec by gravity waves, primarily through interactions with capillary waves through periodic modulations of surface tension, and secondarily by very small direct variations in surface slope (gravity waves break before slopes reach 6°). [In SIMBAD measurements of polarized surface radiance, for example, the oscillations associated with the primary swell appear clearly in the data. The minimum values are selected in the data processing. (R. Frouin, Pers. Comm.)]

The average surface slope variability, in combination with angular variability in $L_{sky}\left(\lambda,\theta_{sky},\phi_{sky}\in\Omega'_{FOV};\theta_o\right)$, introduces strong variability in the skylight reflectance term of (12.1), which increases remarkably with a large Ω_{FOV} (Mobley 1999; Fougnie *et al*. 1999; Toole *et al*. 2000). With a very small Ω_{FOV}, on the other hand, measurements made from close above the surface view an extremely small area that is subject to large temporal variations in slope, and thus also in the directions in which the sky is viewed through surface reflection. The ideal, which can only be effectively realized from satellite orbital elevations above the earth's surface, is a very small Ω_{FOV} (to minimize viewing angle variation across the FOV) combined with a subtended surface area (pixel) large enough to average surface slope variations associated with wind gusts, capillary waves and gravity waves.

Large FOV measurements also integrate over a significant range of variability in the ocean's BRDF, and it may prove difficult to determine exact normalized remote sensing reflectance $R_{RS}^{ex}(\lambda)$ [Equation (12.5)] from these data (Chapter 13, and references cited therein).

Full-angle FOV's used, or assumed in model computations, by various investigators have ranged from approximately 2° (*e.g.* Fougnie *et al.* 1999) up to 18° (*e.g.* Gould *et al*. 2000).

Radiance Measurements

The surface and sky radiance measurements should be made from a location that minimizes both shading and reflections from superstructure. A good position for measuring the water-leaving radiance may often be found near the bow of the ship. Especially while steaming, ocean color radiance measurements should usually be made from the bow, because from this location it is practical to view a spot where the water is undisturbed by the ship's wake or associated foam. It must also be easy, in the selected position, to point in a direction away from the sun to reduce specular reflection of sunlight.

To measure $L_{sfc}\left(\lambda,\theta,\phi\in\Omega_{FOV};\theta_o\right)$ the radiometer should be pointed toward the sea surface at viewing angles, measured at the pixel, $(\theta, \phi) = (40\text{-}45^o, 135^o)$, if possible (Mobley 1999; Fougnie et al. 1999), and in all circumstances the viewing azimuth must be in the range $90^o < \phi < 180^o$ relative to the sun's azimuth. For polarized measurements a viewing angle of $\theta = 45^o$ is strongly recommended (Fougnie et al. 1999). A viewing angle that is 180° away from the sun's azimuth should be avoided. The measurements at this angle may be contaminated by the *glory* phenomenon, and ship shadow might also be a problem in this configuration. Measurements should also not be made when the sun is close overhead ($\theta_o < 20^o$), for reasons discussed in Section 12.4 (Mobley et al. 1999). In addition, whitecaps, foam and floating material should be avoided during measurements, but at wind speeds exceeding 10 m s^{-1} extensive whitecap coverage may unavoidably contaminate the data record to some extent.

Because of temporal variability in surface reflectance, due to wind gusts and waves, it is important to record a number of spectra within a period of several seconds, or minutes if necessary. With filter radiometers (Mueller 1997; Fougnie et al. 1999; Hooker et al. 1999, 2000), it is feasible to sample individual spectra at rates of several Hz, and the electronic gain changes account for the different magnitudes of the water and sky signals.

If miniature, fiber-optic spectroradiometers are used, on the other hand, the detector integration time is varied to provide the necessary dynamic range. Sky radiances may be integrated over a few hundred msec, while the ocean surface radiance may be integrated over 1 to 2 sec. A separate dark reading must be obtained each time the integration time is changed. A typical measurement sequence with this type of spectroradiometer is to measure plaque-reflected, sea and sky and radiances (each preceded by a dark offset reading), in that order, and repeat the sequence 5 or more times.

Data records of longer duration may be advisable to improve averaging over modulation of capillary waves by wind variability and gravity waves, but there has been little research on that aspect of the problem. Before calculating final mean and standard deviation spectra, positive outliers due to briefly viewed foam patches, whitecaps and strong glint should be removed by inspection of the data record.

When using *Method 3*, described above, only $L_{\mathrm{sfc}}\left(\lambda,\theta,\phi\in\Omega_{\mathrm{FOV}};\theta_{\mathrm{o}}\right)$ need be measured, together with a sun photometer measurement, and $L_{\mathrm{sky}}\left(\lambda,\theta_{\mathrm{sky}},\phi_{\mathrm{sky}}\in\Omega'_{\mathrm{FOV}};\theta_{\mathrm{o}}\right)$ and $E_S(\lambda;\theta_o)$ are modeled. This can only be done accurately when clouds do not obscure the solar disk and fractional cloud cover is less than 20 %. These are the necessary conditions for the measurement.

To measure $L_{\mathrm{sky}}\left(\lambda,\theta_{\mathrm{sky}},\phi_{\mathrm{sky}}\in\Omega'_{\mathrm{FOV}};\theta_{\mathrm{o}}\right)$ (*Methods 1 and 2*), the radiometer is pointed upward to view the sky at angles (θ_{sky}, ϕ_{sky}) = (θ, ϕ), *e.g.* (40°, 135°). When pointing the radiometer, θ_{sky} is measured from the zenith, and θ from the nadir, direction as seen from the ship. In radiative transfer calculations, the origin is taken to be located at the pixel and both angles are zenith angles (following the usual convention used in, *e.g.*, ocean color atmospheric correction algorithms). When measurements are made in partly cloudy sky conditions, viewing angles should be selected to cover a clear segment of the sky, if possible. Corrections for reflected sky radiance are problematic unless the cloud fraction is very small in the hemisphere centered on the selected viewing azimuth (Mobley 1999).

Ideally, it can be argued that sky radiance should be measured simultaneously with $L_{\mathrm{sfc}}\left(\lambda,\theta,\phi\in\Omega_{\mathrm{FOV}};\theta_{\mathrm{o}}\right)$ and $E_S(\lambda;\theta_o)$, using separate radiometers (*e.g.* Hooker et al. 1999). For reasons of economy, however, most investigators will use the same radiometer for both radiance measurements, which therefore, must be measured sequentially (*e.g.* Carder and Steward 1985; Lee et al. 1997; Mueller 1997). If separate radiometers are used, they must be calibrated and fully characterized (Chapters 5 and 6), following the approach described above as *Method 1* (although one could use two calibrated radiance sensors, and still use a reflectance plaque to estimate $E_S(\lambda;\theta_o)$ as in *Method 2*).

Incident Irradiance Measurements

Measurements of $E_S(\lambda;\theta_o)$ with a calibrated irradiance sensor are an essential component of *Method 1* (above). The radiometer should be mounted in a location that is free of both shadows and reflections of light from any part of the ship's superstructure (see also Section 10.2). This can usually be accomplished by mounting the radiometer high on a mast, albeit in some combinations of location and ship's heading, intermittent shadowing by antennas, stays and other parts of the ship's rigging may contaminate the $E_S(\lambda;\theta_o)$ measurements. The data must also be edited to remove measurements when the irradiance collector's orientation is more than 5° away from horizontal. When a hand-held irradiance sensor is used to measure $E_S(\lambda;\theta_o)$ at the same location where $L_{\mathrm{sfc}}\left(\lambda,\theta,\phi\in\Omega_{\mathrm{FOV}};\theta_{\mathrm{o}}\right)$ and $L_{\mathrm{sky}}\left(\lambda,\theta_{\mathrm{sky}},\phi_{\mathrm{sky}}\in\Omega'_{\mathrm{FOV}};\theta_{\mathrm{o}}\right)$ are measured, it may be more difficult to find an ideal location on some.

Time series of $E_S(\lambda;\theta_o)$ should be recorded synchronously with measurements of both $L_{\mathrm{sfc}}\left(\lambda,\theta,\phi\in\Omega_{\mathrm{FOV}};\theta_{\mathrm{o}}\right)$ and $L_{\mathrm{sky}}\left(\lambda,\theta_{\mathrm{sky}},\phi_{\mathrm{sky}}\in\Omega'_{\mathrm{FOV}};\theta_{\mathrm{o}}\right)$. If the average incident irradiances associated with the surface and sky radiance measurements agree within a few percent, their ratio should be used to scale one, or the other, radiance to adjust for the apparent change in atmospheric radiometric conditions during the time interval between the two measurements. If the average $E_S(\lambda;\theta_o)$ values differ significantly, the entire measurement sequence is suspect and the data should be flagged as suspect, and probably discarded.

In this quality control context, time series measurements of $E_s(\lambda;\theta_o)$ with a deck cell may also be useful when either *Method 2* or *3* is used to determine $R_{RS}\left(\lambda,\theta,\phi \in \Omega_{FOV};\theta_o\right)$.

Reflectance Plaque Measurements

When following *Method 2* (above), a Spectralon (or alternative material) reflectance plaque having a known BRDF is used to normalize the uncalibrated radiance measurements for $E_s(\lambda;\theta_o)$. In this approach, an accurately characterized BRDF for the plaque is as critical as are the accuracies of radiometric calibrations in *Methods 1 and 3*. Traditionally, gray reflectance plaques with approximately 10 % nominal reflectance have been used for this measurement (Carder and Steward 1985; Rhea and Davis 1997; Hooker et al. 1999), but white Spectralon plaques with 99 % reflectance offer better homogeneity in BRDF (over the plaques surface area) and have been used by some investigators (*e.g.* Hooker et al. 1999; Toole et al. 2000).

The plaque must be held horizontally, and exposed to the sun and sky in a position free from both shading by, and reflections from, any part of the ship's superstructure, observer, or radiometer. It may be difficult, on some ships, to find a location that meets this requirement and also affords an unobstructed view of the sea surface at an acceptable (θ, ϕ) relative to the sun. In such situations, the alternative approaches should be considered. With the horizontal plaque thus located, it is viewed by the radiance sensor at the angles consistent with the solar direction and the plaque's BRDF characterization. The simplest approach is to determine the BRDF for the sensor view normal to the plaque center and use that viewing geometry in the field. Finally, the radiance reflected from the plaque is recorded.

Sun Photometer Measurements

It is strongly recommended that sun photometer measurements be made to determine aerosol optical thickness, following the protocols of Chapter 14, coincident with every set of above-water remote-sensing reflectance measurements. Note that this measurement is an important element of *Method 3* (above), where it is needed to correctly model $L_{sky}\left(\lambda,\theta_{sky},\phi_{sky} \in \Omega'_{FOV};\theta_o\right)$ and $E_s(\lambda;\theta_o)$ (Fougnie *et al.* 1999).

Ancillary Measurements and Records

The following ancillary data and information must be recorded in header files and/or logs for each radiometric measurement:

1. date and time (UTC) of the station and cast;
2. geographic location (latitude and longitude in decimal degrees to the nearest 0.001);
3. the viewing zenith and azimuth angles of surface and sky radiance, and the solar azimuth relative to the ship's heading;
4. the direction of the sun relative to the ship's heading;
5. cloud cover and sky conditions;
6. wind speed and direction;
7. sea state, as significant wave height, whitecap fraction, and the direction, height and period of the dominant swell. period);
8. barometric pressure;
9. Secchi depth;
10. dark (zero-offset) data file, to be recorded, and the dark filename logged, at the time of the measurements;
11. times, locations and file identification of associated CTD, in situ fluorescence, in-water radiometry and inherent optical property profiles, if any;

12. geographic locations, times and depths of associated water samples, if any;
13. names of files with data from comparisons with a portable irradiance and radiance reference standard made in the field and used to track the instrument's stability during a deployment (Chapter 7);
14. instrument identification; and
15. calibration date and file identification (constant throughout a cruise, usually).

Protocols describing measurement and analysis methods for the standard ancillary variables (Chapter 3, Table 3.1) are presented in Chapter 9.

Wind speed and direction, sea state, and sky conditions are essential information for accurate corrections for reflected sky radiance (see below). Photographs of sky and sea surface conditions are highly desirable. Viewing and solar geometry are fundamental to this type of measurement.

It is desirable to also measure in-water radiometric and IOP profiles at stations where above-water measurements of remote-sensing reflectance are made.

12.4 SKY RADIANCE REFLECTANCE OF THE SEA SURFACE

For a flat sea surface and a uniform sky radiance distribution, ρ reduces to the Fresnel reflectance of the sea surface averaged over Ω_{FOV}. In this limit, $\rho \approx 0.02$ for $\theta \leq 30°$ and increases slowly to $\rho \approx 0.03$ at $\theta \cong 40°$ (Austin 1974). The sea surface is usually wave-roughened and clear sky radiance distributions are not uniform, however, with the result that ρ can be much significantly larger than these simple values and is furthermore very difficult to determine for most wind and sea state conditions (Mobley, 1999; Fougnie *et al.* 1999; Lee *et al.* 1997; Mueller *et al*. 1997; Toole *et al.* 2000).

Clear Skies

In general, the sky radiance reflectance of the sea surface is an apparent optical property that has a functional dependence on many variables, $\rho = \rho(\theta_{sky}, \phi_{sky}, \theta, \phi, \Omega_{FOV}$, wind speed, sea state, sky radiance distribution), the complexities of which have been rigorously explored using radiative transfer computations by Mobley (1999) for unpolarized radiance. Assuming $(\theta, \phi) = (40^o, 135^o)$ and a clear-sky radiance distribution for a solar zenith angle $\theta_o = 30^o$, Mobley's results show that ρ increases from 0.026 with wind speed U = 0 m s^{-1} to approximately 0.043 when U = 15 m s^{-1}. As solar zenith angles increase, the upper limit of ρ at U = 15 m s^{-1} decreases monotonically to a value $\rho \approx 0.036$ at $\theta_o = 80^o$. For viewing angles $(\theta, \phi) = (30^o, 90^o)$, the clear-sky ρ at U = 15 m s^{-1} is ~0.08 when $\theta_o = 30^o$ and is comparable to $(\theta, \phi) = (40^o, 135^o)$ for $\theta_o > 40^o$. For solar zenith angles $\theta_o > 30^o$, Mobley found that the clear-sky ρ for $(\theta, \phi) = (40^o, 135^o)$ was independent of wavelength at all wind speeds. For viewing angles $(\theta, \phi) = (30^o, 90^o)$, however, he found that clear-sky ρ at U = 15 m s^{-1} varied by factor of 2 over wavelength due to the spectral differences between reflected skylight and sun glint. For both sets of viewing angles, the reflectance factor ρ increases much more rapidly with wind speed for $\theta_o < 30^o$, due to increased sun glint, and this type of measurement would not seem to be practical at solar zenith angles $\theta_o < 20^o$. It is perhaps noteworthy that, at least with present atmospheric correction algorithms, sun glint also renders satellite ocean color measurements unusable when the sun is less than 20° from zenith.

Fougnie et al. (1999) made similar model calculations, and experimentally verified them, for vertical and horizontally polarized components of reflected skylight. Their model calculations showed that for a rough water surface, the zenith angle where vertically polarized reflectance is a minimum shifts from the Brewster angle, approximately $\theta = 52^o$, to approximately $\theta = 45^o$. They also found that the minimum reflected skylight effect was obtained at viewing angles $(\theta, \phi) = (45^o, 135^o)$. For the more widely used viewing angles $(\theta, \phi) = (30^o, 90^o)$ (Carder and Steward 1985; Lee et al. 1997; Mueller et al. 1997), vertically and horizontally polarized reflectances are both larger and nearly equal, which explains why no

significant differences were found between total and vertically polarized measurements at these angles by Lee *et al.* (1997), or Mueller *et al*. (1997).

Scattered and Broken Clouds

Radiance scattered from clouds is typically greater than, and spectrally different from, clear-sky radiance. Therefore, the presence of randomly distributed clouds within 90° of the viewing azimuth ϕ may significantly increase the magnitude of reflected skylight and alter its wavelength dependence, a phenomenon noted by many investigators (*e.g.* Mobley 1999; Toole et al. 2000; Fougnie et al. 1999). Moreover, the temporal variability and uncertainty of both attributes of reflected skylight will increase. Obviously, effects related to mixed cloudy and cloud-free segments of the sky become progressively more pronounced as wind speed increases, and the effectiveness of correction algorithms becomes problematic in these circumstances (Mobley 1999).

Overcast Skies

When skies are totally overcast, the sky radiance distribution becomes more uniform and its wavelength dependence becomes gray (Mobley 1999; Toole et al. 2000). There is some evidence that $R_{\mathrm{RS}}\left(\lambda,\theta,\phi\in\Omega_{\mathrm{FOV}};\theta_{\mathrm{o}}\right)$ determined from above-water measurements under overcast skies may have significantly lower uncertainty than can be realized in either clear skies or partially cloudy skies (Toole 2000). Measurements under cloudy skies are of little interest in the context of SIMBIOS and SeaWiFS validation studies. On the other hand, measurements under overcast conditions provide insight into phytoplankton dynamics under conditions that cannot be observed from space.

Residual Reflectance Corrections

If the ocean is assumed to be totally absorbing ("black") at 750 nm (and longer wavelengths), then we should find $R_{\mathrm{RS}}\left(750,\theta,\phi\in\Omega_{\mathrm{FOV}};\theta_{\mathrm{o}}\right)=0$ if the reflected skylight term is properly estimated in equation (12.1). Following the "quick and easy" algorithm of Carder and Steward (1985), if it is further assumed that any error in skylight reflection term is white (not wavelength dependent), one may apply a calculated value of $R'_{\mathrm{RS}}\left(750,\theta,\phi\in\Omega_{\mathrm{FOV}};\theta_{\mathrm{o}}\right)\neq 0$ as a simple offset correction at other wavelengths, *i.e.*

$$R_{\mathrm{RS}}\left(\lambda,\theta,\phi\in\Omega_{\mathrm{FOV}};\theta_{\mathrm{o}}\right)=R'_{\mathrm{RS}}\left(\lambda,\theta,\phi\in\Omega_{\mathrm{FOV}};\theta_{\mathrm{o}}\right)-R'_{\mathrm{RS}}\left(750,\theta,\phi\in\Omega_{\mathrm{FOV}};\theta_{\mathrm{o}}\right).$$

This adjustment was previously recommended as part of the provisional protocol for determining above-water remote sensing reflectance (Mueller and Austin 1995). Other suggested wavelengths that have been suggested for determining such a "black-ocean" residual offset include 670, 765, 865 and 1012 nm (Hooker et al. 1999).

In turbid coastal waters, where the above-water technique would be most useful, it is clearly not appropriate to assume that $R_{\mathrm{RS}}\left(750,\theta,\phi\in\Omega_{\mathrm{FOV}};\theta_{\mathrm{o}}\right)=0$ (Sydor and Arnone 1997; Sydor et al. 1998; Lee et al. 1997; Gould et al. 2000). Moreover, skylight reflection variability, and uncertainty in its estimation, is largely associated with sun glint and radiance from clouds, neither of which produces a strictly white offset (Lee et al. 1997; Mobley 1999).

Lee et al. (1997) proposed an alternative algorithm which partitions the skylight reflectance term of (12.1) into Rayleigh (λ^{-4} dependence) and aerosol (λ^{-n} dependence, n to be determined on a case-by-case basis) scattering terms, using a non-linear optimization analysis to minimize residuals from expected spectral variations in remote-sensing reflectance at a selected set of wavelengths.

Gould et al. (2000) proposed an algorithm to partition the surface radiance at 720 nm into remote-sensing reflectance and sky reflectance components estimated from the difference between apparent reflectances measured at 715 and 735 nm. Following Lee *et al.* (1997), they assumed a coefficient for exponential wavelength dependence and extrapolated the skylight reflectance to lower wavelengths. When *in situ* IOP are also measured at a station, they derived an improved wavelength dependence model for the sky reflectance correction based on remote-sensing reflectance at 40 nm calculated from *a*(400) and *b*(400).

Sydor *et al.* (1998) proposed combining polarized and unpolarized measurements to derive an estimate of the wavelength dependence of reflected skylight. These wavelength-dependency approaches show initial promise, and with further development and experimental validation, some variant on these methods may yet lead to a robust algorithm for correcting above-water determinations of remote-sensing reflectance.

So far, evaluations of the uncertainty associated with the simple white-offset adjustment have not supported its general use, on either experimental (Lee et al. 1997; Hooker et al. 1999; Toole et al. 2000) or theoretical (Mobley 1999) grounds. Its use is not recommended in the present version of the protocols, even though the results of Toole et al. (2000) suggest it may be appropriate under totally overcast skies.

12.5 DISCUSSION AND RECOMMENDATIONS

The protocols recommended, provisionally, in Mueller and Austin (1995) for above-water measurements of $R_{\mathrm{RS}}\left(\lambda,\theta,\phi\in\Omega_{\mathrm{FOV}};\theta_{\mathrm{o}}\right)$ were seriously flawed. The viewing zenith angles (20°) recommended there were too small to avoid serious sun glint contamination. The recommendation that one might measure sky radiance using a first surface mirror would, if followed, introduce significant repolarization of the measured radiance and yield a serious radiometric artifact. And finally, two key equations of that protocol contained serious typographical errors. The Mueller and Austin (1995) protocols related to above-water measurements of water-leaving radiance and remote-sensing reflectance should not be followed under any circumstances.

The above-water methods for determining normalized remote-sensing reflectance (NRSR)[3], as described above, and their associated uncertainty budgets, have been discussed at length in several meetings and workshops over the last few years, as well as in the literature cited here. In particular, a SIMBIOS sponsored NRSR Workshop was held at Old Dominion University (Norfolk, VA) in December 1997. At that workshop, the participants agreed that the uncertainty budgets associated with the above-water methods proposed for determining NRSR are poorly known, and that a unified data set was needed as a basis for correcting that deficiency. It was also the workshop consensus that additional research and analyses should be pursued to:

1. Determine uncertainties in and between $E_s(\lambda;\theta_o)$ determined by a) direct measurement with a calibrated radiometer (*Method 1*), b) estimation based on measurement of radiance reflected from a gray target have a known BRDF (*Method 2*), and radiative transfer models for clear sky conditions (*Method 3*), with and without independent measurements of aerosol and ozone optical thicknesses;
2. Determine uncertainties between the different *Methods 1, 2 and 3* for measuring $R_{\mathrm{RS}}\left(\lambda,\theta,\phi\in\Omega_{\mathrm{FOV}};\theta_{\mathrm{o}}\right)$;
3. Determine uncertainties between NRSR values determined from above- and in-water radiance measurements; and
4. Evaluate uncertainties between NRSR measured, either above- or in-water, NRSR modeled from measured inherent optical properties (IOP), and NRSR modeled based on IOP estimated from phytoplankton pigments (*e.g.* chlorophyll a) and other optically important constituents of the water column.

The workshop participants recommended the following priorities, guidelines and constraints for this research:

1. Preceding any intercomparisons of measured $R_{\mathrm{RS}}\left(\lambda,\theta,\phi\in\Omega_{\mathrm{FOV}};\theta_{\mathrm{o}}\right)$, all measurements must be *normalized* to account for the influence of the solar zenith angle and the ocean's BRDF, following the methods of Morel and Gentili (1996). This applies both to in-water and above-water methods (Section 8.3).

[3] The concept of "normalized remote-sensing reflectance" (NRSR) is extended here and in Chapter 13 to "exact normalized remote-sensing reflectance" as defined in Equation (12.6), with reference to Chapter 13 (J. Mueller, 2001).

2. Initial intercomparisons should be limited to wavelengths $\lambda < 600$ nm, relatively clear waters where $K_d(490) < 0.1\ m^{-1}$, cloud cover < 20 %, wind speeds $U < 10\ m\ s^{-1}$, and solar zenith angles in the range $30^o < \phi_o < 60^o$. In these limited circumstances, an uncertainty of approximately 5 % may be assumed for NRSR determined from in-water profile measurements of upwelled radiance, an estimate based on results of profile analyses (Siegel et al. 1995) and radiometric calibration uncertainties (Mueller et al. 1996; Johnson et al. 1996).

Finally, the workshop participants agreed that a viewing zenith angle of $\theta = 40^o$, rather than the then more widely used $\theta = 30^o$, should be routinely used for above-water measurements of $R_{\mathrm{RS}}\left(\lambda,\theta,\phi\in\Omega_{\mathrm{FOV}};\theta_{\mathrm{o}}\right)$ without a polarizer.

Hooker et al. (1999) and Hooker and Lazin (2000) report experimental intercomparisons, and results of preliminary analyses, which closely follow the above guidelines. The measurement intercomparisons reported by Toole et al (2000) and Fougnie et al. (1999) were made in turbid, to very turbid, coastal water masses, which contributes to the large uncertainties (10 %-15 % for in-water and 20 %-40 % for above-water remote sensing reflectances) they reported. Neither of the latter comparisons was made using normalized reflectances, and the polarized reflectances measured by Fougnie et al. (1999) are not directly comparable to reflectances determined from unpolarized in-water radiance measurements.

There is currently insufficient information on which to conclusively recommend any preference between *Methods 1, 2 or 3* for making above-water measurements of $R_{\mathrm{RS}}\left(\lambda,\theta,\phi\in\Omega_{\mathrm{FOV}};\theta_{\mathrm{o}}\right)$.

For *Method 3*, or any polarized version of either of the other 2 methods, research is needed to establish and validate a robust relationship between vertically polarized $R_{RSv}\left(\lambda,0,0\in\Omega_{FOV};\theta_o\right)$ determined from the above-water measurements and total $R_{\mathrm{RS}}^{\mathrm{ex}}\left(\lambda\right)$ determined from total radiance measurements. Since the water body polarizes incident sunlight, polarized measurements of water-leaving radiance must be corrected to estimate total radiance. For $150\text{-}160^0$, the effect is small (typically 10 %), and can be corrected to within a few percent (Fougnie et al., 1999). Indeed, a method must be developed to determine a polarized equivalent to $R_{\mathrm{RS}}^{\mathrm{ex}}\left(\lambda\right)$.

Again, normalization consists of adjustments from the measured viewing and solar geometry to radiance emitted in the zenith direction with the sun at zenith and adjusted to remove atmospheric effects (Morel and Gentili 1996; Chapter 13). Methods for calculating $R_{\mathrm{RS}}^{\mathrm{ex}}\left(\lambda\right)$ from measurements of total $R_{\mathrm{RS}}\left(\lambda,\theta,\phi\in\Omega_{\mathrm{FOV}};\theta_{\mathrm{o}}\right)$ are given in Chapter 13. The present version of the Ocean Optics Protocols does not provide methods for determining $R_{\mathrm{RS}}^{\mathrm{ex}}\left(\lambda\right)$ from polarized radiance measurements.

It is further recommended that total surface and sky radiances should be measured at $(\theta, \phi) = (\theta_{sky}, \phi_{sky}) = (40^o, 135^o)$ (Fougnie et al. 1999; Mobley 1999). Unpolarized surface reflectance for skylight (*i.e.*, polarized plus unpolarized components) ρ should be estimated as a function of wind-speed following the method of Mobley (1999: Fig. 9), and for completely overcast skies use $\rho \approx 0.028$.

REFERENCES

Austin, R.W., 1974: Inherent spectral radiance signatures of the ocean surface. In: S.Q. Duntley, R.W. Austin, W.H. Wilson, C.F. Edgerton, and S.W. Moran, *Ocean Color Analysis*, SIO Ref. 74-10, Scripps Institution of Oceanography, La Jolla, CA.

Carder, K.L. and R.G. Steward, 1985: A remote-sensing reflectance model of a red tide dinoflagellate off West Florida. *Limnol. Oceanogr.* **30**: 286-298.

Carder, K.L., P. Reinersman, R.F. Chen, F. Muller-Karger, C.O. Davis and M. Hamilton, 1993: AVIRIS calibration and application in coastal oceanic environments. *Remote Sens. Environ.* **44**: 205-216.

Cox, C. and W. Munk, 1954: Measurement of the roughness of the sea surface from photographs of the sun's glitter. *J. Opt. Soc. Am.* **44**: 11838-11850.

Fougnie, B., R. Frouin, P. Lecomte and Pierre-Yves Deschamps, 1999: Reduction of skylight reflection effects in the above-water measurement of diffuse marine reflectance. *Appl. Opt*. **38**: 3844-3856.

Gould, R.A., R.A. Arnone and M. Sydor, 2000: Improved techniques for determining remote sensing reflectance in coastal waters, *Appl. Opt.* (In press).

Hooker, S.B. and G.Lazin, 2000: *The SeaBOARR-99 Field Campaign*. NASA Tech. Memo. 206892, Vol. **8**, S.B. Hooker and E.R. Firestone, eds., NASA Goddard Space Flight Center, Greenbelt, MD. 46pp.

Hooker, S.B., G. Zibordi, G.Lazin, and S. McLean, 1999: *The SeaBOARR-98 Field Campaign*. NASA Tech. Memo. 206892, Vol. **3**, S.B. Hooker and E.R. Firestone, eds., NASA Goddard Space Flight Center, Greenbelt, MD. 40pp.

Johnson, B.C., S.S. Bruce, E.A. Early, J.M. Houston, T.R. O'Brian, A. Thompson, S.B. Hooker and J.L. Mueller, 1996: The Fourth SeaWiFS Intercalibration Round-Robin Experiment (SIRREX-4), May 1995. *NASA Tech. Memo. 104566, Vol. **37**,* S.B. Hooker, E.R. Firestone and J.G. Acker, Eds., NASA Goddard Space Flight Center, Greenbelt, Maryland, 65 pp.

Lee, Z.P., K.L. Carder, T.G. Peacock, C.O. Davis and J.L. Mueller, 1997a: Remote-sensing reflectance and inherent optical properties of oceanic waters derived from above-water measurements. In: *Ocean Optics XIII*, S.G. Ackleson, ed., Proc. SPIE **2693**: 160-166.

Lee, Z.P., K.L. Carder, T.G. Peacock, and R.G. Steward, 1997b: Remote sensing reflectance measured with and without a vertical polarizer. In: *Ocean Optics XIII*, S.G. Ackleson, ed., Proc. SPIE **2693**: 483-488.

Mobley, C.D., 1999: Estimation of the remote-sensing reflectance from above-surface measurements. *Appl. Opt*. **38**: 7442-7455.

Morel, A., and B. Gentili, 1996: Diffuse reflectance of oceanic waters. III. Implication of bidirectionality for the remote-sensing problem. *Appl. Opt*. **35**: 4850-4862.

Mueller, J.L., B.C. Johnson, C.L. Cromer, S.B. Hooker, J.T. McLean and S.F. Biggar, 1996: The Third SeaWiFS Intercalibration Round-Robin Experiment (SIRREX-3), 19-30 September 1994: *NASA Tech. Memo. 104566, Vol. **34**,* S.B. Hooker, E.R. Firestone and J.G. Acker, Eds., NASA Goddard Space Flight Center, Greenbelt, Maryland, 78 pp.

Mueller, J.L., and R.W. Austin, 1995: Ocean Optics Protocols for SeaWiFS Validation, Revision 1. *NASA Tech. Memo. 104566, Vol. **25**,* S.B. Hooker, E.R. Firestone and J.G. Acker, Eds., NASA Goddard Space Flight Center, Greenbelt, Maryland, 67 pp.

Mueller, J.L., J.R.V. Zaneveld, S. Pegau, E. Valdez, H. Maske, S. Alvararez-Borrego and R. Lara-Lara, 1997: Remote sensing reflectance: preliminary comparisons between in-water and above-water measurements, and estimates modeled from measured inherent optical properties, In: *Ocean Optics XIII*, S.G. Ackleson, ed., Proc. SPIE **2693**: 502-507.

Rhea, W.J. and C.O. Davis, 1997: A comparison of the SeaWiFS chlorophyll and CZCS pigment algorithms using optical data from the 1992 JGOFS Equatorial Pacific Time Series. *Deep Sea Res. II* **44**: 1907-1925.

Siegel, D.A., M.C. O'Brien, J.C. Sorenson, D.A. Konnoff, E.A. Brody, J.L. Mueller, C.O. Davis, W.J. Rhea, and S.B. Hooker, 1995: Results of the SeaWiFS Data Analysis Round Robin, July 1994 (DARR-94): *NASA Tech. Memo. 104566, Vol. 26*, S.B. Hooker and E.R. Firestone, Eds., NASA Goddard Space Flight Center, Greenbelt, Maryland, pp 44-48.

Sydor, M. and R.A. Arnone, 1997: Effect of suspended and dissolved organic matter on remote-sensing of coastal and riverine waters. *Appl. Opt*. **36**: 6905-6912.

Sydor, M., R.A. Arnone, R.W. Gould, Jr., G.E. Terrie, S.D. Ladner and C.G. Wood, 1998: Remote-sensing technique for determination of the volume absorption coefficient of turbid water. *Appl. Opt*. **37**: 4944-4950.

Toole, D.A., D.A. Siegel, D.W. Menzies, M.J. Neumann and R.C. Smith, 2000: Remote-sensing reflectance determinations in the coastal ocean environment: impact of instrumental characteristics and environmental variability. *Appl. Opt*. **39**: 456-468.

Chapter 13

Normalized Water-Leaving Radiance and Remote Sensing Reflectance: Bidirectional Reflectance and Other Factors

Andre Morel[1] and James L. Mueller[2]

[1]*Laboratoire d'Oceanographie, Universite Pierre et Marie Curie, Villefranche-sur-Mer, France*

[2]*Center for Hydro-Optics and Remote Sensing, San Diego State University, California*

13.1 NOTATIONS AND FUNDAMENTAL DEFINITIONS

Most of the variables involved in the remote sensing of the ocean color are based on, or derived from, the basic radiometric quantity often called ***water-leaving radiance***; this quantity, commonly denoted $L_W(\lambda)$, is the radiance which emerges from the ocean, determined just above the water-air interface at a level conventionally denoted 0^+. The $L_W(0^+,\lambda)$ radiance field (its angular dependency will be explicitly given below) originates from the in-water upward radiance field, $L_u(0^-,\lambda)$, determined just beneath the interface at a level denoted 0^-. Since $L_W(\lambda)$ is defined only at the upper side of the interface, the explicit notation 0^+ will be omitted. Two other radiance fields are also involved, namely the downward radiance fields, just above the surface, $L_d(0^+,\lambda)$, and just beneath the surface, $L_d(0^-,\lambda)$. The reflection and refraction processes govern the transfer through the interface of the corresponding fields, namely the transformation of $L_u(0^-,\lambda)$ into $L_W(\lambda)$, and that of $L_d(0^+,\lambda)$ into $L_d^t(0^-,\lambda)$, the transmitted component of the total downward radiance distribution[4] $L_d(0^-,\lambda)$.

The angular dependencies are introduced by using two couples of angles, (θ, ϕ) and (θ', ϕ) (Figure 13.1); ϕ is the azimuth angle [0, 2π], θ is the zenith angle for above-water radiances [0, π/2], and θ' the nadir angle for the in-water (upward) directions [0, π/2]. If Ξ_d represents the upper hemisphere (2π sr), containing all downward directions), Ξ_u represents the lower hemisphere (containing the upward directions), and $d\omega = \sin\theta d\theta d\phi$ is the differential element of solid angle, the following integrals of the radiance fields

$$E_d(0^+,\lambda) \equiv \int_{\Xi_d} L_d(0^+,\lambda,\theta,\phi)\cos\theta d\omega, \tag{13.1}$$

$$E_d(0^-,\lambda) \equiv \int_{\Xi_d} L_d(0^-,\lambda,\theta',\phi)\cos\theta' d\omega', \tag{13.2}$$

$$E_u(0^-,\lambda) \equiv \int_{\Xi_d} L_u(0^-,\lambda,\theta',\phi)\cos\theta' d\omega, \text{ and} \tag{13.3}$$

[4] The radiance distributions emanating downward from the underside of the air-sea interface, and upward from its upper side, are each the sum of radiances transmitted through and reflected from the interface. In other words, $L_d(0^-,\lambda) = L_d^t(0^-,\lambda) + \rho L_u(0^-,\lambda)$ and $L_u(0^+,\lambda) = L_W(\lambda) + \rho L_d(0^+,\lambda)$, where ρ is the Fresnel reflectance of the interface. The reflected components of these radiance distributions will not be examined here as vector fields.

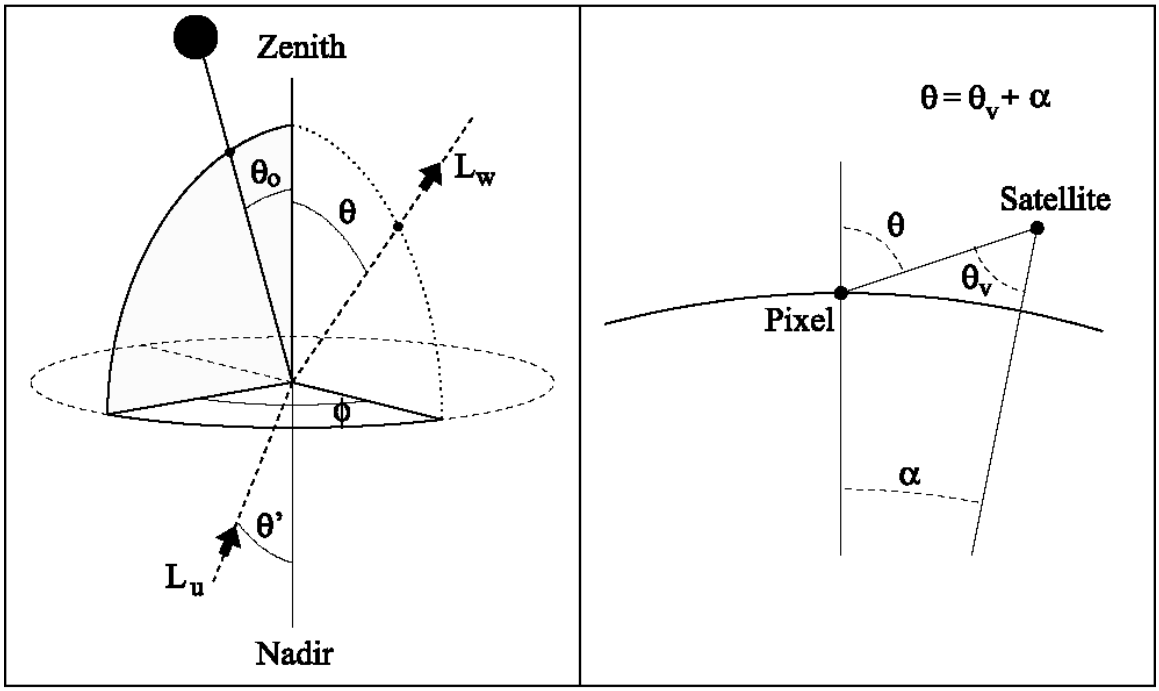

Figure 13.1: Schematic views of the geometry and symbols used in this chapter. The polar angles that specify the radiances correspond to the direction of photon travel and are measured from the local zenith for water-leaving radiance (θ') and zenith sun angle (θ_o), or from nadir when dealing with the in-water upwelling radiance (θ'). The azimuth angle ϕ is 0 and π for the sun and the antisolar directions, respectively. The viewing direction, denoted θ_v, is the direction the satellite is pointed to aim at the pixel, and is always smaller than θ.

$$E_u\left(0^+,\lambda\right) \equiv \int_{\Xi_d} L_u\left(0^+,\lambda,\theta,\phi\right)\cos\theta d\omega,\ \mu\text{W cm}^{-2}\text{nm}^{-1}, \tag{13.4}$$

are the ***downwelling irradiances*** above or below the surface, $E_d(0^+, \lambda)$ and $E_d(0^-, \lambda)$, and the ***upwelling irradiances*** below and above the surface, $E_u(0^-, \lambda)$ and $E_u(0^+, \lambda)$, respectively. The irradiance ratio, or ***irradiance reflectance***, is defined immediately below the surface as

$$R\left(0^-,\lambda\right) \equiv \frac{E_u\left(0^-,\lambda\right)}{E_d\left(0^-,\lambda\right)}. \tag{13.5}$$

Note that the corresponding quantity above the surface, $R\left(0^+,\lambda\right)$, is not in common use.

From Equation (13.3), another quantity, ***Q***, can be defined as

$$Q\left(0^-,\lambda,\theta',\phi\right) \equiv \frac{E_u\left(0^-,\lambda\right)}{L_u\left(0^-,\lambda,\theta',\phi\right)},\ \text{sr}, \tag{13.6}$$

It can be noticed that if the $L_u\left(0^-,\lambda,\theta',\phi\right)$ field was isotropic, or in other words, if $L_u\left(0^-,\lambda\right)$ was constant whatever the angles θ'and ϕ, *Q* would take the particular value π. The argument 0^- will hereafter be abandoned, as the *Q* quantity is always defined for the in-water radiant field at the interface.

All the above relationships, (13.1) to (13.6), describe the radiance vector fields and are purely of geometrical nature. Physical processes will be briefly examined, first at the interface (Section 13.2), and then inside the water body (Section 13.3).

In addition to the above general definitions, several derived quantities are specifically used in ocean color science, in particular the two following ones:

The ***remote sensing reflectance*** is defined as

$$R_{\mathrm{RS}}(\lambda,\theta,\phi)=\frac{L_{\mathrm{w}}(\lambda,\theta,\phi)}{E_{\mathrm{d}}(0^{+},\lambda)},\ \mathrm{sr}^{-1}. \tag{13.7}$$

In general (i.e., if not otherwise stated), the water-leaving radiance considered in Equation (13.7) is the vertically upward radiance originating from nadir, and traveling toward zenith ($\theta = 0$); its accurate writing is thus $L_{\mathrm{w}}(\lambda,0,0)$, when this quantity has to be distinguished from other slant radiances (actually ϕ is undetermined, not 0).

The other quantity is the ***normalized water-leaving radiance***, $L_{\mathrm{WN}}(\lambda,\theta,\phi)$ {sometimes denoted nL_W, or $[L_W]n$, in references cited below}, originally introduced by Gordon and Clark (1981). The underlying rationale was to produce, from measured $L_{\mathrm{W}}(\lambda,\theta,\phi)$ values, normalized quantities that are comparable; with this aim, these quantities must be independent from the measurement conditions, which are determined by the actual solar zenith angle and atmospheric transmittance. These environmental influences can be removed by forming the following quantity

$$L_{\mathrm{WN}}(\lambda,\theta,\phi)=\frac{L_{\mathrm{W}}(\lambda,\theta,\phi)}{E_{\mathrm{d}}(0^{+},\lambda)}\bar{F}_{\mathrm{o}}(\lambda)=R_{RS}(\lambda,\theta,\phi)\bar{F}_{\mathrm{o}}(\lambda),\ \mu\mathrm{W\ cm^{-2}nm^{-1}sr^{-1}}, \tag{13.8}$$

where the measured radiance is divided by the actual irradiance at the sea level and then multiplied by the solar irradiance at the top of the atmosphere, $\bar{F}_{\mathrm{o}}(\lambda)$, at the mean sun-earth distance (d_0). The same quantity can be interpreted in another way: the normalized leaving radiance is the radiance which would be measured, if the sun were at zenith, in absence of atmosphere, and when the earth is at its mean distance from the sun. In spite of this interpretation, the normalized water-leaving radiance is still a quantity depending on θ and ϕ, as far as the initial measurement of the quantity $L_{\mathrm{W}}(\lambda,\theta,\phi)$ has been performed under these specific angular conditions.

13.2 PHYSICAL PHENOMENA AT THE INTERFACE

Because the refractive indices n of the two media differ, ($n \cong 1$ for air and $n \cong 1.34$ for sea water), the processes of reflection and refraction occur at the interface and modify the radiance fields transmitted from one medium to the other. If the interface is perfectly level, Fresnel's law applies for water-incident or air-incident rays; if the interface is wavy, the same law applies for each facet, and the numerical computations are less simple. The incident and refracted directions, θ and θ' respectively (Figure 1), obey the Snell's law, with $\theta'=\sin^{-1}\left(\frac{\sin\theta}{n}\right)$, where n is the refractive index of water. Another consequence of this law is the so-called n^2 law for radiance, which expresses the conservation of flux along a path through media with various indices (apart from the Fresnel transmittance effect, if physical boundaries between media exist).

Coming back to the propagation of the $L_{\mathrm{d}}(0^{+},\lambda,\theta,\phi)$ field through the interface, the correspondence between the above- and in-water transmitted radiances is expressed as

$$L_{\mathrm{d}}^{\mathrm{t}}(0^{-},\lambda,\theta',\phi)=L_{\mathrm{d}}(0^{+},\lambda,\theta,\phi)\left[1-\rho(\theta,\theta')\right]n^{2},\ \mu\mathrm{W\ cm^{-2}nm^{-1}sr^{-1}}, \tag{13.9}$$

where $\rho(\theta, \theta')$ is the Fresnel reflectance for the associated directions θ and θ', and thus the bracket represents the transmittance. For the upward fields, the reciprocal relationship is written

$$L_{\mathrm{W}}(\lambda,\theta,\phi)=L_{\mathrm{u}}\left(0^{-},\lambda,\theta',\phi\right)\frac{\left[1-\rho(\theta',\theta)\right]}{n^{2}},\ \mu\mathrm{W\ cm^{-2}nm^{-1}sr^{-1}}. \tag{13.10}$$

Note that $\rho(\theta,\theta')=\rho(\theta',\theta)$, so that the reflectances are independent from the direction of propagation. Note also that $\rho(\theta',\theta)\equiv 1$ when θ' exceeds the critical angle, $\theta'_{\mathrm{c}}\cong 48°$ for $n=1.34$.

The upwelling irradiance $E_{\mathrm{u}}^{\mathrm{t}}\left(0^{+},\lambda\right)$ transmitted through the air-sea interface is obtained by integrating Equation (13.10) for a quasi-isotropic upwelling radiance distribution within the cone limited by θ'_{c}, yielding the approximate expression $E_{\mathrm{u}}^{\mathrm{t}}\left(0^{+},\lambda\right)\cong 0.52E_{\mathrm{u}}\left(0^{-},\lambda\right)$, which means that about half of the in-water upward flux incident upon a horizontal surface is able to emerge. In corollary, about half of this flux is returned back, and thence is added to the downward flux. This last remark explains why integrating Equation (13.9) does not provide straightforwardly the in-water downward irradiance, which can be approximately expressed through

$$E_{\mathrm{d}}\left(0^{-},\lambda\right)\cong E_{\mathrm{d}}\left(0^{+},\lambda\right)\frac{1-\bar{\rho}}{1-\bar{r}R\left(0^{-},\lambda\right)}. \tag{13.11}$$

The existence of the reflected downward flux is accounted for by the denominator. $\left[1-\bar{r}R\left(0^{-},\lambda\right)\right]$, which combines the irradiance reflectance with $\bar{r}$ the mean (water-air) Fresnel reflectance for the whole diffuse upward flux (about 0.48). Similarly, the term $\bar{\rho}$ stands for the (air-water) Fresnel reflectance at the interface that applies to the whole downward irradiance from the sun and the sky. This mean reflectance $\bar{\rho}$ typically amounts to 4 % to 6 %, but may deviate from these values according to the sky state and the sea state. The approximate character of Equation (13.11) originates from these two mean reflectances, $\bar{r}$ and $\bar{\rho}$.

The first determinant of the $L_{\mathrm{d}}\left(0^{+},\lambda,\theta,\phi\right)$ distribution, in a cloudless atmosphere, is the sun position, described by the solar zenith angle θ_{o}. The diffuse sky radiance also contributes to the formation of $L_{\mathrm{d}}\left(0^{+},\lambda,\theta,\phi\right)$, and the proportions of the direct solar flux and the diffuse sky radiation actually vary, not only with θ_{o} and wavelength λ, but also with the varying content in aerosol. This aerosol load is conveniently described by its optical thickness, τ_{a} at a selected reference wavelength, often 550 nm. Finally, a more accurate writing (still incomplete, as, for instance, the aerosol nature is also involved) for this downward field is $L_{\mathrm{d}}\left(0^{+},\lambda,\theta,\phi,\theta_{\mathrm{o}},\tau_{\mathrm{a}}\right)$.

Below the interface, the same dependences (with respect to λ, θ_{o}, τ_{a}) are maintained, but in addition, the transmittance through the interface may be modified because of the presence of capillary and gravity waves. To the extent that these waves, and especially their slopes, can be related to the wind speed, *W*, this new argument must be considered; finally, to account for all these factors, the in-water transmitted downward radiance field must be written $L_{\mathrm{d}}^{\mathrm{t}}\left(0^{-},\lambda,\theta',\phi,\theta_{\mathrm{o}},\tau_{\mathrm{a}},W\right)$.

13.3 THE IN-WATER RADIANT FIELD: PHYSICAL CONSIDERATIONS

The upward radiance field $L_{\mathrm{u}}\left(z,\lambda,\theta',\phi\right)$ at a depth z (including z = 0^{-}) is an *apparent optical property*, (AOP, *sensu* Preisendorfer 1960), and as such depends both on the *inherent optical properties* (IOP) of the water, and on the way this water body is illuminated.

In absence of reflecting bottom, the illumination conditions are those prevailing just beneath the surface. Therefore, for a given water mass, i.e. for a given set of IOP, the $L_{\mathrm{u}}\left(0^{-},\lambda,\theta',\phi\right)$ field is strongly

dependent on the downward radiance field $L_{\mathrm{d}}^{\mathrm{t}}\left(0^{-},\lambda,\theta',\phi,\theta_{\mathrm{o}},\tau_{\mathrm{a}},W\right)$, at least for the upper layers[5]. Moreover, for given boundary conditions, expressed by the $L_{\mathrm{d}}^{\mathrm{t}}\left(0^{-},\lambda,\theta',\phi,\theta_{\mathrm{o}},\tau_{\mathrm{a}},W\right)$ vector field, the resulting $L_{\mathrm{u}}\left(0^{-},\lambda,\theta',\phi\right)$ field will depend on the IOP, not only for its magnitude, but also for its geometrical structure. The structure of the $L_{\mathrm{u}}\left(0^{-},\lambda,\theta',\phi\right)$ vector field in the principal plane of the sun ($\phi = 0$ or π) is illustrated schematically in Figure 13.2, where any radial distance from the origin to the upwelling radiance contour indicates the magnitude of radiance in that direction.

The magnitude of the upward flux is intuitively related to the antagonistic processes of backscattering, which allows downwelling photons to travel backward, and of absorption, which annihilates photons and so cancels their chance of being backscattered. The corresponding IOP quantifying these two opposite processes are the backscattering coefficient[6], $b_{\mathrm{b}}(z,\lambda)$, and the absorption coefficient, $a(z,\lambda)$, or if for simplicity, we consider a vertically homogeneous medium, $b_{\mathrm{b}}(\lambda)$ and $a(\lambda)$. Therefore, the irradiance reflectance $R\left(0^{-},\lambda\right)$, as defined in Equation (13.5), must in some way, be related to the ratio of the above coefficients, $\frac{b_{\mathrm{b}}(\lambda)}{a(\lambda)}$, or $\frac{b_{\mathrm{b}}(\lambda)}{a(\lambda)+b_{\mathrm{b}}(\lambda)}$. Note that even though irradiance reflectance is a finite quantity constrained to $R\left(0^{-},\lambda\right)\leq 1$, the first ratio is *a priori* unbounded, whereas the second ratio lies within the interval [0,1] when $b_{\mathrm{b}}(\lambda)$ becomes much larger than $a(\lambda)$. By assuming that $b_{\mathrm{b}}(\lambda)$ is small compared to $a(\lambda)$, the irradiance reflectance can be expressed as

$$R\left(0^{-},\lambda\right) = f(\lambda)\frac{b_{\mathrm{b}}(\lambda)}{a(\lambda)}, \tag{13.12a}$$

and more conveniently, particularly when b_{b} is not small compared to a, through

$$R\left(0^{-},\lambda\right) = f'(\lambda)\frac{b_{\mathrm{b}}(\lambda)}{a(\lambda)+b_{\mathrm{b}}(\lambda)} \tag{13.12b}$$

with a straightforward relationship between the two factors

$$f'(\lambda) = f(\lambda)\left[1+\frac{b_{\mathrm{b}}(\lambda)}{a(\lambda)}\right]. \tag{13.12c}$$

Like $R\left(0^{-},\lambda\right)$, *f'* tends toward unity for extremely high $\frac{b_{\mathrm{b}}(\lambda)}{a(\lambda)}$ values, whereas *f* tends toward 0. These factors, *f* or *f'*, actually rule the magnitude of the irradiance reflectance and relate this global reflectance to the IOP.

---

[5] In the deep asymptotic regime the dependence on the $L_{\mathrm{d}}^{\mathrm{t}}\left(0^{-},\lambda,\theta',\phi,\theta_{\mathrm{o}},\tau_{\mathrm{a}},W\right)$ vector field vanishes, and the $L_{\mathrm{u}}\left(z,\lambda,\theta',\phi\right)$ field progressively takes the character of an IOP.

[6] Recall that any scattering coefficient, $b_{\mathrm{x}}(\lambda)$ is related to the corresponding volume scattering function (a basic IOP), denoted $\beta_{\mathrm{x}}(\lambda,\psi)$, through

$$b_{\mathrm{x}}(\lambda) = 2\pi\int_{0}^{\pi}\beta_{\mathrm{x}}(\lambda,\Psi)\sin\Psi d\Psi,$$

where ψ is the scattering angle. The backscattering coefficient $b_{\mathrm{bx}}(\lambda)$, is obtained when the above integral extends only over the interval $\pi/2$ to π.

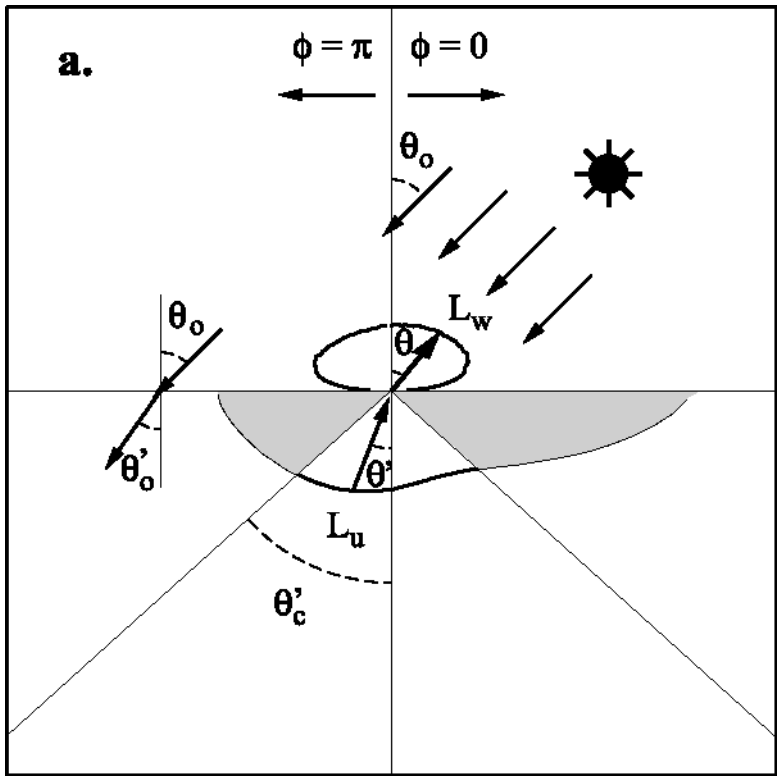

Figure 13.2: Conventional representation of the upward radiance field, $L_u\left(0^-,\lambda,\theta',\phi\right)$ in the vertical plane containing the sun, *i.e.* the *solar principal plane*. The polar diagram represents in-water radiances as vectors, the length of which corresponds to magnitude, ending at the center. The shaded area, limited by the critical angle θ_c', contains those radiances that do not emerge, but are totally and internally reflected. The corresponding water-leaving radiance field $L_W\left(\lambda,\theta,\phi\right)$ is also represented (by definition at z = 0^+).

The influence of the IOP on the geometrical structure of the upward light field, and therefore on the $Q\left(\lambda,\theta',\phi\right)$ factor, is slightly more complex, but can be, at least qualitatively, predicted. The shape of the volume scattering function (VSF) of seawater is obviously involved. The VSF, $\beta\left(\lambda,\Psi\right)$, of any water body is the sum of the VSF due to water molecules, $\beta_w\left(\lambda,\Psi\right)$, and the VSF due to the various particles in suspension, $\beta_p\left(\lambda,\Psi\right)$. The former is symmetrical and not far from being spherical, whereas the latter is strongly elongated in the forward direction, and exhibits a weak minimum around ψ = 140°. Therefore, the shape of the resulting VSF is determined by the relative proportions of the two components, conveniently expressed by the parameter

$$\eta = \frac{b_w\left(\lambda\right)}{b\left(\lambda\right)}, \tag{13.13}$$

namely the ratio of molecular scattering, $b_w\left(\lambda\right)$, to the total scattering coefficient $b\left(\lambda\right) = b_w\left(\lambda\right) + b_p\left(\lambda\right)$, where $b_p\left(\lambda\right)$ represents the scattering coefficient due only to the suspended particles. A ratio similar to η, but involving only the backscattering coefficients, is also useful; it is expressed as

$$\eta_b = \frac{b_{bw}\left(\lambda\right)}{b_b\left(\lambda\right)}, \tag{13.14}$$

where the backscattering coefficient $b_b(\lambda) = b_{bw}(\lambda) + b_{bp}(\lambda)$ is the sum of the backscattering coefficients for molecules and particles, respectively.

The diffuse upward radiant field is built up by photons that have been scattered at least once, and may have experienced several, and even many scattering events before being redirected toward the atmosphere. It is conceivable that if single scattering prevails, the upward radiant field is governed by, and thus is similar in shape to, the backward lobe of the VSF. Conversely, in a multiple scattering regime, the highly diffuse light field tends to become isotropic. The more or less diffuse character of the upward radiant field actually depends on the average number, $\tilde{n}$, of scattering events the photons have undergone before reaching the interface ($z = 0^-$). This number is simply related to the IOP through (Morel and Gentili, 1991)

$$\tilde{n}(\lambda) = \left[1 - \varpi(\lambda)\right]^{-1}, \tag{13.15}$$

where $\varpi(\lambda) \equiv \dfrac{b(\lambda)}{a(\lambda) + b(\lambda)}$ is the ***single scattering albedo***. It is straightforward to show that (13.15) may alternatively be written $\tilde{n}(\lambda) = 1 + \dfrac{b(\lambda)}{a(\lambda)}$, or $\tilde{n}(\lambda) = \dfrac{a(\lambda) + b(\lambda)}{a(\lambda)}$.

Therefore, in a strongly scattering medium ϖ is close to 1, $\tilde{n}$ is extremely high, multiple scattering of high orders is the common rule, and finally the radiance distribution tends to be isotropic. Conversely, in a strongly absorbing medium, ϖ is small, $\tilde{n}$ is not much above 1, single scattering dominates over higher orders, and the radiance pattern tends to mimic that of the VSF (single scattering). In such a case, if molecular scattering dominates (η large, and η_b tending toward 1), the shape of the VSF is more or less symmetrical and the radiance field is accordingly rather round-shaped, but if particle scattering dominates (η small, and η_b tending toward 0), the shape of the VSF is extremely elongated in the forward direction and the radiance field is more structured. Figure 13.3 illustrates hypothetical examples of the upward radiant field and its bidirectional character, for optically pure water (no particles), or for marine particles alone (without water); the average number of scattering events is either 2, or 61, and the sun is at zenith, or 60° away from zenith. The conventions in the polar plots of Figure 13.3 are the same as in Figure 13.2.

Fluorescence and Raman Scattering

In all that has been said before, the only physical processes considered were absorption and scattering. In other words the medium was considered as purely passive. Other phenomena occur, when the medium contains *sources*, which in seawater are mainly fluorescence emission and Raman scattering.

Fluorescence emission creates light at certain wavelengths, typical of the substance responsible for the emission. For instance, Chlorophyll *a* (borne by algal cells) fluoresces around 683 nm with a bandwidth of about 25 nm, whereas the fluorescence emitted by colored dissolved organic matter (CDOM) is more complex and spectrally broader. Fluorescence may be excited by photons at any wavelength shorter than that of the emission, although the excitation efficiency may vary with wavelength (due largely to the absorption spectrum of the material in question). These emissions are obviously dependent on the concentration of the fluorescing substances.

The Raman (inelastic) scattering is characterized by a constant frequency shift between the excitation and emitted light, and the shift is only determined by the molecule structure of the medium (here water). This emission occurs throughout the visible spectrum, at wavelengths larger than those of the exciting light. Because it is a physical property of the water molecule, it is always present, even if its influence is hardly detected in the upper layers, where the elastic scattering process dominates the upward radiant field.

From the viewpoint of the directional properties of the upward field, these emissions, isotropic for fluorescence and quasi-isotropic for Raman scattering, add a component that is angularly constant and thus tends to smooth out the structures generated by elastic scattering (particularly by particle scattering). Note that the coefficients describing these emissions (the reverse of absorption) belong to the category of IOP (see also Chapter 10, Section 10.4).

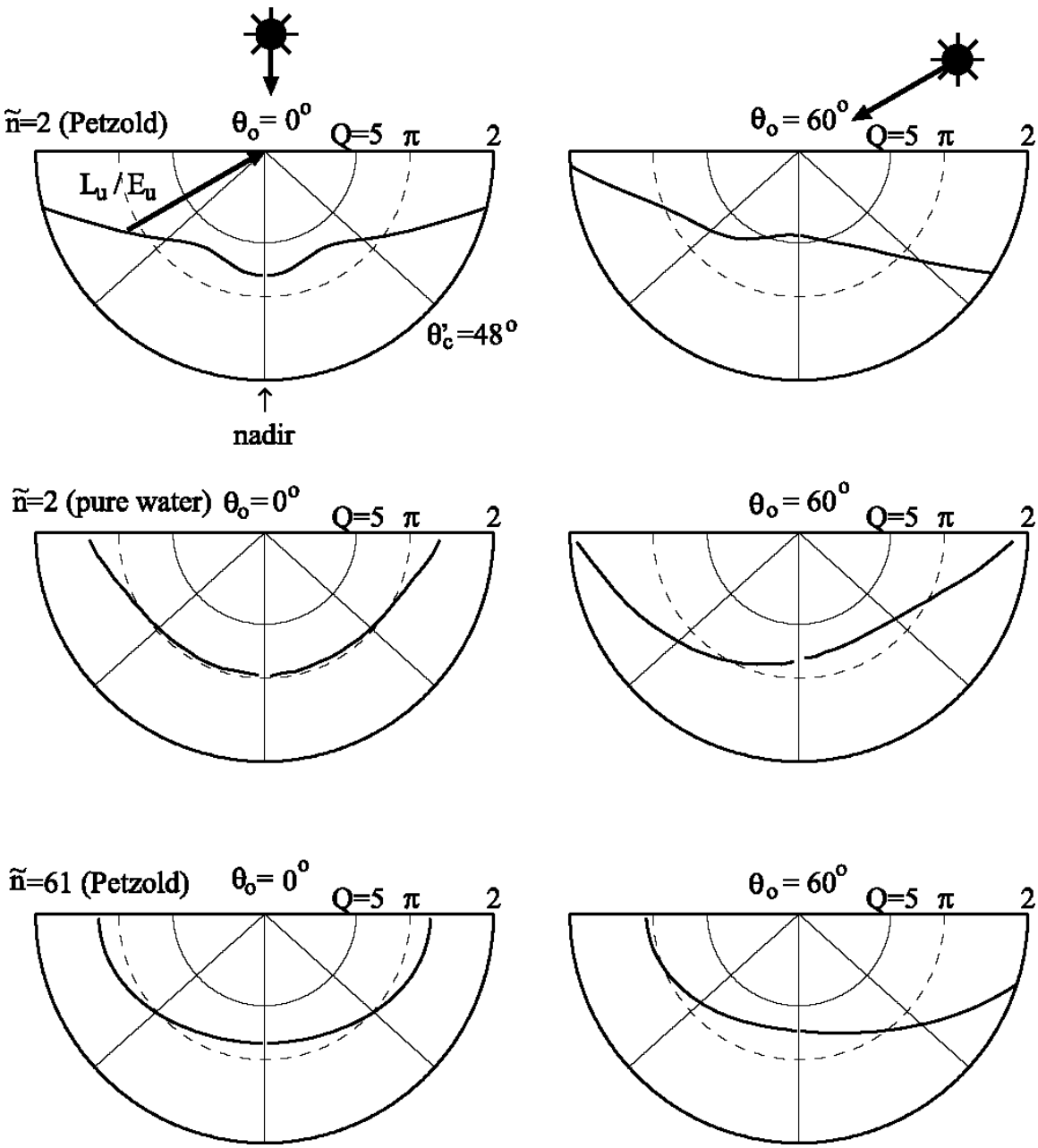

Figure 13.3: The above diagrams make use of the same form of representation and display as in Figure 13.2, but for the ratio $\left[L_u\left(0^-,\lambda,\theta',\phi\right)\div E_u\left(0^-,\lambda\right)\right]$, i.e. of $\left[Q\left(\lambda,\theta',\phi\right)\right]^{-1}$ [Equation (13.6)], not the radiance vector itself. When the sun is at zenith, ϕ is undetermined; when it is at θ_o = 60°, the half-plane containing the sun (ϕ = 0) is on the right side of the diagram. The first row is for a water mass where ñ = 2 (double scattering, on average), and the VSF is that of Petzold (1972). For the second row, ñ is again 2, and the particle VSF is replaced by the VSF for molecules. The third row represents the situation of an extremely turbid water mass, with ñ = 61 [i.e. $b\left(\lambda\right)=60a\left(\lambda\right)$] and the Petzold VSF.

13.4 PRACTICAL CONSIDERATIONS: THE f, Q AND ℜ FACTORS

Basic relationships

Only the processes and radiative properties of the near-surface layer are considered in what follows. In Equation (13.12a), or (13.12b), above, the *f*, or *f'*, factors are dimensionless quantities. It is worth emphasizing that they are not simply *coefficients*, but *functions*. Indeed, they are varying for two reasons. Inasmuch as the upward field is not isotropic, it is understandable that its angular structure will be sensitive to the directionality of the incident illumination. In simplified terms, for a given water body and given $a(\lambda)$ and $b(\lambda)$ values, *f* will be essentially dependent on the solar angle (and to a lesser extent on the sea state, and therefore, on *W*, the wind speed). In turn, for a given solar angle, the response of the medium, and thus the resulting *f* value will depend on the IOP, and on the VSF in particular. In total, *f* {or *f'*} is a function of two independent categories of variables, environmental and IOP, and thus must be expressed as $f\left[\lambda,(\theta_o,\tau_a,W),a(\lambda),\beta(\lambda,\Psi)\right]$ {or $f'\left[\lambda,(\theta_o,\tau_a,W),a(\lambda),\beta(\lambda,\Psi)\right]$}.

In its initial definition [Equation (13.6)], the geometrical quantity $Q(\lambda,\theta',\phi)$ was not related to the physical causes of its variations. These physical processes and variables giving rise to the geometric shape of the upward radiant field, and thus to the *Q* function, were shown in Section 13.3 to be determined by $L_d^t\left(0^-,\lambda,\theta',\phi,\theta_o,\tau_a,W\right)$, the VSF $\beta(\lambda,\Psi)$, and the average number of scattering events $\tilde{n}\left(\frac{b(\lambda)}{a(\lambda)}\right)$. To indicate the dependence of the *Q* function on these environmental variables and IOP, it is properly expressed as $Q\left[(\lambda,\theta',\phi),(\theta_o,\tau_a,W),a(\lambda),\beta(\lambda,\Psi)\right]$.

Radiative transfer computations, or measurements, give access to $f\left[\lambda,(\theta_o,\tau_a,W),a(\lambda),\beta(\lambda,\Psi)\right]$ and $Q\left[(\lambda,\theta',\phi),(\theta_o,\tau_a,W),a(\lambda),\beta(\lambda,\Psi)\right]$ functions, ultimately via their basic definitions, Equations (13.12) and (13.6) respectively. The generic formulations stand for a passive medium, deprived of internal sources[7]. They do not presume the relations that may exist between the IOP and the dissolved or particulate substances present in the water. In other words, the dependencies that they express are equally valid for Case 1 and Case 2 waters. For simplicity of presentation, the remainder of this chapter will consider only vertically homogeneous, Case 1 waters, in which a simplified representation of the *f* and *Q* functions is possible. Nevertheless, one need only revert to the above representations of *f* and *Q* functions, and add dependence on depth to the IOP, to restore full generality to the equations that follow

When dealing exclusively with Case 1 waters, the above formulations can be simplified. To the extent that in such waters, and at a given wavelength, it is (by definition) assumed that the IOP are universally related to the chlorophyll concentration (*Chl*) (Morel and Prieur 1977; Smith and Baker 1978), the functional dependencies in the previous expressions can be written as $f\left[\lambda,(\theta_o,\tau_a,W),Chl\right]$ $\left\{\text{or } f'\left[\lambda,(\theta_o,\tau_a,W),Chl\right]\right\}$ and $Q\left[(\lambda,\theta',\phi),(\theta_o,\tau_a,W),Chl\right]$. It must be underlined that the simplified expression, as well as any predictive computations, are possible if, not only $a(\lambda)$ and $b_p(\lambda)$ have been related to *Chl*, but also $\beta(\lambda,\Psi)$. This means that the VSF for particles $\beta_p(\lambda,\Psi)$ must be known. The most common approach is to make $b_p(\lambda)$ varying with *Chl*, and to keep constant the shape of the VSF, *e.g.* by assuming that the scattering phase function of particles, $\tilde{\beta}_p(\lambda,\Psi)\equiv\frac{\beta_p(\lambda,\Psi)}{b_p(\lambda)}$, is constant in shape. Other assumptions about this phase function are also possible (see below).

[7] Here, the sources are Raman or fluorescence emissions. The *f* and *Q* functions may, of course, be corrected to account for these sources in radiative transfer computations.

Expressing slant water-leaving radiances

All needed quantities are now set up, and their expressions include all the dependencies with respect to geometry (viewing and solar angles), as well as with respect to the IOP (actually via λ and *Chl*). It is, therefore, possible to express any slant water-leaving radiance as a function of all variables. The steps are as follows (in a simplified writing):

- $L_{\mathrm{W}}(\lambda,\theta,\phi)$ is derived from $L_{\mathrm{u}}(0^-,\lambda,\theta',\phi)$ via Equation (13.10).
- $L_{\mathrm{u}}(0^-,\lambda,\theta',\phi)$ is related to $E_{\mathrm{u}}(0^-,\lambda)$ and $Q\left[(\lambda,\theta',\phi),(\theta_{\mathrm{o}},\tau_{\mathrm{a}},W),Chl\right]$ by Equation (13.6).
- $E_{\mathrm{u}}(0^-,\lambda)$ is related to $E_{\mathrm{d}}(0^-,\lambda)$ and $R(0^-,\lambda)$ by Equation (13.5).
- $E_{\mathrm{d}}(0^-,\lambda)$ is expressed as a function of $E_{\mathrm{d}}(0^+,\lambda)$ via Equation (13.11).
- $R(0^-,\lambda)$ is related to the IOP and $f\left[\lambda,(\theta_{\mathrm{o}},\tau_a,W),Chl\right]$ by Equation (13.12a) {or $f'\left[\lambda,(\theta_{\mathrm{o}},\tau_a,W),Chl\right]$ and Equation (13.12b}.

These steps lead to the final result

$$L_{\mathrm{W}}(\lambda,\theta,\phi,\theta_{\mathrm{o}},\tau_{\mathrm{a}},Chl)=E_{\mathrm{d}}(0^+,\lambda,\theta_{\mathrm{o}},\tau_{\mathrm{a}})\Re(\theta',W)\frac{f(\lambda,\theta_{\mathrm{o}},\tau_{\mathrm{a}},Chl)}{Q(\lambda,\theta',\phi,\theta_{\mathrm{o}},\tau_{\mathrm{a}},Chl)}\frac{b_{\mathrm{b}}(\lambda,Chl)}{a(\lambda,Chl)}, \qquad (13.16)$$

where the factor $\Re(\theta',W)$ merges all the effects of reflection and refraction, entering from Equations (13.10) and (13.11), and is written

$$\Re(\theta',W)=\left[\frac{1-\bar{\rho}(\theta_{\mathrm{o}})}{1-\bar{r}R(0^-,\lambda,\theta_{\mathrm{o}},Chl)}\frac{1-\rho(\theta',\theta;W)}{n^2}\right]. \qquad (13.17)$$

Note that in principle $\Re(\theta',W)$ depends on *Chl* and λ through $R(0^-,\lambda,\theta_{\mathrm{o}},Chl)$, but not significantly, because the product $\bar{r}R(0^-,\lambda,\theta_{\mathrm{o}},Chl)$ is small ($R(0^-,\lambda,\theta_{\mathrm{o}},Chl)\le 0.1$ and $\bar{r}\cong 0.48$). Because of its direct dependence on the Fresnel reflectance $\rho(\theta',\theta;W)$, however, when $\theta\ge 30°$ $\Re(\theta',W)$ varies strongly with θ and wind speed *W*, which parameterizes sea state, (Figure 13.4). In contrast, for $\theta\lesssim 25°$, $\Re(\theta',W)$ is practically insensitive to wind speed and may be assumed to be a constant $\Re_{\mathrm{o}}=0.529$. Finally, the wind speed *W* dependence of the ratio $\frac{f(\lambda,\theta_{\mathrm{o}},\tau_{\mathrm{a}},W,Chl)}{Q(\lambda,\theta',\phi,\theta_{\mathrm{o}},\tau_{\mathrm{a}},W,Chl)}$ is very weak (Morel and Gentili 1996), and therefore, it is not explicitly indicated in Equation (13.16), or below in Equations (13.19) through (13.22).

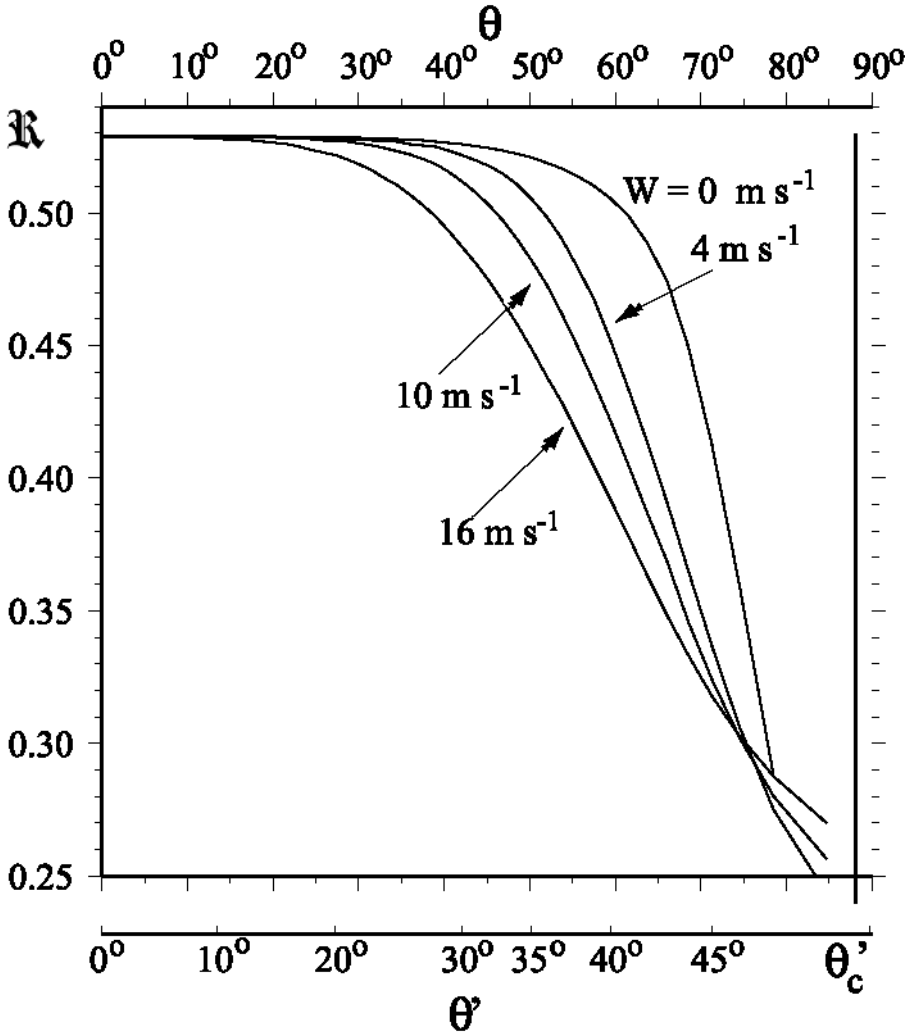

Figure 13.4: Evolution of the reflection-refraction term $\Re(\theta', W)$ [Equation (13.17)] as a function of θ and θ', for various wind speeds (W), and assuming a surface free of whitecaps. These results have been obtained through Monte-Carlo simulations, which combine the Gaussian distribution of capillary wave slopes (Cox and Munk 1954) and Fresnel's formula for reflectance at the sea surface.

13.5 IMPLICATIONS OF BIDIRECTIONALITY IN REMOTE SENSING

Two implications of bidirectionality for ocean color remote sensing are successively examined below. The first one is specifically related to ocean color radiance measurements made from a ***satellite-borne radiometer***. The second aspect is related to ***field*** measurements of radiances made at the sea level, usually in support of algorithm development, validation, and calibration of sensors aboard satellites in earth orbit.

The bidirectionality impacts the two quantities used in ocean color science, remote sensing reflectance $R_{RS}(\lambda, \theta, \phi)$ and normalized water-leaving radiance $L_{WN}(\lambda, \theta, \phi)$ as defined in Equations (13.7) and (13.8), respectively. To the extent that the emerging radiance field structure involves both the viewing geometry

and the illumination geometry, neither of these quantities, which are both based on $L_W(\lambda,\theta,\phi,\theta_o,\tau_a,W,Chl)$, is fully normalized [cf. Equation (13.16)].

Satellite remotely sensed radiances

A remote sensor aims at the ocean under various angles, θ_v related to θ and θ' as illustrated in Figure 13.1, and generally captures slant radiances originating from the ocean (except for the sub-satellite pixel, where $\theta_v = \theta = \theta' = 0$). In general, the vertical plane containing the sun at zenith angle θ_o is separated by an azimuth angle φ from the vertical plane containing the sensor. The spectral water-leaving radiance that is determined by removing the atmospheric effects from the radiance measured by the satellite sensor may be written $L_W^S[\lambda,(\theta,\phi)\in\Omega_{FOV},\theta_o,\tau_a,W,Chl]$, where the superscript S stands for "Satellite" and Ω_{FOV} represents the solid angle of the sensor centered on the direction (θ,φ). For a given instrument Ω_{FOV} is constant, and this argument will no longer be repeated. It is also assumed that the above marine signal has been properly extracted from the total signal recorded by the satellite borne sensor, which implies that the atmospheric correction has been "perfectly" effected. Therefore the corrected water-leaving radiance measured by the sensor, is represented by Equation (13.16), and if it is divided by $E_d(0^+,\lambda)$, it provides the remote sensing reflectance $R_{RS}^S(\lambda,\theta,\phi)$ as defined by Equation (13.7). When $R_{RS}^S(\lambda,\theta,\phi)$ is multiplied by $\bar{F}_o(\lambda)$, it provides the normalized water-leaving radiance $L_{WN}^S(\lambda,\theta,\phi)$ conforming to the Gordon and Clark (1981) definition of Equation (13.8), which may also be expressed in the form

$$L_{WN}^S(\lambda,\theta,\phi)=\frac{L_W^S[\lambda,\theta,\phi,\theta_o,\tau_a,W,Chl]}{t(\lambda,\theta_o)\cos\theta_o\left(\frac{d_o}{d}\right)^2}, \tag{13.18}$$

since $E_d(0^+,\lambda)$ can be calculated as $E_d(0^+,\lambda)=\bar{F}_o(\lambda)t(\lambda,\theta_o)\cos\theta_o\left(\frac{d_o}{d}\right)^2$, where d_0 and d are the mean and actual sun-earth distances, respectively, and $t(\lambda,\theta_o)$ is the diffuse transmittance of the atmosphere when the solar zenith angle is θ_o. Although not shown explicitly, $t(\lambda,\theta_o)$ also depends on the optical depths of aerosols and ozone, and on variations in the Rayleigh optical depth with surface atmospheric pressure.

Although the full dependence of $L_{WN}^S(\lambda,\theta,\phi)$ on geometric, environmental and IOP factors is not indicated explicitly in its traditional notation, the quantity retains a strong bidirectional nature that can be clearly seen by substituting Equation (13.16) for the numerator on the right-hand-side of Equation (13.18). Because of these remaining dependencies, satellite normalized water-leaving radiances $L_{WN}^S(\lambda,\theta,\phi)$ are not directly comparable, from one pixel of the scene to another one, from one day to another day for the same pixel, or from one ocean color sensor to another one. The mapping, or merging of such quantities, when for instance *level 3* products are derived, is neither meaningful nor licit. A way to circumvent these drawbacks consists of assuming that the sun was at zenith and that the pixel has been seen vertically, and thus to determine an ***exact normalized water-leaving radiance*** $L_{WN}^{ex}(\lambda)$ that is no longer dependent on bidirectional factors. To transform $L_{WN}^S(\lambda,\theta,\phi)$ to $L_{WN}^{ex}(\lambda)$, Equation (13.8) is used to first express the ratio

$$\frac{L_{WN}^{ex}(\lambda)}{L_{WN}^S(\lambda,\theta,\phi)}=\frac{E_d(0^+,\lambda,\theta_o)L_W[\lambda,0,0,0,\tau_a,W,Chl]}{E_d(0^+,\lambda,0)L_W^S[\lambda,\theta,\phi,\theta_o,\tau_a,W,Chl]}, \tag{13.19}$$

where $E_d(0^+,\lambda,0)$ and $L_W[\lambda,0,0,0,\tau_a,W,Chl]$ are respectively the unknown incident irradiance and water-leaving radiance that would have been measured for $\theta=\theta'=\theta_o=0$ and φ, although indeterminate,

is denoted also as $\phi = 0$. When Equation (13.16) is used to expand $L_W\left[\lambda, 0, 0, 0, \tau_a, W, Chl\right]$ and $L_W\left[\lambda, \theta, \phi, \theta_o, \tau_a, W, Chl\right]$ in (13.19), the solution obtains as

$$L_{WN}^{ex}(\lambda) = L_{WN}^{S}(\lambda, \theta, \phi)\frac{\Re_o}{\Re(\theta', W)}\frac{f_o(\lambda, \tau_a, Chl)}{Q_o(\lambda, \tau_a, Chl)}\left(\frac{f(\lambda, \theta_o, \tau_a, Chl)}{Q(\lambda, \theta', \phi, \theta_o, \tau_a, Chl)}\right)^{-1}, \tag{13.20}$$

where $f_o(\lambda, \tau_a, Chl)$ is the particular value taken by the function f when $\theta_O = 0$, and $Q_o(\lambda, \tau_a, Chl)$ is the particular value of the function Q when $\theta_O = 0$ and $\theta = \theta' = 0$. As in Equation (13.16), the wind speed dependence is retained only in $\Re(\theta', W)$ (Figure 13.4), as it is neglibly weak for the $\frac{f}{Q}$ ratios (see Fig. 9 in Morel and Gentili 1996).

Field measurements

The water-leaving radiances are determined either from above-water measurements (typically at $\theta \approx 40°$, $\theta' \approx 29°$ and $\phi \geq 90°$; see Chapter 12), or from in-water measurements extrapolated to z = 0^- and transmitted through the interface ($\theta = \theta' = 0$; see Chapters 10 and 11). Since usually, $E_d(0^+, \lambda, \theta_o)$ is also determined during such measurements, the transformations into remote sensing reflectance and normalized water-leaving radiance are straightforward. The bidirectionality problems are identical to the previous one. These field water-leaving radiances, after the normalization leading to $L_{WN}^{abw}(\lambda, \theta, \phi)$ for above-water measurements, or $L_{WN}^{inw}(\lambda)$ for in-water measurements, are still not comparable with each other, nor with the corresponding satellite quantity $L_{WN}^{S}(\lambda, \theta, \phi)$. They also must be transformed into $L_{WN}^{ex}(\lambda)$ to allow comparisons to be made.

When the measurements are effected via the ***above-water method***, the geometry is exactly the same as that for a satellite sensor, so that the transformation of $L_{WN}^{abw}(\lambda, \theta, \phi)$ into $L_{WN}^{ex}(\lambda)$ is performed using Equation (13.20), with fixed (θ', ϕ) values determined by the measurement protocol (Chapter 12).

When the measurements are effected via the ***in-water method***, the sole difference comes from the nadir viewing strategy $(\theta = \theta' = 0)$, which simplifies the transformation from $L_{WN}^{inw}(\lambda)$ to $L_{WN}^{ex}(\lambda)$. In this situation, $\Re(\theta', W)$ reduces to $\Re_o$, and $Q(\lambda, \theta', \phi, \theta_o, \tau_a, Chl)$ reduces to the restricted form $Q_n(\lambda, \theta_o, \tau_a, Chl)$ relevant for nadir viewing. With these substitutions, Equation (13.20) reduces to

$$L_{WN}^{ex}(\lambda) = L_{WN}^{inw}(\lambda)\frac{f_o(\lambda, \tau_a, Chl)}{Q_o(\lambda, \tau_a, Chl)}\left(\frac{f(\lambda, \theta_o, \tau_a, Chl)}{Q_n(\lambda, \theta_o, \tau_a, Chl)}\right)^{-1}. \tag{13.21}$$

The different angular dependencies in normalized water-leaving radiances derived from above-water, or in-water, measurements, may be emphasized by dividing (13.20) by (13.21) to obtain

$$L_{WN}^{inw}(\lambda) = L_{WN}^{abw}(\lambda, \theta, \phi)\frac{\Re_o}{\Re(\theta', W)}\frac{Q(\lambda, \theta', \phi, \theta_o, \tau_a, Chl)}{Q_n(\lambda, \theta_o, \tau_a, Chl)}. \tag{13.22}$$

These radiances derived from field experiments must be transformed into exact normalized water-leaving radiances if they are to be compared to those derived from space measurements [already transformed according to Equation (13.20)].

Other useful relationships

The irradiance reflectance, Equation (13.5), has been extensively determined at sea, and also has been modeled. As only irradiances are involved in its definition, its only angular dependencies are related to the illumination geometry, via the factor $f\left(\lambda,\theta_o,\tau_a,Chl\right)$ in equation (13.12a). The irradiance reflectance and the exact normalized water-leaving radiance are related through Equations (13.12a) and (13.16) as

$$L_{WN}^{ex}\left(\lambda\right)=\frac{R\left(0^-,\lambda,\theta_o\right)\bar{F}_o\left(\lambda\right)\Re_o}{Q_n\left(\lambda,\theta_o,\tau_a,Chl\right)}. \tag{13.23}$$

13.6 GENERATION AND BEHAVIOR OF THE ℜ, f, AND Q QUANTITIES

The reflection-refraction term $\Re$

In correspondence with n = 1.34, a typical value for seawater (salinity of 35 PSU, temperature 15°C, and λ = 550 nm), the n^{-2} term amounts to 0.557. Actually, at a given temperature T, $n\left(\lambda,T\right)$ decreases by about 1 % throughout the visible spectrum, and at a given wavelength, decreases by 0.1 % for a temperature varying from 0 to 30°C. Therefore, extreme values for the n^{-2} term would range from 0.547 (at 400 nm, and at 0°C) to 0.561 (at 700 nm, and 30°C) (Austin and Halikas 1976). It can safely be considered as constant, for practical applications.

The transmittance factor $\left(1-\bar{\rho}\right)$ which applies to the downward irradiance (sun + sky) is approximately 0.957. It decreases to 0.925 for low solar elevation and increasing atmospheric turbidity; while it increases and may reach 0.97 for extremely clear blue skies, small solar zenith angle, and red wavelengths. The internal reflectance $\left[1-\bar{r}R\left(0^-,\lambda,\theta_o\right)\right]$, where $\bar{r}\cong 0.49$, may vary between 1 and 0.951 for an irradiance reflectance $0<R\left(0^-,\lambda,\theta_o\right)\leq 0.1$. In total, these variations are rather weak.

The most important term governing the variations in $\Re\left(\theta',W\right)$ is the downward reflection $\rho\left(\theta',\theta;W\right)$, which prevents part of the upward radiance from emerging. The resulting transmittance is nearly constant and essentially independent from the sea state with a value $\left[1-\rho\left(\theta',\theta;W\right)\right]\cong 0.979$ for $\theta<25°$. At the other extreme, as θ' approaches the critical angle, the upward transmittance decreases abruptly toward 0, and the slope of this decrease for slant emerging radiances depends heavily on the capillary wave slopes, as governed by wind speed W (Figure 13.4). This rapid decrease in the $\Re\left(\theta',W\right)$ values for $\theta>30°$ (or $\theta'>22°$) is, at least in part, at the origin of difficulties in assessing marine radiance at the edge of the swath for a satellite ocean color sensor. Note also that most applications [Equations (13.20) and (13.21)] actually involve the ratio $\frac{\Re_o}{\Re\left(\theta',W\right)}$ for two specified directions (0 and θ'). Therefore, the variations of such ratios are more sensitive to the changes in the transmittance term (and to the θ' angle and wind speed), rather than to the selection of constant and approximate values for $\bar{r}$ and $\bar{\rho}$, variations in which tend to cancel out.

Prediction of the f and Q factors

These quantities have been scarcely determined at sea. Therefore, their prediction presently relies essentially on computations, by which the radiative transfer equation (RTE) is accurately solved for various IOP and prescribed boundary conditions corresponding to the incident radiative regime to be simulated. Such computations must address simultaneously the two media, atmosphere and ocean, inasmuch as the boundary conditions depend i) on the sun position, the optical thickness and nature of aerosols, and ii) on the sea state, derived from the wind speed through the Cox and Munk (1954) surface slopes statistics. They also can include the inelastic processes. As far as the numerical aspects are concerned, there is no

difference between Case 1 and Case 2 waters. The major difference, however, originates from the unequal abilities in modeling the needed IOP for the two kinds of waters.

For Case 2 waters, the optically significant substances (phytoplankton, colored dissolved organic matter, and all kinds of non-algal particles) are varying in wide proportions, and independently from each other. The non-algal component may contain various organic and mineral particles, likely with differing VSF. Therefore computations have to be made case-by-case, with the relevant IOP as input parameters, to the extent they are known. In the particular case of extremely turbid waters, with high reflectance and a well-established multiple scattering regime, Q tends to approach π, albeit very slowly, whatever the VSF (Loisel and Morel 2001).

In Case 1 waters, beside the water molecules themselves, the optically significant components are phytoplankton and their associated materials living or inanimate, particulate or dissolved, collectively called the *biogenic material*. The quantification of this biogenic material has been operationally made through the concentration [mg m^{-3}] of a major pigment, chlorophyll *a* (*Chl*). By definition therefore, the IOP of these waters depend on, and have historically been related to, *Chl* concentration. In this way, the IOP of Case 1 waters can, in principle, be universally expressed for all wavelengths as functions of *Chl*. This obviously is a useful empirical approximation, but only an approximation.

In a first series of papers (Morel and Gentili 1991,1993,1996), empirical relationships were introduced, by which $a(\lambda)$ and $b(\lambda)$ were expressed as functions of *Chl*. The additional hypothesis was to consider that the particle phase function for the biogenic material was well represented by the Petzold (1972) mean phase function, as used in Mobley *et al.* (1993) and tabulated in Mobley (1994). It was emphatically acknowledged that the adoption of a unique phase function for oceanic particulates is undoubtedly a weakness, especially because the backscattering probability, $\tilde{b}_{\mathrm{bp}}(\lambda) \equiv \frac{b_{\mathrm{bp}}(\lambda)}{b_{\mathrm{b}}(\lambda)}$, resulting from the Petzold mean phase function is too high ($\tilde{b}_{\mathrm{bp}}(\lambda) \cong 0.019$). This assumption is, moreover, incompatible with the empirical parameterization of $\tilde{b}_{\mathrm{bp}}(\lambda)$ as a function of *Chl* (Morel and Maritorena, 2001). This drawback prevented the Q values from being reliable at $Chl > 1$ mg m^{-3}.

In an attempt to remove this drawback, a *Chl*-dependent particle phase function has been adopted (Morel and Gentili, in prep.), in such a way that $\tilde{b}_{\mathrm{bp}}(\lambda)$ is allowed to decrease with increasing *Chl*, and thus it becomes fully compatible with the empirical relationship. The parameterizations of $a(\lambda)$ and $b(\lambda)$ with respect to *Chl* have also been slightly adjusted according to new results presented in Loisel and Morel (1998) and Morel and Maritorena (2001). With respect to the previously published results, as displayed and discussed in Morel and Gentili (1996), the above changes have a minor impact on the results for f and Q when the chlorophyll concentration is low enough ($Chl < 1$ mg m^{-3}). Above this threshold, the newly adopted (and *Chl*-dependent) phase function, which is less steep in backward directions than the Petzold (1972) mean phase function, leads to smoother Q-patterns. At very low concentration ($Chl < 1$ mg m^{-3}), important changes in f result if Raman emission is included in its determination. The data shown below as examples in Figures 13.5 through 13.10 have been derived using this new parameterization.

Variations of the f-factor

Early studies have shown that $f \approx \frac{1}{3}$ when the sun is near zenith. Later it was realized (Kirk 1984; Gordon 1989) that it varies appreciably with solar altitude, and also that this sun position dependence is influenced by the relative importance of the molecular and particle scattering in the total scattering process (Morel and Gentili 1991). The global range of variation in the f function is from about 0.30 to 0.60 (and f may take even greater values for high *Chl* at $\lambda = 560$ nm). As a general rule, for any given *Chl* concentration and wavelength, f takes its minimal values f_{o} when the sun is at zenith, and increases systematically with increasing solar zenith angle (Figures 13.5a, 13.5b, and 13.6).

The magnitude of the *f* function and its variations are determined by the IOP. The dimensionless parameters η_b and ϖ derived from the IOP give convenient clues to gain some understanding of the physical processes underlying this dependence. When ϖ is below approximately 0.8, the *f* is essentially governed by η_b; it is progressively less sensitive to the sun position when η_b increases, because molecular scattering predominates (the nearly isotropic shape of the molecular VSF explains this diminishing sensitivity to the sun's position). When ϖ exceeds 0.9, both parameters (η_b and ϖ) play a part in fixing *f* (Morel and Gentili, 1991). When ϖ approaches 1 (high $\tilde{n}$ values), a highly diffuse regime prevails and *f*' tends monotonically toward 1. In contrast, *f* tends toward 0 and it is not a monotonic function of $\tilde{n}$, the average number of scattering events (Loisel and Morel, 2001). Such a quasi-isotropic regime becomes insensitive to the solar illumination geometry, and consequently the *f* variations with θ_o tend to lessen. This may happen in very turbid case 2 waters, but never happens in case 1 waters, as shown in Fig. 13.5.

The behavior of the function *f* for various *Chl* and wavelengths can be interpreted by keeping in mind the corresponding values taken by η_b and ϖ. In Case 1 waters, $\varpi(\lambda) < 0.9$ for all wavelengths as long as $Chl < 3$ mg m^{-3}; $\varpi(\lambda)$ may slightly exceed 0.9 in the green part of the spectrum (555 nm to 565 nm) only when $Chl > 3$ mg m^{-3}. Referring to the examples displayed in Figure 13.5, when $Chl = 0.03$ mg m^{-3} and $\lambda = 412.5$ nm, $\varpi(412.5)$ is slightly below 0.8, $\eta_b(412.5) = 0.85$ is maximum, and $f(412.5)$ remains rather flat (indicating molecular scattering). With increasing *Chl*, $\eta_b(412.5)$ decreases strongly (down to 0.1 when $Chl = 10$ mg m^{-3}), while $\varpi(412.5)$ remains practically unchanged, the $f(412.5)$ values are larger and more dependent on the sun position. At 560 nm, and for increasing *Chl*, the situation is more complex, since $\eta_b(560)$ decreases (as for 412.5), but $\varpi(560)$ is no longer steady and now varies from 0.3 to 0.9. Therefore, $f(560)$ becomes more widely changing and exhibits higher values than at 412.5 nm. The preceding examples are derived under the hypothesis of elastic scattering only.

Because the Raman emission adds a flux to the elastically backscattered flux, this process directly increases *f* for all wavelengths, regardless of the sun position. This effect is maximal when the elastic scattering is minimal, namely for waters with low *Chl* and low particle content. Consider the situation when $Chl = 0.03$ mg m^{-3} (Figure 13.6). In the red, where elastic scattering due to water and particles (at low concentration) is weak, $f(660)$ increases by 15 %. On the other hand, in the blue portion of the spectrum, where the $\lambda^{-4.3}$ dependent elastic scattering by water is strong, $f(442.5)$ increases by only 5 %. The Raman emission has no significant effect on the *f* function when the elastic scattering, becomes important as it is the case at high chlorophyll concentration (*e.g.*, $Chl > 1$ mg m^{-3}).

In summary (see Figures 13.5 and 13.6):

- Whatever the wavelength, $f(\lambda, \theta_o, \tau_a, Chl)$ is minimal when $\theta_o = 0$, and always increases with increasing θ_o.
- For a given θ_o and fixed wavelength, $f(\lambda, \theta_o, \tau_a, Chl)$ always increases with increasing *Chl*.
- The sun-dependent variations in $f(\lambda, \theta_o, \tau_a, Chl)$ are increasingly wider for increasing *Chl*.
- The Raman effect systematically increases $f(\lambda, \theta_o, \tau_a, Chl)$, relative to corresponding values when this effect is ignored.
- At low *Chl*, the Raman effect impacts significantly $f(\lambda, \theta_o, \tau_a, Chl)$, but the effect practically vanishes for $Chl > 1$ mg m^{-3}.

Variations of the bidirectional function $Q(\lambda, \theta', \phi, \theta_o, \tau_a, Chl)$

By virtue of its definition [Equation (13.6)], the magnitude of $Q(\lambda,\theta',\phi,\theta_o,\tau_a,Chl)$ in any direction (θ',ϕ) is inversely proportional to that of $L_u(0^-,\lambda,\theta',\phi,\theta_o,\tau_a,Chl)$, the angular distribution of which is illustrated in Figures 13.2 and 13.3. The solar principal plane $(\phi = 0 \text{ and } \pi)$ is a plane of symmetry for the upward light field; the maximum and minimum values of $Q(\lambda,\theta',\phi,\theta_o,\tau_a,Chl)$ are found in this plane, and are respectively coincident with the minimum and maximum values of $L_u(0^-,\lambda,\theta',\phi,\theta_o,\tau_a,Chl)$ (Figure 13.3). The minimal values of $Q(\lambda,\theta',\phi,\theta_o,\tau_a,Chl)$ occur for almost horizontal directions $\left(\theta' \text{ approaching } \frac{\pi}{2}\right)$ that are not involved in remote sensing. The maximal values of $Q(\lambda,\theta',\phi,\theta_o,\tau_a,Chl)$ occur in directions $(\theta',\phi = 0 \text{ or } \pi)$ that depend on the sun zenith angle θ_o and on the IOP, expressed here as functions of *Chl* (Figure 13.3).

The effect of increasing aerosol loading, indexed by τ_a is to increase the diffuse component of the downward radiant illumination field. This effect tends to smooth the $Q(\lambda,\theta',\phi,\theta_o,\tau_a,Chl)$ distribution, but only slightly, and the influence of τ_a may be neglected for the present discussion. Nevertheless, there still remain 5 variables that strongly influence $Q(\lambda,\theta',\phi,\theta_o,Chl)$. The description of such 5-dimensional lookup table is rather difficult, and is necessarily simplified.

Considered first is the case when both the viewing and solar zenith angles are held fixed at $\theta' = 0$ and $\theta_o = 0$, respectively, i.e. the quantity $Q_o(\lambda,Chl)$ [τ_a neglected] introduced above in Equation (13.20). Assuming only elastic scattering, simulated variations of $Q_o(\lambda,Chl)$ with wavelength $(410 \le \lambda \le 660 \text{ nm})$ and chlorophyll concentration $(0.03 \le Chl \le 10 \text{ mg m}^{-3})$ are illustrated as solid lines in Figure 13.7a; $Q_o(\lambda,Chl)$ increases monotonically with increasing *Chl*, and is only weakly dependent on wavelength λ.

The second step consists of examining the evolution with the sun angle θ_o of the quantity $Q_n(\lambda,\theta_o,Chl)$, introduced in Equation (13.21) for nadir viewing cases $(\theta' = 0)$ when generally $\theta_o \ne 0$. Again considering only elastic scattering, the solid curves in Figure 13.7b show the variability in $Q_n(\lambda,\theta_o,Chl)$ with variations in θ_o $(0° \le \theta_o \le 75°)$ for 4 chlorophyll concentrations and 4 wavelengths. Variations of $Q_n(\lambda,\theta_o,Chl)$ with chlorophyll $(0.03 \le Chl \le 10 \text{ mg m}^{-3})$, with Raman emission included (see below), are shown in Figure 13.8 for 6 wavelengths and 4 solar zenith angles θ_o. The $Q_n(\lambda,\theta_o,Chl)$ function exhibits the following properties (Figures 13.7b and 13.8):

- It is always minimal when $\theta_o = 0$, and steadily increases when θ_o increases, for all wavelengths and all chlorophyll concentrations.
- The span of its variation with θ_o is relatively wider at high *Chl* than at low *Chl*.
- Its highest values are found in the red part of the spectrum when $\theta_o = 75°$ and $Chl \ge 3 \text{ mg m}^{-3}$, *e.g.* $Q_n(660 \text{ nm}, 75°, 3 \text{ mg m}^{-3}) > 6$ in Figure 13.7b.

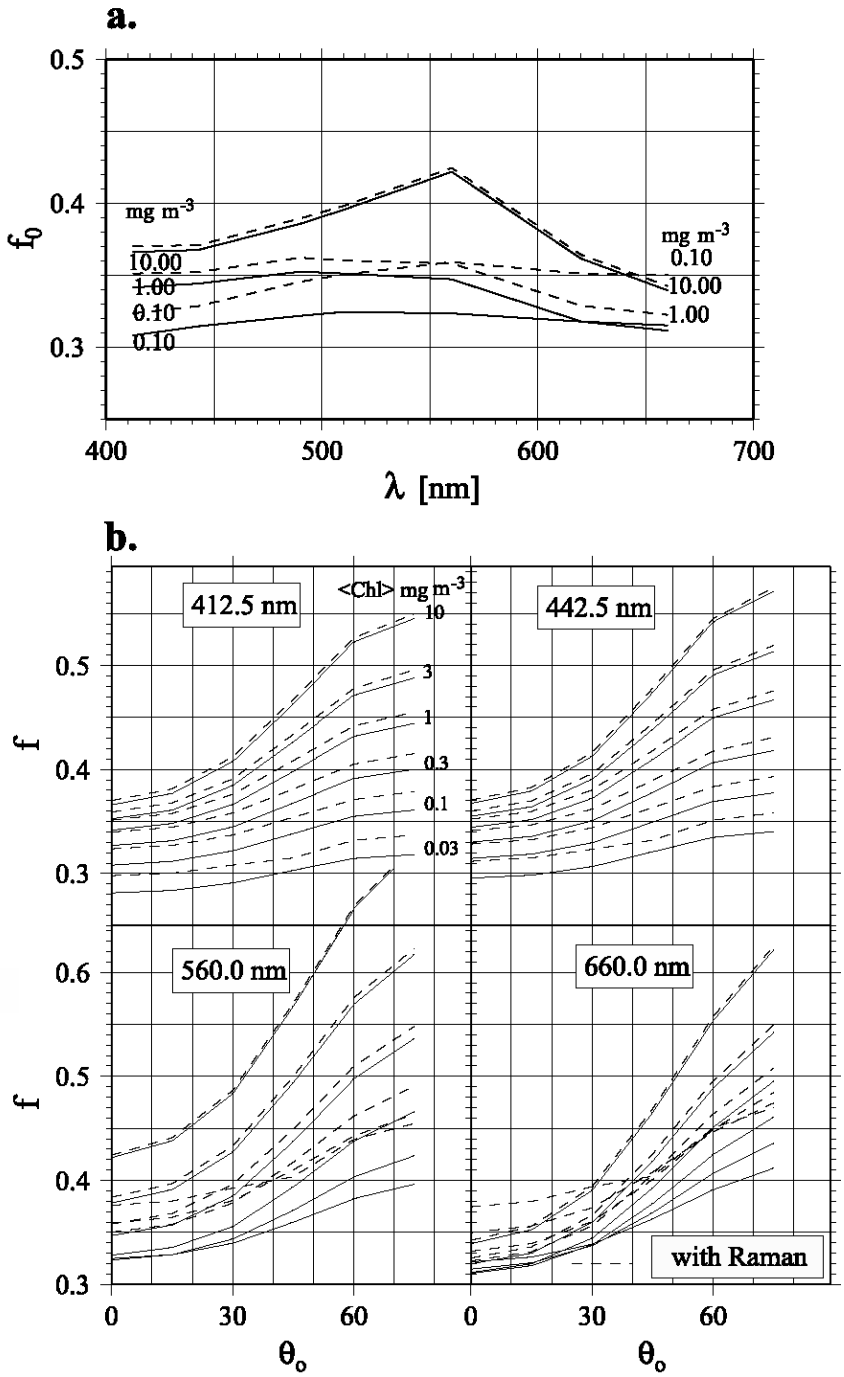

Figure 13.5: a): Spectral distribution of f_0, the particular value of the function f when the sun-zenith angle is 0, for different Chl values, as indicated. The solid curves are for elastic scattering only, and the dashed curves include the effect of the Raman emission. b): Evolution of the function f (Equation 13.12a) with the zenith solar angle (up to 75°), for various wavelengths as indicated. From bottom to top in each panel, the curves are for Case 1 waters with Chl = 0.03, 0.1, 0.3, 1, 3, and 10 mg m^{-3}, respectively. Solid and dashed curves respectively correspond to determinations without, or with, Raman scattering.

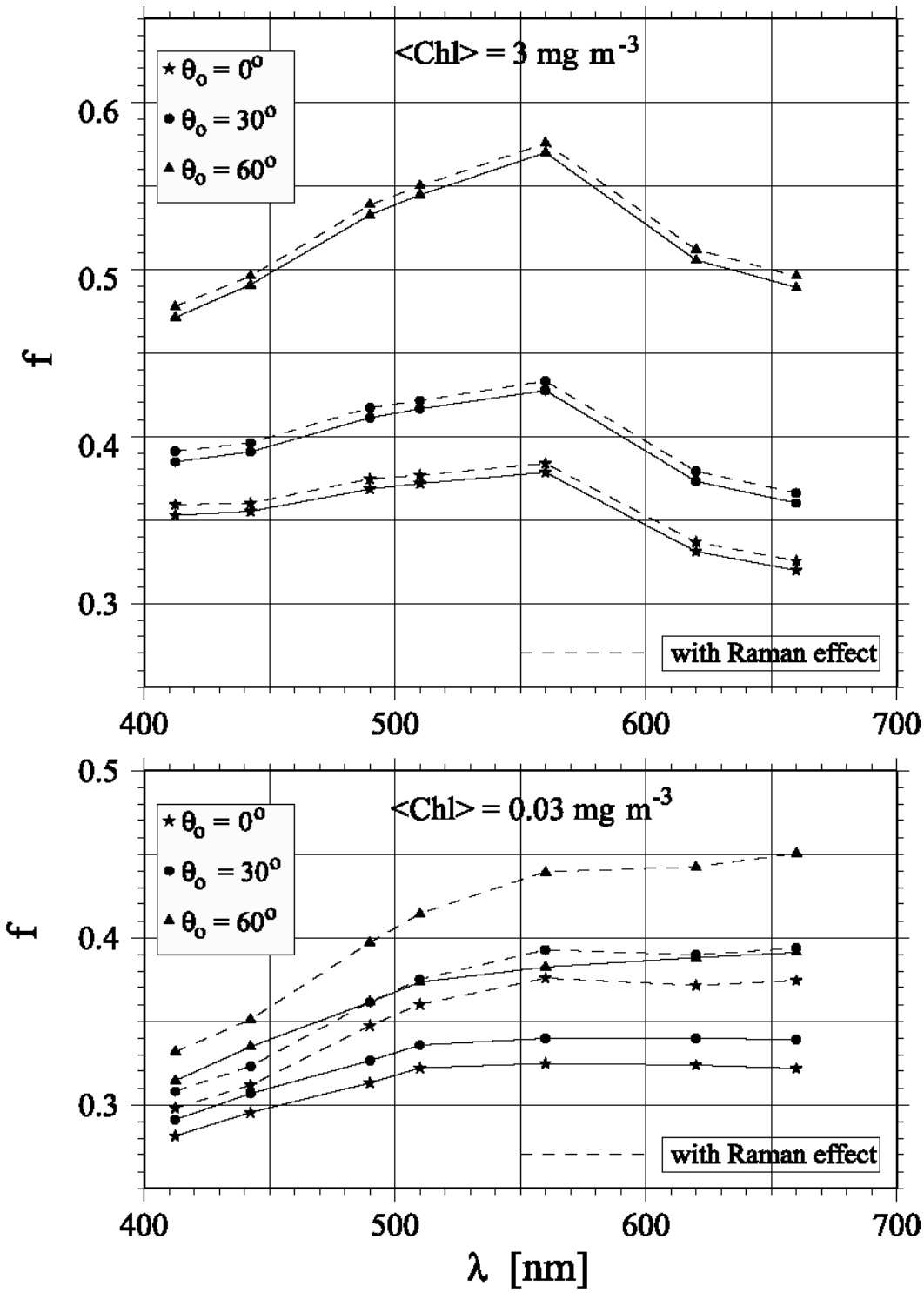

Figure 13.6: Spectral distribution of the function f, with and without the Raman contribution, for 2 chlorophyll concentrations and 3 solar zenith angles, θ_o, as indicated.

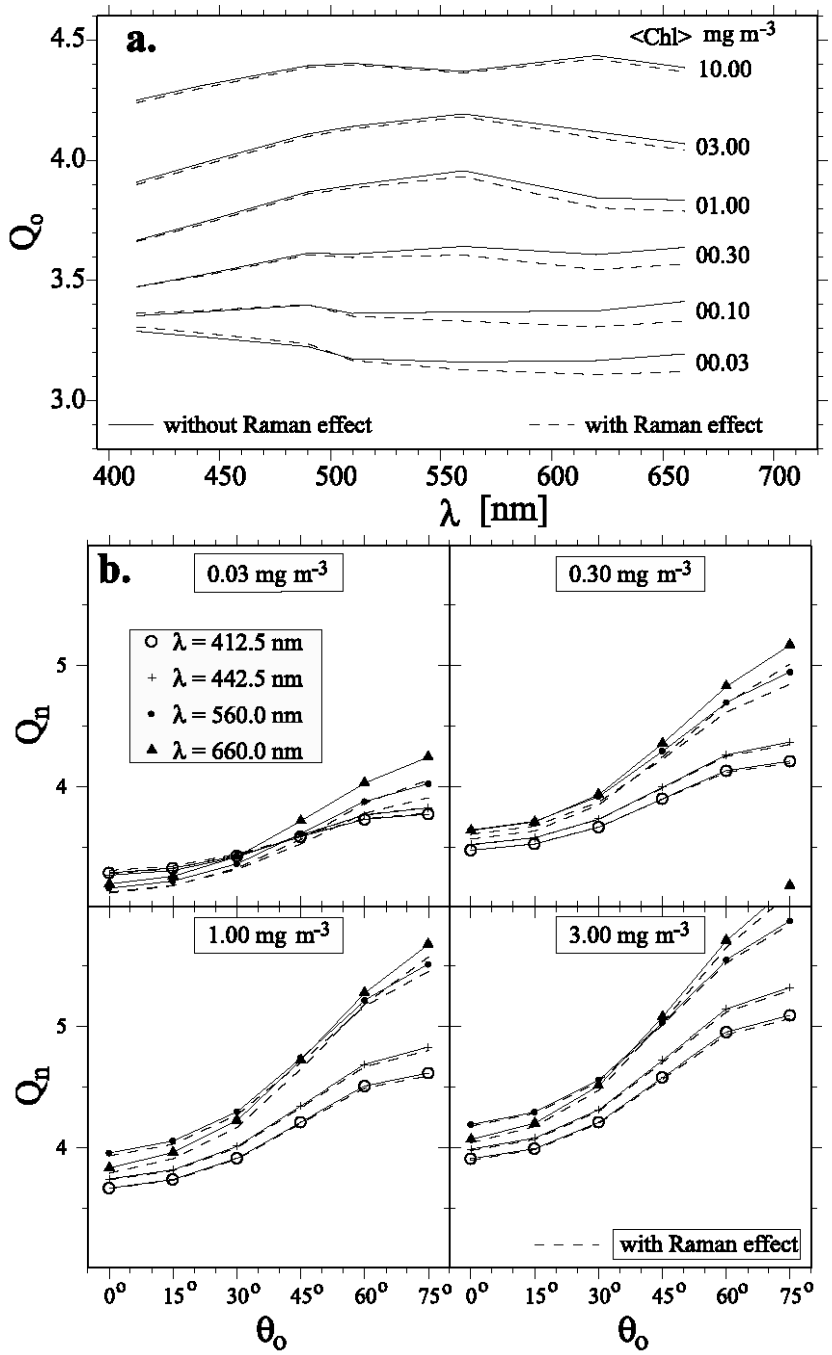

Figure 13.7: a): Spectral values of Q_0, the particular value of Q when θ' and $\theta_o = 0$, for increasing Chl, with and without the Raman contribution. b): Evolution of Q_n (Eqs. 13.6 and 13.26) with solar zenith angle, θ_o, for 4 wavelengths, and 4 chlorophyll concentrations, as indicated.

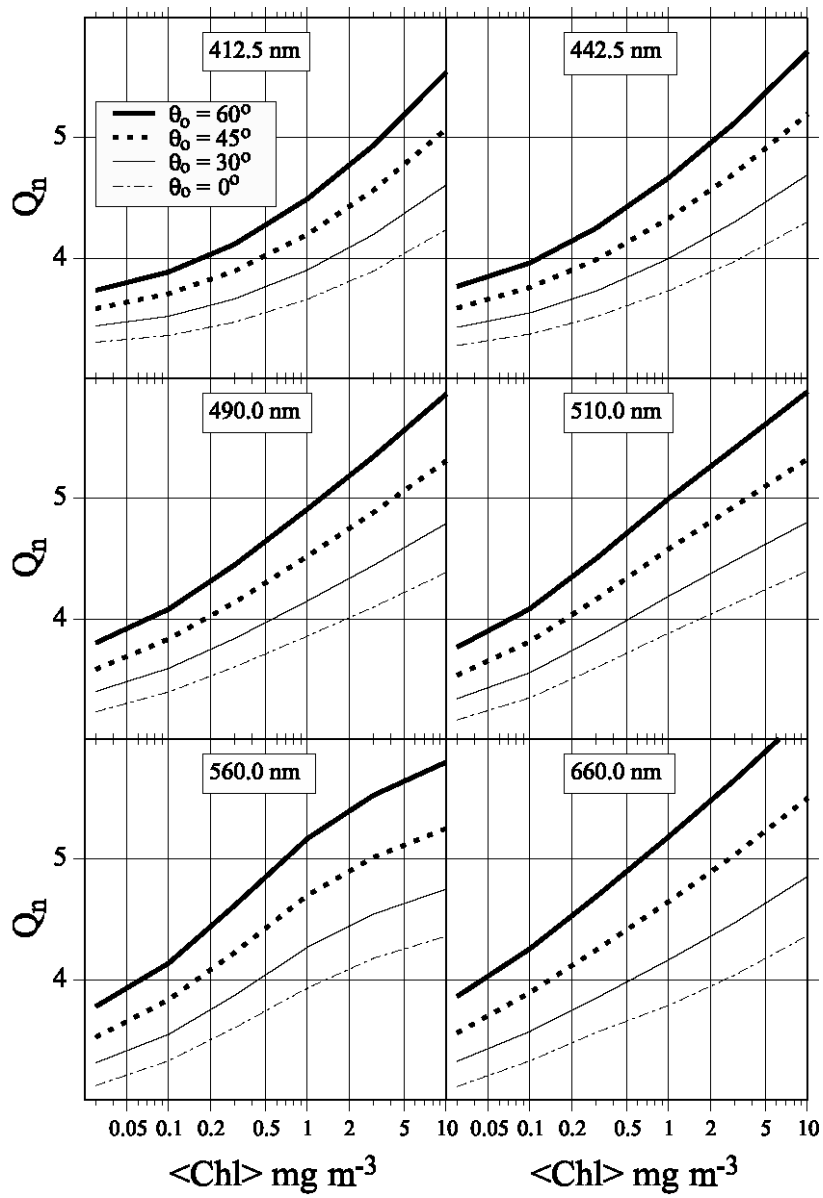

Figure 13.8: Evolution of the Q_n function with increasing chlorophyll concentration, for 6 wavelengths, and 4 solar zenith angles, as indicated. These Q_n values account for the Raman influence.

As was previously discussed in Section 13.3, the quasi-isotropic angular distribution of Raman scattering tends to smooth out the angular structure which particle scattering imposes on the upward radiance field. However, Raman emission has only a modest influence on the $Q(\lambda, \theta', \phi, \theta_o, Chl)$ function, as illustrated for $Q_o(\lambda, Chl)$ and $Q_n(\lambda, \theta_o, Chl)$ by dashed lines in Figure 13.7, for two simple reasons. At low *Chl* concentrations, Raman emission is a significant contribution to the upward radiant field, but its angular distribution and that of the underlying, predominately molecular elastic scattering are similarly quasi-isotropic. At high Chl, on the other hand, the elastic scattering by particles is much larger in magnitude than the Raman emission. In this situation, the tendency of Raman scattering to smooth the more structured pattern of the radiance field is simply too weak to be significant. In all cases illustrated in Figure 13.7, the influence of Raman emission, although weak, is most apparent at longer wavelengths. As

λ increases in the spectral region $\lambda > 565\ \text{nm}$, the molecular scattering contribution to $\beta(\lambda,\Psi)$ progressively decreases, while $a_w(\lambda)$ progressively increases. These tendencies with increasing λ progressively reduce the $\frac{b_b(\lambda)}{a(\lambda)}$ ratio and upward radiant field due to elastic scattering and increase the angular structure of the radiance distribution (especially at large θ_o). Under these conditions, the Raman emission becomes a concomitantly larger fraction of the upwelled radiant field, and its tendency to smooth the angular pattern of the field is enhanced as well.

Polar diagrams are the most convenient way to visualize the behavior of the $Q(\lambda,\theta',\phi,\theta_o,Chl)$ function with θ' (see *e.g.*, Fig 5 in Morel and Gentili 1993). Examples of the angular pattern of the quantity $\frac{L_u(0^-,\lambda,\theta',\phi,\theta_o,Chl)}{E_u(0^-,\lambda)}$ $(i.e.\ Q^{-1})$ in the principal plane containing the sun are shown in Figure 13.9 for a fixed solar zenith angle $\theta_o = 30°$. The contours for $Q = 5,\ \pi$, and 2 are indicated, as are also the radial lines corresponding to the critical angle $\theta_c \cong 48°$. These examples practically encompass all possible cases, and thus it is worth noting that inside the Snell cone $\theta' < \theta'_c$, $\pi \le Q(\lambda,\theta',\phi,30°,Chl) \le 5$ for all λ and *Chl*. The largest difference in angular patterns is between a) the case when $\lambda = 442.5\ \text{nm}$, $Chl = 0.03\ \text{mg m}^{-3}$, $\eta_b = 0.88$, and molecular scattering dominates backscattering, and b) the case when $\lambda = 660\ \text{nm}$, $Chl = 10\ \text{mg m}^{-3}$, $\eta_b = 0.04$, and particle scattering dominates backscattering.

Variations of the $\frac{f}{Q}$ *ratio*

Examination of Figures 13.5b and 13.7b shows that both the *f* and Q_n functions experience concomitant increases when the sun zenith angle increases. Therefore, their ratio is less dependent on θ_o. The variations of the particular quantity $\frac{f_o(\lambda,\tau_a,Chl)}{Q_o(\lambda,\tau_a,Chl)}$ are examined at first in Figure 13.10a, where examples are shown as functions of the wavelength for varying chlorophyll concentrations. The influence of the Raman scattering (dashed lines in Figure 13.10a)) is considerable when $Chl < 1\ \text{mg m}^{-3}$, due to strong enhancement of $f_o(\lambda,\tau_a,Chl)$. The overall variation of this quantity is in the range $0.075 \le \frac{f_o}{Q_o} \le 0.12$, and the extreme limiting values both occur in the red part of the spectrum. In the blue spectral region $(\lambda < 450\ \text{nm})$, the variations are within the narrower interval $0.085 \le \frac{f_o}{Q_o} \le 0.097$.

Regarding the general quantity $\frac{f(\lambda,\theta_o,\tau_a,Chl)}{Q(\lambda,\theta',\phi,\theta_o,\tau_a,Chl)}$, the strongest variations are expected to occur within the sun's principal plane $(\phi = 0 \text{ and } \pi)$; and minimal angular variations are in the perpendicular plane $\left(\phi = \frac{\pi}{2} \text{ and } \frac{3\pi}{2}\right)$. Typical variations of this ratio are shown in Figure 13.10b for the principal plane and perpendicular half-plane; they essentially remain within the range $0.08 \le \frac{f}{Q} \le 0.15$, centered about the

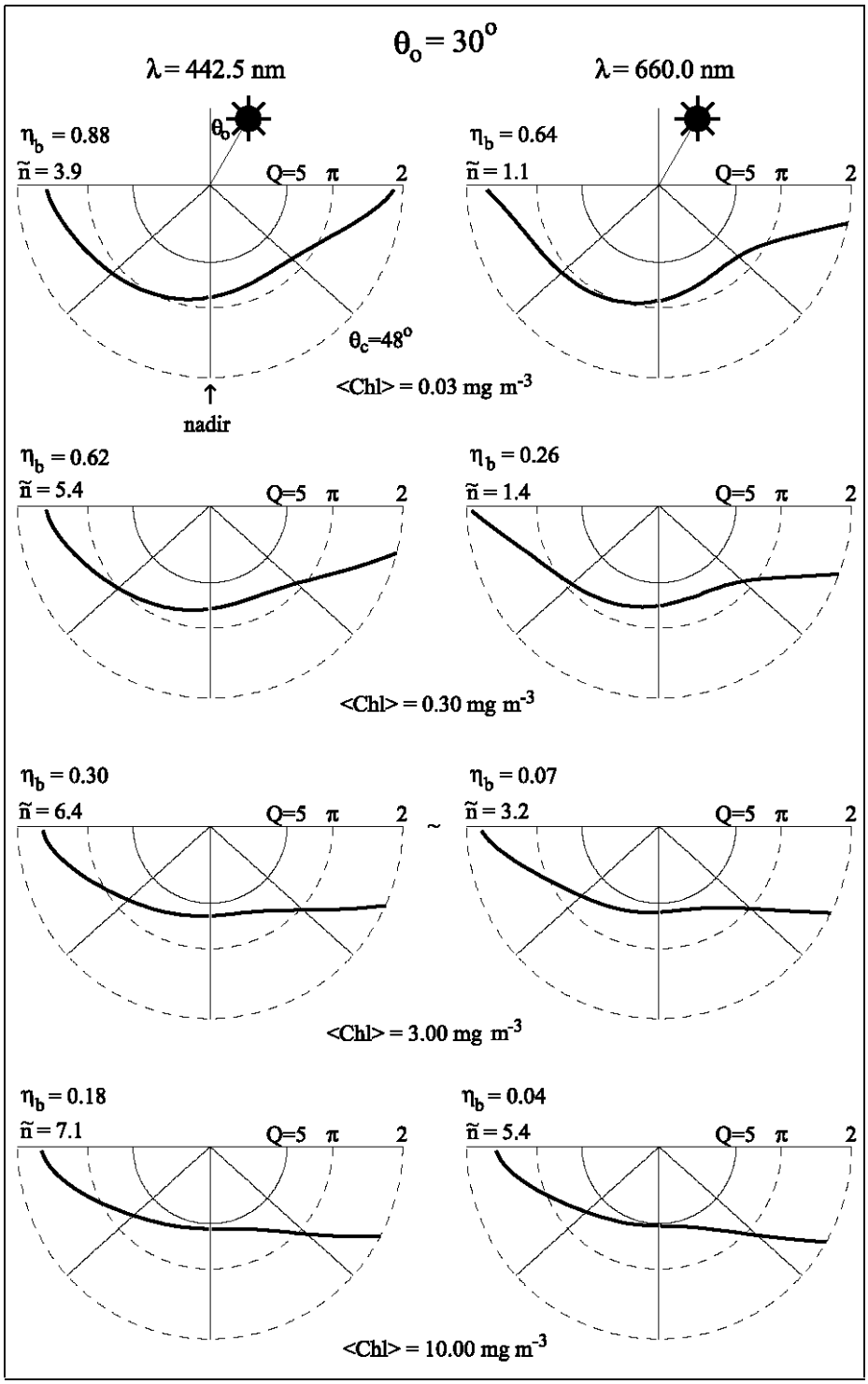

Figure 13.9: Selected examples of the upward radiance field within the sun's principal plane (plotted as in Fig. 13.3), for 2 wavelengths, and 4 chlorophyll concentrations, as indicated. Also provided are the backscattering ratios η_b and average numbers of photon scattering events $\tilde{n}$ [see Equations (13.14) and (13.15)] corresponding to each case. The sun position is the same for all graphs (θ_o = 30°). These radiance fields include Raman emission.

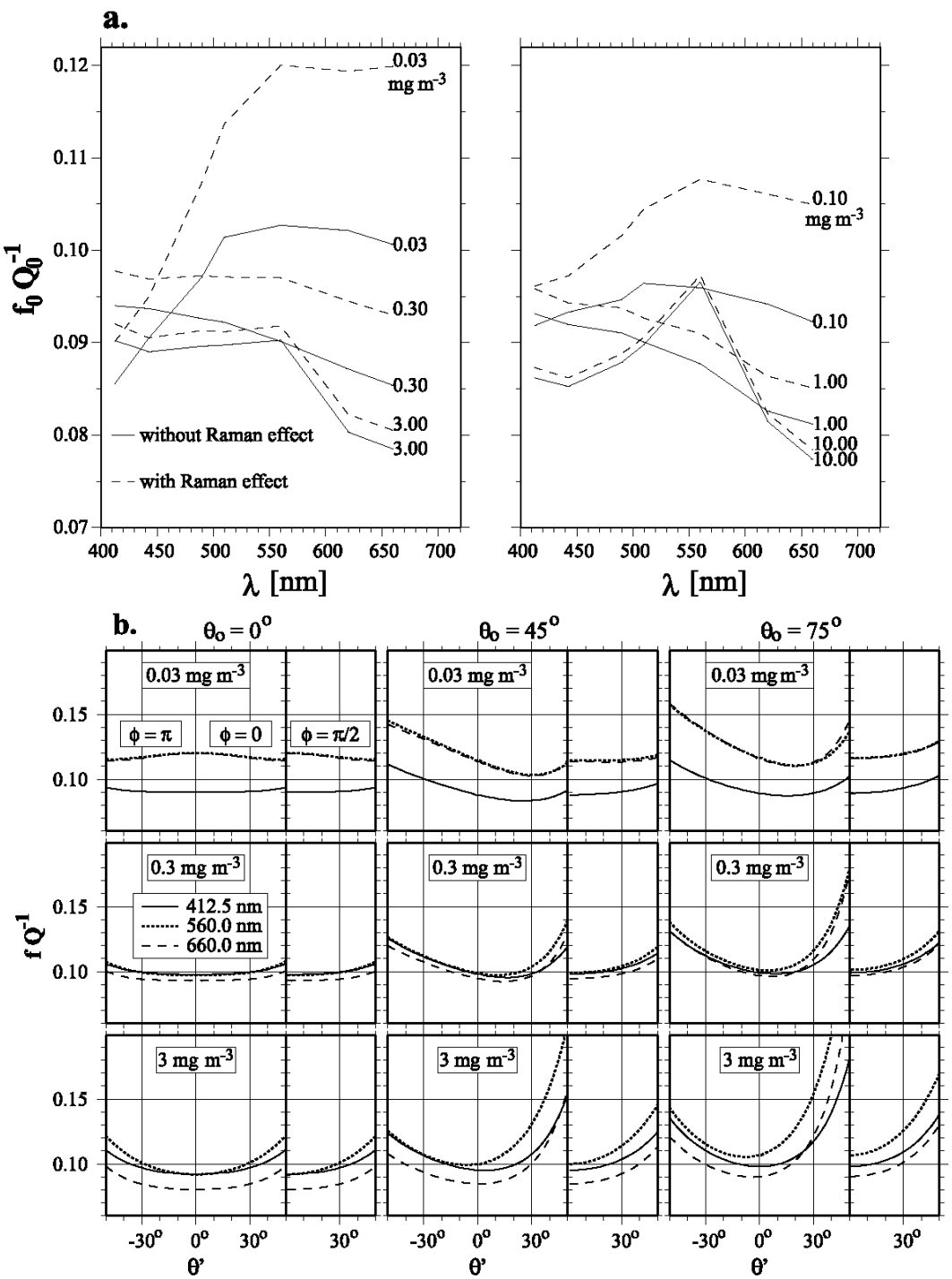

Figure 13.10: a): Spectral values of the ratio $f_o Q_o^{-1}$, with and without the Raman effect, for various chlorophyll concentrations. b): The $f Q^{-1}$ ratio as a function of θ' for 3 chlorophyll concentration, 3 solar zenith angles and 3 wavelengths (as indicated). The curves are plotted within the principal plane $[\phi = 0 \text{ and } \pi]$ and the vertical half-plane perpendicular to the principal plane $[\phi = \pi/2]$.

These values include the Raman scattering effect mean value 0.11 found by Gordon *et al.* (1988). When approaching the critical angle, higher $\frac{f}{Q}$ values are possible, particularly for large sun-zenith angle, and high chlorophyll concentration. The spectral dependency of the $\frac{f}{Q}$ ratio is marked for low *Chl* $\left(e.g.\text{ when } Chl = 0.03 \text{ mg m}^{-3}\right)$, essentially because the influence of the Raman scattering is important for the green and red radiation, and therefore, it enhances *f*. When $Chl \approx 0.3 \text{ mg m}^{-3}$, the spectral dependency of $\frac{f}{Q}$ has practically vanished; it reappears at $Chl \approx 3 \text{ mg m}^{-3}$, and now the lowest $\frac{f}{Q}$ values occur at 660 nm. Strongly featured $\frac{f}{Q}$ angular patterns at all wavelengths are typical of high *Chl* concentrations. It must be noticed that the asymmetrical $\frac{f}{Q}$ pattern occurring when the solar angle departs from 0, is reversed from low to high chlorophyll concentrations.

13.7. **CORRECTION PROCEDURES FOR BIDIRECTIONALITY**

The correction consists of operating Equations (13.8) and (13.20) or (13.21), in order to derive the exact normalized water-leaving radiance from water-leaving radiances, as determined from satellite measurements, or from in-water or above-water measurements in the field. These transformations require the quantities $\frac{f}{Q}$, Q (or f), and $\Re$. Conveniently, these values can be determined by interpolation within precomputed lookup tables, which are built by solving the RTE under specified boundary conditions, using the appropriate IOP describing the water bodies of interest. For the last point, various parameterizations are possible, so that everybody may have his own preference and can produce his own lookup tables. Very likely several of these will be built in the near future.

The lookup tables succinctly described below are ready for use, and may be obtained over the Internet (see below). These tables offer investigators an option for parameterizing the IOP of Case 1 waters as functions of the chlorophyll concentration, as described in Morel and Maritorena (2001), and summarized below. Such tables must be seen as a first attempt to provide a tool for making the birectionality correction.

The spectral absorption values, as a function of *Chl*, derive from the statistical analysis of the diffuse attenuation coefficient for downward irradiance (K_d) through an iterative procedure (Equations 8, 8', and 8'', in Morel and Maritorena, 2001).

The particle scattering coefficient at 550 nm depends on Chl according to (Loisel and Morel 1998)

$$b_p\left(550, Chl\right) = 0.416\left[Chl\right]^{0.766}, \tag{13.24}$$

and the wavelength dependence is represented through

$$b_p\left(\lambda, Chl\right) = b_p\left(550, Chl\right)\left[\frac{\lambda}{550}\right]^{v}, \tag{13.25}$$

where the varying exponent *v* is expressed as

$$\begin{aligned} v &= \frac{\log_{10}\left(Chl\right) - 0.3}{2}, \text{ when } 0.02 < Chl < 2 \text{ mg m}^{-3}, \text{ and} \\ v &= 0, \text{ when } Chl \geq 2 \text{ mg m}^{-3}. \end{aligned} \tag{13.26}$$

The volume scattering phase function for particles, $\tilde{\beta}_p(\Psi)$, is assumed to be independent of wavelength and is varied with chlorophyll concentration to satisfy the constraint that the particle backscattering efficiency fulfills the condition

$$\tilde{b}_{bp} = 0.007 - 0.0025 \log_{10}(Chl). \tag{13.27}$$

The Raman scattering coefficient at 488 nm is 2.6×10^{-4} m^{-1}, with a λ^{-5} spectral dependence (Bartlett *et al.* 1998). Multispectral RTE computations in the purely elastic mode are needed to determine the excitation flux in the wavelength band corresponding to emission at the wavelength of interest (*e.g.* see Mobley 1994).

Chl must be known to enter the lookup tables. Although the best estimate of *Chl* is derived from the exact normalized water-leaving radiance, the structure of the remote sensing *Chl* algorithms allows this difficulty to be overcome in successive steps. In case 1 waters, the usual ocean color *Chl* algorithms are based on a so-called "blue-green" ratio of water-leaving radiances, *e.g.* $\frac{L_{WN}^{ex}(443)}{L_{WN}^{ex}(555)}$. In a rough first approximation, the bidirectional corrections for a given *Chl* do not differ greatly between these two wavelengths. Therefore, the ratio of uncorrected radiances $\frac{L_{WN}(443)}{L_{WN}(555)}$, and *Chl* retrievals determined from it, are much less affected by bidirectional effects than are the radiances themselves. This Chl can be used as an initial entry for the lookup tables to determine a first estimate of the exact water-leaving radiances. At iterative procedure may be then followed alternately improve the *Chl* and $L_{WN}^{ex}(\lambda)$ estimates in successive steps (Morel and Gentili 1996).

The main characteristics of these tables are listed and summarized below:

1- Only vertically homogeneous case 1 waters have been considered.

2- The quantities $\Re(\theta', W)$ are tabulated in a separate file at a θ' increment of 1° for a perfectly level interface, and for wind speeds W = 0, 4, 10, and 16 m s^{-1} (cf. Figure 13.4). Residual capillary waves still exist when W = 0, according to the Cox and Munk (1954) formula, so that $\Re(\theta', W)$ differs slightly from values computed with a perfectly flat interface.

3- The quantities $f(\lambda, \theta_o, Chl)$ and $\frac{f(\lambda, \theta_o, Chl)}{Q(\lambda, \theta', \phi, \theta_o, Chl)}$ are tabulated as functions of five parameters, organized as follows:

   a. Wavelength, λ (7 values: 412.5, 442.5, 490, 510, 560, 620, 660 nm).

   b. Zenith-sun angle, θ_o (6 values: 0°, 15°, 30°, 45°, 60°, and 75°).

   c. Chlorophyll concentration, *Chl* (6 values: 0.03, 0.1, 0.3, 1.0, 3.0, and 10 mg m^{-3}).

   The results for the above combinations of λ, θ_o and *Chl* are stored in 252 separate files; and each file contains 13 columns and 17 lines for:

   d. Azimuth difference, ϕ (13 values from 0° to 180°, spaced at an increment of 15°), where the convention for the sign of ϕ is as in Figure 13.2.

   e. Nadir angle, θ' (17 values in degrees: 1.078[8], 3.411, 6.289, 9.278, 12.300, 15.330, 18.370, 21.410, 24.450, 27.500, 30.540, 33.590, 36.640, 39.690, 42.730, 45.780, and 48.830).

[8] This value must be used for any angle $\theta' < 1.078°$, in particular for $\theta' = 0$.

Note that wind speed and the aerosol optical thickness dependent variations in f and $\frac{f}{Q}$ are neglected, following the assumptions discussed above in Sections 13.4 and 13.6. The f and $\frac{f}{Q}$ tables described here were computed assuming $W \equiv 0$, and a maritime aerosol with optical thickness $\tau_a(550) \equiv 0.2$, at the reference wavelength $\lambda = 550$ nm.

4- There are two sets of tables in the format described in 3 above, one set for computations with the Raman effect included, and one without this effect. The tables including the Raman emission must be preferred for most applications. The tables produced in the purely elastic mode are provided for the convenience of those who wish to study the sensitivity of the bidirectional properties to the IOP model, without inteference by the Raman contribution.

5- When $60° \geq \theta_o \geq 0°$, the variations of f and Q_n with θ_o (see Figures 13.5b and 13.7b) are well represented, with a relative uncertainty less than 2 %, by linear functions of the form

$$X = X_o + S_X(1 - \cos\theta_o),$$

where X_o is f_o or Q_o and the associated slopes are S_f or S_{Qn}. A similar linear approximation is also possible for the ratio f/Q_n, which remains valid for q_o up to 75°; this relationship is less accurate, however, and divergences between the exact and approximate values may reach 3.4 %. In this case, X is f_o/Q_o and S_X is $S_{f/Qn}$. The associated X_o and S_X valuses are tabulated as functions of wavelength and chlorophyll concentration (as 6 sub-tables) in the file *lin-approx*.

Copies of the above files may be obtained over the Internet, using anonymous ftp, from oceane.obs-vlfr.fr. Once connected, the user should login as "anonymous" and provide his complete E-mail address as the password. The procedure is as follows:

- ftp oceane.obs-vlfr.fr
- LOGIN: anonymous (and provide password)
- cd pub/gentili
- bin
- get README_FIRST
- get DISTRIB_FQ_with_Raman.tar.gz
- get DISTRIB_FQ_without_Raman.tar.gz
- get rgoth.dat
- get lin-approx.tar
- bye

The file README_FIRST may be of some help in accessing and using the tables.

REFERENCES

Austin, R.W. and G. Halikas, 1976: The index of refraction of seawater. *SIO Ref. 76-1*, Vis. Lab., Scripps Inst. of Oceanography, La Jolla, California, 64pp.

Bartlett, J.S., K.J. Voss, S. Sathyendranath, and A. Vodacek, 1998: Raman scattering by pure water and seawater. *Appl. Opt.*, **37:** 3324-3332.

[5] This value must be used for any angle $\theta' < 1.078°$, in particular for $\theta' = 0$.

Cox, C. and W. Munk, 1954: Measurement of the roughness of the sea surface from photographs of the sun's glitter. *J. Opt. Soc. Am.*, **44:** 11838-11850.

Gordon, H.R., 1989: Dependence of the diffuse reflectance of natural waters on the sun angle. *Limol. Oceanogr.*, **34:** 1484-1489.

Gordon, H.R. and D.K. Clark, 1981: Clear water radiances for atmospheric correction of Coastal Zone Color Scanner imagery. *Appl. Opt.*, **20:** 4174-4180.

Gordon, H.R., O.B. Brown, R.H. Evans, J.W. Brown, R.C. Smith, K.S. Baker, and D.K. Clark, 1988. A semi-analytic radiance model of ocean color. *J. Geophy. Res.*, **93:** 10,909-10,924.

Kirk, J.T.O, 1984: Dependence of relationship between inherent and apparent optical properties of water on solar altitude. *Limnol. Oceanogr.*, **29:** 350-356.

Loisel, H., and A. Morel, 1998: Light scattering chlorophyll concentration in case 1 waters: A reexamination. *Limnol. Oceangr.*, **43:** 847-858.

Loisel, H. and A. Morel, 2001: Non-isotropy of the upward radiance field in typical coastal (Case 2) waters. *Int. J. Remote Sensing*, **22:** 275-295.

Mobley, C.D., 1994: *Light and Water; Radiative Transfer in Natural Waters*. Academic Press, San Diego, California. 592pp.

Mobley, C.D., B. Gentili, H.R. Gordon, Z. Jin, G.W. Kattawar, A. Morel, P. Reinersman, K. Stamnes and R.H. Stavn, 1993: Comparison of numerical models for computing underwater light fields. *Appl. Opt.*, **32:** 7484-7504

Morel, A. and B. Gentili, 1991: Diffuse reflectance of oceanic waters: its dependence on sun angle as influenced by the molecular scattering contribution. *Appl. Opt.*, **30:** 4427-4438.

Morel, A. and B. Gentili, 1993: Diffuse reflectance of oceanic waters. II. Bidirectional aspects. *Appl. Opt.*, **32:** 6864-6879.

Morel, A. and B. Gentili, 1996: Diffuse reflectance of oceanic waters. III. Implication of bidirectionality for the remote sensing problem. *Appl. Opt.*, **35:** 4850-4862.

Morel, A. and S. Maritorena, 2001: Bio-optical properties of oceanic waters: A reappraisal. *J. Geophys. Res.*, **106:** 7163-7180.

Morel, A. and L. Prieur, 1977. Analysis of variations in ocean color. *Limnol. Oceanogr.*, **22**(4): 709-722.

Petzold, T.J., 1972: Volume scattering functions for selected ocean waters. SIO Ref. No. 72-78, Scripps Inst. of Oceanography, La Jolla, California, 79pp.

Preisendorfer, R.W. 1960: Recommendation on the standardization of concepts, terminology and notation of hydrologic optics. Scripps Inst. Of Oceanogr., SIO Report, 96pp.

Smith, R.C and K.S. Baker, 1978: The bio-optical state of ocean waters and remote sensing. *Limnol. Oceanogr.*, **23:** 247-259.

Chapter 14

Sun and Sky Radiance Measurements and Data Analysis Protocols

Robert Frouin[1], Brent Holben[2], Mark Miller[3], Christophe Pietras[4], Kirk D. Knobelspiesse[5], Giulietta S. Fargion[4], John Porter[6] and Ken Voss[7]

[1]*Scripps Institution of Oceanography, University of California, San Diego, California*
[2]*Biospheric Sciences Branch, NASA Goddard Space Flight Center, Greenbelt, Maryland*
[3]*Department of Applied Science, Brookhaven National Laboratory, Upton, New York*
[4]*SAIC General Sciences Corporation, Beltsville, Maryland*
[5]*Science Systems and Applications, Inc., Greenbelt Maryland*
[6]*School of Ocean & Earth Science & Technology, University of Hawaii, Hawaii*
[7]*Physics Department, University of Miami, Florida*

14.0 INTRODUCTION

This chapter is concerned with two types of radiometric measurements that are required to verify atmospheric correction algorithms and to calibrate vicariously satellite ocean color sensors. The first type is a photometric measurement of the direct solar beam to determine the optical thickness of the atmosphere. The intensity of the solar beam can be measured directly, or obtained indirectly from measurements of diffuse global upper hemispheric irradiance. The second type is a measurement of the solar aureole and sky radiance distribution using a CCD camera, or a scanning radiometer viewing in and perpendicular to the solar principal plane.

From the two types of measurements, the optical properties of aerosols, highly variable in space and time, can be derived. Because of the high variability, the aerosol properties should be known at the time of satellite overpass. Atmospheric optics measurements, however, are not easy to perform at sea, from a ship or any platform. This complicates the measurement protocols and data analysis. Some instrumentation cannot be deployed at sea, and is limited to island and coastal sites. In the following, measurement protocols are described for radiometers commonly used to measure direct atmospheric transmittance and sky radiance, namely standard sun photometers, fast-rotating shadow-band radiometers, automated sky scanning systems, and CCD cameras. Also discussed are methods of data analysis and quality control, as well as proper measurement strategies for evaluating atmospheric correction algorithms and atmospheric parameters derived from satellite ocean color measurements.

14.1 AUTOMATIC SUN PHOTOMETER AND SKY RADIANCE SCANNING SYSTEMS

The technology of ground-based atmospheric aerosol measurements using sun photometry has changed substantially since Volz (1959) introduced the first hand-held analog instrument almost four decades ago. Modern digital units of laboratory quality and field hardiness collect data more accurately and quickly and are often equipped for onboard processing (Schmid et al. 1997; Ehsani 1998, Forgan 1994; and Morys et al. 1998). The method used remains the same, i.e., a detector measures through a spectral filter the extinction of direct beam solar radiation according to the Beer-Lambert-Bouguer law:

$$V(\lambda) = V_o(\lambda)\left(\frac{d_o}{d}\right)^2 \exp\left[-\left(\tau(\lambda)M\right)\right]t_g(\lambda), \tag{14.1}$$

where $V(\lambda)$ is the measured digital voltage, $V_0(\lambda)$ is the extra-terrestrial voltage, M is the optical air mass, $\tau(\lambda)$ is the total optical depth, λ is wavelength, d and d_o are respectively the actual and average earth-sun distances, and $t_g(\lambda)$ is the transmission of absorbing gases. The total optical depth is the sum of the Rayleigh and aerosol optical depth.

The earth-sun distance correction is calculated using the approximation

$$\left(\frac{d_o}{d}\right)^2 = 1 + 0.034\cos\frac{2\pi \cdot J}{365}, \tag{14.2}$$

where J is the number of the day of the year (Iqbal 1983).

Air mass M is a function of the sun zenith angle. Currently, the same value of air mass is used for Rayleigh, ozone, and aerosol factors. Air mass is calculated as

$$M = \left\{\cos\frac{\pi\theta_o}{180^\circ} + 0.15 * \left(93.885 - \theta_o\right)^{-1.253}\right\}^{-1}, \tag{14.3}$$

where the sun zenith angle θ_o is expressed in degrees.

Sky-scanning spectral radiometers that measure the spectral sky radiance at known angular distances from the sun have expanded the aerosol knowledge base. They provide, through inversion of the sky radiance, aerosol physical properties, such as size distribution, and optical properties, such as the aerosol scattering phase function (Nakajima et al., 1983, 1996; Tanré et al., 1988; Shiobara et al., 1991; Kaufman et al., 1994; Dubovik et al., 2000; and Dubovik and King, 2000). The inversion technique to calculate these aerosol properties requires precise aureole measurements near the solar disk and good stray-light rejection. Historically these systems are cumbersome, expensive, and not weather hardy . The CIMEL and PREDE (French and Japanese manufacturers respectively) sun and sky scanning spectral radiometers overcome most of such limitations, providing retrievals of aerosol and water vapor abundance from direct sun measurements, and of aerosol properties from spectral sky radiance measurements. Since the measurements are directional and represent conditions of the total column atmosphere, they are directly applicable to satellite and airborne observations, as well as to studies of atmospheric processes. When equipped with a sophisticated tracking system with fast responding motors, the PREDE can be installed onboard a ship, or other moving platform, to monitor aerosol optical properties at sea. In the following, we focus on the CIMEL system, since the measurement protocols are similar for both CIMEL and PREDE systems.

Description

The CIMEL Electronique 318A spectral radiometer, manufactured in Paris, France, is a solar powered, weather hardy, robotically pointed sun and sky spectral radiometer. At each wavelength, this instrument has approximately a 1.2^o field-of-view (full angle) and filtered solar aureole and sky radiance. The 33 cm collimators were designed for 10^{-5} stray-light rejection for measurements of the aureole 3° from the sun. The robot mounted sensor head is pointed at nadir when idle to prevent contamination of the optical windows from rain and foreign particles. The sun/aureole collimator is protected by a quartz window, allowing observation with an ultraviolet enhanced silicon detector with sufficient signal-to-noise for spectral observations between 300 and 1020 nm. The sky collimator has the same 1.2^o field of view, but uses an order of magnitude larger aperture-lens system to improve dynamic range for measuring the sky radiance. The components of the sensor head are sealed from moisture and packed in dessicant to prevent damage to the electrical components and interference filters. Eight ion assisted deposition interference filters are located in a filter wheel rotated by a direct drive stepping motor. A thermistor measures the temperature of the detector, allowing compensation for any temperature dependence in the silicon detector.

A polarization model of the CE-318 is also used in SIMBIOS. This version executes the same measurement protocol as the standard model, but makes additional hourly measurements of polarized sky radiance at 870 nm in the solar principal plane (Table 14.1 and 14.2).

Installation

The installation procedures for the CIMEL instrument are summarized below. More detailed information is available from the AERONET web page (http://aeronet.gsfc.nasa.gov:8080).

The site should have a clear horizon and be representative of the regional aerosol regime. The basic assembly is relatively simple to mount. The cables are labeled clearly and most fit only in one place. Once the robot is assembled, it should be oriented so the zenith motor casing is pointing roughly east (the metal claw to which the sensor head is attached, then points to the west). The round connector end of the data cable should be attached to the sensor head, and the flat connector should be plugged into the white CIMEL control box. Strap the sensor head to the robot metal claw using the silver metal band. Make sure that the face of the sensor head is flush with the edge of the metal claw. Also, ensure that the long axis of the collimator cross-section is perpendicular to the axis of the zenith motor casing and claw. Verify that the robot itself is level. Do not use the embedded bubble level on top of the robot. Place the supplied bubble level on top of the flat ledge of the central robot tubular body (below the sensor head motor) This should be level in both the N/S and E/W axes. Verify that the CIMEL control box “TIME” and “DATE” are correct, i.e., that they agree with the VITEL transmitter clock. If the Time or Date is wrong, the CIMEL will <u>not</u> find the sun on a “GOSUN” command.

Next, put the CIMEL in manual mode using the white control box display screen. In Manual mode, the main screen reads: “PW MAN SCN VIEW”. Do a “PARK” procedure. When “PARK” is complete the sensor head collimator should be pointing down, perpendicular to the ground. Place the bubble level on the top of the metal claw arm and verify that this is level. If not, loosen the zenith bolt's hex nut (below the permanent bubble level on the top of the robot) and level it by rotating the zenith motor casing with your hand. Re-tighten the zenith nut tightly. It is important to perform another “PARK” procedure, or two, and make sure it is in fact level.

Using the right 2 buttons, change the display to read “GOSUN”. Select “GO” to initiate. The sensor head should point to the sun. The hole at the top of the collimator should allow the sunlight to illuminate the marker spot at the base of the collimator. When the bright spot is on the mark, the instrument is aligned. If it is off to the left or right, rotate the robot base to align it. After you rotate the robot, you will need to verify that the robot is still level as before. Park the instrument and perform another “GOSUN” to check that the alignment is still good. If not, ensure that the robot is level, and that the sensor head is level when manually parked. One note: when you level the sensor head and do a “GOSUN”, repeat this process a few times to be sure of the alignment. The first “GOSUN” after leveling is often not correct, because moving the sensor head while leveling can temporarily offset the robot's zeroing point. Re-parking the sensor and doing a second “GOSUN” should yield a more accurate alignment. Repeat this procedure until the alignment remains accurate and consistent on repetition.

Press “PW” then increment to 4, and place the instrument in “AUTO” mode. The main “AUTO” mode display should read: “PW AUTORUN VIEW”. The CIMEL should be left in this mode in order to perform automatic measurement sequences.

The VITEL transmitter has a multi-level menu with “TIME DATE” etc in top level, and sub categories below each top-level item. The exact menu structure varies with software version (2.01, 2.9, and 2.11). Refer to the version most similar to your particular transmitter. One may operate the VITEL display by using the control buttons. To initiate an action, press the “SET-UP” button, then press the “SCROLL” button repeatedly to view the categories in the current menu level. To choose any subcategory, press the “SELECT” button when the desired feature is shown in the display window. To change a parameter use the right 2 buttons “CHANGE” and “ENTER”'. At any time, one may return to the previous (higher) menu level by pressing the “SET-UP” button.

Measurement Protocols

The radiometer makes only two basic measurements, either direct solar flux, or sky radiance. Each type of measurement involves several programmed sequences.

Direct sun measurements are made in eight spectral bands distributed between 340 and 1020 nm (440, 670, 870, 940 and 1020 nm are standard). Each measurement requires approximately 10 seconds. A sequence of three such measurements are taken 30 seconds apart creating a triplet observation per

wavelength. Triplet observations are made during morning and afternoon Langley calibration sequences and at standard 15-minute intervals in between (Table 14.1). The time variation of clouds is typically much greater than that of aerosols, and therefore significant variation in the triplets may be used to screen cloud-contaminated measurements from the data. Variability over the 15-minute interval also allows another check for cloud contamination at a lower frequency.

Sky measurements are performed at 440, 670, 870 and 1020 nm (Table 14.1). A single spectral measurement sequence (Langley sky) is made immediately after the Langley air mass direct sun measurement, with the sensor pointed 20° from the sun. This is used to assess the stability of the Langley plot analysis (O'Neill *et al.* 1984). Two basic sky observation sequences are made, "almucantar" and "principal plane". The objective of these sequences is to retrieve size distribution, phase function and aerosol optical thickness (AOT). This is approached by acquiring aureole and sky radiance observations spanning a large range of scattering angles, relative to the sun's direction, assuming a constant aerosol profile.

An "almucantar sequence" is a series of measurements taken at the same sun elevation for specified azimuth angles relative to the Sun position. The range of scattering angles decrease as the solar zenith angle decreases, thus almucantar sequences made at an optical air mass of 2, or more, achieve scattering angles of 120°, or larger. Scattering angles of 120° are typical of many sun-synchronous viewing satellites, and thus a measure of the satellite path radiance is approximated from the ground station. During an almucantar measurement, observations from a single channel are made in a sweep at a constant elevation angle across the solar disk and continue through 360° of azimuth in about 40 seconds (Table 14.2). This is repeated for each channel to complete an almucantar sequence. A direct sun observation is also made during each spectral almucantar sequence.

More than four almucantar sequences are made daily at optical air masses of 4, 3, 2 and 1.7, both morning and afternoon. An almucantar sequence is also made hourly between 9 AM and 3 PM local solar time for the standard instrument and skipping only the noon almucantar for the polarization instrument.

The standard principal plane sky radiance measurement sequence is similar to the almucantar sequence, but the sensor scans in the principal plane of the sun, and therefore all angular distances from the sun are scattering angles, regardless of solar zenith angle. This measurement pointing sequence begins with a sun observation, moves 6° below the solar disk then sweeps through the sun's principal plane, taking about 30 seconds for each of the four spectral bands (Table 14.2). Principal plane observations are made hourly when the optical air mass is less than 2 to minimize the variations in radiance due to the change in optical air mass.

Polarization measurements of the sky at 870 nm are an option with this instrument. The sequence is made in the principal plane at 5° increments between zenith angles of -85° and $+85^o$. The configuration of the filter wheel requires that a near-IR polarization sheet be attached to the filter wheel. Three spectrally matched 870 nm filters are positioned in the filter wheel exactly 120° apart. Each angular observation is a measurement of the three polarization filter positions. An observation takes approximately 5 seconds and the entire sequence about 3 minutes. This sequence occurs immediately after the standard measurement sequence in the principal plane.

Data Analysis

The present protocols adopt the data analysis procedures established for the AERONET program (Holben et al, 1998), with specific components and characteristics summarized in Table 14.3.

The AERONET algorithms impose a processing standardization on all of the data taken in the network, thus facilitating comparison of spatial and temporal data between instruments.

A link from the SIMBIOS Web Page to the AERONET archival system allows the ocean color community to access either the raw, or processed, data via internet for examination, analysis and/or reprocessing, as needed. Alternatively a user may connect directly to the AERONET web page: aeronet.gsfc.nasa.gov:8080.

The algorithms, inputs, corrections, and models used in computing the aerosol optical thickness, precipitable water (Pw), spectral irradiance, and sky radiance inversions are referenced in Table 14.3. The

algorithms comprise two principal categories; time dependent retrievals such as AOT and Pw, and sky radiance retrievals such as size distribution, asymmetry parameter, single scattering albedo and complex index of refraction. As new and improved approaches and models are accepted within the community, the revised processing methods may be applied uniformly to the network-wide database. The specific implementation used by the SIMBIOS Project to compute AOT is described below in Sect. 14.5.

Sky radiance Inversion Products

Optical properties of the aerosol in the atmospheric column are retrieved by two inversion algorithms: that of Nakajima et al. (1983, 1996) and the new algorithm developed by the AERONET Project (Dubovik and King 2000; Dubovik *et al*. 2000).

a) Inversions by the Nakajima et al.'s (1983, 1996) algorithms

The code inverts sky radiance in two ways:

1. simultaneously at four wavelengths (440; 670; 870 and 1020 nm) in the aureole angular range (scattering angle between 2.8^o and 40°;
2. separately at each of four wavelengths (440; 670; 870 and 1020 nm) in the whole solar almucantar (scattering angle greater than 2.8^o) --option "single channel inversion".

The inversion assumptions are that aerosol particles are homogeneous spheres with a fixed index of refraction: n(λ) = 1.45, k(λ) = 0.005. The retrieved variables are: $\frac{dV(r)}{d\ln r}$ (in $\mu m^{-3}/\mu m^{-2}$), the volume particle size distribution in range of sizes: 0.057 µm < r < 8.76 µm, the scattering optical thickness at 440,670,870,1020nm, and the phase function at 440, 670, 870 and 1020 nm (including an asymmetry parameter).

b) Inversions by the new AERONET code (Dubovik and King 2000; Dubovik et al. *2000)*

The code inverts $\tau_a(\lambda)$ and sky radiances simultaneously at four wavelengths (440; 670; 870 and 1020 nm) in the whole solar almucantar (scattering angles greater than 2.8^o). Aerosols are assumed to be homogeneous spheres, but the index of refraction is not fixed.

The retrieved variables are $\frac{dV(r)}{d\ln r}$ (in $\mu m^{-3}/\mu m^{-2}$), the volume particle size distribution in the range of sizes 0.05 µm $< r <$ 15 µm, and the volume concentration, volume mean radius, standard deviation, and effective radius for total (t), fine (f), and coarse (c) modes.

Note that the fine and coarse mode variables can be used only if the retrieved $\frac{dV(r)}{\ln r}$ is bi-modal. There is no automatic check for bi-modality. Also retrieved are the real and imaginary parts of the complex refractive index, m(λ) = n(λ) – i k(λ), (1.33 < $n(\lambda)$ < 1.6; 0.0005 < k(λ) < 0.5) at 440,670,870, and 1020nm, the single scattering albedo, and the phase function (including its asymmetry parameter) at 440, 670, 870, and 1020 nm. It is assumed that particles in the range 0.05-0.6 µm are fine mode and those in the range 0.6-15 µm are coarse mode aerosols (Dubovik et al., 2000). This definition is not completely correct in all size distributions. Nevertheless, experience has shown it to hold true in the majority of practical cases.

Quality Control

The AERONET $\tau_a(\lambda)$ quality assured data are cloud screened following the methodology of Smirnov et al. (2000), and here we present just a brief outline of the procedure. The principal filters used for the cloud screening are based on temporal variability of the $\tau_a(\lambda)$, with the assumption being that greater temporal variance in τ_a is due to the presence of clouds. The first filter is a check of the variability of the three τ_a values measured within a one-minute period. If the difference between minimum and

maximum $\tau_a(\lambda)$ within this one-minute interval is greater than 0.02 or $\tau_a(\lambda)$*0.03 then the measurement is identified as cloud contaminated. Then the remaining points are analyzed. If the standard deviation for $\tau_a(500nm)$ is less than 0.015, then the entire day's data are passed. If not, the $\tau_a(\lambda)$ time series are checked for the presence of rapid changes or spikes in the data. A filter based on the second derivative of the logarithm of $\tau_a(\lambda)$, as a function of time, is employed to identify rapid variations, which are then filtered as observations affected by clouds. This filter value is expressed as

$$D = \sqrt{\frac{1}{(n-2)} \sum \left[\frac{Ln\tau_i - Ln\tau_{i+1}}{t_i - t_{i+1}} - \frac{Ln\tau_{i+1} - Ln\tau_{i+2}}{t_{i+1} - t_{i+2}} \right]^2} \tag{14.4}$$

where ***t*** is the time, expressed as the fraction of the day, for data point ***i***, and ***n*** is the number of data points in the day. If the value of D is greater than 16, the day is deemed cloudy. The data point whose value contributed most to D is removed, and D is recalculated. This is repeated until the value for D falls below 16 or there are less than three points left (at which point all data for the day are rejected). After this, data whose $\tau_a(500nm)$ or Angstrom parameter, $\boldsymbol{\alpha}$, value exceeds three standard deviations from the mean for that day are rejected. Unscreened data are fully available from the AERONET homepage (aeronet.gsfc.nasa.gov). Automatic cloud screening of the almucantar and principal plane data is done by checking the distributions of data about the solar disc for symmetry and smoothness.

14.2 SKY RADIANCE DISTRIBUTION CAMERA SYSTEMS

Camera systems for sky radiance distribution are useful to collect the entire hemisphere of sky radiance data in a quick manner. The resulting data images usually contain the sun, so that the measurement geometry can be determined accurately and unambiguously. Also images can be checked for cloud contamination and other measurement artifacts more easily than can be done with data from scanning systems. The limitation of camera systems is that the dynamic range of the whole scene must be contained in each image. Therefore, the camera system must have large dynamic range and some method must be used to attenuate the direct sunlight before it strikes the imaging optics. To get a complete sky radiance distribution, including the solar aureole, it may be necessary to have an auxiliary system to measure the sky radiance near the sun (Ritter and Voss, 2000).

In addition, a sky radiance system, fitted with polarizers, can measure the Stokes parameters dealing with linear polarization (Voss and Liu, 1997). These additional parameters are useful for investigating the polarization properties of the atmospheric aerosols, and improving the aerosol optical models.

One of the most important areas of the sky radiance distribution to measure is the area near the horizon, opposite the sun, in the principal plane (the plane containing the sun and the zenith direction). This portion of the sky contains information on the large scattering angle portion of the atmospheric aerosol phase function, and is very important for determining the aerosol optical properties relevant to atmospheric correction for ocean color satellites.

The second very important region of the sky is the solar aureole, the region near the sun. Because the aerosol scattering phase function is strongly peaked in the forward direction, information in this region is important in determining the aerosol single scattering albedo. Techniques for converting sky radiance measurements to aerosol properties have been described in Wang and Gordon (1993), Gordon and Zhang (1995) and Zhang and Gordon (1997a, b).

An example of a camera system for sky radiance distribution is described in Voss and Zibordi (1989). The system described has been upgraded, for greater dynamic range, with a cooled CCD array. The basic system consists of a fisheye lens, a spectral/polarization filter changer, and a digital camera. To block direct sunlight from hitting the array, an occulter is manually adjusted to shadow the fish-eye lens. The size of the occulter is approximately $\pm 20^o$ of the almucantar when the sun is at 60° zenith angle; the effect of the occulter is obvious in data images shown in Liu and Voss (1997). Four spectral filters select the wavelength

range to be measured. Polarization filters are used to collect 3 planes of polarization in data images. These images can be combined to determine the linear polarization stokes vectors.

Measurement Protocols

Obviously, the first order requirement is that the field of view of the camera system be as unobstructed as possible, and that the measurement site be located in an appropriate place with respect to the ships stack exhaust. If the whole field of view cannot be clear (as is usually the case), then one should try for a clear hemisphere, where data between obstructions in the other hemisphere can be used for checking the sky symmetry.

As the desired objective is to derive the aerosol scattering parameters, the sky must also be cloud free. Clouds cause two problems. The first is easy to detect and is the direct effect of having the bright cloud in the scene (in particular on the almucantar or principle plane). Almost any cloud will overwhelm the effect of aerosols in determining the sky radiance. This effect of clouds is usually quite evident in the sky radiance image. The second problem is the indirect effect of clouds, while not directly causing a problem, shadowing aerosols and reducing the skylight caused by aerosol scattering. This second effect is more difficult to handle and places a more stringent requirement on the state of cloudiness during a measurement sequence. This effect can often be quite visible when the atmospheric aerosol loading is high, causing light beams to be evident in the aerosol layer. For these reasons, measurements with clouds present should be avoided if at all possible.

The maximum scattering angles existing in the sky radiance distribution occur near the horizon in the principle plane opposite the sun. For a given solar zenith angle, the maximum scattering angle is given by adding • /2 to the solar zenith angle. Since knowledge of the aerosol phase function at large scattering angles is important for the atmospheric correction process, measurements of the sky radiance distribution should be taken when the sun is at large zenith angles. The optimum angle is a compromise between getting large scattering angles and working too close to the horizon where multiple scattering effects are large (because of long optical paths through the atmosphere). A solar zenith angle of 60^0 has been chosen as optimum, because of these constraints.

Concurrent with the sky radiance measurements, it is important to measure the aerosol optical depth. By combining the aerosol optical depth and sky radiance distribution, the aerosol scattering properties can be determined, together with the single scattering albedo of the aerosols (Wang and Gordon, 1993; Gordon and Zhang, 1995; Zhang and Gordon, 1997a).

Data Analysis Protocols

Data reduction of the sky radiance data is very straightforward, and is described in Voss and Zibordi (1989). Basically with camera images, the data reduction process consists of simple image processing. Each image is multiplied by an absolute calibration factor and by an image that corrects for camera lens roll-off. This last factor is very important with a fisheye lens, as the important portion of the image is near the edge where the roll-off can become very significant. Once the image has been converted to radiometric data, specific areas can be selected for further analysis. In particular the almucantar and principal plane can easily be extracted for use in inversion routines.

Reduction of the sky radiance data to get the polarization properties is slightly more complicated. The current method is described in Voss and Liu (1997). Basically the Mueller matrix of the camera system is described as interacting with the Stokes vector of the skylight. There are three orientations of a linear polarizer in the system providing three separate Mueller matrices describing the camera system. For each sky direction (a pixel in the camera images), these Mueller matrices and the resultant intensities measured by the camera form a set of simultaneous equations with the unknowns being the sky Stokes vectors. For each pixel, these equations are inverted to obtain the Stokes vector of the skylight. While these images have been evaluated qualitatively (Liu and Voss, 1997), work is currently being done to do more quantitative inversions following the methods of Zhang and Gordon (1997b).

14.3 HAND-HELD SUN PHOTOMETERS

These instruments offer the simplest and most cost-effective means to collect data on aerosol optical thickness at sea. They are based on the measurement of the solar beam intensity, and therefore, the direct atmospheric transmittance. From this transmittance, after proper correction for attenuation by air molecules, the aerosol optical thickness may be obtained (Equation 15.1). The technique is straightforward in principle. It is difficult for an observer to point the photometer at the sun accurately from a moving platform, but this difficulty is obviated with modern-day instruments. The interest of these instruments also resides in the fact that, in most of the oceans, aerosol optical thickness measurements at the time of satellite overpass are sufficient to verify the atmospheric correction of ocean color (Schwindling *et al.* 1998). They allow one to estimate, via the Angstrom coefficient, the "pseudo" phase function of the aerosols (the product of the single-scattering albedo and the phase function), a key atmospheric correction variable.

Many types of sun photometers have been built and are available commercially. In the following, we focus on two instruments, the MicroTops sun photometer, manufactured by Solar Light, Inc., and the SIMBAD radiometer, built by the University of Lille.

The NASA SIMBIOS Program maintains a set of these instruments for use during ocean-color evaluation cruises. The objective is to collect accurate aerosol optical thickness measurements during the ship cruises for comparison with values derived from satellite algorithms.

a) MicroTops

The Solar Light, Inc. MicroTops sun photometer is a hand held radiometer used by many investigators throughout the world. The popularity of MicroTops sun photometers is due to their ease of use, portability, and relatively low cost. The instruments have five channels whose wavelengths can be selected by interference filters. In order to follow the specifications given by the World Meteorological Organization (WMO), the wavelengths are typically chosen at 440, 500, 675, 870 nm, with an additional channel at 940 nm to derive integrated water vapor amounts. If an additional sun photometer is available, then it is also desirable to make measurements at 380 and 1020 nm.

The MicroTops sun photometers use photodiode detectors coupled with amplifiers and A/D converters. The collimators are mounted in a cast aluminum block with a 2.5^{o} full field of view. The MicroTops sun photometer has built-in pressure and temperature sensors and allows for a GPS connection to obtain the position and time. A built in microprocessor can calculate the aerosol optical depth, integrated water vapor, and air mass in real time and display these values on a LCD screen. Frequency of measurements is around 3Hz. Temperature effects are corrected by taking dark count measurements with the lid covered on startup. Further information on MicroTops sun-photometers can be found in Morys (1998).

b) SIMBAD

The SIMBAD radiometer was designed by the University of Lille to measure both aerosol optical thickness and diffuse marine reflectance, the basic atmospheric correction variables. The radiometric measurements are made in 5 spectral bands centered at 443, 490, 560, 670, and 870 nm. The ocean surface and the sun are viewed sequentially. The same 3° field-of-view optics, interference filters, and detectors are used in both ocean and sun viewing modes. A different electronic gain, low and high, is used for each mode, respectively. A specific mode allows measurement of the dark current. The optics are fitted with a vertical polarizer to reduce reflected skylight when the instrument is operated in ocean-viewing mode (Fougnie et al., 1999). The polarizer does not affect the sun intensity measurements, because direct solar radiation is not polarized.

A GPS unit is attached to the instrument for automatic acquisition of geographic location at the time of measurement. Also acquired automatically are pressure, temperature, and view angles. Frequency of measurements is 10 Hz. In sun-viewing mode, only the highest intensity measured over one second is kept to avoid sun-pointing errors on a moving platform. Data is stored internally and downloaded onto diskette at the end of the day, or cruise. The instrument is powered with batteries, allowing 6 hours of continuous use. In normal use during a cruise (see below), the internal memory and batteries allow for 3 months of operations without downloading data or recharging the batteries.

Installation and Maintenance

The MicroTops and SIMBAD instruments need to be pointed at the sun manually. The sun is correctly aligned when its image appears in the cross hair on a small screen (MicroTops) or on a target (SIMBAD). After 10-20 minutes of practice the user will become familiar with the pointing procedure and the process will become second nature. It is important to get familiar with this pointing procedure on land as ship based measurements require more skill.

The exterior of the instrument lenses can accumulate salt spray and should be inspected and cleaned if needed. For the open ocean, salt is the primary contaminant. Under these conditions, a lens tissue can be wet with clean (filtered if possible) water or ethanol and used to remove the salt, then a dry lens tissue used to remove remaining water drops.

Faulty electronics pose a potential problem that is not always easy to detect when using MicroTops instruments. In the past it has been found that a leaky capacitor lowered the power and created erratic behavior for the shorter wavelengths where more gain is required. One can also get some idea of the instrument stability by taking numerous measurements with the lid covered. The voltage on all five channels should be less than $\pm$ 0.03 mV. If the values are greater than this the unit should be sent back to the manufacturer for repair. Voltage variability will give some idea of the noise present in the photometer.

Measurement Protocols

During stable conditions (land or calm seas) pointing the radiometers at the sun is straightforward and most of the measurements will be accurate. Under rough ocean conditions, pointing at the sun can become the major source of uncertainty, with many of the measurements being off the sun. The measurements that are off the sun will have higher apparent aerosol optical depths, artifacts that bias the average positively. For data acquired under rough sea conditions, repeated measurements of aerosol optical depths are typically distributed in a comet shaped pattern, with a cluster of lower values and a tail extending to higher values. In these cases, the smaller optical depth values are more accurate and the larger values, which are likely due to pointing error, must be removed in post processing. Since many measurements may be discarded in post processing, it is suggested that 25 or more measurements should be made within a short period of time (less than 5 minutes).

In general, the SIMBAD instrument is used alternatively in sun- and ocean-viewing mode. The sun intensity measurements also allow one to compute down-welled solar irradiance accurately in clear sky conditions, or when the sky is partly cloudy (<30%) with the sun not obscured by clouds. The modeled values of solar irradiance are used to normalize water-leaving radiance measurements.

The recommended protocol is to make consecutively one “dark” measurement, three measurements in sun-viewing mode, one “dark” measurement, three measurements in ocean-viewing mode, one “dark” measurement, three measurements in sun-viewing mode, and one “dark” measurement. It requires about 15 minutes to collect a complete data set (ocean, sun, optical zero), including deploying the instrument and logging ancillary data (wind speed, sea state, cloud cover, etc.).

The current protocol (K. Knobelspiesse, Pers. Comm.) is to set the MicroTops to internally record the highest of 20 sequential measurements, and repeat the measurement at least 15 times. This procedure will allow measurements made when the instrument was not pointed accurately at the sun to be filtered and removed during post-processing.

The Microtops sun photometer performs dark current measurements when it is first turned on. If the instrument’s temperature changes since this dark current measurement, the calculated aerosol optical thickness value can be incorrect. (Porter *et al*. 2000). Exposure to the sun for only a few minutes can have an effect, so the MicroTops should be turned off and on frequently. It is recommended that the MicroTops be shut off and on every ten seconds when making measurements, or after every five continuous measurements. Temperature variations should not be a problem for the SIMBAD, since the measurement protocol involves gathering dark current measurements before and after in situ measurements.

On several instances we have found condensation to be a problem when radiometers were stored in an air-conditioned room prior to making measurements in the humid marine atmosphere. Condensation may occur outside the SIMBAD radiometer, but can also occur inside the MicroTops (i.e. it is not always

possible to wipe it off). This problem can be avoided by storing the instrument at temperatures expected during measurement.

For the MicroTops sun photometer, the latitude, longitude and time can be set manually, or by connecting the GPS unit directly to the radiometer. Using either method, the time can be set to within one second of GMT. The latitude and longitude can also be stored in the MicroTops for measurements at fixed sites. The embedded GPS unit in the SIMBAD automatically acquires the geographic location and time at the beginning of each acquisition in the dark-current, sun-viewing, and ocean-viewing modes.

In order to maintain the quality of the aerosol optical thickness measurements, the procedures suggested above should be followed and the radiometers should be calibrated at least twice a year (more frequently if the calibration site is not stable – see Chapter 7). When possible, it is also advisable to make measurements with two types of instruments. This redundancy will help to determine if any problems are occurring.

Data Analysis

Several types of external data need to be gathered to before the conversion from instrument voltages to aerosol optical thickness values. The air mass, $\boldsymbol{M}$, must be calculated for the location and time of the measurement. $\boldsymbol{M}$ is a function of the solar zenith angle, and is determined as shown in equation 14.3. The optical depth values due to water vapor, ozone, trace gas and molecular scattering must all be determined and removed from the signal. Calculation of these values is described in detail in section 14.5.

Once AOT values have been calculated, points representing erroneous measurements must be removed. It can be difficult to point a hand held sun photometer at the sun accurately from a moving platform, like a boat at sea. Measurements that were taken when the instrument wasn't pointed at the sun will produce erroneous AOT values. A poorly pointed instrument mistakenly records less than the full direct solar radiance, so the computed AOT is much higher than reality. This is a significant problem with the Microtops II sun photometer, as its measurement cycle of about 3Hz is not always fast enough to avoid ship motion (Porter *et al*. 2000). This is less of a problem with the SIMBAD, as its measurement cycle is about 10Hz.

Erroneous measurements from the SIMBAD are removed manually by plotting the data and removing large values that are not part of a systematic trend. Poor pointing artifacts will appear as noise, while real aerosol variations will have a more systematic behavior when plotted as a short time series. This visual inspection and removal of large values is done for each channel, as erroneous measurement can be made in one channel that do not affect another channel. In this process, a final optical depth variability of 20% of the final average value or 0.025 may be permitted when the optical depths are below 0.08. This approach may slightly bias the data to lower values but it will remove the unrealistic larger values that would occur if the data were not filtered.

Two steps were taken to reduce the possibility of recording erroneous measurements with the Microtops. First, the measurement protocol was changed. Unlike the default protocol, which saves the average of the 4 largest (out of 32) voltage values, the new protocol logs the largest single value of 20 measurements. This has several advantages. The largest voltage is the only value recorded, so the chance of keeping a contaminated point is minimized. In addition, the total time needed to make this measurement is smaller than with the default protocol, so more measurements can be taken in a short period of time. After the experiment, a post-processing algorithm is applied. This algorithm calculates the coefficient of variation (standard deviation divided by the mean, or CoV) for each set of measurements in each band. If the CoV is above an arbitrary threshold of 0.05, the lowest voltage (highest AOT) value is removed, and the CoV recalculated. This is repeated until it is less than 0.05 or there are not enough points left to calculate the standard deviation. The passed points are those that passed this iterative process in all bands.

14.4 FAST-ROTATING SHADOW-BAND RADIOMETERS

An estimate of τ_a can be made from calibrated measurements of the solar beam irradiance, $E_N(\lambda)$, at normal incidence when there are no clouds in front of the solar disk. Two sun photometer designs are

commonly used to measure $E_N(\lambda)$: a narrow-beam detector mechanically pointed at the solar disk and a wide-field-of-view radiometer with a solar occulting apparatus. The first type of sun photometer requires careful angular positioning and can provide additional information about the forward scattering phase functions that help characterize the aerosol constituents. In contrast, a radiometer equipped with an occulting apparatus, known as a shadow-band radiometer, measures the diffuse and global (upper hemispheric) irradiance and computes $E_N(\lambda)$ from the difference between the two. The device gets its name from the hemispherical metal strip that rotates around the detector and blocks the direct solar beam to yield a signal that is from the sky only (after the effect of the arm is included).

The multiple wavelength rotating shadow-band radiometer (Harrison et al., 1994) uses independent interference-filter-photodiode detectors and an automated rotating shadow-band technique to make spatially resolved measurements at seven wavelength pass-bands. The uncertainty of the direct-normal spectral irradiance measurement made with this type of sun photometer is comparable with that made by narrow-beam tracking devices. A significant advantage of the shadow-band technique is that the global and diffuse irradiance measurements can be used to study the solar radiation budgets and the fractional cloud cover at the time of the measurement. The latter capability is particularly important for satellite validation studies. In the SIMBIOS context, direct solar and diffuse sky irradiances are critical terms for correcting down-looking in-water radiometers for self shading (Gordon and Ding 1995).

A marine version of the multiple-wavelength rotating shadow-band radiometer has been developed at the Brookhaven National Laboratory (BNL). The BNL marine version uses a slightly modified version of the detector used for continental applications. It has seven channels: one broadband silicon detector and six ten-nm-wide channels at 415, 500, 610, 660, 870, and 940 nm. Modifications to the detector circuitry used for continental applications are necessary, because the response time of the original circuitry is too slow for use on a moving ship. If the response time of the detector is too slow, wave action may cause the orientation of the radiometer to change appreciably during the time the shadow-band is occulting the sun. The rotation of the shadow-band itself must be sufficiently fast for the same reason. The marine version of the shadow-band radiometer is hereafter referred to as the BNL Fast-Rotating, Shadow-band Radiometer (FRSR). Implicit in this terminology is that the FRSR is a multi-filter or “spectral” radiometer.

The response of the silicon cell in the detector used for continental applications is faster than one millisecond, yet the internal preamplifiers have integrating low-noise amplifiers that slow the overall response. The response time of the detector is made faster for marine applications by reducing the magnitude of the low-pass filter capacitors. Laboratory tests do not show additional noise in the measurements as a result of this modification. The processing algorithms, which incorporate pitch, roll and heading measurements, are key to the instrument's ability to derive direct-normal beam irradiance without gimbals and a gyro-stabilized table.

Installation and Maintenance

The installation location of the instrument on a ship must be carefully selected. Ideally, FRSRs should be mounted in an exposed location as high as possible and free of nuisance shadows from other objects. This is often difficult. Radiation measurements on a ship always need to consider errors from the ubiquitous masts and antennas. A ship's communication antennas have highest vertical priority as do the running lights, and one must be careful of radar beams that can cause severe electronic noise. Once a suitable location has been found and the instrument mounted, the diffuser should be rinsed with distilled water and wiped with a moistened cloth at least once per day. The FRSR is typically mounted as a part of a portable radiation package that includes independent broadband solar and IR radiometers. The glass domes on these radiometers should be rinsed with distilled water and wiped with a moistened cloth.

Calibration is the most essential element of a radiation measurement program. A thorough and on-going calibration process is required before the FRSR can make accurate radiometric measurements at sea. To ensure accurate measurements, there are two important elements for FRSR measurement protocol: calibration of the instrument circuitry, which includes temperature stabilization of the detector during measurements, and determination of the extra-terrestrial constants. These elements are discussed in Chapter 7.

Data Analysis

The shadow-band radiometer must properly measure the global and diffuse irradiances from which the direct-beam solar irradiance is derived by the subtraction as

$$E_{\mathrm{sun}}(\lambda) = E_{\mathrm{s}}(\lambda) - E_{sky}(\lambda), \tag{14.5}$$

where $E_{sun}(\lambda)$ is the direct-beam solar incident irradiance projected onto a horizontal plane, $E_s(\lambda)$ is the global irradiance incident on the horizontal plane, and $E_{sky}(\lambda)$ is the diffuse incident irradiance from non-forward scattering. The global irradiance, $E_s(\lambda)$, is measured when the band is out of the field of view and the sensor is exposed to full sunlight. The irradiance normal to the incident solar beam is determined as

$$E_{\mathrm{N}}(\lambda) = E_{\mathrm{s}}(\lambda)\sec\theta_{\mathrm{o}}. \tag{14.6}$$

A correction for the amount of sky that is blocked by the occulting band is essential for an accurate measurement. An automatic correction for the shadowband is possible through measurement of ``edge'' irradiance as is done with the land-based shadow-band radiometers. The shadow irradiance, $E_{shadow}(\lambda)$, occurs when the sun is completely covered by the shadowband, but a portion of the diffuse irradiance is also blocked. The edge irradiance, $E_{edge}(\lambda)$, is measured when the band is just to one side of the solar disk and provides a good estimate of the global irradiance minus the portion of sky that is blocked by the shadowband at the time it blocks the solar disk. In practice, $E_{edge}(\lambda)$ is selected from two measurements taken when the shadow is on one side or the other of the diffuser. Generally an average is taken, but in some cases in the early morning or late evening only one of the edges is acceptable. It is easy to show that the fully corrected direct solar incident irradiance is

$$E_{\mathrm{sun}}(\lambda) = E_{\mathrm{edge}}(\lambda) - E_{\mathrm{shadow}}(\lambda). \tag{14.7}$$

With the fast-rotating technique, an advantage of using (14.7) to determine $E_{sun}(\lambda)$ is that the edge and shadow measurements are made in a very short time, which reduces noise significantly, especially on partly cloudy days. Also, if the electronics have a constant bias, the bias is removed by the subtraction. On a moving platform, some smoothing of the data is necessary. It was found that simple averages over a two-minute period (16 sweeps) would reduce the sampling uncertainty by a factor of approximately 4, and yield worst-case measurement uncertainties of about 5 $\mathrm{Wm^{-2}}$ for the global values and less than 1 $\mathrm{Wm^{-2}}$ for the shadow value. For perspective, two minutes is the approximate time for the sun to move by one diameter across the celestial sphere. A discussion and an example of the effectiveness of the two-minute averaging process are shown in Reynolds *et al.* (2000).

The shadow-band theory must be modified for a moving platform, when the radiometric collector head might not be oriented in a horizontal plane. Three measurement quantities for each channel are computed from the two-minute mean voltages: the global signal, υ'_G, the shadow signal, υ'_S, and the edge value, υ'_E. The primes indicate the measurement is referenced to the plane of the head, which can be different than a horizontal plane. The two global measurements, υ_{G1} and υ_{G2}, are combined to produce the best estimate of global voltage, υ'_G. The mean shadow voltage is υ'_S. The edge value is selected from the two-minute composite sweep using an objective algorithm that accounts shadow width dependence on solar zenith and relative azimuth angles. The objective selection of the edge voltage uses one or a mean of both edge measurements to get the best estimate of υ'_E. The voltage due to direct-beam irradiance falling onto the plane of the instrument is given by

$$\upsilon'_{\mathrm{H}} = \upsilon'_{\mathrm{E}} - \upsilon'_{\mathrm{S}}. \tag{14.8}$$

This equation automatically corrects for the sky that is blocked by the shadow-band and also removes any bias term in the calibration equation. An important point in (14.8) is that the right-hand quantities are measured in a few tenths of a second, while the shadow crosses the diffuser. In such a short time interval the ship attitude changes insignificantly and interference from moving clouds is minimized. The diffuse component of the irradiance signal is computed from

$$\upsilon'_{\mathrm{D}} = \upsilon'_{\mathrm{G}} - \upsilon'_{\mathrm{H}}. \tag{14.9}$$

As we have stated previously, υ'_D is relatively unaffected by small amounts of platform motion.

The exact azimuth and elevation of the solar beam relative to the head must be computed from the following variables measured externally:

$$\{\alpha_{\mathrm{h}},\theta_{\mathrm{h}}\} = f\left(\alpha_{\mathrm{S}},\phi_{\mathrm{P}},\phi_{\mathrm{R}},\alpha_{\mathrm{r}},\theta_{\mathrm{r}}\right), \tag{14.10}$$

where $\{\alpha_h,\theta_h\}$ are the solar azimuth angle and solar zenith angle relative to the plane of the head, α_s is the mean heading of the ship in true coordinates, ϕ_P is the ship mean pitch, and ϕ_R is the corresponding mean roll over the two-minute period. The relative solar azimuth and zenith angles in geographic coordinates, as seen by the observer, are α_r and θ_r. Equation (6) uses three two-dimensional coordinate transformations in heading, pitch, and roll to shift the solar beam vector to a coordinate system aligned with the FRSR head. The matrix transformation technique is well known and discussed in many textbooks on matrix algebra. Once α_h and θ_h are known, the calibration table can be consulted and an interpolated correction value, $\chi(\alpha_h,\theta_h)$, can be derived.

The direct beam intensity on a horizontal plane relative to the instrument, υ'_H, is converted to a direct-beam intensity into a plane normal to the solar beam using the relationship

$$\upsilon_{\mathrm{N}} = \frac{\upsilon'_{\mathrm{H}}}{\chi\left(\alpha_{\mathrm{h}},\theta_{\mathrm{h}}\right)\cos\theta_{\mathrm{h}}}. \tag{14.11}$$

The global and horizontal voltages are re-computed for the Earth frame of reference:

$$\upsilon_{\mathrm{H}} = \upsilon_{\mathrm{N}}\cos\theta_{\mathrm{r}}, \tag{14.12}$$

and

$$\upsilon_{\mathrm{G}} = \upsilon_{\mathrm{H}} + \upsilon_{\mathrm{D}}. \tag{14.13}$$

The calibration equation is used to compute E_s, E_{sky}, E_{sun}, and E_N from υ'_G, υ'_D, υ'_H, and υ'_N respectively. From these terms, the Beer-Lambert-Bouguer law [equation (14.1)] can be used for estimating the calibration constant or $\tau_a(\lambda)$.

Cloud filtering is the most important challenge for FRSR data processing. Because the FRSR operates autonomously, cloud observations are naturally part of the signal that must be processed to obtain τ. The cloud filter that is currently used is based on two steps: computing signal statistics over windows of periods of less than two hours and using these statistics to judge the quality of the observation under consideration. If the standard deviation of the observations in a two-hour moving window is less than 0.05, a subjectively defined threshold, and the observation at the center of the window is also less than 0.05, the central observation is accepted. The underpinning of this cloud filtering technique is that τ is relatively constant over a period of two hours, while the cloud signal is highly variable. This approach has proven relatively successful, although improvements in the filter are expected in the future.

14.5 SIMBIOS PROJECT AOT EXTRACTION PROTOCOLS

The SIMBIOS Project is concerned with ocean color satellite sensor intercomparison and merger for biological and interdisciplinary studies of the global oceans. Imagery from different ocean color sensors can now be processed by a single software package using the same algorithms, adjusted by different sensor spectral characteristics, and the same ancillary meteorological and environmental data. This capability enables cross-comparisons to be made between similar data products derived from different satellite sensors. Internally consistent cross-validation of these products may then be approached by integrating *in situ* measurements of ocean and atmospheric parameters. The objective of these analyses is to merge the data products from the different satellites to provide continuity of ocean color information over long temporal and large spatial scales. Atmospheric correction of satellite radiances and, in particular, estimation of aerosol effects on the upwelling radiance at the top of the atmosphere, is one of the most difficult aspects of satellite ocean color remote sensing. Analyses comparing aerosol properties obtained from *in situ* observations with those derived from satellite ocean color sensor data are essential elements in the validation of the atmospheric correction algorithms. The uncertainty sources and magnitudes of AOTs determined from *in situ* measurements are discussed in earlier sections of this chapter. When the *in situ*

measurements are matched against atmospheric properties derived using data from a satellite sensor, additional uncertainties result from the different viewing angles of the satellite and surface instruments, and from discrepancies in time between the satellite and *in situ* observations. In the case of the atmosphere, these uncertainties are considerable. The uniform calibration, measurement, data analysis and quality control protocols described in this chapter are designed to minimize these overall sources of uncertainty.

Extraction of in situ AOTs

The Project has recently implemented its own correction strategy for instrument voltages corresponding to AOTs. The approach ensures a uniform AOT processing for all instruments, making the AOTs comparable amongst the instruments and between instruments and satellite sensor AOTs derived by means of the atmospheric correction. Also, the method uses a consistent set of tuning variables, such as ancillary data, concurrently applied for the correction of satellite radiances. Therefore, some stages of the satellite and *in situ* data processing are identical, contributing to increasing confidence in the match-ups.

First, instrument-specific procedures are used to retrieve sun intensity measurements, V(λ), from individual sun photometers. In the case of the shadow-band radiometer, the data must be processed to determine direct beam intensity on a plane normal to the solar beam (Equation 14.10). The following processing is otherwise uniform for all instruments, taking account, however, of the distinct spectral wavelengths used by each sensor.

The Beer-Lambert-Bouguer law (equation 14.1) can be expanded as

$$V(\lambda) = V_{\mathrm{o}}(\lambda) * \left(\frac{d_{\mathrm{o}}}{d}\right)^2 e^{-M(\theta_{\mathrm{o}})\left(\tau_{\mathrm{R}}(\lambda)+\tau_{\mathrm{O_3}}(\lambda)+\tau_{\mathrm{a}}(\lambda)\right)}, \tag{14.14}$$

where τ_{R}, τ_{O3},and τ_{a} are the molecular (Rayleigh) and ozone and aerosol optical thickness, respectively, and the other terms have been previously defined. Equation (14.14) assumes that the signal, $V(\lambda)$, is measured when the instrument is pointing directly at the sun and that gaseous absorption is only due to ozone.

The earth-sun distance adjustment, $(d_0/d)^2$ and air mass, M, are calculated using equations 14.2 and 14.3, respectively. Currently, the same value of air mass M is used for Rayleigh, ozone, and aerosol factors.

The desired AOT τ_a is extracted from equation (14.14) by calculating all other variables, using known constants from references in Table 14.3, and measured ancillary data. The following estimations of earth and atmospheric parameters to obtain AOT coincide with the SeaWiFS satellite sensor correction, including the choice of meteorological and ozone ancillary data.

Rayleigh optical thickness is calculated using contemporary atmospheric pressure readings obtained from the daily global pressure maps provided by the National Centers for Environmental Prediction. The Rayleigh optical thickness is extracted as

$$\tau_{\mathrm{R}}(\lambda) = k_{\mathrm{Ray}}(\lambda) * e^{-\frac{A}{7998.9}} * \frac{P}{P_{\mathrm{o}}}, \tag{14.15}$$

where A is the altitude in m, P is the current atmospheric pressure in hPa, P_0 is the standard atmospheric pressure of 1013.25 hPa (Kasten and Young 1989), and. k_{Ray} is defined as

$$k_{\mathrm{Ray}}(\lambda) = 28773.597886\left\{e^{-8}\left[8342.13 + \frac{2406030}{130-\lambda^{-2}} + \frac{15997}{38.9-\lambda^{-2}}\right]\right\}^2 \lambda^4. \tag{14.16}$$

The ozone optical thickness is acquired from spatial and temporal interpolation of daily satellite global measurements of ozone amounts. Preferably, ozone data are determined from the Total Ozone Mapping Spectrometer (TOMS) data. If TOMS data are unavailable, ozone counts from the TIROS Operational Vertical Sounder (TOVS) are used. Finally, if TOVS data are missing, ozone climatology files are applied. The ozone optical thickness is calculated from the ozone amount, in *Dobson* units, using a scaling factor $k_{oz}(\lambda)$,

$$\tau_0(\lambda) = k_{oz}(\lambda) * \frac{Dobson}{1000}, \tag{14.17}$$

where $k_{oz}(\lambda)$ is the specific absorption coefficient (per *Dobson*) given below for the following spectral bands (Nicolet at al., 1981):

λ = (315, 340, 380, 400, 415, 440, 443, 490, 500, 560, 610, 660, 670, 675, 862, 870, 936, 1020 nm);

and

$k_{oz}(\lambda)$ = (1.35, 0, 0.00025, 0.00065, 0.00084, 0.0034, 0.00375, 0.02227, 0.0328, 0.10437, 0.12212, 0.05434, 0.04492, 0.0414, 0.00375, 0.0036, 0, 0).

REFERENCES

Bass, A.M. and R.J. Paur, 1984: The ultraviolet cross-section of ozone:1. *The measurements, in Atmospheric Ozone*, edited by C.S. Zerefos & A. Ghazi, pp. 606-610, Reidel, Dordrecht.

Bruegge, C.T., J.E. Conel, R. O. Green, J.S. Margolis, R.G. Holm, and G. Toon, 1992: Water vapor column abundance retrievals during FIFE. *J.Geophys. Res*., **97**(D19), 18759-18768.

Burcholtz, A., 1995: Rayleigh-scattering calculations for the terrestrial atmosphere, *Appl. Opt.*, **34**, 2765-2773.

Dubovik**,** O. and M.D.King,, 2000: A flexible inversion algorithm for retrieval of aerosol optical properties from Sun and sky radiance measurements, *J. Geophys. Res*., (submitted).

Dubovik**,** O., A.Smirnov, B.N.Holben, M.D.King, Y.J. Kaufman, T.F.Eck, and I.Slutsker, 2000: Accuracy assessments of aerosol optical properties retrieved from AERONET Sun and sky-radiance measurements, *J. Geophys. Res*., **105**, 9791-9806.

Edlen, B., 1966: The refractive Index of Air, *Meteorol*., **2**, 71-80.

Ehsani, A. R., J. A. Reagan, and W. H. Erxleben, 1998: Design and performance analysis of an automated 10-channel solar radiometer instrument, *J. Atmos. Ocean. Tech*., *15*, (in press).

Forgan, B.W., 1994: General method for calibrating Sun photometers, *Applied Optics*, **33**, 4841-4850.

Fougnie, B., R, Frouin, P. Lecomte, and P-Y. Deschamps, 1999: Reduction of skylight reflection effects in the above-water measurement of marine diffuse reflectance. *Applied Optics*, **38**, 3844-3856.

Gordon, H. R., J. W. Brown, and R. H. Evans, 1988: Exact Rayleigh scattering calculations for use with the Nimbus-7 coastal zone color scanner, *Applied Optics*, **27**, 862-871.

Gordon, H.R., and K. Ding, 1992: Self shading of in-water optical instruments. *Limnol. Oceanogr.*, **37**, 491--500.

Gordon, H. R. and T. Zhang, 1995: Columnar aerosol properties over oceans by combining surface and aircraft measurements: simulations. *Applied Optics*, **34**, 5552 – 5555.

Hansen, J. E., and L. D. Travis, 1974: Light scattering in planetary atmospheres. *Space Sci. Rev.*, **16**, 527-610.

Harrison, L. and J. Michalsky, 1994: Objective algorithms for the retrieval of optical depths from ground-based measurements, *Applied Optics*, **33** ,5126-5132.

Harrison, L., J. Michalsky, and J. Berndt, 1994: Automated multi-filter rotating shadow-band radiometer: an instrument for optical depth and radiation measurements, *Applied Optics*, **33,** 5126-5132.

Holben, B.N., T. F.Eck, I.Slutsker, D.Tanre, J.P.Buis, A.Setzer, E.Vermote, J.A.Reagan, Y.Kaufman, T.Nakajima, F.Lavenu, I.Jankowiak, and A.Smirnov 1998: AERONET - A federated instrument network and data archive for aerosol characterization, *Rem. Sens. Environ*., **66**, 1-16.

Iqbal., M., 1983: *An introduction to Solar Radiation*, Academic, San Diego, Calif., 390 pp.

Kasten F. and A. T. Young, 1989: Revised optical air mass tables an approximation formula, *Applied Optics*, **28**: 4735-4738.

Kaufman, Y.J., A. Gitelson, A. Karnieli, E. Ganor, R.S. Fraser, T. Nakajima, S. Mattoo, B.N. Holben, 1994: 'Size Distribution and Phase Function of Aerosol Particles Retrieved from Sky Brightness Measurements', *J. Geophys. Res.*, **99**, 10341-10356.

Kneizys, F.X., E.P. Shettle, L.W. Abreu, J.H. Chetwynd, G.P. Anderson, W.O. Gallery, J.E.A. Selby, and S.A. Clough, 1988: Users Guide to LOWTRAN 7, AFGL-TR-88-0177, (NTIS AD A206773), Air Force Geophysics Laboratory, Hanscom Air Force Base, Massachusetts.

Komhyr, W. D., R. D. Grass, and R. K. Leonard, 1989: Dobson Spectrophotometer 83: a standard for total ozone measurements, 1962-1987, *J. Geophys. Res*., **94,** 9847-9861.

Liu, Y. and K. J. Voss, 1997: Polarized radiance distribution measurements of skylight: II. experiment and data. *Applied Optics*, **36**,8753 - 8764.

London, J., R. D. Bojkov, S. Oltmans, and J. I. Kelley, 1976: Atlas of the global distribution of total ozone July 1957 - June 1967, *NCAR Technical Note 133+STR*, National Center for Atmospheric Research, Boulder, Colorado, 276 pp.

Michalsky, J. J., 1988: The astronomical almanac's algorithm for approximate solar position (1950 - 2050), *Solar Energy*, **40**, 227 - 235.

Morys, M., F.M. Mims III, and S.E. Anderson, 1998: Design, calibration and performance of MICROTOPS II hand-held ozonometer.

Nakajima, T., M. Tanaka and T. Yamauchi, 1983: Retrieval of the optical properties of aerosols from aureole and extinction data. *Applied Optics*, **22**, 2951-2959.

Nakajima, T., G. Tonna, R. Rao, P. Boi, Y. Kaufman, and B. Holben, 1996: Use of sky brightness measurements from ground for remote sensing of particulate polydispersions, *Applied Optics*, **35**, 2672-2686.

Nicolet M., 1981: The solar spectral irradiance and its action in the atmospheric photodissociation processes, Planet. *Space Sci*., **29**, 951-974.

Penndorf, R., 1957: Tables of the Refractive Index for Standard Air and the Rayleigh Scattering Coefficient for the Spectral Region Between 0.2 and 20.0 Microns and their Application to Atmospheric Opt., *J. Opt. Soc. Am*., **47,** 176-182.

Porter, J. N., M. Miller, C. Pietras, and C. Motell, 2000: Ship-based sun photometer measurements using MicroTops sun photometers, *J. Ocean. Atmos. Tech*. (in press).

Reagan, J.A., K.J. Thome, and B.M. Herman, 1992: A simple instrument and technique for measuring columnar water vapor via Near-IR differential solar transmission measurements. *IEEE Trans. Geosci. Remote Sensing*, **30**, 825-831.

Reynolds, R.M., M.A. Miller, and M.J. Bartholomew, 2000: Design, Operation, and Calibration of a Shipboard Fast-Rotating Shadow-band Spectral Radiometer, *Jour. Atmos. Ocean. Tech*., (accepted).

Ritter, J. M. and K. J. Voss, 2000: A new instrument to measure the solar aureole from an unstable platform. J. Atmos. Ocean. Tech., in press.

Schmid, B., C. Matzler, A. Heimo and N. Kampfer, 1997: Retrieval of Optical Depth and Particle Size Distribution of Tropospheric and Stratospheric Aerosols by Means of Sun Photometry, *IEEE Trans. on Geosci. and Rem Sens*., **15**, 172-182.

Schwindling, M., P.-Y. Deschamps, and R. Frouin. 1998: Verification of aerosol models for satellite ocean color remote sensing. *J. Geophys. Res.*, 24,919-24,935.

Shaw, G. E., 1983: Sun Photometry, *Bull. Amer. Meteor. Soc*., **64**, 4-11.

Shiobara, M., T. Hayasaka, T. Nakajima and M. Tanaka, 1991: Aerosol monitoring using a scanning spectral radiometer in Sendai, Japan. *J. Meteorol. Soc. of Japan*, **60**, 57-70.

Smirnov, A., B.N.Holben, T.F.Eck, O.Dubovik, and I.Slutsker, 2000: Cloud screening and quality control algorithms for the AERONET data base. *Rem. Sens. Environ*., (accepted).

Tanré, D., C. Devaux, M. Herman and R. Santer, 1988: Radiative properties of desert aerosols by optical ground-based measurements at solar wavelengths. *J. Geophys. Res*., **93**, 14223-14231.

Tanré, D., C. Deroo, P. Duhaut, M. Herman, J.-J. Morcrette, J. Perbos, and P.-Y. Deschamps, 1990: Description of a computer code to simulate the signal in the solar spectrum: the 5S code. *Int. J. Remote Sensing*, **11**, 659-668.

Young, A.T., 1980: Revised Depolarization Corrections for Atmospheric Extinction, *Applied Optics*, **19**, 3427-3428.

Vigroux, E., 1953: Contribution a l'etude experimentale de l'absorption de l'oxone, *Annales de Phys*., **8**, 709.

Volz, F.E., 1959: Photometer mit Selen-photoelement zurspektralen Messung der Sonnenstrahlung und zer Bestimmung der Wallenlangenabhangigkeit der Dunsttrubung. *Arch. Meteor. Geophys Bioklim*. **B10**, 100-131.

Voss, K. J. and Y. Liu, 1997: Polarized radiance distribution measurements of skylight: I. system description and characterization. *Applied Optics*, **36**, 6083-6094.

Voss, K. J., 1989: Electro-optic camera system for measurement of the underwater radiance distribution. *Optical Engineering*, **28**, 241-247.

Voss, K. J. and G. Zibordi, 1989: Radiometric and geometric calibration of a spectral electro-optic "fisheye' camera radiance distribution system. *J. Atmos. Ocean. Tech*.., **6**, 652-662.

Wang, M. and H. R. Gordon, 1993: Retrieval of the columnar aerosol phase function and single-scattering albedo from sky radiance over the ocean: simulations. *Applied Optics*, **32**,4598 – 4609.

Zhang, T. and H. R. Gordon, 1997a: Columnar aerosol properties over oceans by combining surface and aircraft measurements: sensitivity analysis. *Applied Optics***, 36**, 2650 – 2662.

Zhang, T. and H. R. Gordon, 1997b: Retrieval of elements of the columnar aerosol scattering phase matrix from polarized sky radiance over the ocean: simulations. *Applied Optics*, **36**,7948 – 7959.

Table 14.1: Measurement sequences of the CIMEL Sun/Sky scanning spectral radiometer.

	Spectral Range nm	**Target**	**No. Obs.**	**Obs. Interval**	**Application**
BASIC DIRECT SUN	340 to 1020	Sun	1 each λ	~ 8 sec. for. 8 λ	AOT, Pw, α
Triplet Observation	340 to 1020	Sun	Three direct sun	3 @ 30 sec. apart, 1 min total	AOT, Pw, α & cloud screening
Standard Measurement Sequence	340 to 1020	Sun	Variable: depends on day length	Ea. 15 min m=2 AM to m=2 PM	AOT, Pw, α
Langley	340 to 1020	Sun	16, am & PM between m 7 & 2	m=7 - 5, incr of.5 m m=5 - 2, incr. of.25	Langley, Cal., AOT, Pw, α
BASIC SKY	440 to 1020	Sky	1 each λ	none	Sky Radiance
Langley sky	440 to 1020	Sky	16 between m 7 & 2	m=7 - 5,.5; m=5- 2,.25	Stability of Lngly Plot
Almucantar	440 to 1020	Sky	72 (Table 2)	>8/day: m= 4, 3, 2, 1.7 hrly 9AM to 3PM	Size Dist. and P(θ), AOT, α
Polarization	870	Sky	42 (Table 2)	hourly m=3 AM to m=3 PM	Size Dist. and P(θ)
Principal Plane	440 to 1020	Sky	42 (Table 2)	hourly m=3 am to m=3 PM	Size Dist. and P(θ) AOT, α

Table 14.2: Almucantar and Principal Plane sequences for the standard and polarization instruments.

	Sun	**Sky (°)**
ALMUCANTAR Azimuth angle relative to sun	0°	6.0, 5.0, 4.5, 4.0, 3.5, 3.0, 2.5, 2.0, -2.0,-2.5, -3.0, -3.5, -4.0, -4.5, -5.0, -6.0, -8.0, -10.0, -12.0, -14.0, -16.0, -18.0, -20.0, -25.0, -30.0, -35.0, -40.0, -45.0, -50.0, -60.0, -70.0, -80.0, -90.0, -100.0, -110.0, -120.0, -130.0, -140.0, -160.0, -180.0 Duplicate above sequence for a complete counter clockwise rotation to –6
PRINCIPAL PLANE: Standard Scattering Angle from sun (negative is below the sun)	0°	-6.0, -5.0, -4.5, -4.0, -3.5, -3.0, -2.5, -2.0, 2.0, 2.5, 3.0, 3.5, 4.0, 4.5, 5.0, 6.0, 8.0, 10.0, 12.0, 14.0, 16.0, 18.0, 20.0, 25.0, 30.0, 35.0, 40.0, 45.0, 50.0, 60.0, 70.0, 80.0, 90.0, 100.0, 110.0, 120.0, 130.0, 140.0
PRINCIPAL PLANE: Polarization Scattering Angle from sun (negative is in the anti solar direction)	-	-85.0, -80.0, -75, -70, -65.0, -60.0, -55.0, -50.0, -45.0, -40.0, -35.0, -30.0, -25.0, -20.0, -15.0, -10.0, -5.0, 5.0, 10.0, 15.0, 20.0, 25.0, 30.0, 35.0, 40.0, 45.0, 50.0, 55.0, 60.0, 65.0, 70.0, 75.0, 80.0, 85.0

Table 14.3: Procedure of the AERONET Program

Variable, algorithm or correction	**Comments**	**References**
Basic Computations		
Rayleigh Optical Depth, τ_r refractive index of air depolarization factor	Input elevation in m	Penndorf, 1957 Edlen, 1966 Young, 1980 Burcholtz, 1995
Solar Zenith Angle, θo		Michalsky, 1988
Earth sun distance, d		Iqbal, 1983
Ozone amount, O_3	Table lookup by 5° lat. long.	London et al., 1976
Aerosol optical air mass, m_a		Kasten and Young, 1989
Rayleigh optical air mass, m_r		Kasten and Young, 1989
O_3optical air mass, m_o		Komhyr et al., 1989
Corrections		
Temperature, T	~0.25%/°C for 1020 nm specific for each inst.	Hamamatsu Inc. and Lab measurements
Water Vapor for 1020 AOT	from Pw retrieval, Lowtran	Kneizys et al, 1988
Rayleigh, all wavelengths	from elevation	
O_3 abs. coef. $\lambda > 350$ nm		Vigroux, 1953
O_3 abs. coef. $\lambda < 350$ nm		Bass and Paur, 1984
Time, t	CIMEL, UTC, DAPS time stamps, ±1 second	Refer to Homepage
Retrievals		
Spectral direct Sun AOT,Langley Plots	Beer's Law	Shaw, 1983
Pw: (a, k, Vo)	Modified Langley	Bruegge et al., 1992; Reagan et al., 1992
Size Dist., Phase function	From spectral sky radiance	Nakajima et al., 1983 Dubovik and King, 2000
Procedures		
Cloud Screening	Thresholds, λ AOT & t	Smirnov et al., 2000
Climatology, Direct Sun	AOT, Pw, Wavelength Exp.	Refer to Homepage
Climatology, Sky	Size Dist., Phase function, g	Refer to Homepage

Chapter 15

Determination of spectral absorption coefficients of particles, dissolved material and phytoplankton for discrete water samples

B. Greg Mitchell, Mati Kahru, John Wieland and Malgorzata Stramska
Scripps Institution of Oceanography, University of California San Diego, California

15.1 INTRODUCTION

The spectral absorption coefficient is one of the inherent optical properties that influence the reflectance of aquatic systems. The absorption coefficient $a(\lambda)$, in m^{-1}, at any point within a natural water body can be described in terms of the additive contribution of its components as

$$a(\lambda) = a_{\mathrm{w}}(\lambda) + a_{\mathrm{p}}(\lambda) + a_{\mathrm{g}}(\lambda),\ \mathrm{m}^{-1}, \tag{15.1}$$

where $a_{\mathrm{w}}(\lambda)$, $a_{\mathrm{p}}(\lambda)$ and $a_{\mathrm{g}}(\lambda)$ are the spectral absorption coefficients of water, particles, and soluble components, respectively. The spectral absorption coefficients of pure water adopted for the protocols are identified in Chapter 2, and combine the results of Pope and Fry (1997), Sogandares and Fry (1997), Fry (2000) and Smith and Baker (1981). The depth (z) dependence of the absorption coefficients is omitted for brevity. The particle absorption coefficient may be further decomposed as

$$a_{\mathrm{p}}(\lambda) = a_{\varphi}(\lambda) + a_{\mathrm{d}}(\lambda),\ \mathrm{m}^{-1}, \tag{15.2}$$

where $a_{\varphi}(\lambda)$ and $a_{\mathrm{d}}(\lambda)$ are the spectral absorption coefficients of phytoplankton, and de-pigmented particles, respectively. Laboratory methods are described for determining operational estimates of these fractions. It is conceptually possible to further separate $a_{\mathrm{d}}(\lambda)$ into absorption fractions due to de-pigmented organic and inorganic particles, but at present, there are no well established protocols for separately determining the absorption coefficient for inorganic particles.

To interpret aquatic spectral reflectance and better understand photochemical and photobiological processes in natural waters, it is essential to quantify the contributions of the individual constituents to the total absorption coefficients in the ultraviolet (UV) and visible region of the spectrum. The protocols presented here are based on the evolution, starting with articles by Kalle (1938) and Yentsch (1962), of methods for analyzing the absorption by soluble and particulate material in natural waters. Laboratory measurements and data analysis protocols are described for separating the total spectral absorption coefficient, $a(\lambda)$, into its components by spectrophotometric measurements of samples prepared from filtration of discrete water samples.

The spectral absorbance of the filters and filtrate from these samples, as measured in a spectrophotometer, are expressed in units of Optical Density (OD), defined as $OD(\lambda) = \mathrm{Log}_{10}\left[V_{\mathrm{o}}(\lambda)\right] - \mathrm{Log}_{10}\left[V_{\mathrm{t}}(\lambda)\right]$. $V_{\mathrm{o}}(\lambda)$ is the spectrometer response for spectral flux transmitted

through the reference material and $V_t(\lambda)$ is the response for spectral flux transmitted through the sample. For the methods presented here the reference is either a properly hydrated GF/F blank filter for particle absorption, or a clean quartz glass optical cuvette filled directly from a purified water source for soluble material absorption. Note that OD is a dimensionless quantity. The use of base-10 logarithms in this context is a carryover from common practice in chemical spectroscopy and is the typical output of commercial spectrophotometers routinely used for these methods. Therefore, it is necessary to convert the OD measurements described in this chapter to the base-e representation of absorbance, *i.e.* to multiply OD by 2.303, to conform to the convention used throughout the ocean optics protocols. In general, these protocols are written assuming that the instrument that is used directly computes the optical density of the sample relative to the appropriate reference sample.

There has been considerable research to develop robust protocols that provide the most accurate estimates of absorption for various material fractions in natural waters. NASA-sponsored workshops were held at Scripps Institution of Oceanography and Bigelow Laboratory for Ocean Sciences to review absorption protocols, evaluate instrumentation, and define areas of consensus as well as areas of uncertainty that warrant further research (Mitchell *et al.* 2000).

The most widely used approach for estimating absorption by particulate matter in water samples involves analysis of the particles concentrated on filters (Yentsch, 1957). Absorption of phytoplankton suspensions determined using procedures that capture most of the forward scattered light (Shibata, 1958) can be related to the absorption measured on the filters to make quantitative corrections for the pathlength amplification effect (β) caused by the highly scattering filter medium (Duntley, 1942; Butler, 1962). The pathlength amplification parameter was symbolized as β by Kiefer and SooHoo (1982) following the nomenclature of Butler (1962). This symbol should not to be confused with the volume scattering coefficient $\beta(\lambda,\Psi)$ used in other chapters of this Technical Memorandum.

Kiefer and SooHoo (1982) reported a constant to scale the red peak of chlorophyll absorption for natural particles retained on GF/C filters to the diffuse absorption coefficients determined on suspensions by Kiefer et al. (1979). The diffuse absorption coefficient is double the value of the volume absorption coefficient of interest here (Preisendorfer, 1976). Mitchell and Kiefer (1984, 1988a) made direct estimates of volume absorption coefficients for phytoplankton suspensions and absorbance on glass fiber filters with the same particles to develop empirical equations that relate the amplification factor to the glass fiber sample optical density. This procedure is the basis of most laboratory methods for determining particle absorption in water samples.

Field applications of these quantitative estimates of $a_p(\lambda)$ were reported by Mitchell and Kiefer (1984, 1988b) and Bricaud and Stramski (1990). More detailed empirical results to correct for pathlength amplification were reported by Mitchell (1990) for various filter types and diverse cultures coccoid cyanobacteria, nanochlrophytes, diatoms, chrysophytes and dinoflagellates with sizes ranging from 2 μm to 20 μm. Cleveland and Weidemann (1993) and Tassan and Ferrari (1995) found that the empirical relationships of Mitchell (1990) were consistent with similar types of phytoplankton, but Moore *et al.* (1995) reported large differences in the amplification factor for *Synechococcus sp*. (WH8103) and *Prochlorococcus marinus* that were about half the size of the smallest cells studied by Mitchell (1990). Similar results were obtained by Allali et al. (1997) for natural populations of the Equatorial Pacific dominated by picoplankton. For samples with substantial turbidity and scattering due to inorganic matter (coastal, shelf, coccolithophore blooms), methods to correct for resulting artifacts have been described by Tassan and Ferrari (1995a, 1995b). Table 15.1 provides a summary of various published results for pathlength amplification factors.

Separation of the particle fraction into phytoplankton and other components is of considerable ecological and biogeochemical interest. Early efforts to separate absorbing components for natural particles included treatment with organic solvents, UV radiation, and potassium permanganate (references can be found in Shifrin, 1988, and Bricaud and Stramski, 1990). The most widely used chemical method is based on methanol extraction (Kishino *et al.* 1985, 1986). A recent method consists of bleaching the phytoplankton pigments by sodium hypochlorite (Tassan and Ferrari, 1995a; Ferrari and Tassan, 1999).

Spectral fluorescence methods to estimate the fraction of photosynthetically active absorption, if separate total particulate absorption has been determined, have been reported by Sosik and Mitchell, (1995).

Soluble absorption observations were described by Bricaud et al. (1981) for diverse ocean environments, including oligotrophic and eutrophic regions. Other field reports can be found in the references listed in more recent articles (Carder *et al.*, 1989a, 1989b; Blough *et al.*, 1993; Vodacek *et al.*, 1996; Hoge *et al.*, 1993; Nelson *et al.*, 1998; D'Sa et al., 1999). Spectrophotometric measurement of absorption by dissolved materials is straightforward, but has limits due to the very small signal for short pathlengths routinely employed (usually 10 cm), and to difficulties in maintaining quality control of purified water used as a reference.

This chapter defines protocols for the operational determinations of absorption coefficients for particulate and soluble matter in water samples. Methods are specified for separating particulate and soluble material by filtration, partitioning total particulate absorption into contributions by phytoplankton and de-pigmented particles (detritus), and corrections for pathlength amplification due to semi-diffuse transmittance of the filters. Recommendations are made based on widely accepted methods and processing procedures. NASA-sponsored workshops have confirmed various aspects of previously reported methods (Mitchell *et al*. 2000).

15.2 SAMPLE ACQUISITION

Water samples should be taken using Niskin (or similar) bottles at the site of, and simultaneously with, the surface in-water optical measurements, and at depth increments sufficient to resolve variability within at least the top optical depth. When possible, samples should be acquired at several depths distributed throughout the upper 300m of the water column (or in turbid water, up to seven diffuse attenuation depths for PAR irradiance, $\ln(E(0)/E(z))=7$), to provide a basis for relating the spectroscopic measurements of absorption to *in situ* profile measurements. Samples should be drawn immediately from the *in situ* sampling bottles into clean sampling bottles using clean silicon rubber or Tygon tubing or by directly filling the sample bottles from the Niskin bottle spigot. If Niskin bottles will not be sampled immediately, precautions must be taken to ensure large particles that settle are re-suspended. This can be done by transferring all water from the Niskin to a bottle or carboy larger than the total volume of the Niskin so that the entire water sample can be mixed (invert bottle numerous times to mix by turbulence), or by draining a small amount of water from the Niskin and manually inverting the entire Niskin prior to sub-sampling. Sample bottles should be kept cool (ideally near *in situ* temperatures), and dark prior to sample preparations. Preparations should be completed as soon as possible after sampling, but no later than several hours after the sample was acquired.

15.3 SPECTROPHOTOMETER CHARACTERISTICS AND CALIBRATION

A spectrophotometer used for absorption measurements following the protocols presented in this chapter must meet the following minimum performance specifications:

1. The unit's monochromator, or spectrograph, must yield a Full-Width at Half-Maximum (FWHM) bandwidth ≤ 4 nm. A larger FWHM bandwidth will not adequately resolve the red chlorophyll *a* absorption band.
2. The instrument's baseline spectrum characteristics, specified below, must be maintained over the range from 300 nm to 850 nm for measuring absorption by particles concentrated on filters, and from 250 nm to 850 nm for measuring absorption by dissolved materials.
3. For measuring absorption by particles concentrated on filters, baseline noise must be <0.01 OD, and noise <0.005 OD is strongly recommended.
4. For measuring absorption by dissolved materials, baseline noise must be <0.001 OD units, and noise <0.0005 OD is strongly recommended.

5. The instrument's baseline spectrum must be relatively flat over the wavelength range of interest and its shape and magnitude must be stable over time. Any tendencies for the spectral shape and magnitude of an instrument's baseline to drift must be well-behaved and slow enough that the rate of baseline drift may be characterized with an uncertainty less than the noise levels specified above. It is recommended to check the instrument baseline at intervals of 1 hr to 2 hr during an extended series of measurements.

Other desirable, but not absolutely essential, spectrophotometer features are variable slit width (to allow reducing the FWHM spectral resolution, when desired), automatic baseline corrections (the adequacy of which must nevertheless be verified), and automatic spectral calibration during instrument warm-up (using mercury emission lines supplied by an internal lamp source).

The spectral accuracy of the spectrometer should be verified by scanning a holmium oxide filter, with reference to an air-to-air baseline. This spectral calibration should be repeated each time the instrument is turned on, and at the conclusion of a series of measurements. Alternatively, a spectrophotometer's spectral characteristics may be calibrated using an internal line source (*e.g.* a mercury lamp), if the instrument is so equipped, but independent checks with the holmium oxide filter are also strongly advised. A set of absorbance reference filter standards, of known OD, must be used to calibrate a spectrophotometer's responses over the range of OD associated with the samples to be measured. This calibration, together with instrument baseline spectrum determinations, should be repeated at intervals necessary to characterize (within the noise tolerances given above) any measurable drifts in the instrument baseline and/or OD response. Unless the investigator can confirm the stability of the instrument that is used, these calibration procedures should be repeated each time the spectrophotometer is turned on. As a minimum they should be performed at any time there is a change of lamp source, blocking filter, or other instrument setup characteristic that affects the optical response and on a regular basis during routine work.

The present version of these protocols is written assuming the use of a commercial dual-beam spectrophotometer, with the sample and reference targets illuminated by the collimated output of a grating monochromator. The protocols also apply, with minimal modifications, to measurements using a single-beam monochromator or otherwise similar optical configuration. Mitchell *et al*. (2000) report comparisons between OD measurements of a common set of GF/F filtered particle samples using several spectrophotometers of these types, as well as spectrophotometers based on very different optical configurations. For a diatom culture measured during the Scripps workshop, several commercial dual beam spectrophotometers estimated sample filter OD spectra consistently within 5 % (Figure 15.1). Some of the differently configured instruments were within 10 % of the selected reference dual-beam instrument but in some cases had limited spectral range either in the UV or the near-infrared, or both (data not shown). The largest divergence was found for a grating spectrograph instrument that illuminates the filter with diffuse white light (Figure 15.1). This unit yielded OD values that were significantly higher than, albeit linearly related to (with a slope of approximately 0.7), the OD measurements made with conventional dual beam spectrophotometers (Mitchell *et al*. 2000). This result indicates that the pathlength amplification (β factor) associated with this instrument is significantly different from previously published values (Table 15.1), which were derived using conventional dual beam spectrophotometers. An investigator using this type of spectrophotometer, or another design with yet a different optical configuration, must either compare filter OD spectra measurements to reference measurements on the same filters with a "conventional" spectrophotometer to derive an OD scaling function, or otherwise determine pathlength amplification factors for the instrument configuration, using methods discussed in Mitchell *et al*. (2000) and references cited therein.

15.4 PARTICLE ABSORPTION: SAMPLE FILTER PREPARATION AND ANALYSIS

The procedures described in this section are recommended for determining the spectral absorption coefficients of particles in discrete samples of natural waters. These laboratory measurements are complementary to methods for measuring *in situ* profiles of absorption, as described in Chapters 4 and 9 of this document, and provide additional information on the partition of particle absorption by phytoplankton and other particles. Water samples are filtered and absorbance spectra of the filter, $OD_{\mathrm{fp}}(\lambda)$, are estimated

for the retained particles using a laboratory spectrophotometer. After measurement, the sample filters are soaked in chemical solvents to extract, or bleach, phytoplankton pigments (Kishino et al., 1985; Tassan and Ferrari 1995a) then rinsed to remove the chemicals and pigments from the material retained on the filter. The $OD_{\mathrm{fd}}(\lambda)$ spectrum of the filter is then determined in the spectrophotometer to obtain the absorption component of the de-pigmented particles, which are sometimes referred to as detritus or tripton. Depending on the method used to de-pigment the samples, this fraction also includes bleached cells and phycobilipigments that are not extractable in methanol and also inorganic minerals that may be important absorbers in some water samples. The raw $OD_{\mathrm{fp}}(\lambda)$ and $OD_{\mathrm{fd}}(\lambda)$ data are used to calculate total particulate and de-pigmented absorption coefficients $a_{\mathrm{p}}(\lambda)$ and $a_{\mathrm{d}}(\lambda)$, respectively. The absorption coefficient of phytoplankton, $a_{\phi}(\lambda)$, is then calculated as the difference $a_{\mathrm{p}}(\lambda) - a_{\mathrm{d}}(\lambda)$.

Filtration

The Whatman GF/F™ filter (which is binder-free and combustible, with a nominal pore size of 0.7 µm) is recommended for particle absorption sampling. This type of filter is also recommended by (JGOFS 1991) for various particulate and pigment analyses. Some authors have reported that particulate material less than 0.7 µm in size will not be retained by the GF/F filter, and that this fraction may contain up to 10 % or 15 % of the phytoplankton biomass as measured by chlorophyll concentration. Chavez *et al*. (1995), however, found no statistical difference between GF/F and 0.2 µm filters for chlorophyll and productivity measurements. The absorption of particles having diameters between 0.22 µm and 0.7 µm may be selectively determined by filtering the GF/F filtrate again through a 0.22 µm Millipore cellulose acetate membrane filter, and measuring its absorbance with a spectrophotometer (Ferrari and Tassan, 1996). Note that Mitchell (1990) reported pathlength amplification factors for cellulose acetate filters that are substantially different than those for GF/F filters and also described the relative difficulty of keeping cellulose acetate filters properly hydrated.

The optical transparency of the GF/F filter relative to air decreases significantly below 380 nm but many spectrophotometers can still make optical density determinations to 300 nm with these filters. The transparency of the filter also increases with hydration; so all samples must be fully - but not excessively - hydrated for proper performance of analytical procedures and accurate optical corrections. Pre-soaking GF/F filters 1 to 2 hrs before use can lead to less variability between individual filters (Bricaud and Stramski 1990). For oceanic water samples, seawater filtered through a 0.2 µm filter should be used to hydrate the filters. Freshly filtered seawater should be used since water that is left standing in clear containers may grow considerable amounts of algae over relatively short periods of time if there are any nutrients in the filtered seawater. For fresh inland water samples, purified fresh water may be used.

Glass fiber, cellulose acetate, and other strongly diffusing filters have large scattering coefficients, which increase the optical path length of photons in the measurement beam. Filtration volume V_f should be adjusted so that the optical densities of the filter samples, relative to the blank filter satisfy the criteria that $0.05 < OD_{\mathrm{fp}}(675) \leq 0.25$ and $OD_{\mathrm{fp}}(440) \leq 0.4$ OD (Mitchell 1990). Optical density spectra of the sample filters should be measured as soon as possible following filtration, because pigment decomposition may occur (Stramski 1990). If filters must be stored, immediately place the unfolded filters into flat tissue containers designed for liquid nitrogen storage. Liquid nitrogen storage is recommended because alternative freezing methods were shown to have more artifacts in comparison tests (Sosik, 1999).

a. Sample Filter Preparation

- Collect water samples, and maintain them in the dark at, or near, *in situ* water temperature.
- Prepare 0.2 µm filtered seawater (FSW) in sufficient volume for hydrating sample and blank filters.
- Set up and maintain the filter apparatus in dim light to minimize photodegradation of the samples.
- For each sample, place a GF/F filter onto the filtration rig. Also prepare two blank GF/F filters by soaking them in ~25 ml of 0.2 µm filtered water while mounted on the filtration funnel (with valves closed) during the sample filtration.

- Filter the samples on GF/F filters under low vacuum (~125 mm Hg).
- Filter a sufficient volume of water V_f to yield sample optical density relative to the blank filter in the range specified above. For field samples collected in the upper 100-150 m and filtered onto 25 mm GF/F filters, V_f is typically in the range 0.5 L to 5 L, depending on the *in situ* density concentration of particles.
- Do not let the preparations run dry during filtration. Turn off the vacuum to each sample as it completes filtering. Immediately place samples on a drop of 0.2 µm FSW in the appropriate container, depending on how they will be stored.
- Record the filter and filtration funnel type, the diameter D_f of the area on the filter that contains the concentrated particles, and the volume of water filtered V_f.
- Measure the absorption spectra in a spectrophotometer, or store the filters in liquid nitrogen, as soon as possible.

b. Sample Filter Storage

- If the filter samples will be analyzed immediately, store each filter in a labeled petri dish (e.g. Gelman™ snap-top dishes). Ensure proper hydration of the sample by placing the GF/F filter on a small drop of 0.2 µm FSW. Store each filter sample in the dark and refrigerate it (~4 deg. C) until it is to be measured in the spectrophotometer.
- If the spectrophotometric measurements will be delayed more than 24 hours following sample filtration, the filter samples should be prepared for liquid nitrogen storage. Samples should be stored in containers that allow the filter to remain flat, and which are specifically designed for immersion in liquid nitrogen (e.g. Fisher Histoprep™ tissue capsules). One pair of blank filters should also be prepared each day for use as the reference blank for samples collected that day. Samples may be stored in liquid nitrogen for extended periods, but it is strongly recommended to analyze them as soon as possible.
- Non-pressurized liquid nitrogen dewars generally retain liquid nitrogen for 2-4 weeks. Pressurized liquid nitrogen dewars can be rented at low cost for extended cruises (4-5 weeks) so that the sample dewars may be replenished and kept full. Care must be taken at sea, and in return shipping, to ensure that the samples are properly frozen. Samples should be shipped in liquid nitrogen dry shippers, which will maintain proper temperatures for 2 to 3 weeks, if they are properly charged and in good condition.
- Air transport of liquid nitrogen dry shippers is approved under International Air Transportation Agreement (IATA 41st Edition Section A800; US Federal Aviation Administration Dangerous Good Bulletin DGAB-98-03; August 25, 1998). That approval notwithstanding, many investigators have experienced difficulties in clearing customs, and in transport of liquid nitrogen dry shippers via commercial airfreight, or as checked baggage. The investigator should contact the carriers in advance and provide the IATA approval and FAA bulletins pertaining to liquid nitrogen dry shipper transport. If the dry shipper is to be transported as checked baggage, advanced coordination with the airline is strongly recommended to avoid confiscation of samples and delays in return shipment. When samples are shipped as checked baggage or freight, the IATA memo, DOT memo, and manufacturer's certificate should be affixed to the dry shipper to minimize potential delays.
- Temporary storage of filter samples on dry ice can be considered during transport. But maximum duration of dry ice in insulated shipping boxes is several days, so the use of liquid nitrogen dry shippers is strongly recommended.

Determination of spectral optical density of sample filters

After preparation, the optical density spectrum of each sample filter is measured using a laboratory spectrophotometer. The performance characteristics and calibration requirements of the spectrophotometer used for these measurements are described above in Section 15.3.

a. Reference Blank Spectra

With a dual beam spectrophotometer, two reference filter blanks saturated with FSW are used to measure the reference spectrum, and one is left in the reference beam during sample measurements. For typical single beam instruments, generally the reference is scanned, and then samples are placed into the beam and scanned. Most modern spectrophotometers, whether single or double beam, automatically store the instrument's reference spectrum and recorded sample spectra are automatically corrected to yield $OD_{\mathrm{fp}}(\lambda)$ relative to the reference blank filter. A new instrument reference baseline scan should be measured each time the spectrophotometer is powered up, and whenever its configuration has been changed. The baseline should also be checked regularly (every 1 hr to 2 hr) during extended periods of analysis. Frequency of baseline verification will depend on the performance and stability of each instrument and should be determined by the investigator prior to executing routine work. Uncorrected baseline drift, and changes in sorting filters or lamp source can cause systematic measurement anomalies. Wavelength accuracy and measurement precision should also be checked during the analyses (Sect. 15.3 above).

b. Spectrophotometric Measurement Procedure

- Warm up the spectrophotometer for 30 minutes.
- Measure the initial instrument baseline and wavelength calibration.
- If using frozen samples, remove the filters from the storage container and place them in petri dishes on FSW to ensure hydration. Allow the samples to thaw for approximately 5 min and then refrigerate them in the dark until each filter is ready for analysis.
- An instrument-specific sample-mounting device is recommended to hold filters against a quartz glass mounting plate. These mounts should be secure when placed in the sample compartment and hold the sample perpendicular to the illumination beam so only the filter and the quartz plate are in the beam. Usually, these mounts must be custom fabricated specifically for each different instrument.
- Clean the quartz faceplates of the mounting device with purified water and detergent if needed. Rinse them with purified water and ethanol, and dry them thoroughly using lint-free laboratory tissues.
- Set the appropriate instrument parameters according to the manufacturer's instructions.
- Mount two pre-soaked and water saturated blank filters (one for the sample beam, and one for the reference beam).
- To test for proper filter hydration, confirm that there is a drop of FSW left on the mounting plate when the filter is lifted. With the filter on the mounting plate there should be a slight sheen on the top surface of the filter, and a very narrow (~1 mm) border of water around the edges of the filter. Be careful not to use too much water, or the sample may wash away.
- Examine the back of the filter on the mounting plate to be sure that no bubbles are trapped between the filter and the quartz glass plate on the sample holder. There should be a uniform layer of water between the filter and quartz glass mounting plate. If bubbles are present, which will be obvious, pick up the filter with forceps, and replace it on the plate with a slight dragging motion across a drop of filtered seawater. Re-inspect the back of the filter and repeat the foregoing procedure until no bubbles are present. Adjust the amount of FSW as necessary to ensure proper hydration.

- Alternative mounts that expose both sides of the filter to air may be used to avoid bubbles altogether. Sample hydration is more difficult to maintain when using this type of filter mount so the investigator must develop a satisfactory procedure to ensure proper hydration of sample and reference.
- Run the instrument baseline correction using the two blanks. For most commercial units, this baseline will be automatically used as the reference to calculate $OD_{\mathrm{fp}}(\lambda)$. Immediately after the baseline correction is finished, and without touching the blank filters, run the two blanks as a sample scan to confirm that baseline performance is within acceptable tolerance over the spectral range of determination (Sect. 15.3 above). This spectrum should be flat spectrally. Baseline noise less than $\pm\ 0.005\,OD$ is recommended. Save this scan for confirmation of instrument performance. If a spectrally flat baseline cannot be achieved over the spectral range of interest, the stored baseline must be subtracted from subsequent measurements of sample filter $OD_{\mathrm{fp}}(\lambda)$.
- If using a single beam instrument, or instruments run in the single beam mode the blank is not kept in the instrument so one does not need to rehydrate the blank reference filter regularly. Most modern single beam spectrophotometers will also automatically use the blank reference stored in memory for estimates of $OD_{\mathrm{fp}}(\lambda)$.
- Remove the blank filter from the quartz glass sample mount in the measurement beam, and replace it with a sample filter, ensuring proper hydration of the sample (see above). Measure the sample $OD_{\mathrm{fp}}(\lambda)$ spectrum, save it in a digital file, and record all relevant information.
- The blank reference filter will dry out over time, and must be hydrated regularly. If absorption signal deviates significantly from zero (more than 0.02 OD) in the infrared (750-800 nm), this often indicates a dry reference or sample filter. If using a quartz plate, check the reference filter after every 5-6 scans, and hydrate as needed. If the filters are mounted in air, hydrate the blank before every scan.

Sample Filter Preparation for De-pigmented Particle Absorption

After preparing an $a_{\mathrm{p}}(\lambda)$ filter sample and determining its $OD_{\mathrm{fp}}(\lambda)$ spectrum on the spectrophotometer, the sample should be processed to remove its pigments and determine $a_{\mathrm{d}}(\lambda)$. The shape of the $a_{\mathrm{d}}(\lambda)$ spectrum usually decreases monotonically with wavelength, following exponential form that is flatter than the shape of the soluble absorption spectrum. Since the goal is generally to get an estimate of phytoplankton absorption, if there is a residual chlorophyll *a* absorption peak in the red near 675 nm, the extraction process should be repeated to remove it. Variations of this method include use of hot or boiling methanol and varying extraction times. Use of hot methanol has risks due to flammability, and volatility. If this process is used, extra precautions must be taken.

Bleaching of the organic pigments can also be accomplished for situations with difficult to extract pigments including phycobilins or other chemically polar pigments that do not extract well in methanol. Pigment extraction in a chemical solvent, such as methanol, is a fundamentally different chemical process than bleaching the pigments using sodium hypochlorite (NaClO). Bleaching involves placing a small amount of 0.1 % active chlorine solution onto the filter, then rinsing it off with FSW. The NaClO oxidizes the pigment molecules, making their light absorption negligible. FSW rinses then remove the excess NaClO, which absorbs negligibly at wavelengths >400 nm, but absorbs strongly at shorter wavelengths. The bleaching method of pigment removal has been shown to be effective in situations where methanol cannot be used, as on cellulose membranes such as the 0.22 µm Millipore filter, or when phycobilins are present (Tassan and Ferrari 1995a; Mitchell *et al*. 2000). This procedure can also be adapted for use with particulate suspensions.

Neither methanol extraction, nor NaClO oxidation, provides an ideal means of separating particulate absorption into ‘algal’ and ‘detrital’ components. In each case, the action of the chemical agent is not well

understood, and in many situations the two methods will yield very different results. The decision to apply either the bleaching, or methanol extraction, method will depend on the situation. For example, in inland waters where either cyanobacteria, or chlorophytes, are dominant, the bleaching technique is preferred, because of the presence of phycobilins and of extraction resistant algae (e.g. Porra 1990). In coastal oceanic waters, on the other hand, the methanol technique is preferred, because the results will be comparable to previously published results and there is no particular advantage to using bleach. In open-ocean samples (e.g. the Sargasso Sea), however, absorption by phycobilins is small, but present in some particulate absorption samples and in methanol-extracted filters (N.B. Nelson unpublished data). The methanol technique will provide results which are comparable to earlier studies, but with errors due to incomplete extraction and wavelength shifts in the phycobilin absorption bands.

a. Methanol Extraction method

- Replace the sample and blank filters on the filtration system. Treat blank filters exactly as if they were sample filters.
- Add 5 mL to 10 mL of 100 % methanol to each filter by gently pouring it down the sides of the filter funnel to minimize resuspension of the sample particles, and let stand for 1 min.
- Filter the methanol through the sample, turn off the vacuum, close the valves and add 10 - 15 mL of methanol.
- Allow the sample to stand in methanol for approximately 1 hr. Do not allow the filter to go dry during the extraction period. Time of extraction will vary depending on the filter load and phytoplankton species composition. Place aluminum foil over the filtration cups to minimize contamination during extraction.
- After extraction is complete, turn on the vacuum and draw the methanol and dissolved pigments through the filter. Rinse the sides of the filter tower twice with small amounts of methanol. Finally, rinse the sides of the filter tower three times with ~20 mL of 0.2 μm FSW. Also rinse the blanks with FSW after methanol extraction to minimize filter dehydration during spectrophotometric analysis.
- Pigment extraction is complete when the 675 nm chlorophyll *a* absorption peak is not present in the $OD_{\mathrm{fd}}(\lambda)$ spectrum.
- Successive, short extractions of 10 minutes can sometimes improve the pigment extraction.
- Phycobilins, and some eukaryotic pigments, will not be extracted efficiently by methanol.

b. Sodium Hypochlorite oxidation method

- Prepare NaClO solution:
- For freshwater samples: 0.1 % active chlorine in purified water (e.g. Milli-Q water).
- For marine samples: 0.1 % active chlorine in purified water containing 60 gl^{-1} Na_2SO_4, to match osmotic pressure of sample cells.
- The volume of 0.1% active chlorine solution needed to bleach pigments from a filter sample has been empirically shown to be approximately $3OD_{\mathrm{fp}}(440)$ mL .
- Place the sample, particle side up, on the filtration system (closed valves).
- Gently pour the solution down the sides of the filter funnel.
- Let the solution act for 5 min to 10 min, adding solution as necessary to compensate for loss through the filter.
- Cover the filtration cup with aluminum foil to prevent contamination during bleaching.

- Rinse the sample by gentle filtration of 50 mL of water (either fresh water or FSW, depending on sample source).
- Complete bleaching of the pigments is indicated by the absence of a 675 nm peak, together with a concave shape near 440 nm, in the $OD_{\mathrm{fd}}(\lambda)$ spectrum of the bleached filter. If evidence of residual pigment absorption persists, repeat the NaClO oxidation treatment, as indicated above.

Spectrophotometric Measurement of De-pigmented Optical Density Spectra

- The $OD_{\mathrm{fd}}(\lambda)$ spectrum of the de-pigmented samples should be measured in the spectrophotometer, as described above for $OD_{\mathrm{fp}}(\lambda)$.
- Note that methanol-extracted sample and blank filters will tend to dry out quickly if the methanol is not thoroughly rinsed from the filters prior to spectrophotometric measurements.
- NaClO oxidized sample and reference filters must be thoroughly rinsed with FSW (or fresh water for inland water samples) to extend the spectral range below 400 nm.

15.5 SOLUBLE ABSORPTION SAMPLE PREPARATION AND ANALYSIS

The measurement methods described in this section are used to determine $a_{\mathrm{g}}(\lambda)$, the spectral absorption coefficient spectrum of gelbstoff, often referred to as dissolved organic matter (CDOM). Water samples are collected and particulate material is removed by filtration. The absorption of the filtrate is measured, relative to purified water, using a spectrophotometer. All equipment utilized to prepare soluble absorption samples must minimize contamination by organic, or otherwise colored, material. Samples must be protected from photo-degradation during preparation and measurements. Plastic or glass filtration apparatus may be used, provided that the units are equipped with mesh filter supports made either of stainless steel or plastic, and not with ground glass frits. Glass frits tend to become clogged over time, and may cause uneven distribution on the filter, reduce the rate of filtration and may contaminate the sample filtrate.

Membrane filters with 0.2 µm pore size (*e.g.*, Nuclepore™ polycarbonate filters) are recommended for this procedure. The membrane filters should be pre-soaked in 10% HCl, rinsed with 75-100 mL of freshly purified water, and rinsed again with a 75 – 100 mL of the sample before it is used. Tests with purified water have shown that all filters leach contamination that resembles soluble absorption (data not shown). Using polycarbonate membrane filters, an acid soak, pure water rinse and sample rinse minimizes this contamination. Still, we have found the sample preparation procedure increases the apparent absorption spectra of purified water that is prepared as though it were a sample when referenced to purified water drawn directly into the measuring cuvette from the pure water system. Therefore correction for this sample preparation blank is recommended.

Glass fiber filters should be avoided if possible because they have been shown to cause rather severe contamination of the filtrate in tests using purified water. For samples collected from very turbid waters, glass fiber filters have routinely been used as a pre-filter to minimize clogging of the final filtration with a membrane filter (Kowalczuk, 1999). In such cases the investigator must develop a procedure to rinse the glass fiber filter to ensure that the contamination from this method is minimized. Since situations requiring pre-filtration often coincide with large soluble absorption coefficients, the effects may be easily corrected but it is the responsibility of the investigator to demonstrate this. Careful assessment of the contamination of any method, and proper corrections must be carried out and reported.

Previously we recommended the use of amber-colored borosilicate glass bottles (*e.g.* Qorpak™ bottles), that screen ambient light, for sample preparation and to store laboratory prepared standard water. However, recent work (details not shown) indicate that the amber bottles may leach some colored material into the purified standard water that is prepared before cruises and used to assess the quality of purified water prepared at sea. Therefore we now recommend use of clear borosilicate Qorpak™ bottles (or

equivalent) for sample preparations and for the preparation of the standard reference water. Prior to each experiment, all filtration apparatus and storage bottles should be thoroughly cleaned.

Purified water for soluble absorption measurements

Purified water freshly drawn from a water purification system, such as the Millipore Milli-Q, Millipore Alpha-Q, and Barnstead Nanopure units, or their equivalent, is strongly recommended for use at sea in preparing pure water for absorption reference, blanks and for equipment rinses specified in these protocols. Mitchell et al. (2000) compared the water-to-air baseline reference of purified water prepared with these three water purification systems. All three systems provided similar results in baseline tests relative to air at wavelengths between 300 nm and 900 nm, while small differences were found below 300 nm. It is also recommended to prepare a set of standard purified water samples prior to a field deployment as a reference to check daily for pure-water system degradation, *e.g*. due to poor quality feed water. Even though bottled purified water standards have been found to deteriorate slightly over time, especially from 250 nm to 325 nm, they provide invaluable quality control and an alternative source of reference water in situations when the purification system performance degrades dramatically.

Pre-cruise preparations

- Sample bottles (clear borosilicate Qorpak™ with polyethylene lined caps) used to collect sample filtrate or to store standard reference water need to be thoroughly cleaned in advance to remove any potential organic contaminants. Sequential soaks and rinses in dilute detergent, purified water, and 10 % HCl, followed by a final copious rinse in purified water, are recommended.
- Rinse plastic caps with 10 % HCl, twice with freshly prepared purified water (e.g. using a Millipore Alpha-Q system), and dry them at 70° C for 4 hr to 6 hr.
- Combust bottles with aluminum foil covers at 450° C for 4 hr to 6 hr.
- Fill clean, combusted bottles with fresh purified water drawn directly from the purification unit.
- Assemble the combusted bottles and clean caps. Store in the dark.
- These standards are used daily during cruises to evaluate the quality of purified water freshly prepared at sea.
- This carefully prepared standard water sometimes must be used as the reference material for actual sample analysis. If this is planned, the investigator should determine the optical density of the standard water preparations before and after a cruise relative to fresh purified water drawn directly into the quartz cuvettes. An assessment of the change in this water over time may indicate a need to use a time-dependent reference water correction.
- As a precaution, even if the investigator intends to have high quality purified water at sea, it is wise to determine the standard water optical density relative to freshly purified water before a cruise, and as a time-series to understand the quality of the purified water system used for reference.

Soluble Absorption Sample Preparation, Storage and Analysis

- Wash hands with soap and water to avoid contaminating the samples.
- Use 0.2 μm polycarbonate filters (e.g. Nuclepore or equivalent). Do not use irgalan black stained (low fluorescence background) polycarbonate filters for this preparation. Other membrane filters, or Sterivex cartridges, may also be used, but the investigator must then test for any contamination by the filter and ensure that no artifacts are introduced.
- The filtration system used should be equipped with control of vacuum for each individual filtration funnel and with a provision for direct filtration into clean bottles. An example of a suitable soluble absorption filtration assembly is illustrated in Mitchell et al. (2000).

- Pre-soak each filter for at least 15 min in 10 % HCl. Rinse the filter thoroughly with purified water. Mount the filter on a filtration funnel and filter ~100 mL of purified water through it into a sample bottle. Shake the bottle, and discard the water, pouring it over the inside of the cap to rinse it. Cover the filtration funnel with aluminum foil until ready to filter the sample.
- Collect ~200 mL of seawater into a clean sample bottle. For the blanks, use purified water drawn directly from the purification unit into 2 clean sample bottles.
- Filter ~75 mL of the samples and 1 blank directly into clean bottles at low vacuum (<120 mm Hg). Do not allow filters to go dry during sample rinsing. Shake the bottles, and discard the water.
- Filter ~75 mL of the samples into bottles. For the blank, filter ~75 mL of purified water. When finished, cap the bottles and store them until they are to be measured in the spectrophotometer.
- If the samples will be measured within 4 hr, store them in the dark at room temperature.
- If the samples will be measured 4 hr to 24 hr later, refrigerate them in the dark.
- Longer storage is not recommended, because artifacts of undocumented magnitude are known to occur. Several researchers have reported results from measurements of frozen samples, but no systematic evaluation of possible artifacts resulting from freezing has yet been reported.
- Warm refrigerated samples to room temperature before beginning optical density measurements. If it is practical to do so, control the samples and the reference water to equal temperatures during the spectrophotometric measurements. Absorption by water is strongly temperature dependent at red and near infrared wavelengths (Pegau and Zaneveld 1993).
- Qorpak bottles can be re-used at sea. After spectrophotometric analysis is completed, thoroughly rinse each bottle and its cap three times with purified water, pour in 20 mL of 10 % HCl acid, and close the cap. Before the bottle is reused, shake it well, discard the 10 % HCl, rinse the bottle and cap copiously with purified water, and fill the bottle with purified water, to be used later to rinse a new sample filter. Purified water should be drawn directly from the pure water system.

Determination of Optical Density of Soluble Absorption Preparations

- If samples have been refrigerated, allow them to warm to room temperature.
- Allow the spectrophotometer to warm up for 30 min. Confirm that the optical windows of the spectrophotometer are clean. If necessary, clean them with purified water and ethanol, sequentially, and dry them thoroughly with lint-free laboratory tissues.
- Verify the instrument's spectral characteristics and precision as described in Section 15.3.
- Wash hands with soap and water to avoid contamination
- Between use, 10 cm quartz window spectrophotometer cuvettes should be stored with purified water. For analysis, discard the purified water in the cuvettes, rinse inside and outside of cuvettes twice with 10 % HCl, twice with ethanol, then rinse them inside and outside using copious volumes of purified water. After the cuvettes have been cleaned, use laboratory tissues to handle them. Avoid contacting the cuvettes with bare-hands, and do not contaminate their optical windows by touching them.
- Fill both cuvettes with purified water drawn directly from the water preparation system. Use of purified water stored in containers is not recommended. However, if freshly purified water is not available at sea, the carefully prepared standard water in combusted bottles can be used as a reference, but the investigator must document its degradation over time relative to air (see above).
- Carefully dry the cuvettes. Bulk dry with paper towels, but dry the quartz optical windows with lint-free laboratory wipes only (e.g. Kimwipes™).
- Inspect cuvettes carefully, especially along their optical paths, to ensure that they are clean. Make sure there are no bubbles, floating dust, or contaminants on the optical windows, or in suspension.

Looking through the cuvette against a black background can usually identify any problems in the samples. Repeat cleaning and drying procedures as needed to obtain a clean sample.

- Run an air–to-air baseline reference spectrum for the spectrophotometer. Record the digital air baseline. This spectrum should be spectrally flat, with noise less than ± 0.0005 OD.
- Place the reference cuvette in spectrophotometer and scan $OD_{\mathrm{rwa}}(\lambda)$, the optical density of purified water relative to air. Remove the reference cuvette and repeat the measurement for the sample cuvette. Store both spectra noting which file is for the cuvette to be used as reference in subsequent analyses, and which is to be used for samples. See Figure 15.2 for spectra of $OD_{\mathrm{rwa}}(\lambda)$ determined during ACE-Asia.
- Compare the spectra of $OD_{\mathrm{rwa}}(\lambda)$ determined for the reference and sample cuvettes to each other, and with a digital library of previous reference water to air optical density spectra. Ensure that the two cuvettes are well matched optically, and that both conform to tolerance of pure water relative to air. Note anomalies and plan to make any needed corrections during data processing. If anomalies are associated with poor preparation of the cuvette, repeat the preparation and run new water-to-air baseline reference scans.
- Put both reference and sample cuvettes filled with purified reference water into the spectrophotometer for a double beam unit. For a single beam unit this will be done sequentially. Run a baseline correction for purified water. After the water-to-water baseline optical density measurement is complete, record the pure water baseline as a sample, $OD_{\mathrm{rww}}(\lambda)$. This spectrum should be spectrally flat, with magnitude less than ± 0.0005 OD. Save the digital baseline spectrum. Ensure the baseline is flat and stable over time and note any anomalies. It is common for the baseline to exhibit temperature-dependent artifacts 650-800 nm. These should be minimized if possible by ensuring the purified water in the sample and reference cuvette are at the same temperature.
- If the baseline reference spectrum $OD_{\mathrm{rww}}(\lambda)$ is not flat and stable during analysis according to specifications summarized in section 15.3, the precision of any estimate of soluble absorption may be seriously questioned. It is the investigator's responsibility to ensure satisfactory performance of the instruments and use of proper methods to ensure that the final result is reasonable. Significant deviation from the specifications in section 15.3 or improper consideration of sample preparation protocols may result in estimates of soluble absorption that are not meaningful given the small magnitude of this estimate in the visible spectral region of most interest for ocean color applications.
- Remove the sample cuvette and discard the liquid. Rinse the inside of the cuvette three times with ~5 mL to 10 mL of the next sample to be measured. A copious rinse is desired, but sample volume is often limited. Several vigorously shaken small sample rinses are recommended if the volume is extremely limited.
- Fill the sample cuvette with the purified water that has been filtered as though it were a sample and record the blank spectrum, $OD_{\mathrm{bs}}(\lambda)$, relative to the reference cuvette filled directly from the purified water source..
- Repeat the rinsing for each subsequent sample. The first sample rinse for seawater samples is most important to eliminate all purified water, especially for seawater samples due to refractive index differences between fresh and salt water. Fill the cuvette with the next water sample.
- Prior to running each sample, dry the exterior of the sample cuvette carefully, and inspect it, as described above, to ensure a clean sample.
- Replace the sample cuvette in the spectrophotometer, and measure the $OD_s(\lambda)$ spectrum relative to freshly purified water. Store the digital data and record all necessary information.

15.6 DATA PROCESSING AND ANALYSIS

The protocols in this section should be followed to compute particle and soluble material absorption coefficients from the spectrophotometric OD measurements described above. The following discussion assumes that all measured $OD(\lambda)$ spectra, whether for samples, or reference blanks, have been corrected for the instrument baseline spectrum, either automatically, or by post-measurement calculations appropriate to a particular spectrophotometer configuration (see above in Section 15.3, and specific reference spectrum measurement checks in the protocols of Sections 15.4 and 15.5).

Computations for absorption coefficients of particles concentrated on filters, and for materials dissolved in water, differ primarily in the determination of optical pathlength and in the treatment of reference blanks.

Soluble Absorption Coefficients

For soluble absorption, the calculations are directly proportional to the sample optical density relative to the pure water reference after correction for the pure water blank and specification of a null absorption

$$a_g(\lambda) = \frac{2.303}{l}\left[[OD_{\mathrm{s}}(\lambda) - OD_{\mathrm{bs}}(\lambda)] - OD_{\mathrm{null}}\right], \tag{15.3}$$

where l is the cuvette pathlength (usually 0.1 m), $OD_{\mathrm{s}}(\lambda)$ is the optical density of the filtrate sample relative to purified water, $OD_{\mathrm{bs}}(\lambda)$ is optical density of a purified water blank treated like a sample relative to purified water (see below), and OD_{null} is the apparent residual optical density at a long visible or near infrared wavelength where absorption by dissolved materials is assumed to be zero. Note that as long as the null wavelength region is the same for sample and blank, the sample and blank spectra can be set to zero at the null wavelength independently or after they are subtracted from each other, as indicated in Equation 15.3. Equation 15.3 assumes use of a spectrophotometer that automatically references the sample and blank optical density to freshly purified water. Most modern commercial single or double beam units will compute this optical density directly relative to the reference. The user must record both raw sample and blank optical densities relative to purified water, and assess the stability of the purified water $OD_{\mathrm{rww}}(\lambda)$ reference by routine determinations of the purified water relative to air (e.g. $OD_{\mathrm{rwa}}(\lambda)$; Figure 15.2) and also evaluate the sample preparation methods by determining the blanks routinely (e.g. daily when at sea; Figure 3B).

a. Filtered pure water blank spectra

There are generally small spectral effects of the filtration and preparation procedure that cause blanks prepared from purified water to have a higher $OD_{\mathrm{bs}}(\lambda)$ at short wavelengths compared to the reference cuvette containing purified water drawn directly from the purification system. Examples of filtered blank spectra $OD_{\mathrm{bs}}(\lambda)$ for ACE-Asia where Millipore Alpha-Q water was used as the purified water source in the reference cuvette are illustrated in Figures 15.3B and 15.3D (c.f. Mitchell *et al.* 2000). The $OD_{\mathrm{bs}}(\lambda)$ spectrum should be determined, recorded and included with the data for each sample. It is recommended that the investigator carefully determine these blanks for each station, or at least once per day, during a field program, and evaluate the stability of this blank for quality control purposes. If the purified water system is performing well, and the preparation procedures are carefully implemented, the $OD_{\mathrm{bs}}(\lambda)$ sample blank offsets will generally be very consistent (Figure 15.3B). In such cases, the recommended procedure is to average $OD_{\mathrm{bs}}(\lambda)$ spectra over the entire cruise, and to then fit a smoothed exponential function over wavelength to the overall mean (the bold line in Figure 15.3B). A separate OD_{null} (see discussion below) should be determined for the averaged and smoothed $OD_{\mathrm{bs}}(\lambda)$ spectrum before it is substituted in Equation (15.3). Because the signals are small, instrument noise is a large fraction of the signal, even for high quality spectrophotometers. Therefore subtraction of an individual blank spectrum, including its

noise, is strongly discouraged as this effectively doubles the noise of an already noisy signal. Instead, it is recommended that a smoothed blank be determined from many individual blank spectra provided that the investigator can demonstrate, as in Figure 15.3B that there is consistency among the population of blank spectra that are determined. The procedure of determining blanks at least each day during routine sampling provides an important quality control on the sample preparation protocols. If the blank is found to deviate considerably from the norm, the investigator should immediately determine the cause of the discrepancy.

b. Null point corrections to soluble absorption spectra

The absorption spectrum of pure water varies strongly with temperature, especially in the wavelength region between 650 nm and 750 nm, but at other wavelengths as well (Pegau and Zaneveld, 1993). To avoid temperature related measurement artifacts, the sample and reference should be maintained at the same temperature, but in practice, this is often difficult to do. If strong temperature residuals are apparent in the spectra near 750 nm, one must inspect the data to determine an appropriate wavelength range to use as a null point. For the data in Figure 15.3, it appears that assuming a null point as the average from 590-600 nm is reasonable. This assumption may not be reasonable in turbid lake, bay and coastal waters, however, where large soluble absorption values may persist into the near IR. Selection of wavelengths for null correction must be evaluated carefully for each data set, following principles discussed at more length by Mitchell *et al*. (2000).

Particle Absorption Coefficients

To compute particle absorption $a_{\mathrm{p}}(\lambda)$ in suspension from spectrophotometric $OD_{\mathrm{fp}}(\lambda)$ measured with the particles concentrated on a GF/F filter, it is necessary to appropriately adjust the optical pathlength. This includes substituting the geometric optical pathlength of the particles in suspension, and a scaling factor, β , accounting for the increase in the optical measurement path by scattering within the filter sample. The geometric absorption pathlength l_s of the filtered material in suspension is given by

$$l_s = \frac{V_{\mathrm{f}}}{A_{\mathrm{f}}}, \tag{15.4}$$

where V_f is the volume of water filtered and A_f is the clearance area of the filter calculated from the diameter D_f of the part of each filter that contains the particles. D_f should be determined very carefully on numerous individual filters using AN accurate measurement tool like a caliper that is accurate to at least 0.1 mm.

Scattering of light within the GF/F filter increases the absorption pathlength. The absorption coefficient of filtered particles must be corrected for pathlength amplification and the equivalent absorption coefficient in m^{-1} in suspension is computed as

$$a_p(\lambda) = \frac{2.303 A_{\mathrm{f}}}{\beta V_{\mathrm{f}}}\left[[OD_{\mathrm{fp}}(\lambda) - OD_{\mathrm{bf}}(\lambda)] - OD_{\mathrm{null}}\right], \tag{15.5}$$

where $OD_{\mathrm{fp}}(\lambda)$ is the measured optical density of the sample filter, $OD_{\mathrm{bf}}(\lambda)$ is the optical density of a fully hydrated blank filter, and OD_{null} is a null wavelength residual correction from the infrared where particle absorption is minimal. See also detailed discussion of null point selection in Mitchell et al. (2000)

a. Particle absorption blank spectra

If a spectrophotometer with automatic reference baseline correction is used, and the reference filter blank baseline is flat over the spectral range of interest, $OD_{\mathrm{bf}}(\lambda)$ does not need to be subtracted. Spectra of $OD_{\mathrm{bf}}(\lambda)$ must be determined, recorded and provided with the sample data. Properly prepared blanks generally have flat spectra relative to the reference baseline filters. If the $OD_{\mathrm{bf}}(\lambda)$ is confirmed to be flat, then it is recommended that only a null absorbance is subtracted from the $OD_{\mathrm{fp}}(\lambda)$ to compensate for

baseline offsets. Subtraction of a spectrally flat baseline that varies only due to the instrument noise increases the noise of the result. If the instrument baseline can not be maintained within the recommendations summarized in Section 15.3, the investigator should consider using a different instrument since the errors in the methods caused by using unstable instruments are difficult to control for.

b. Null point corrections to particle absorption spectra

To correct for residual offsets in the sample filter relative to the reference, and for scattering artifacts due to particle loading, it is assumed that a null absorption wavelength in the infrared can be identified. Historically, many investigators used 750 nm as the null absorption wavelength, but recent reports indicate that this wavelength is too short for some waters. It is recommended that the null wavelength be set at 800 nm (or longer), and that the investigator must examine the spectra to evaluate residual absorption structure near the null wavelength. Rather than use a single wavelength, a mean $OD_{\mathrm{fp}}(\lambda)$ in a 10 nm interval (*e.g.* 790 nm to 800 nm) may be used as the null value to minimize the introduction of noise in the null correction procedure. Mitchell *et al.* (2000) discuss, at more length, factors affecting the choice of an appropriate wavelength for estimating OD_{null} . In Case 2 waters, the definition of the null absorption is more difficult and the investigator may consider the benefits of the transmission-reflectance estimates of particle absorption (Tassan and Ferrari, 1995a).

c. Pathlength amplification corrections

To correct for the pathlength increases due to multiple scattering in the filter, the prevalent current practice is to estimate β empirically through either a quadratic or power function that may be expressed in the form

$$\beta = \left[C_1 + C_2 \left[OD_{fp}(\lambda) - OD_{null}(\lambda) \right] \right]^{-1}, \tag{15.6a}$$

or

$$\beta = C_0 + C_1 \left[OD_{fp}(\lambda) - OD_{null}(\lambda) \right]^{C_2}, \tag{15.6b}$$

for quadratic equation or power function fits, respectively. C_0, C_1 and C_2 are coefficients of least squares regression fits of measured data. Recommended coefficients have been reported in the literature (Table 1). The investigator should either choose published coefficients consistent with the species composition, equipment and measurement conditions for a given data set (consider the discussion in Mitchell *et al.* 2000), or independently determine pathlength amplification factors by comparing absorption in suspension and on filters following procedures described previously (Mitchell 1990, Mitchell et al., 2000).

d. De-pigmented Particle and Phytoplankton Absorption Coefficients

The de-pigmented particle absorption coefficients, $a_{\mathrm{d}}(\lambda)$, may be calculated using Equation (15.5), by substituting. $OD_{\mathrm{fd}}(\lambda)$ for $OD_{\mathrm{fp}}(\lambda)$. At present it is recommended to use the same pathlength correction factor for the de-pigmented samples as for the particle absorption sample. The validity of this operational choice of β is difficult to assess, because the de-pigmented particles are created operationally from the treatment, and the relationships between their absorption on filters compared to suspensions may differ from those derived empirically for the original particles.

The spectral absorption coefficient for phytoplankton pigments can be computed as the difference between particulate and de-pigmented estimates:

$$a_{\phi}(\lambda) = a_p(\lambda) - a_d(\lambda). \tag{15.7}$$

15.7 DATA REPORTING

For purposes of data reporting and archiving, the absorption coefficients will be reported in m^{-1} and computed using the equations summarized above. Uncorrected optical density spectra for the filter samples, blank filter referenced to a blank filter, pure water referenced to air, pure water referenced to pure water and soluble absorption blank spectra must be recorded and provided so alternative algorithms could be applied to the original data. The pathlength amplification factor, a description of (or reference to) the method and the procedure for assignment of the null absorption, and any blank or spectral scattering corrections for the soluble absorption calculations must be reported.

15.9 PROTOCOL STATUS AND FUTURE DIRECTIONS

Absorption spectra for particles filtered on GF/F filters

Details of various issues related to this frequently used method for estimating particle absorption for filtered samples are not significantly changed since the summary of the NASA-sponsored Workshops found in Mitchell et al. (2000). It is important to address a few salient issues that are routinely asked by investigators interested in implementing the method. First, most modern dual-beam spectrophotometers that have a grating before the sample and illuminate the sample with spectrally resolved light have negligible differences (a few percent) in terms of determining the raw GF/F filter $OD_{\mathrm{fp}}(\lambda)$ of the particles relative to a properly hydrated blank filter if the protocols are carefully followed. Thus, it is not essential to determine the pathlength amplification factor, β, for each different spectrophotometer that is used as long as the investigator makes an appropriate choice of instrumentation. However, some spectrophotometers have limited spectral range, limited dynamic range, more noise and inferior stability so the investigator should evaluate the unit to be used to ensure suitability by following the recommendations in section 15.3. Second, diode-array systems that illuminate with broad-band light and then disperse the post-sample light using a spectral photodiode array may have significantly different raw OD for the filtered sample. Example OD spectra estimated for a diatom culture for various systems used at the Scripps Workshop are shown in Figure 15.1 (see also details in Mitchell et al. 2000). Note the Hewlett-Packard spectral diode array system has a significantly higher OD than the other instruments. An empirical relation for this offset in the range 400-700 nm is reported in Mitchell et al. (2000) for that specific model. The Hewlett-Packard data is reported only for wavelengths greater than 400 nm because the instrument performs poorly at short wavelengths with the glass fiber filter method. If a user chooses such optical geometry for the determination of particle absorption they should carefully assess the potential issues illustrated in Figure 15.1. We recommend that the user compare several spectrophotometers for raw optical density of properly hydrated samples relative to blank filters and ensure the unit they use does not deviate from the typical result of most systems for which amplifications factors (β) have been determined (Table 15.1). Alternatively one must determine the pathlength amplification for the instrument of choice, a laborious and unnecessary procedure if a spectrophotometer is selected that does not cause the bias illustrated in Figure 15.1.

Absorption spectra for particles transferred to glass slides

An alternative method, developed by Allali et al. (1995), to estimate absorption coefficients of cultures and seawater samples is to freeze transfer the particles to transparent microscope slides, following the protocols of Hewes and Holm-Hansen (1983). The investigator must have an integrating sphere or equivalent scattered transmission accessory to implement this method. This procedure produced results comparable to the GF/F filter method in comparisons reported by Mitchell *et al*. (2000), but sufficient uncertainties remain that the GF/F method continues to be recommended for the present.

Transmission-Reflectance (T-R) Method

Tassan and Ferrari (1995a) described a modification of the light-transmission method that corrects for backscattering. This technique combines light-transmission (T) and light-reflection (R) measurements, carried out using an integrating sphere attached to a dual-beam spectrophotometer. The data analysis is

performed by a theoretical model that eliminates the effect of light backscattering by the particles. At the Scripps workshop, the global error of the T-R method was comparable to the error yielded by the simpler T method for mono-cultures. Subsequent modifications of the T-R experimental routine (Tassan and Ferrari, 1998; Ferrari and Tassan, 1999) yielded a significant reduction of the experimental error. Tassan and Ferrari (1995) reported that for case 1 waters that have negligible inorganic particle load, the amplification factor for GF/F filters determined with the T-R methods is similar to those determined by Mitchell (1990). The T-R method is particularly suited for applications to samples containing highly scattering mineral particles that are commonly found in Case 2 waters. Despite the more complicated procedure including an instrument with an integrating sphere, this method should be considered in special circumstances, and with further development may eventually supercede the presently recommended transmission protocol.

Absorption spectra for seawater filtered through membrane filters or cartridges

For most ocean regions, the optical density of dissolved organic material, relative to purified water in a typical 10 cm pathlength cuvette, is very small in the 400-600 nm region of most interest to ocean color satellite investigations. To ensure a common frame of reference for the global data collected by diverse investigators, we recommend $OD_{\mathrm{rwa}}(\lambda)$ spectra (250-850 nm) be determined relative to air for purified water directly introduced to properly cleaned quartz cuvettes. The purpose of such spectra is to obtain an independent reference of the quality of the purified water. $OD_{\mathrm{rwa}}(\lambda)$ spectra for the sample cuvette used during ACE-Asia are shown in Figure 15.2. $OD_{\mathrm{rwa}}(\lambda)$ should be determined daily for the sample and reference cuvettes used in analyses. The investigator should keep careful records of this data and assess any bias in final estimates that may be attributed to problems with the reference water. By plotting in the range of minimal absorption by water (250-600 nm; Figure 15.2A) one can assess whether or not the reference water on a ship has seriously degraded. Production of impure water by commercial systems is a relatively common problem on ships where the feed water may have serious contamination. If the purified water system fails at sea, the investigator should use the standard water prepared prior to the cruise as the reference. Spectra of $OD_{\mathrm{rwa}}(\lambda)$ of the bottled standard water should be determined before and after a cruise for each lot of bottled standards that are prepared. This precaution is important to assist in any corrections that might be required if standard water is used as a reference, or if the purified water system degrades over time during a cruise.

There are still relatively few spectra of soluble absorption determined fresh at sea using the revised protocols recommended here. Spectra of $OD_s(\lambda)$ and $OD_{\mathrm{bs}}(\lambda)$ collected during ACE-Asia are shown in Figure 15.3. Raw optical density, relative to Millipore Alpha-Q water are shown in 3A. We routinely find small positive off-sets from 600-800 nm that we feel should be compensated by subtracting a null value. Figure 15.3B illustrates $OD_{\mathrm{bs}}(\lambda)$ during ACE-Asia prepared as recommended in section 15.5, but plotted at 10x smaller scale as Figure 15.3A. The recommended procedure is to subtract a cruise (or global) mean of this blank (solid line in Figure 15.3B) from the raw sample OD values, and then to adjust this difference to zero at a null reference (Equation 15.3). The smoothed global blank was determined by taking the mean of all blanks for each cruise we have completed since 1998, subsequently taking the mean of all cruises and lastly fitting an exponential function to the global mean after setting a null point as the average from 590-600 nm. There can be small differences in blank spectra cruise to cruise, but we do not find this to be significant relative to the overall statistics of all cruises or the variance within a single cruse. For relatively weakly absorbing samples like open oceans observed during ACE-Asia, there is negligible apparent absorption > 600 nm and there is clear evidence in 3A of uncompensated temperature effects 650-800 nm. Therefore we chose to set the null value as the mean from 590-600 nm. However, if very strong soluble absorption is present, the temperature effects 650-800 nm will be less significant, and the absorption 590-600 nm may be important. The investigator should evaluate their data to determine the best null point and report that assessment. Figure 15.3C are optical density of spectra for a 10 cm cuvette after correcting for the null value and the blank spectrum The effort to carefully determine the purified water relative to air, and blanks during each cruise will allow different investigators to inter-compare their results better, and will ensure better quality control of data collected over time. We have also determined the time-dependent

change of our standard water (data not shown), and when we use that as a reference due to the failure of our purified water system at sea, we subtract a different blank than the global fit shown in Figure 15.3B.

An alternate method for preparing samples for soluble absorption allows multiple use of Sterivex sealed filtration cartridges. Use of these cartridges has been described by D'Sa et al. (1999) who used the method to prepare samples delivered to a capillary light guide spectrophotometer for estimating absorption by soluble material. The procedure provides high sensitivity and can be adapted to continuous flow determinations. This new method may prove useful in various applications but has not been applied extensively at this time. Evaluation of the performance of the Sterivex cartridges for sample preparation and light guides for spectroscopy warrant further research.

Constraints on the estimate of soluble and particle absorption

To constrain our water sample estimates of particle and soluble absorption we have compared them to spectral estimates of the diffuse attenuation coefficient for downwelling irradiance, $K_{\mathrm{d}}(z,\lambda)$, determined using a free-fall radiometer during a Southern Ocean cruise (AMLR) and a western Pacific Ocean cruise (ACE-Asia). It is well known that accurate estimate of $K_{\mathrm{d}}(z,\lambda)$ in the upper ocean is difficult. Problems include heave of the ship, foam, bubbles, shadow, tilt, sky conditions and other influences on this apparent optical property (see more detailed discussions in other chapters of these protocols). Waters *et al.* (1990) described advantages of free-fall systems and many investigators have adopted this procedure to minimize some of the problems cited above. In 2001 we deployed our Biospherical Instruments PRR 800 system at approximately 80 stations combined between our AMLR and ACE-Asia cruises. We consider this our highest quality radiometric data set because of the free-fall deployment, the spectral range from 312-710 nm and because we acquired 4-5 separate free-fall profiles at each station to improve the confidence in our final estimate. In Figure 15.4 we show estimates of the mean cosine for spectral downwelling irradiance, $\bar{\mu}_{\mathrm{d}}(\lambda)$, of the upper ocean mixed layer (open symbols). Here we define $\bar{\mu}_{\mathrm{d}}(\lambda)$ as the ratio $[a_{\mathrm{w}}(\lambda)+a_{\mathrm{p}}(\lambda)+a_{\mathrm{g}}(\lambda)]/K_{\mathrm{d}}$. For Figure 15.4, values for pure water are estimated from Pope and Fry (1997) for 380-700 nm, Quickenden and Irvin (1980) for 300-320 and a linear interpolation between those values for 320-380 nm as recommended by Fry (2000). If the individual components are accurate, this can be considered a reasonable estimate of the mean cosine near the ocean surface (see Mobley, 1994 for detailed discussion of the mean cosine). Theoretically the values of $\bar{\mu}_{\mathrm{d}}(\lambda)$ should be less than 1.0 and for typical radiance distributions of the upper ocean, they should be in the range of 0.70-0.85 near the surface. For both AMLR and ACE-Asia all absorption data were determined fresh at sea with consistent methods between the two cruises. We found that in the region 500 nm to 650 nm there is little difference between the estimates of $\bar{\mu}_{\mathrm{d}}(\lambda)$ for the Southern Ocean and the western Pacific. However, below 500 nm, the values for ACE-Asia are near 1.0 and below 400 nm they exceed 1.0. For AMLR, values approach 1.0 for wavelengths less than 350 nm.

The ratio of $a_{\mathrm{g}}(\lambda)/a_{\mathrm{t}}(\lambda)$ where $a_{\mathrm{t}}=a_{\mathrm{w}}+a_{\mathrm{p}}+a_{\mathrm{g}}$, is also plotted in Figure 15.4 (filled symbols). The trend clearly illustrates that the soluble component dominates at short wavelength. There are several hypotheses that should be considered to understand the overestimates of $\bar{\mu}_{\mathrm{d}}(\lambda)$ below 400 nm. These could include underestimate of $K_{\mathrm{d}}(z,\lambda)$ or overestimates of any of the absorption components. A combination of these factors may prevail. The filter radiometer in the profiler has good out of band blocking, but the spectrum of surface irradiance is rapidly changing in the region <350 nm and this may cause a red shift in the effective band center of the channels, with an associated underestimate of $K_{\mathrm{d}}(z,\lambda)$. There may be small particles or colloids that pass the 0.2 μm filters causing a spectrally dependent scattering error (Aas, 2000). The particle absorption we estimate is based on Mitchell (1990) which results in higher estimates compared to some other published methods (Table 1). Also, there has not been adequate attention paid to determination of the pathlength amplification factor for the region below 400 nm. It is also possible that the values for pure water absorption are too high. The very reasonable or slightly high (by about 10-15%) values for the mean cosine of downwelling irradiance shown in Figure 15.4 for 400-600 nm indicates that the absorption methods recommended here are rather robust compared

to simple estimates of diffuse attenuation coefficients. Reynolds et al. (2001) and Stramska et al. (2000) have reported reasonable closure between estimates of absorption using these methods, radiometric observations and modeling.

We have used "pure water" absorption for our estimate of $a_w(\lambda)$, and salts should in fact be added, if important, in the comparison of absorption to diffuse attenuation in Figure 15.4. Our estimate of $a_g(\lambda)$ relative to purified water will include absorption by salts, if they are significant. Salts in seawater are significant absorbers at short wavelengths. Lenoble (1956; see also Shiffrin, 1988) reported values for pure salts dissolved in purified water that indicate absorption coefficients near 300 nm comparable to the sample optical density of filtered samples relative to purified water that we routinely determine at sea in this spectral region. This UV absorption (<320 nm), relative to purified water, is generally assumed to be caused by "colored dissolved organic matter" but this may be inaccurate at these short wavelengths. Therefore one must be very cautious interpreting the apparent optical density of seawater filtrates relative to purified water for wavelengths less than 320nm. We recommend that more careful research be carried out on the methods for soluble absorption which appears to have a potentially dominating influence on the overestimates of $\bar{\mu}_d(\lambda)$ less than 400 nm. In particular, the influence of scattering by small particles (organic or mineral) and the role of salt absorption must be more carefully assessed.

REFERENCES

Aas, E., 2000: Spectral slope of yellow substance: problems casued by small particles. Proceedings of Ocean Optics XV, Monaco, 16-20 October, 2000.

Allali, K., A. Bricaud, M. Babin, A. Morel, and P. Chang, 1995: A new method for measuring spectral absorption coefficients of marine particulates. *Limnology and Oceanography.* **40,** 1,526-1,523

Allali, K., A. Bricaud, and H. Claustre, 1997: Spatial variations in the chlorophyll-specific absorption coefficients of phytoplankton and photosynthetically active pigments in the Equatorial Pacific. *Journal of Geophysical Research.* **102,** 12,413-12,423

Blough, N.V., O.C. Zafiriou, and J. Bonilla, 1993: Optical absorption spectra of waters from the Orinoco River outflow: terrestrial input of colored organic matter to the Caribbean. *Journal of Geophysical Research.* **98,** 2,271-2,278

Bricaud, A., A. Morel, and L. Prieur, 1981: Absorption by dissolved organic matter of the sea (yellow substance) in the UV and visible domains. *Limnology and Oceanography.* **26,** 43-53

Bricaud, A., and D. Stramski, 1990: Spectral absorption coefficients of living phytoplankton and non-algal biogenous matter: A comparison between the Peru upwelling area and the Sargasso Sea. *Limnology and Oceanography.* **35,** 562-582

Butler, W.L., 1962: Absorption of light by turbid materials. *Journal of the Optical Society of America.* **52,** 292-299

Carder, K.L., S.K. Hawes, K.S. Baker, R.C. Smith, and R.G. Steward, 1989: Remote sensing algorithms for discriminating marine humus from chlorophyll. *Limnology and Oceanography.* **30**(2), 286-298

Carder, K.L., R.G. Steward, G.R. Harvey, and P.B. Ortner, 1989: Marine humic and fulvic acids: Their effects on remote sensing of ocean chlorophyll. *Limnology and Oceanography.* **34,** 68-81

Chavez, F.P., K.R. Buck, R.R. Bidigare, D.M. Karl, D. Hebel, M. Latasa, L. Campbell, and J. Newton, 1995: On the chlorophyll *a* retention properties of glass-fiber GF/F filters. *Limnology and Oceanography.* **40(2),** 428-433

Cleveland, J.S., and A.D. Weidemann, 1993: Quantifying absorption by aquatic particles: A multiple scattering correction for glass-fiber filters. *Limnology and Oceanography.* **38,** 1321-1327

D'Sa, E.J., R.G. Steward, A. Vodacek, N.V. Blough, and D. Phinney, 1999: Determining optical absorption of colored dissolved organic matter in seawater with a liquid capillary waveguide. *Limnology and Oceanography.* **44,** 1,142-1,148

Duntley, S.Q., 1942: The optical properties of diffusing materials. *Journal of the Optical Society of America.* **32,** 61-70

Ferrari, G.M., and S. Tassan, 1996: Use of the 0.22 µm Millipore membrane for light-transmission measurements of aquatic particles. *Journal of Plankton Research.* **18,** 1,261-1,267

Ferrari, G.M, 1999: A method for removal of light absorption by phytoplankton pigments using chemical oxidation. *Journal of Phycology.* **35,** 1,090-1,098

Fry, E.S., 2000: Visible and near-ultraviolet absorption spectrum of liquid water: comments. *Applied Optics.* **39,** 2,743-2,744

Hewes, C.D., and O. Holm-Hansen, 1983: A method for recovering nanoplankton from filters for identification with the microscope: The filter-transfer-freeze (FTF) technique. *Limnology and Oceanography.* **28,** 389-394

Hoge, F.E., A. Vodacek, and N.V. Blough, 1993: Inherent optical properties of the ocean: retrieval of the absorption coefficient of chromophoric dissolved organic matter from fluorescence measurements. *Limnology and Oceanography.* **38,** 1394-1402

JGOFS, 1991: JGOFS Core Measurements Protocol. *JGOFS Report #6, Scientific Committee on Oceanic Research.* 40

Kahru, M., and B.G. Mitchell, 1998: Spectral reflectance and absorption of a massive red tide off Southern California. *Journal of Geophysical Research.* **103,** 21,601-21,609

Kalle, K., 1938: Zum problem der meerwasserfarbe. *Ann.Hydr.u.martim.Meterol.* **66,** 1.S.55-

Kiefer, D.A., R.J. Olson, and W.H. Wilson, 1979: Reflectance spectroscopy of marine phytoplankton. Part 1. Optical properties as related to age and growth rate. *Limnology and Oceanography.* **24,** 664-672

Kiefer, D.A., and J.B. SooHoo, 1982: Spectral absorption by marine particles of coastal waters of Baja California. *Limnology and Oceanography.* **27,** 492-499

Kishino, M., N. Okami, M. Takahashi, and S. Ichimura, 1986: Light utilization efficiency and quantum yield of phytoplankton in a thermally stratified sea. *Limnology and Oceanography.* **31,** 557-566

Kishino, M., N. Takahashi, N. Okami, and S. Ichimura, 1985: Estimation of the spectral absorption coefficients of phytoplankton in the sea. *Bulletin of Marine Science.* **37,** 634-642

Lenoble, J., 1956: L'absorption du rayonment ultraviolet par les ions presents dans la Mer. *Revue d'Optique.* **35** (10), 526-531

Mitchell, B.G. and D. A. Kiefer, 1988a: Chlorophyll *a* specific absorption and fluorescence excitation spectra for light-limited phytoplankton. *Deep-Sea Research I.* **35,** 639-663

Mitchell, B.G. and D. A. Kiefer, 1988b: Variability in pigment specific particulate fluorescence and absorption spectra in the northeastern Pacific Ocean. *Deep-Sea Research I.* **35,** 665-689

Mitchell, B.G., A. Bricaud, and others, 2000: Determination of spectral absorption coefficients of particles, dissolved material and phytoplankton for discrete water samples, In: Fargion, G.S. and J.L. Mueller, [Eds.] *Ocean Optics Protocols for Satellite Ocean Color Sensor Validation, Revision 2.* NASA/TM-2000-209966, NASA Goddard Space Flight Center, Greenbelt, MD. Chapter 12, pp125-153.

Mitchell, B.G. 1990: Algorithms for determining the absorption coefficient of aquatic particulates using the quantitative filter technique (QFT).*Ocean Optics X.* 137-148

Mitchell, B.G., M. Kahru, and P.J. Flatau, 1998: Estimation of spectral values for the mean cosine of the upper ocean. SPIE, Ocean Optics XIV. **CD-ROM**.

Mitchell, B.G., and D.A. Kiefer 1984: Determination of absorption and fluorescence excitation spectra for phytoplankton. *Marine phytoplankton and productivity.* **8,** 157-169

Moore, L.R., R. Goericke, and S.W. Chisholm, 1995: Comparative physiology of *Synechococcus* and *Prochlorococcus*: influence of light and temperature on growth, pigments, fluorescence and absorptive properties. *Marine Ecology Progress Series.* **116,** 259-275

Nelson, N.B., D.A. Siegel, and A.F. Michaels, 1998: Seasonal dynamics of colored dissolved material in the Sargasso Sea. *Deep-Sea Research.* **45,** 931-957

Pegau, W.S., and J.R.V. Zaneveld, 1993: Temperature-dependent absorption of water in the red and near infrared portions of the spectrum. *Limnology and Oceanography.* **38,** 188-192

Pope, R.M., and E.S. Fry, 1997: Absorption Spectrum (380-700 nm) of Pure Water: II. Integrating Cavity Measurements. *Applied Optics.* **36,** 8,710-8,723

Preisendorfer, R.W., 1976: Hydrologic optics 1. Introduction 2. Foundations 3. Solutions 4. Imbeddings 5. Properties 6. Surfaces 1450

Quickenden, T. I. and J. A. Irvin, 1980: The ultraviolet absorption spectrum of liquid water. *Journal of Chemical Physics*, **72**, 4,416-4,428

Reynolds, R. A., D. Stramski, and B. G. Mitchell, 2001: A chlorophyll-dependent semianalytical reflectance model derived from field measurements of absorption and backscattering coefficients within the Southern Ocean. *Journal of Geophysical Research*, **106(C4)**, 7,125-7,138.

Roesler, C.S., 1998: Theoretical and experimental approaches to improve the accuracy of particulate absorption coefficients derived from the quantitative filter technique. *Limnology and Oceanography.* **43,** 1,649-1,660

Shibata, K., 1958: Spectrophotometry of intact biological materials. Absolute and relative measurments of their transmission, reflection and absorption spectra. *Journal of Biochemistry.* **45,** 599-623

Shifrin, K.S., 1988*: Physical Optics of Ocean Water*. New York, American Institute of Physics, 285

Sogandares, F.M. and E. S. Fry. 1997: Absorption spectrum (340-640 nm) of pure water. I. Photothermal measurements. *Appl. Opt*. **36**: 8699-8709.

Sosik, H.M., 1999: Storage of marine particulate samples for light-absorption measurements. *Limnology and Oceanography.* **44,** 1,139-1,141

Sosik, H.M., and B. G. Mitchell, 1991: Absorption, fluorescence and quantum yield for growth in nitrogen limited *Dunaliella tertiolecta*. *Limnology and Oceanography.* **36,** 910-921

Sosik, H.M. and B. G. Mitchell, 1995: Light absorption by phytoplankton, photosynthetic pigments, and detritus in the California Current System. *Deep-Sea Research I.* **42,** 1,717-1,748

Stramska, M., D. Stramski, B. G. Mitchell and C. D. Mobley, 2000: Estimation of the absorption and backscattering coefficients from in-water radiometric measurements. *Limnology and Oceanography*, **45(3**): 628-641.

Stramski, D., 1990: Artifacts in measuring absorption spectra of phytoplankton collected on a filter. *Limnology and Oceanography.* **35,** 1,804-1,809

Tassan, S. and G.M. Ferrari, 1995a: An alternative approach to absorption measurements of aquatic particles retained on filters. *Limnology and Oceanography.* **40,** 1,358-1,368

Tassan, S., 1995b: Proposal for the measurement of backward and total scattering by mineral particles suspended in water. *Applied Optics.* **34,** 8,345-8,353

Tassan, S., 1998: Measurement of the light absorption by aquatic particulates retained on filters: determination of the optical pathlength amplification by the "Transmittance-Reflectance" method. *Journal of Plankton Research.* **20,** 1,699-1,709

Tassan, S., G.M. Ferrari, A. Bricaud, and M. Babin, 2000: Variability of the amplification factor of light absorption by filter-retained aquatic particles in the coastal environment. *Journal of Plankton Research.* **22,** 659-668

Vodacek, A., N.V. Blough, M.D. DeGrandpre, E.T. Peltzer, and R.K. Nelson, 1996: Seasonal variation of CDOM and DOC in the Middle Atlantic Bight: Terrestrial inputs and photooxidation. *Limnology and Oceanography*. **42,** 674-686

Waters, K. J., R. C. Smith and M. R. Lewis, 1990: Avoiding ship-induced light-field perturbation in the determination of oceanic optical properties. *Oceanography*. November: 18-21

Yentsch, C.S., 1957: A non-extractive method for the quantitative estimation of chlorophyll in algal cultures. *Nature*. **179,** 1302-1304

Yentsch, C.S., 1962: Measurement of visible light absorption by particulate matter in the ocean. *Limnology and Oceanography*, **7,** 207-217

Table 15. 1. Published coefficients for determining pathlength amplification effects. The suspension optical density, OD_{sp}, computed for a GF/F filter with OD_{fp} = 0.2 is provided for comparison.

Quadratic Functions	Particle Type	C_0	C_1	C_2	OD_{sp} (0.2)
Mitchell (1990)	Mixed Cultures	--	0.392	0.655	0.105
Cleveland & Weidemann (1993)	Mixed Cultures	--	0.378	0.523	0.097
Moore et al. (1995)	Prochlorococcus marinus	--	0.291	0.051	0.060
Moore et al. (1995)	Thalassiosira weissflogii	--	0.299	0.746	0.090
Moore et al. (1995)	Synechococcus WH8103	--	0.304	0.450	0.080
Tassan & Ferrari (1995)	Scenedesmus obliqus	--	0.406	0.519	0.102
Nelson et al. (1998)	Dunaliella tertiolecta	--	0.437	0.022	0.088
Nelson et al. (1998)	Phaeodactylum tricornutum	--	0.294	0.587	0.082
Nelson et al. (1998)	Synechococcus WH7803	--	0.277	0.000	0.055
Power Functions					
Mitchell and Kiefer (1988a)	Dunaliella tertiolecta	1.3	0.540	-0.467	0.082
Bricaud and Stramski (1990)	Field samples; D. tertiolecta Cultures of Mitchell & Kiefer (1988a)	0.0	1.630	-0.220	0.086
Kahru and Mitchell (1998)	Mitchell (1990) data	0.0	1.220	-0.254	0.109
Constant					
Roesler (1998)	Assume β = 2.0	--	--	--	0.100

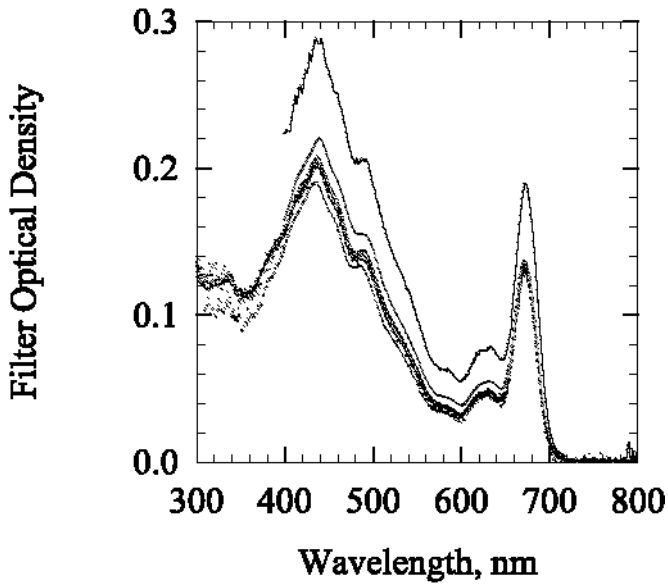

Figure 15.1: Optical density for various spectrophotometers for a diatom culture filtered onto GF/F filters. The average from 790-800 nm was used for a null value and the same volume was used for all samples. The data from the Hewlett Packard diode array system is higher than the other spectrophotometers as discussed in detail in Mitchell et al. (2000). Below 400 nm, the Hewlett Packard unit was too noisy for the glass fiber filter method.

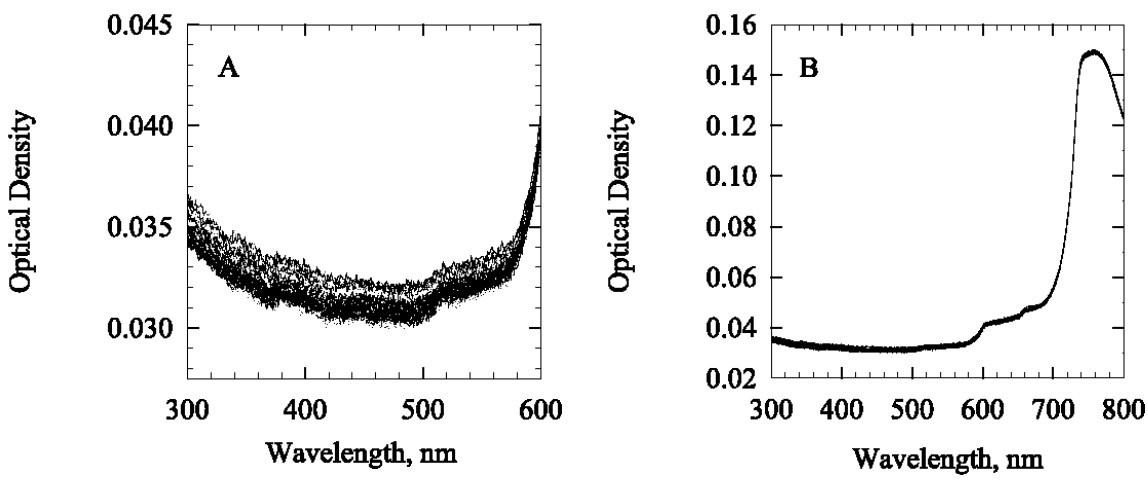

Figure 15.2: Optical density for fresh Millipore Alpha-Q water in the sample cuvette referenced to air in a dual beam spectrophotometer, $OD_{\mathrm{rwa}}(\lambda)$, determined during the ACE-Asia experiment. **A)**. $OD_{\mathrm{rwa}}(\lambda)$ plotted for the spectral range 300 nm to 600 nm. **B)**. Plotted for the spectral range 300 nm to 800 nm.

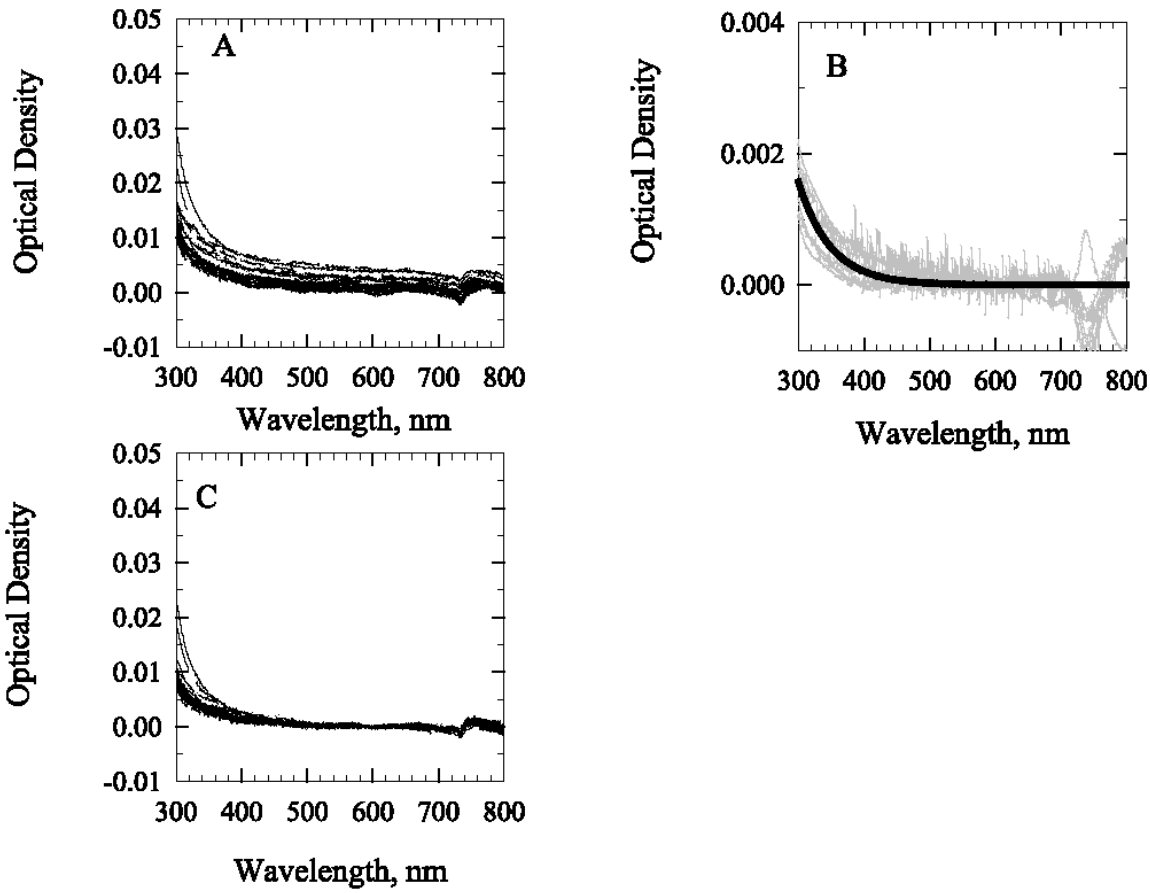

Figure 15.3: Typical results for soluble absorption determined during the ACE-Asia cruise (March – April 2001) in the western Pacific according to the protocols recommended here. **A)**. Raw optical density, $OD_s(\lambda)$, for samples relative to Millipore Alpha-Q water. **B)**. Blank optical density spectra, $OD_{bs}(\lambda)$ (after null offset, gray) compared to a global value (solid line). The global blank is determined by fitting an exponential function to the mean blank for more than 15 cruises from 1998-2001 where the mean for each cruise was determined as the mean of all individual blanks for each cruise. A fitted curve to a cruise or global mean for $OD_{bs}(\lambda)$ is recommended for correction of the soluble sample blank because individual spectra (gray) have significant instrument noise. Note the scale for 3B is approximately 10x smaller than the scale in 3A. **C)**. Estimates of sample optical density spectra after subtraction of the null value (average of raw values 590-600nm) and after subtraction of a global blank according to Equation 15.3. Temperature effects are evident 650-800 nm in the individual spectra.

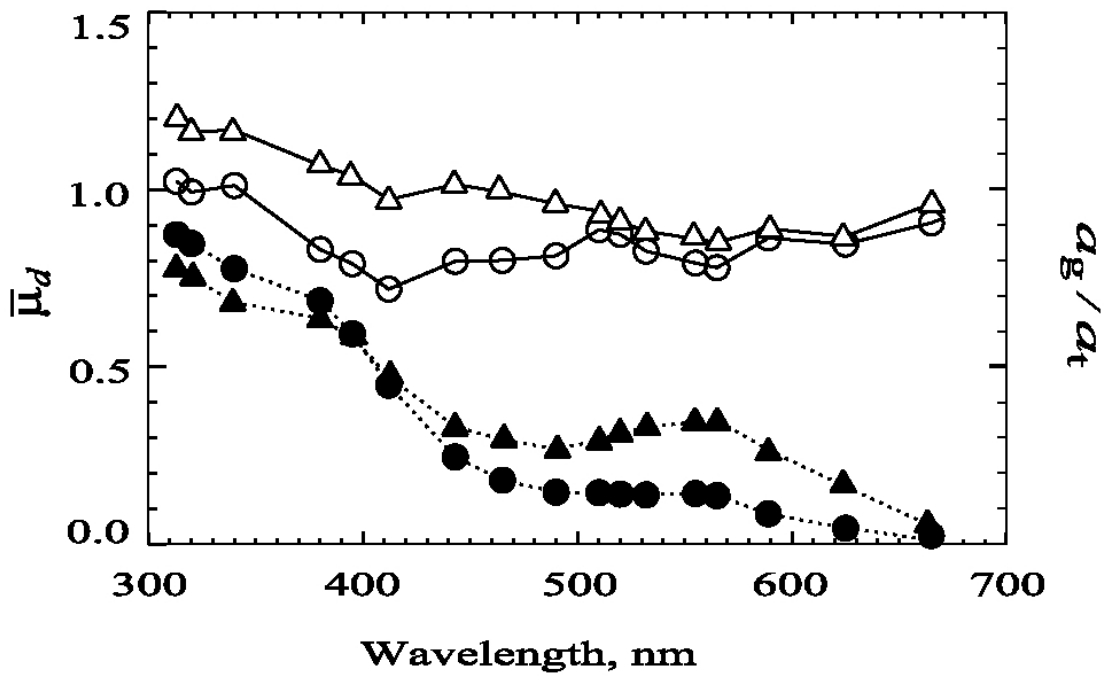

Figure 15.4: Median values for $\bar{\mu}_d(\lambda)$, the mean cosine for downwelling irradiance (open symbols, see text for definition) determined for the upper mixed layer. Values are plotted at each wavelength of the PRR 800 reflectance radiometer deployed during 2001 cruises to the Southern Ocean (AMLR) and the Western Pacific (ACE-Asia). The ratio of $a_g(\lambda)/a_t(\lambda)$ for the same data set are shown in solid symbols and plotted to the same scale. For both sets of spectra, AMLR data are circles and ACE-Asia data are triangles.

Chapter 16

HPLC Phytoplankton Pigments: Sampling, Laboratory Methods, and Quality Assurance Procedures

Robert R. Bidigare[1], Laurie Van Heukelem[2] and Charles C. Trees[3]

[1] *Department of Oceanography, University of Hawaii, Hawaii*

[2]*Horn Point Environmental Laboratory, University of Maryland, Maryland*

[3]*Center for Hydro-Optics and Remote Sensing, San Diego State University, California*

16.1 INTRODUCTION

Marine phytoplankton utilize chlorophyll *a* as their major light harvesting pigment for photosynthesis. Other accessory pigment compounds, such as chlorophylls *b* and *c*, carotenoids and phycobiliproteins, also play a significant role in photosynthesis by extending the organism's optical collection window, thereby improving absorption efficiencies and adaptation capabilities. The important chlorophyll degradation products found in the aquatic environment are the chlorophyllides, phaeophorbides, and phaeophytins. The presence, or absence, of the various photosynthetic pigments is used to separate the major algal groups, and to map the chemotaxonomic composition of phytoplankton in the oceans.

The unique optical properties of chlorophyll *a* have been used to develop spectrophotometric (Jeffrey and Humphrey 1975) and fluorometric (Holm-Hansen *et al.* 1965) measurement techniques. With the commercial availability of fluorometers for routine measurements of chlorophyll *a*, this pigment became a universal parameter in biological oceanography for estimating phytoplankton biomass and productivity. These optical methods can significantly under- or overestimate chlorophyll *a* concentrations, because of the overlap of the absorption and fluorescence bands of co-occurring chlorophylls *b* and *c*, chlorophyll degradation products, and accessory pigments (Trees *et al*. 1985; Smith *et al.* 1987; Hoepffner and Sathyendranath 1992; Bianchi *et al.* 1995; Tester et al. 1995).

The application of HPLC to phytoplankton pigment analysis has lowered the uncertainty for measuring chlorophyll *a* and pheopigments, as well as the accessory pigments, since compounds are physically separated and individually quantified. HPLC has provided oceanographers with a powerful tool for studying the processes affecting the phytoplankton pigment pool. Pigment distribution is useful for quantitative assessment of phytoplankton community composition, phytoplankton growth rate and zooplankton grazing activity.

For low uncertainty determinations of chlorophylls *a*, *b*, and *c*, chlorophyll degradation products, and carotenoid pigments, HPLC techniques are recommended. It should be noted, however, that the reverse-phase C_{18} HPLC method recommended by the Scientific Committee on Oceanographic Research (SCOR) (Wright et al. 1991) is not capable of separating monovinyl chlorophyll *a* from divinyl chlorophyll *a*, nor monovinyl chlorophyll *b* from divinyl chlorophyll *b*. This method, therefore, only provides *estimates*; methods for optically resolving monovinyl chlorophyll *a* and divinyl chlorophyll *a* are given below.

Divinyl chlorophyll *a*, the major photosynthetic pigment found in *Prochlorococcus*, accounts for 10 % to 60 % of the total chlorophyll *a* in subtropical and tropical oceanic waters (Goericke and Repeta 1993; Letelier *et al.* 1993; Andersen *et al*. 1996; Bidigare and Ondrusek 1996; Gibb *et al.* 2000). Divinyl chlorophyll *a* is spectrally different from *normal* (monovinyl) chlorophyll *a* and its presence results in a significant overestimation of total chlorophyll *a* concentration as determined by the conventional HPLC methods (Goericke and Repeta 1993; Letelier *et al.* 1993; Latasa *et al.* 1996). To avoid these errors, it is recommended that monovinyl and divinyl chlorophyll *a* be spectrally resolved, or chromatographically separated, to obtain an unbiased determination of total chlorophyll *a* for ground-truthing satellite ocean color algorithms and imagery. Total chlorophyll *a*, TChl *a*, is the sum of divinyl chlorophyll *a*, monovinyl chlorophyll *a*, chlorophyllide *a*, and chlorophyll *a* epimers and allomers. These co-eluting chlorophyll species can be resolved spectrally following C_{18} HPLC chromatography (Wright et al. 1991) and quantified

using dichromatic equations at 436 nm and 450 nm (Latasa *et al.* 1996). Alternatively, these two chlorophyll species can be separated chromatographically and individually quantified using C_8 HPLC techniques (see below).

The protocols specified below for HPLC pigment analyses follow closely those prescribed in the *JGOFS Core Measurement Protocols* (UNESCO 1994). Both sets of protocols include:

1. Use of Whatman GF/F glass fiber filters, approximately 0.7 μm pore size;
2. Extraction in aqueous acetone; and
3. Calibration with standards.

The present protocols differ from the JGOFS protocols in one critical respect. Absorption of light in seawater, or any other medium, is a volumetric process, even though the volume absorption coefficient may vary with the density of the medium. For ocean color and optical analyses, therefore, the concentrations in seawater of all phytoplankton pigments shall be expressed in units of mass per unit volume of seawater ($\mu g\ L^{-1}$ or $mg\ m^{-3}$). This differs from the JGOFS protocols, which specify that concentrations in seawater of all phytoplankton pigments should be expressed in $ng\ Kg^{-1}$.

In addition to HPLC analyses, it is recommended that the standard fluorometric methodology used for measuring chlorophylls and pheopigments (Holm-Hansen *et al.* 1965, Strickland and Parson 1972) also be applied to the same extracted pigment samples used for HPLC analysis. Protocols for fluorometric measurements of chlorophyll *a* and pheopigments are given here in Chapter 17. For a more in depth review of guidelines for measuring phytoplankton pigments in oceanography see Jeffrey *et al.* (1997)

16.2 SAMPLING PROTOCOLS FOR PHYTOPLANKTON PIGMENTS

Water Samples

Water samples should be taken using, *e.g.*, Niskin bottles at the site of, and simultaneously with, the surface in-water upwelled radiance and reflectance measurements, and at depth increments sufficient to resolve variability within at least the top optical depth. The $K(z,\lambda)$, profiles over this layer will be used to compute optically weighted, near-surface pigment concentration for bio-optical algorithm development (Gordon and Clark 1980).

When possible, samples should be acquired at several depths distributed throughout the upper 200 m of the water column [or in turbid water, up to seven diffuse attenuation depths, *i.e.* $\ln(E(z,\lambda)/E(z,\lambda))=7$, to provide a basis for relating fluorescence signals to pigment mass concentrations.

Samples should be filtered as soon as possible after collection. If processing must be delayed for more than an hour, hold the samples on ice, or in a freezer at 4°C, and protect them from exposure to light. For delays longer than several hours, the samples should be stored in liquid nitrogen. Use opaque sample bottles, because even brief exposure to light during sampling and/or storage might alter pigment values.

Filtration

Whatman GF/F glass fiber filters, with approximately 0.7 μm pore size, are preferred for removing phytoplankton from water. The glass fibers assist in breaking the cells during grinding, accommodate larger sample volumes, and do not form precipitate forms after acidification. Twenty-five mm diameter GF/F glass fiber filters should be used with vacuum (7-8 inches of mercury) or positive pressure (1-2 psi). Positive pressure filtration is recommended, because it filters larger volumes of water at reduced filtration times. The only problem with vacuum filtration is that unobservable air leaks may occur around the filtration holder, and as a result the pressure gradient across the filter is much less than what is indicated on the vacuum gauge. When positive filtration is used, any leakage around the filter holder results in observable dripping water.

Inert membrane filters, such as polyester filters, may be used when size fraction filtration is required. When this is done, it is recommended to also filter a replicate sample through a GF/F to determine the total concentration. Summing the various size-fractionated concentrations may not produce an accurate estimate of the total, because of the potential for cell disruption during filtration.

There has been an ongoing discussion of filter types and retention efficiencies for natural samples. Phinney and Yentsch (1985) showed the inadequacy of GF/F filters for retaining chlorophyll *a* in oligotrophic waters, as did Dickson and Wheeler (1993) for samples from the North Pacific. In response to Dickson and Wheeler (1993), Chavez *et al.* (1995) compared samples collected in the Pacific Ocean using GF/F and 0.2 µm membrane filters with small filtered volumes (100 mL to 540 mL). Their results showed a very close agreement between the two filter types, with GF/F filters having only a slightly positive 5 % bias.

Filtration volume can directly affect the retention efficiency for GF/F filters. Particles can be retained by filters through a variety of ways, such as filter sieving, filter adsorption, electrostatic and van der Waals attractions (Brock, 1983). When water flows through the pores of a Nuclepore filter, streamlines are formed that can align small particles longitudinally, with the result that cell diameter becomes important with these filters. It is known, on the other hand, that Whatman GF/F filters can retain particles much smaller than their rated pore size. Generally, at small volumes (100 mL to 300 mL) filter adsorption, and electrostatic and van der Waals attractions are important, whereas at larger volumes (>2,000 mL) sieving dominates. This has been tested in oligotrophic waters off Hawaii in which small (<500 mL) and large volumes (> 2 L to 4 L) retained similar amounts of chlorophyll *a* on the two types of filters, whereas for intermediate sample volumes the GF/F filters showed lower concentrations. During several cruises off the Hawaiian Islands, differences in retention efficiencies were found for GF/F filters to be a function of sample volume; large sample volumes (2 L and 4 L) retained about 18 % more chlorophyll *a* than replicate 1 L samples.

Filtration volumes are usually limited by the concentration of particles present in each sample. For HPLC analysis it is important to filter as large a volume as possible, so as to accurately measure most of the major pigments. A qualitative check to determine whether a large enough volume has been filtered is to count the number of accessory pigments (chlorophylls *b*, c_1, c_2, c_3, and carotenoids) quantified, excluding chlorophyll degradation products (Trees et al. 2000). Most algal groups (excluding phycobiliprotein-containing groups) contain at least *four* HPLC-measurable accessory pigments (see Jeffrey et al. 1997). Therefore, pigment samples that do not meet this minimum accessory pigment criterion may have detection limit problems related to low signal-to-noise ratios for the HPLC detectors and/or inadequate concentration techniques (e.g. low filtration volumes). It is generally recommended that the following volumes be filtered for HPLC pigment analyses: 3 L to 4 L for oligotrophic waters, 1 L to 2 L for mesotrophic waters, and 0.5 L to 1 L for eutrophic waters.

It is recommended to not pre-filter seawater samples to remove large zooplankton and particles, because this practice may exclude pigment-containing colonial and chain-forming phytoplankton, such as diatoms and *Trichodesmium* sp. Forceps may be used to remove large zooplankton from the GF/Fs following filtration.

Sample Handling and Storage

Samples should be filtered as quickly as possible after collection and stored immediately in liquid nitrogen. Liquid nitrogen is the best method for storing samples with minimum degradation for short, as well as, longer storage times (*e.g.* 1 year). Placing samples in liquid nitrogen also assists in pigment extraction by weakening the cell wall and membrane during this rapid temperature change. Ultra-cold freezers (-90 ^{o}C) can be used for storage, although they have not been tested for longer than 60 days (Jeffrey et al. 1997). Conventional deep freezers should not be used for storing samples more than 20 hours before transferring them to an ultra-cold freezer, or liquid nitrogen. Again, storage of samples in liquid nitrogen immediately after filtration is the preferred method.

Samples should be folded in half with the filtered halves facing in. This eliminates problems of rubbing particles off the filter during placement in sample containers and storage.

It is strongly recommended to use aluminum foil wrappings for sample containers. This simple, but effective, container is both inexpensive and easy to use. Cut small pieces of heavy-duty aluminum foil into approximately 4 cm squares. Fold each piece in half, and using a fine-point permanent marker, write a short sample identifier (*e.g.* first letter of the cruise and a sequential sample number) on the foil. Writing on the folded foil, prior to placement of the filter, both avoids puncturing the foil with the marking pen, and improves the legibility of the sample identifier. Place the folded filter in the aluminum foil. Fold the three open sides to form an envelope that is only slightly larger than the folded filter (~3 cm x 1.5 cm).

The use of foil containers minimizes the size requirement of the storage container. It is also acceptable to use either cryogenic tubes, or HistoPrep tissue capsules, but they occupy more storage volume per sample, and they are more expensive than aluminum foil. If fluorometric analysis is to be done soon after collection, it is still recommended to place the samples in liquid nitrogen to assist in pigment extraction, and on removal from the liquid nitrogen to place them immediately in chilled 90 % acetone.

Recordkeeping

Information regarding sample identification should be logged in a laboratory notebook with the analyst's initials. For each filter sample record the sample identifier (as written on the sample container), station number for the cruise, water volume filtered (V_{FILT}) in mL, and depth of the water sample, together with the date, time, latitude, and longitude of the bottle cast during which the sample was acquired.

16.3 LABORATORY METHODS FOR HPLC PHYTOPLANKTON PIGMENT ANALYSIS

Internal Standard and Solvent Preparation

In addition to daily calibration of the HPLC system with external standards, an internal standard (*e.g.* canthaxanthin) should be used to determine the extraction volume. It is important to verify that the internal standard employed is not a *naturally* occurring analyte in the field samples to be analyzed by HPLC. Canthaxanthin is recommended as an internal standard because it has a restricted distribution in ocean waters, and it is readily available in high purity from commercial sources. For additional background on the use of internal standards see Snyder and Kirkland (1979). The internal standard should be added to the sample prior to extraction and used to correct for the addition of GF/F filter-retained seawater and sample volume changes during extraction. When new external and internal standards are prepared they should be verified against previous standards and a standard reference solution if available. An internal standard with an HPLC peak removed from those of all the pigments, canthaxanthin, is added at a fixed concentration to the HPLC-grade acetone solvent used to extract the pigments from the filtered samples. A sample of canthaxanthin spiked acetone solvent is injected into the HPLC system and its peak area $A_{\mathrm{STD}}^{\mathrm{Cantha}}$ is recorded to provide a baseline internal standard for monitoring the solvent concentration in each extracted sample.

Extraction

Filters are removed from the liquid nitrogen, briefly thawed (~1 min), and placed in glass centrifuge tubes for extraction in acetone. Three mL HPLC-grade acetone is added to each tube, followed by the addition of a fixed volume of internal standard (typically 50 µL canthaxanthin in acetone). Alternatively, canthaxanthin spiked HPLC-grade acetone solvent may be prepared in advance, in a batch large enough for all samples, and 3 mL is added to each tube in a single step. Since GF/F filters retain a significant amount of seawater following filtration (ca. 0.2 mL per 25 mm filter), the final acetone concentration in the pigment extracts is ~ 94 % (acetone:water, by volume); by measuring the canthaxanthin peak area $A_{\mathrm{STD}}^{\mathrm{Cantha}}$ for each sample, the ratio $A_{\mathrm{STD}}^{\mathrm{Cantha}} / A_{\mathrm{Sample}}^{\mathrm{Cantha}}$ may be used to adjust for sample to sample variations in the extraction volume.

Samples are disrupted by sonication, placed in a freezer, and allowed to extract at 0°C for 24 h. Alternatively, the cells can be mechanically disrupted using a glass/Teflon tissue grinder and allowed to extract at 0°C for 24 h. If after disrupting the cells, it is necessary to rinse the tissue grinder, or mortar and

pestle, then a known volume of 90 % acetone, measured using a Class A volumetric pipette, should be used. The ease with which the pigments are removed from the cells varies considerably with different phytoplankton. In all cases, freezing the sample filters in liquid nitrogen improves extraction efficiency.

Prior to analysis, pigment extracts are vortexed and centrifuged to minimize cellular debris. To remove fine glass fiber and cellular debris from the extract, as well as enhance the life expectancy of the HPLC column, filter the extract through 13 mm PTFE (polytetrafluoroethylene) membrane syringe filters (0.2 μm pore size). The use of Nylon filters is not recommended as they may bind certain hydrophobic pigments.

Apparatus

The HPLC system consists of solvent pumps, sample injector, guard and analytical columns, absorption (and fluorescence) detector, and a computer. A temperature-controlled autosampler is optional, but highly recommended, to chill the samples chilled prior to injection and to reduce uncertainties during sample preparation and injection. A variety of companies manufacture HPLC systems (e.g. Agilent Technologies, Beckman, ThermoQuest, Waters Associates). For a review of hardware and software requirements for measuring chlorophylls and their degradation products, as well as carotenoids, see Jeffrey *et al.* (1997).

HPLC Eluants and Gradient Programs

There are several currently recognized HPLC methods for separating chlorophylls, chlorophyll derivatives and taxonomically important carotenoids. The C_{18} method of Wright *et al.* (1991) is recommended by SCOR and separates more than 50 chlorophylls, carotenoids, and their derivatives using a ternary gradient system. This HPLC method is described in detail below. Briefly, pigments are separated on an Spherisorb ODS-2 C_{18} column using a three solvent gradient system [Solvent A: 80:20 methanol: 0.5 M ammonium acetate (by volume); Solvent B: 90:10 acetonitrile: water (by volume); Solvent C: ethyl acetate] at a flow rate of 1 mL min^{-1}. The separation of the various pigments requires about 30 minutes. Prior to injection, 1000 μL of the aqueous acetone pigment extract is diluted with 300 μL HPLC-grade water to increase the affinity of pigments for the column during the loading step. This procedure results in sharper peaks, allowing greater loading than can be obtained with undiluted samples.

This method does not separate monovinyl and divinyl chlorophylls *a* and *b*. The presence of divinyl chlorophylls *a* and *b*, can cause errors if they are not separated either physically on the column, or by a channels ratio method from the monovinyl forms. Latasa *et al.* (1996) showed that the use of a single response factor (only for monovinyl chlorophyll *a*) could result in a 15 % to 25 % overestimation of total chlorophyll *a* concentration if divinyl chlorophyll *a* was present in significant concentrations. Although monovinyl and divinyl chlorophyll *a* co-elute, each compound absorbs differently at 436 nm and 450 nm and it is therefore possible to deconvolve the absorption signals due to these pigments (Latasa *et al.* 1996).

Alternatively, these two chlorophyll species can be separated chromatographically and individually quantified using the C_8 HPLC techniques described by Goericke and Repeta (1993) and Van Heukelem and Thomas (2001). The latter technique uses a two solvent system and elevated column temperature to achieve desired separations.

Regardless of the method or column-packing material used (C_{18} or C_8), it is important that HPLC performance be validated before and during use. This would include validation that resolution between peaks is acceptable, or when peaks are not chromatographically resolved, that equations based on spectral deconvolution are possible in order to quantify relative proportions of each pigment in a co-eluting pair (*Sect. 16.4 below*).

Determination of Algal Chlorophyll and Carotenoid Pigments by HPLC (Wright et al. 1991):

a. Equipment and reagents:

1. *Reagents*: HPLC grade acetone (for pigment extraction); HPLC-grade water, methanol, acetonitrile and ethyl acetate; 0.5 M ammonium acetate aq. (pH = 7.2); and BHT (2,6-di-tert-butyl-p-cresol, Sigma Chemical Co.).

2. *High-pressure injector valve* equipped with a 200 µL sample loop.
3. *Guard-column* (50 mm x 4.6 mm, ODS-2 Spherisorb C_{18} packing material, 5 µm particle size) for extending the life of the primary column.
4. *Reverse-phase HPLC column* with end capping (250 mm x 4.6 mm, 5 µm particle size, ODS-2 Spherisorb C_{18} column).
5. *Variable wavelength or filter absorbance detector* with low volume flow through cell. Detection wavelengths are 436 nm and 450 nm.
6. *Data recording device*: a strip chart recorder, or preferably, an electronic integrator and computer equipped with hardware and software for chromatographic data analysis.
7. *Glass syringe (500 µL) or HPLC autosampler.*
8. *HPLC Solvent*: solvent A (80:20, by volume; methanol:0.5 M ammonium acetate aq., pH=7.2; 0.01 % BHT, w:v), solvent B (87.5:12.5, by volume; acetonitrile:water; 0.01 % BHT, w:v) and solvent C (ethyl acetate). Solvents A and B contain BHT to prevent the formation of chlorophyll *a* allomers. Use HPLC-grade solvents. Measure volumes before mixing. Filter solvents through a solvent resistant 0.4 µm filter before use, and degas with helium, or an in-line vacuum degassing system, during analysis.
9. *Calibration standards*: Chlorophylls *a* and *b* and β, and β-carotene can be purchased from Sigma Chemical Co. (St. Louis, MO 63178, USA). Other pigment standards can be purchased from the International Agency for ^{14}C Determination, VKI Water Quality Institute, Agern Allé 11, DK-2970 HØrsholm, Denmark. The concentrations of all standards in the appropriate solvents should be determined, using a monochromator-based spectrophotometer, prior to calibration of the HPLC system (Latasa *et al.* 1999). Spectrophotometric readings should be made at a bandwidth $\leq$ 2 nm and the optical density (*OD*) of the pigment standards should range between 0.2 to 0.8 OD units at λ_{max} (Marker *et al.* 1980). The recommended extinction coefficients for the various phytoplankton pigments can be found in Appendix E of Jeffrey *et al.* (1997). Absorbance is measured in a 1 cm cuvette at the peak wavelength λ_{max}, and at 750 nm to correct for light scattering.

   Concentrations of the standards are calculated as

$$C^i_{\mathrm{STD}} = \frac{10^6[A^i(\lambda^i{}_{\max}) - A^i(750)]}{bE^i_{1\mathrm{cm}}}, \tag{16.1}$$

   where C^i_{STD} is the concentration (µg L^{-1}) of the standard for pigment *i*, $A^i\left(\lambda^i{}_{\max}\right)$ and $A^i(750)$ are absorbances at $\lambda^i{}_{\max}$ and 750 nm, respectively, *b* is the pathlength of the cuvette (cm), and $E^i_{1\mathrm{cm}}$ is the weight-specific absorption coefficient (L g^{-1} cm^{-1}) of pigment *i*. Values for $\lambda^i{}_{\max}$ and $E^i_{1\mathrm{cm}}$ are given in Appendix E of Jeffrey *et al.* (1997). Standards stored under nitrogen in the dark at -20°C do not change appreciably over a one-month period, provided that they are stored in containers proven to prevent evaporation (*e.g.* glass or Teflon bottles/vials).

b. Procedure:

1. Set up and equilibrate the HPLC system with eluant A at a flow rate of 1 mL min^{-1}.
2. Calibrate the HPLC system using working standards prepared, on the day of use, by diluting the primary standard with the appropriate solvent (Jeffrey *et al.* 1997, Appendix E). When preparing calibration standards, one should only use dilution devices for which the precision and uncertainty have been validated with the solvent to be measured. Prepare at least 5 concentrations (µg L^{-1}) of working standards for each pigment spanning the concentration range appropriate for the samples to be analyzed.
3. For each working standard, mix 1000 µL with 300 µL of distilled water, shake, and equilibrate for 5 min prior to injection (diluting the standards and sample extracts with water increases the affinity of pigments for the column in the loading step, resulting in an improved separation of the

more polar pigments). Rinse the sample syringe twice with 300 µL of the diluted working standard and draw 500 µL of the working standard into the syringe for injection. Place the syringe in the injector valve, overfilling the 200 µL sample loop 2.5-fold. To check for possible interferences in the extraction solvent and/or filter, prepare a blank by extracting a glass fiber filter in 90 % acetone, mixing 1000 µL of the 90 % acetone filter extract and 300 µL distilled water, and injecting the mixture onto the HPLC system. For each pigment *i*, plot absorbance peak areas (arbitrary system units) against working standard pigment masses (concentrations multiplied by injection volume). The HPLC system response factor F^i (area μg^{-1}) for pigment *i* is calculated as the slope of the regression of the peak areas of the parent pigment (plus areas of peaks for structurally-related isomers if present) against the pigment masses of the injected working standards (µg). Structurally related isomers (*e.g.* chlorophyll *a* allomer) contribute to the absorption signal of the standards and disregarding them will result in the over-estimation of analytes in sample extracts (Bidigare 1991).

4. Prepare pigment samples for injection by mixing a 1000 µL portion of the aqueous acetone pigment extract and 300 µL distilled water, shake, and equilibrate for 5 min prior to injection. Inject the sample onto the HPLC column. Samples that are pre-mixed with distilled water (or other injection buffer) should not be allowed to reside in autosampler compartments for extended durations, because hydrophobic pigments will precipitate out of solution (Mantoura et al. 1997). For additional information regarding HPLC method implementation and injection conditions see Wright and Mantoura (1997).

5. Following injection of the sample onto the HPLC system, use a gradient program to optimize the separation of chlorophyll and carotenoid pigments (Table 16.1). Degas solvents with helium or an in-line vacuum degassing system during analysis. It should be noted that method performance varies significantly between HPLC systems because of differences in dwell volume, equilibration time, and injection conditions. It is, therefore, recommended that analysts validate that desired peak separations are attained for pigment pairs of interest by calculating the peak resolution indices R_s as

$$R_s = \frac{2\left(t_{R2} - t_{R1}\right)}{w_{B1} + w_{B2}}, \tag{16.2}$$

where t_{R1} and t_{R2} are the retention times (min) of peaks 1 and 2, and w_{B1} and w_{B2} are the widths (min) of peaks 1 and 2 at their respective bases (Wright 1997). Peak separation values $R_s < 1.0$ are insufficient for accurate quantification of peak areas (Wright 1997).

6. Peak identities are routinely determined by comparing the retention times of sample peaks with those of pure standards. Peak identities can be confirmed spectrophotometrically by collecting eluting peaks from the column outlet (or directly with an on-line diode array spectrophotometer). Absorption maxima for the various phytoplankton pigments can be found in Part IV of Jeffrey *et al.* (1997).

7. Calculate individual pigment concentrations as

$$C^i_{\text{Sample}} = \frac{A^i_{\text{Sample}} V_{\text{Extracted}} A^{\text{Cantha}}_{\text{STD}}}{F^i V_{\text{Injected}} V_{\text{Sample}} A^{\text{Cantha}}_{\text{Sample}}}, \tag{16.3}$$

where C^i_{Sample} is the individual pigment concentration ($\mu g\ L^{-1}$), A^i_{Sample} is the area of individual pigment peak for a sample injection, $V_{\text{Extracted}}$ is the volume extracted (mL, to nearest 0.1 mL), V_{Injected} is the volume injected (mL, measured to the nearest 0.001 mL), V_{Sample} is the sample volume filtered (L, measured to the nearest 0.001 L), and the other coefficients are defined above.

8. This method is designed for the separation of chlorophyll and carotenoid pigments, but it is also capable of separating the major chlorophyll breakdown products.

9. The uncertainty of the HPLC method was assessed by performing triplicate injections of a mixture of phytoplankton and plant extracts; coefficients of variation (standard deviation/mean x 100 %) ranged from 0.6 % to 6.0 %. The use of an appropriate internal standard, such as canthaxanthin, will decrease the uncertainty.

16.4 QUALITY ASSURANCE PROCEDURES

Quality assurance procedures outlined here should be routinely employed to insure accurate, precise and representative results.

As a means of monitoring an instrument's performance, individual pigment response factors (F^i) should be charted as functions of time (Clesceri *et al.* 1998). These quality control graphs should be retained with the data analysis logbooks to document the quality of each data set.

A selected number of samples should be analyzed in duplicate (or triplicate) to assess representativeness and uncertainty in the method and instrumentation. In multi-ship/investigator studies, replicate samples should be collected and archived for future intercalibration checks.

Fortified samples should be analyzed as part of the quality assurance effort. Fortified samples are prepared in duplicate by spiking a sample with known quantities of the analytes of interest at concentrations within the range expected in the samples. Fortified samples are used to assess the method's uncertainty in the presence of a typical sample matrix.

The method detection limit (*MDL*) for the analytes of interest can be determined by measuring seven replicate standard injections (Glaser et al. 1981). The standard deviation S_c of the seven replicate measurements is calculated, and the *MDL* is computed as

$$MDL = t(6, 0.99) S_c. \tag{16.4}$$

where $t(6, 0.99)$ is the Student's t value for a one-tailed test at the 99 % confidence level, with (N-1)=6 degrees of freedom. For this particular sample size (N=7) and the 99% confidence level, $t(6, 0.99) = 3.707$ (Abramowitz and Segun 1968, Table 26.10).

System and spiked blanks should be routinely analyzed. A system blank consists of a filter, reagents, and the glassware and hardware utilized in the analytical scheme. The system blank is quantified under identical instrumental conditions as the samples and is analyzed by appropriate quantitative methods. The system blank may not contain any of the analytes of interest above the *MDL* or corrective action must be taken. A spiked blank is defined as a system blank plus an authentic external standard containing the analytes of interest. Each set of samples should be accompanied by a spiked blank and is quantified under the same instrumental conditions as the samples.

16.5 PROTOCOL STATUS AND FUTURE DIRECTIONS FOR RESEARCH

Recent studies have identified the presence of novel bacterial phototrophs in coastal and oceanic waters. These include proteorhodopsin-containing *Bacteria* (Béjà *et al.* 2000, 2001) and anoxygenic aerobic phototrophic *Bacteria* (Kolber *et al.* 2000, 2001). Sequence analysis of BAC clone libraries prepared from Monterey Bay, Station ALOHA and the Southern Ocean revealed that numerous uncultivated members of the γ-*Proteobacteria* contain genes that code for proteorhodopsin. This membrane-bound pigment contains *trans*-retinal, absorbs at blue-green to green wavelengths, and functions as a light-driven proton pump. In an unrelated study, Kolber *et al.* (2000) used an infrared fast repetition rate (IRFRR) fluorometer to document the widespread occurrence of anoxygenic aerobic phototrophs (AAPS) in the world oceans. These microbes possess low amounts of bacteriochlorophyll *a* (λ_{max} = 358, 581 and 771 nm) and unusually high levels of bacteriocarotenoids (λ_{max} = 454, 465, 482 and 514 nm). They require molecular oxygen for growth. One of us (RRB) has initiated HPLC pigment analysis of these latter clones and retinal-related compounds to determine if the Wright *et al.* (1991) method can be used for their separation and quantification.

REFERENCES

Abramowitz, A. and I.A. Segun, 1968: Handbook of Mathematical Functions, Dover, New York (5th Printing), 1046pp.

Andersen, R.A., R.R. Bidigare, M.D. Keller, and M. Latasa, 1996: A comparison of HPLC pigment signatures and electron microscopic observations for oligotrophic waters of the North Atlantic and Pacific Oceans. *Deep-Sea Res. II*, **43**, 517-537.

Béjà O, L. Aravind, E. V. Koonin, M. T. Suzuki, A. Hadd, L. P. Nguyen, S. B. Jovanovich, C. M. Gates, R. A. Feldman, J. L. Spudich, E. N. Spudich, and E. F. DeLong, 2000: Bacterial rhodopsin: Evidence for a new type of phototrophy in the sea. *Science*, **289**, 1902-1906.

Béjà, O., E. N. Spudich, J. L. Spudich, M. LeClerc, and E. F. DeLong, 2001: Proteorhodopsin phototrophy in the ocean. *Nature*, **411**, 786-789.

Bianchi, T. S., C. Lambert, and D. C. Biggs. 1995: Distribution of chlorophyll *a* and pheopigments in the northwestern Gulf of Mexico: a comparison between fluorometric and high-performance liquid chromatography measurements. *Bull. Mar. Science* **56** ,25-32.

Bidigare, R.R., 1991: Analysis of algal chlorophylls and carotenoids. In: *Marine Particles: Analysis and Characterization*, D.C. Hurd and D.W. Spencer, Eds., Am. Geophys. Union, Washington, DC, 119-123.

Bidigare, R.R., and M.E. Ondrusek, 1996: Spatial and temporal variability of phytoplankton pigment distributions in the central equatorial Pacific Ocean. *Deep-Sea Res. II*, **43**, 809-833.

Brock, T.D., 1983: *Membrane filtration: a user's guide and reference manual*. Science Tech., Madison, WI, 381 pp.

Chavez, F., K.R. Buck, R.R. Bidigare, D.M. Karl, D. Hebel, M. Latasa, L. Campbell, and J. Newton, 1995: On the chlorophyll *a* retention properties of glass-fiber GF/F filters. *Limnol. Oceanogr*., **40**, 428-433.

Clesceri, L.S., A.E. Greenberg, and A.D. Eaton (editors), 1998: Part 10000, Biological Examination, Section 1020 B. *in* Standard Methods for the Examination of Water and Wastewater. 20th ed. Balitmore (MD): American Public Health Association, American Water Works Association, Water Environment Federation.

Dickson, M.-L., and P.A. Wheller, 1993: Chlorophyll *a* concentrations in the North Pacific: Does a latitudinal gradient exist? *Limnol. Oceanogr*., **38**, 1813-1818.

Gibb, S.W, R.G. Barlow, D.G. Cummings, N.W. Rees, C.C. Trees, P. Holligan and D. Suggett, 2000: Surface phytoplankton pigment distribution in the Atlantic: an assessment of basin scale variability between 50°N and 50°S. Progress in Oceanography (in press).

Glaser, J.A., D.L. Foerst, G.D. McKee, S.A. Quave, and W.L. Budde, 1981: Trace analyses for wastewaters. *Environ. Sci. Technol.*, **15**, 1426-1435.

Goericke, R., and D.J. Repeta, 1993: Chlorophylls *a* and *b* and divinyl chlorophylls *a* and *b* in the open subtropical North Atlantic Ocean. *Mar. Ecol. Prog. Ser*., **101**, 307-313.

Gordon, H.R., and D.K. Clark, 1980: Remote sensing optical properties of a stratified ocean: an improved interpretation. *Appl. Optics*, **19**, 3,428-3,430.

Hoepffner, N., and S. Sathyendranath, 1992: Bio-optical characteristics of coastal waters: absorption spectra of phytoplankton and pigment distribution in the western North Atlantic. *Limnol. Oceanogr.* **37**,1660-1679.

Holm-Hansen, O., C.J. Lorenzen, R.W. Holmes, and J.D.H. Strickland, 1965: Fluorometric determination of chlorophyll. *J. du Cons. Intl. Pour l'Expl. de la Mer.*,**30**, 3-15.

Jeffrey, S.W., and G.F. Humphrey, 1975: New spectrophotometric equations for determining chlorophylls *a*, *b*, c_1 and c_2 in higher plants, algae and natural phytoplankton. *Biochem. Physiol. Pflanzen*, **167**, 191-194.

Jeffrey, S.W., R.F.C. Mantoura, and S.W. Wright (eds.), 1997: *Phytoplankton Pigments in Oceanography*, Monographs on Oceanographic Methodology, UNESCO, 661 pp.

Kolber, Z. S., C. L. Van Dover, R. A. Niederman, and P. G. Falkowski, 2000: Bacterial photosynthesis in surface waters of the open ocean. *Nature*, **407**, 177-179.

Kolber, Z. S., F. G. Plumley, A. S. Lang, J. T. Beatty, R. E. Blankenship, C. L. VanDover, C. Vetriani, M. Koblizek, C. Rathgeber, and P. G. Falkowski, 2001: Contribution of aerobic photoheterotrophic bacteria to the carbon cycle in the ocean. *Science*, **292**, 2492-2495.

Latasa, M., R. R. Bidigare, M. E. Ondrusek, and M. C. Kennicutt II, 1996: HPLC analysis of algal pigments: A comparison exercise among laboratories and recommendations for improved analytical performance. *Mar. Chem*., **5*1***, 315-324.

Latasa, M., R. R. Bidigare, M. E. Ondrusek, and M. C. Kennicutt II, 1999: On the measurement of pigment concentrations by monochromator and diode-array spectrophotometers. *Mar. Chem.*, **66**, 253-254.

Letelier, R.M., R.R. Bidigare, D.V. Hebel, M.E. Ondrusek, C.D. Winn, and D.M. Karl, 1993: Temporal variability of phytoplankton community structure at the U.S.-JGOFS time-series Station ALOHA ($22^0$45'N, 158^0W) based on HPLC pigment analysis. *Limnol. Oceanogr*., **38**, 1,420-1,437.

Mantoura, R.F.C., R.G. Barlow and E.J.H. Head, 1997: Simple isocratic HPLC methods for chlorophylls and their degradation products. Ch. 11 *in* Jeffrey, S.W., R.F.C. Mantoura, and S.W. Wright (editors), Phytoplankton pigment in oceanography: guidelines to modern methods. Vol. 10, Monographs on oceanographic methodology. UNESCO Publishing, 661 pp.

Marker, A.F.H., E.A. Nusch, H. Rai and B. Riemann, 1980: The measurement of photosynthetic pigments in freshwaters and standardization of methods: conclusion and recommendations. Arch. Hydrobiol. Beih. Ergebn. Limnol. **14**: 91-106.

Phinney, D.A., C.S. Yentsch, 1985: A novel phytoplankton chlorophyll technique: Toward automated analysis. *J. Plankton Res*., **7**, 633-642.

Smith, R. C., R. R. Bidigare, B. B. Prezelin, K. S. Baker, and J. M. Brooks, 1987: Optical characterization of primary productivity across a coastal front. *Mar. Biol*. **96**, 575-591.

Snyder, L.R. and Kirkland, J.J, 1979: Quantitative and trace analysis. In: Introduction to modern liquid chromatography, John Wiley and Sons, New York, 541-574.

Strickland, J.D.H., and T.R. Parsons, 1972: *A Practical Handbook of Sea Water Analysis*, Fisheries Research Board of Canada, 310 pp.

Tester, P. A., M. E. Geesey, C. Guo, H. W. Paerl, and D. F. Millie, 1995: Evaluating phytoplankton dynamics in the Newport River estuary (North Caroline, USA) by HPLC-derived pigment profiles. *Mar. Ecol. Prog. Ser*. **124**, 237-245.

Trees, C.C., M.C. Kennicutt II, and J.M. Brooks, 1985: Errors associated with the standard fluorometric determination of chlorophylls and pheopigments. *Mar. Chem*., **17**, 1-12.

Trees, C.C., D.C. Clark, R.R. Bidigare, M.E. Ondrusek and J.L. Mueller, 2000. Accessory pigments versus chlorophyll *a* concentrations within he euphotic zone: a ubiquitous relationship. *Limnol. Oceanogr*., **45**(5): 1130-1143.

UNESCO, 1994: Protocols for the Joint Global Ocean Flux Study (JGOFS) Core Measurements, Manual and Guides **29**, 170pp.

Van Heukelem, L. and C.S. Thomas, 2001: Computer-assisted high-performance liquid chromatography method development with applications to the isolation and analysis of phytoplankton pigments. *J. Crom. A*. **910**:31-49.

Wright, S.W., S.W. Jeffrey, R.F.C. Mantoura, C.A. Llewellyn, T. Bjornland, D. Repeta, and N. Welschmeyer, 1991: Improved HPLC method for the analysis of chlorophylls and carotenoids from marine phytoplankton. *Mar. Ecol. Prog. Ser.*, **77**, 183-196.

Wright, S.W., 1997: Summary of terms and equations used to evaluate HPLC chromatograms. Appendix H *in* Jeffrey, S.W., R.F.C. Mantoura, and S.W. Wright (editors), Phytoplankton pigment in oceanography: guidelines to modern methods. Vol. **10**, Monographs on oceanographic methodology. UNESCO Publishing, 661 pp.

Wright, S.W., and R.F.C. Mantoura, 1997: Guidelines for selecting and setting up an HPLC system and laboratory. Ch. 15 *in* Jeffrey, S.W., R.F.C. Mantoura, and S.W. Wright (editors), Phytoplankton pigment in oceanography: guidelines to modern methods. Vol. **10**, Monographs on oceanographic methodology. UNESCO Publishing, 661 pp.

Table 16.1 HPLC solvent programs (after Wright et al. 1991)

Time (min)	Flow Rate (mL min^{-1})	%A	%B	%C	Conditions
A. Analysis Protocol					
0.0	1.0	100	0	0	Injection
2.0	1.0	0	100	0	Linear gradient
2.6	1.0	0	90	10	Linear gradient
13.6	1.0	0	65	35	Linear gradient
18.0	1.0	0	31	69	Linear gradient
23.0	1.0	0	31	69	Hold
25.0	1.0	0	100	0	Linear gradient
26.0	1.0	100	0	0	Linear gradient
34.0	1.0	100	0	0	Hold
B. Shutdown Protocol					
0	1.0	100	0	0	Analysis complete
3.0	1.0	0	100	0	Linear gradient
6.0	1.0	0	0	100	Linear gradient
16.0	1.0	0	0	100	Washing
17.0	1.0	0	0	100	Shutdown

Chapter 17

Fluorometric Chlorophyll *a*: Sampling, Laboratory Methods, and Data Analysis Protocols

Charles C. Trees[1], Robert R. Bidigare[2], David M. Karl[2] Laurie Van Heukelem[3] and John Dore[2]

[1]*Center for Hydro-Optics & Remote Sensing, San Diego State University, California*
[2] *Department of Oceanography, University of Hawaii, Hawaii*
[3]*Horn Point Laboratory, University of Maryland Center for Environmental Science, Horn Point, Maryland*

17.1 INTRODUCTION

In addition to HPLC analyses, it is recommended that the standard fluorometric methodology used for measuring chlorophylls and pheopigments also be applied to (i) the same extracted pigment samples used for HPLC analysis, and (ii) additional independent samples. Analysis of fluorometric chlorophyll *a* concentration is a far simpler procedure than HPLC analysis, especially at sea. On a given research cruise, therefore, it is economically feasible to acquire and process many more fluorometric than HPLC samples and to statistically relate fluorometric and HPLC chlorophyll *a* concentrations using linear regression analysis. This additional analysis will also enable a direct link to the historical bio-optical algorithms and database development during the CZCS validation experiments.

Protocols for fluorometric determination of the concentrations of chlorophyll and pheopigments were developed initially by Yentsch and Menzel (1963) and Holm-Hansen et al. (1965), and are described in detail by Strickland and Parsons (1972). Holm-Hansen et al. (1965) and Strickland and Parsons (1972) used first principles of fluorescence spectroscopy to derive these fluorometric equations. The equation proposed by Yentsch and Menzel (1963) is only indirectly linked to first principles, through debatable assumptions, and its use is not recommended. Although these measurements have been shown to contain errors as compared to HPLC determinations (Trees et al. 1985; Smith et al. 1987; Hoepffner and Sathyendranath 1992; Bianchi et al. 1995; Tester et al. 1995), the CZCS phytoplankton pigment concentration algorithms were based on them entirely. The SeaWiFS protocols for this analysis will be those given in Strickland and Parsons (1972) as updated by this chapter.

Pigment databases generally show a log-normal distribution, which is consistent with that proposed by Campbell (1995) for bio-optical properties. Therefore, it is appropriate to perform log-linear regressions on HPLC determined total chlorophyll *a* (chlorophyllide *a*, chlorophyll *a* epimer, chlorophyll *a* allomer, monovinyl chlorophyll *a* and divinyl chlorophyll *a*) and fluorometrically determined chlorophyll *a*, using model I regressions. Standard Model I regressions were selected because HPLC determined total chlorophyll *a* concentrations are to be predicted from fluorometrically determined chlorophyll [Model I regressions are appropriate for both predictions and determining functional relationships, whereas Model II regressions should not be used to predict values of y given x (page 543, Sokal and Rohlf 1995)].

Examples of regression models predicting log HPLC total chlorophyll *a* (following Chapter 16 HPLC protocols) from log fluorometric chlorophyll *a* are shown in Figures 17.1, 17.2, and 17.3 for three cruises in different geographic areas. In each example, the regression slopes are significantly different from a one-to-one relationship, although for the Gulf of California (GoCAL November 1996, Figure 17.3) the slope is close to unity. One-to-one ratios have also been found for other geographic areas, but not necessarily during all seasons. Therefore, the relationship (slope and offset) between HPLC total chlorophyll *a* and fluorometric chlorophyll *a* must be determined for a selected number of samples for each cruise, so that a cruise-specific scaling factor can be applied to other fluorometric samples.

The protocols specified below for fluorometric chlorophyll *a* analyses follow closely those prescribed in the *JGOFS Core Measurement Protocols* (UNESCO 1994), but they differ in one important respect. Absorption of light in seawater, or any other medium, is a volumetric process, even though the volume absorption coefficient may vary with the density of the medium. For ocean color and optical analyses, therefore, the concentration of chlorophyll *a* shall be expressed in units of mass per unit volume of seawater, either in $\mu g\ L^{-1}$, or $mg\ m^{-3}$. This differs from the JGOFS protocols, which specify that concentrations in seawater of chlorophyll a and pheopigments should be expressed in $\mu g\ kg^{-1}$.

17.2 SAMPLE ACQUISITION AND STORAGE

Water samples should be taken using, e.g., Niskin bottles at the site of, and simultaneously with, the surface in-water upwelled radiance and reflectance measurements, and at depth increments sufficient to resolve variability within at least the top optical depth.

The K(z), profiles over this layer will be used to compute optically weighted, near-surface pigment concentration for bio-optical algorithm development (Gordon and Clark 1980). When possible, samples should also be acquired at several depths distributed throughout the upper 200 m of the water column [or in turbid water, up to seven diffuse attenuation depths, i.e. $\ln(E(0)/E(z))=7$, to provide a basis for relating fluorescence signals to pigment mass concentration.

Samples should be filtered as soon as possible after collection. If processing must be delayed for more than an hour, hold the samples on ice, or in a freezer at $4^{o}C$, and protect them from exposure to light. For delays longer than several hours, the samples should be stored in liquid nitrogen. Use opaque sample bottles, because even brief exposure to light during sampling and/or storage might alter pigment values.

Filtration

hatman GF/F glass fiber filters, with approximately 0.7 μm pore size, are preferred for removing phytoplankton from water. The glass fibers assist in breaking the cells during grinding and no precipitate forms after acidification. Twenty-five mm diameter GF/F glass fiber filters should be used with a vacuum or positive pressure with a pressure differential equivalent to 180-200 mm of mercury. Large filtration volumes are not required, because of the increased sensitivity of the fluorescence measurement.

Inert membrane filters, such as polyester filters, may be used when size fraction filtration is required. When this is done, it is recommended to also filter a replicate sample through a GF/F to determine the total concentration. Summing the various size-fractionated concentrations may not produce an accurate estimate of the total, because of the potential for cell disruption during filtration.

There has been an ongoing discussion on filter types and retention efficiencies for natural samples. Phinney & Yentsch (1985) showed the inadequacy of GF/F filters for retaining chlorophyll *a* in oligotrophic waters, as did Dickson and Wheeler (1993) for samples from the North Pacific. In response to Dickson and Wheeler (1993), Chavez et al. (1995) compared samples collected in the Pacific Ocean using GF/F and 0.2 μm membrane filters with small filtered volumes (100-540 mL). Their results for small volumes showed a very close agreement between the two filter types with GF/F filters having only a slightly positive 5% bias.

Filtration volume can directly affect the retention efficiency for GF/F filters. Particles can be retained by filters through a variety of ways, such as filter sieving, filter adsorption, electrostatic and van der Waals attractions (Brock, 1983). When water flows through the pores of a Nuclepore filter, streamlines are formed that can align small particles longitudinally, with the result that cell diameter becomes important with these filters. It is known, on the other hand, that Whatman GF/F filters can retain particles much smaller than their rated pore size. Generally, at small volumes (100-300 mL) filter adsorption, and electrostatic and van der Waals attractions are important, whereas at larger volumes (> 2,000 mL) sieving dominates. This has been tested in oligotrophic waters off Hawaii in which small (< 500 mL) and large volumes (> 2-4 liters) retained similar amounts of chlorophyll *a* on the two types of filters, whereas for intermediate sample volumes the GF/F filters showed lower concentrations. As a general rule, it is recommended that the following volumes be filtered for these water types: 0.5-1.0 liter for oligotrophic, 0.2-0.5 liter for mesotrophic, and 0.1 liter and less for eutrophic water.

It is recommended to not pre-filter seawater samples to remove large zooplankton and particles, because this practice may exclude pigment-containing colonial and chain-forming phytoplankton, such as diatoms and *Trichodesmium* sp. Forceps should be used to remove large zooplankton from the GF/Fs following filtration.

Sample Handling, and Storage

Samples should be filtered as quickly as possible after collection, and the filters stored immediately in liquid nitrogen. Liquid nitrogen is the best method for storing filter samples with minimum degradation for short, as well as, longer storage times (e.g. 1 year). Placing samples in liquid nitrogen also assists in pigment extraction by weakening the cell wall and membrane during this rapid temperature change. Ultra-cold freezers (-90°C) can be used for storage, although they have not been tested for longer than 60 days (Jeffrey et al. 1997). Conventional deep freezers should not be used for storing samples more than 20 hours before transferring them to an ultra-cold freezer, or liquid nitrogen.

Again, storage of samples in liquid nitrogen immediately after filtration is the preferred method. The addition of $MgCO_3$ at the end of the filtration process to stabilize chlorophyll has not been used for many years as a routine oceanographic method, because of the uncertainty in pigment absorption by $MgCO_3$.

If samples are to be stored for any length of time prior to fluorometric analysis, they should be folded in half with the filtered halves facing in. This eliminates problems of rubbing particles off the filter during placement in sample containers and storage.

It is strongly recommended to use aluminum foil wrappings for sample containers. This simple, but effective, container is both inexpensive and easy to use. Cut small pieces of heavy-duty aluminum foil into approximately 4 cm squares. Fold each piece in half, and using a fine-point permanent marker, write a short sample identifier (e.g. first letter of the cruise and a sequential sample number) on the foil. Writing on the folded foil, prior to placement of the filter, both avoids puncturing the foil with the marking pen, and improves the legibility of the sample identifier. Place the folded filter in the aluminum foil. Fold the three open sides to form an envelope that is only slightly larger than the folded filter (~3cm x 1.5cm).

The use of foil containers minimizes the size requirement of the storage container. It is also acceptable to use either cryogenic tubes, or HistoPrep tissue capsules, but they occupy more storage volume per sample, and they are more expensive than aluminum foil. If fluorometric analysis is to be done soon after collection, it is still recommended to place the samples in liquid nitrogen to assist in pigment extraction, and on removal from the liquid nitrogen toplace them immediately in chilled 90% acetone.

Recordkeeping

Information regarding sample identification should be logged in a laboratory notebook with the analyst's initials. For each filter sample record the sample identifier (as written on the sample container), station number for the cruise, water volume filtered (V_{FILT}) in mL, and depth of the water sample, together with the date, time, latitude, and longitude of the bottle cast during which the sample was acquired.

17.3 LABORATORY METHODS FOR FLUOROMETRIC DETERMINATION OF CHL. *a* AND PHEOPIGMENT CONCENTRATIONS

Chlorophyll and pheopigments can be determined using either a Turner Designs (or Sequoia) fluorometers equipped with the standard light sources and Corning excitation and emission filters, following the manufacture's recommendation for measuring extracted chlorophyll. The fluorometric instrument should be warmed-up for at least 30 to 45 minutes prior to making measurements.

Because of the acidification requirement for the standard fluorometric method (Holm-Hansen et al. 1965), differences in excitation and emission wavelength bands between fluorometers can produce uncertainties (Trees et al. 1985). The sensitivity with which a particular instrument is able to differentiate between chlorophyll and pheopigment is a function of the excitation wavelength. This effect is measured

during calibration of the fluorometer and is called the tau factor (τ). Saijo and Nishizawa (1969) have shown that τ can vary from 1 to 11.5, depending upon the excitation wavelength (in the range between 410 nm and 440 nm). For example, a comparison between aTurner Designs (Model 10-005R) analog fluorometer and a Turner Designs (Model 10-AU-005) digital fluorometer showed statistically significant differences for 42 oceanic samples (slope = 1.06), even though both were calibrated with exactly the same standards (Figure 17.4). The departure from a unit slope is attributable to differences in the excitation bands for the two fluorometers.

Fluorometer Calibrations

Bench fluorometers used to measure concentrations of extracted chlorophyll and pheopigments should be calibrated using authentic chlorophyll *a* standards, as prescribed also in the HPLC Protocols (Chapter 16). Chlorophyll *a* standards can be purchased from Sigma Chemical Co. (St. Louis, MO 63178, USA).

If a fluorometer has been shipped for a cruise, or if it has been unused for several weeks, it is strongly recommended that it be recalibrated with an authentic chlorophyll *a* standard. The use of solid standards, like those provided by Turner Designs and other manufacturers, can only provide a check for instrumental drift. They cannot be used as primary pigment standards. However, the solid standard should be used at frequent intervals during each day's analyses to monitor instrument drift.

The concentration of the chlorophyll *a* standard, in the appropriate solvent, must be determined using a monochromator-based spectrophotometer prior to calibrating the fluorometer. The recommended extinction coefficients for chlorophyll *a* in several solvents can be found in Appendix E of Jeffrey et al. (1997). Absorbance is measured in a 1 cm cuvette at the peak wavelength λ_{max}, and at 750 nm to correct for light scattering. The bandwidth of the spectrophotometer should be between 0.5 and 2 μm, with the standard concentration being such that the absorbance falls between 0.1 and 1.0 optical density units (Clesceri *et al*., 1998a). The concentration of the standard is calculated as

$$C_{\mathrm{STD}} = \frac{10^6[A(\lambda_{\max}) - A(750)]}{bE_{1\mathrm{cm}}}, \tag{17.1}$$

where C_{STD} is the concentration (μg L^{-1}) of the chlorophyll *a* standard, $A(\lambda_{\max})$ and $A(750)$ are absorbances at $\lambda_{\max}$ and 750 nm, *b* is the pathlength of cuvette (cm), and $E_{1\mathrm{cm}}$ is the specific absorption coefficient (L g^{-1} cm^{-1}) of chlorophyll *a* in 90% acetone. For 90% acetone $E_{1\mathrm{cm}}$ =87.67 L g^{-1} cm^{-1}, and for 100% acetone $E_{1\mathrm{cm}}$ =88.15 L g^{-1} cm^{-1}, when applied to the absorption measured at the peak wavelength $\lambda_{\max}$ (Jeffrey et al. 1997, Appendix E). The peak wavelength $\lambda_{\max}$ must be determined by inspection of the measured spectrum, because its location may shift due to interactions between the particular solvent and mixture of pigment compounds in each sample. Standards stored under nitrogen in the dark at -20°C do not change appreciably over a one-month period, provided that they are stored in containers proven to prevent evaporation (e.g. glass or Teflon bottles/vials).

The stock chlorophyll *a* standard, with its concentration measured on a spectrophotometer as described above, should be diluted using calibrated gas-tight syringes, and Class A volumetric pipettes and flasks. The minimum number of dilutions of the stock standard for calibrating a fluorometer depends on whether it is a digital model (Turner Designs 10-AU-005), or it is an analog model with a mechanical mode for changing sensitivity (e.g. Turner Designs 10-005). A minimum of 5 dilutions is required for calibrating a digital fluorometer. Analog fluorometers with a variety of door settings, such as the Turner Designs Model 10-005, must be calibrated for each door setting using at least three standard concentrations per door. The diluted standard pigment concentrations used in calibrating the fluorometer must bracket the range of concentrations found in the samples being analyzed.

Each diluted chlorophyll *a* standard is placed in the fluorometer and the signal (F_b) is recorded, after waiting a short period of time (60 seconds) for it to stabilize. The standard is removed and diluted HCL acid (2 drops of 5 %, or 1 drop of 10 %, both concentrations by volume) is added and mixed within the test tube. The tube is then placed back into the fluorometer, and after stabilization, the acidified fluorescence

signal (F_a) is recorded. Following acidification of the chlorophyll *a* standard, the fluorescence signal stabilizes relatively quickly. This is not the case for natural samples that contain a mixture of pigment compounds, however, and stabilization time may vary from sample to sample. Stabilization time has to be the same for both pigment standards and for natural samples. To minimize this source of uncertainty, and to standardize this measurement technique, it is recommended that both acidified natural sample and acidified pigment standards be allowed to react with the acid for one minute prior to recording the acidified fluorescence signal (F_a). Two drops of 5 % (by volume) hydrochloric acid is added to each of the pigment standards and natural samples. Once the acid is added, the sample in the test tube should be mixed by inverting the tube several times, using parafilm as a stopper. All fluorometric measurements for both pigment standards and natural samples should be carried out at room temperature. A 90 % (by volume) acetone blank (Blk_b) and an acidified acetone blank (Blk_a) should also be measured, even though the acidified blank (Blk_a) is frequently found to be equal to the non-acidified blank (Blk_b). The fluorometer's sensitivity to pheopigments, τ, is calculated as

$$\tau = \frac{F_b - Blk_b}{F_a - Blk_a}, \tag{17.2}$$

and is averaged over all concentrations of the chlorophyll *a* standard. For the mechanical door model fluorometers, data from the higher gain door settings will often become noisy and computed τ values will begin to decrease. These data should be excluded from the average. The fluorometer's response factor, F_R (μg L^{-1} per fluorescence signal), is determined as the slope of the simple linear regression equation

$$C_{STD} = F_R \left(F_b - Blk_b\right), \tag{17.3}$$

calculated for the sample of diluted concentrations of the pigment standard, and forcing a zero intercept. With a digital fluorometer, the regression analysis is applied to the data from the entire 5, or more, concentrations and a single F_R factor is determined for the instrument. With a mechanical fluorometer, the regression is applied to the data from the 3, or more, concentrations of the standard, and a separate F_R factor is determined, for each door setting. As a means of monitoring an instrument's performance, F_R factors from successive calibrations should be charted as functions of time (Clesceri *et al.*, 1998b). These quality control graphs should be retained with the data analysis logbooks to document the quality of each data set for which that fluorometer is used.

Solvent Preparation.

It is recommended that 90 % acetone (by volume) be used to extract pigments for the fluorometric analysis. Richard and Thompson (1952) were the first to propose 90 % acetone as a solvent to extract pigments from marine phytoplankton. Their results indicated improved extraction efficiencies, and also showed that the procedure minimized the activity of the naturally occurring chlorophyllase enzyme, which degrades the pigment. With a graduated cylinder, make up 90 % acetone by first pouring in distilled water, followed by 100 % acetone. Using volumetric pipettes, or auto-pipettes, accurately measure 8 mL to 10 mL of 90 % acetone and place it in a centrifuge tube. Record this volume as V_{EXT}. A number of such tubes containing acetone are then stored in a freezer and individually removed as filter samples are collected. Pre-chilling the solvent in this way reduces the possibility of temperature induced pigment degradation.

Extraction

Filters are removed from liquid nitrogen and placed in the chilled centrifuge tubes for extraction in V_{EXT} mL of 90% acetone. Samples are disrupted by sonication, placed in a freezer, and allowed to extract at 0^oC for 24 h. Alternatively, the cells can be mechanically disrupted using a glass/Teflon tissue grinder and allowed to extract at 0^oC for 24 h. If after disrupting the cells, it is necessary to rinse the tissue grinder, or mortar and pestle, then a known volume of 90% acetone, measured using a Class A volumetric pipette, should be used. The ease at which the pigments are removed from the cells varies considerably with different phytoplankton. In all cases, freezing the sample filters in liquid nitrogen improves extraction efficiency. Prior to analysis, pigment extracts are swirled into a vortex to remove particles from the sides of the tube, and then centrifuged to minimize cellular debris.

Measurement

Following the same measurement procedure described above under *Fluorometer Calibration*, each extracted sample is placed in the fluorometer and its non-acidified and acidified responses, Fb and Fa, are measured and recorded. The concentration of chlorophyll [Chl] (μg L^{-1}) in the sample is calculated as

$$[Chl] = \left(F_{\mathrm{b}} - F_{\mathrm{a}} - Blk_{\mathrm{b}} + Blk_{\mathrm{a}}\right)\frac{\tau}{\tau - 1}F_{\mathrm{R}}\frac{V_{\mathrm{EXT}}}{V_{\mathrm{FILT}}}, \tag{17.4}$$

and pheopigments concentration [Pheo] (μg L^{-1}) as

$$[Pheo] = \left\{\left(F_{\mathrm{a}} - Blk_{\mathrm{a}}\right)\tau - \left(F_{\mathrm{b}} - Blk_{\mathrm{b}}\right)\right\}\frac{\tau}{\tau - 1}F_{\mathrm{R}}\frac{V_{\mathrm{EXT}}}{V_{\mathrm{FILT}}}, \tag{17.5}$$

where volumes extracted V_{EXT} and filtered V_{FILT} are in mL. Pheopigment concentrations determined using the standard fluorometric method of Holm-Hansen *et al.* (1965) have not been reported in published articles for many years. This is based on the fact that (i) there is always a residual amount of pheopigments in all natural samples (Smith and Baker, 1978; 25% of the summed chlorophyll plus pheopigment), (ii) pheopigment concentrations are overestimated in the presence of chlorophyll *b* (Lorenzen and Jeffrey, 1980; Vernet and Lorenzen, 1987), and (iii) HPLC measured pheopigments, generally contribute very little to the chlorophyll *a* pigment pool (e.g., Hallegraeff, 1981; Everitt et al., 1990; and Bricaud et al., 1995). Trees *et al.* (2000a) assembled an extensive HPLC pigment database (5,617 samples) extending over a decade of sampling and analysis, and including a variety of environments ranging from freshwater to marine, oligotrophic to eutrophic, and tropical to polar, and found that the average pheopigment to chlorophyll *a* ratio was only 0.037. This global scale result emphasizes the problems associated with estimating pheopigments using the standard fluorometric method.

17.4 *In Situ* CHLOROPHYLL a FLUORESCENCE PROFILES

An *in situ* fluorometer should be employed to measure a continuous profile of chlorophyll fluorescence. The fluorometer should be mounted on the same underwater package as the water sampler, ideally together with a CTD, transmissometer and other inherent optical properties (IOP) sensors. In some cases it may be desirable to also include a radiometer on this package, if shading effects associated with the package and/or ship are not significant.

In situ fluorometers produce nearly continuous profiles of artificially stimulated fluorescence. Fluorometer data (in volts) should be corrected by subtracting an offset, determined by shading the instrument on deck. These unscaled fluorescence responses are adequate to provide guidance in K-profile analysis and interpretation.

To produce vertical continuous profiles of pigment concentration, HPLC-derived pigment concentrations from water samples taken at discrete depths may be interpolated, with the aid of *in situ* fluorescence profiles. These *fluorescence interpolated* profiles should then be used with $K_d(z,\lambda)$ profiles to compute the optically weighted average pigment concentration over the top attenuation length (Gordon and Clark 1980).

The A/D channel used to acquire and record signal voltages from the *in situ* fluorometer must be calibrated, and its temperature-dependent response to known voltage inputs characterized. The range dependent A/D bias coefficients should be determined at approximately 5^0 C intervals over the range from 0-25^0 C to characterize the temperature sensitivity of the data acquisition system.

Zero fluorescence offsets should be measured on deck before and after each cast; the optical windows should be shaded to avoid contamination of the zero offset value by ambient light. Before each cast, the fluorometer windows should be cleaned following the manufacturer's instructions.

17.5 PROTOCOL STATUS AND FUTURE DIRECTIONS FOR RESEARCH

In order to minimize interferences caused by the overlapping excitation and emission wavebands of chlorophylls *a*, *b*, *c* and pheopigments, Turner Designs (Sunnyvale, CA) manufactures the multi-spectral fluorometer TD-700. This instrument was recently tested using samples collected at the US JGOFS Hawaii Ocean Time-series Station ALOHA (22.75^0N, 158^0W). A set of replicate monthly (May - Dec 2000) pigment samples collected between the surface and 175 m were analyzed by HPLC using the protocols described in Chapter 16. Duplicate samples were subsequently analyzed in 100% acetone with the TD-700 using the manufacturer's calibration. The results of these comparisons are illustrated in Figures 17.5, 17.6 and 17.7 for chlorophylls *a*, *b*, and *c*, respectively. The Model I regression equations predicting each HPLC pigment (in mg m^{-3}) from the equivalent TD700 estimate are:

- HPLC Chl *a* = 0.729[TD-700 Chl *a*] + 0.0144; (r^2 = 0.894).
- HPLC Chl *b* = 0.607[TD-700 Chl *b*] – 0.0163; (r^2 = 0.816).
- HPLC Chl *c* = 1.083[TD-700 Chl *c*] – 0.00249; (r^2 = 0.906).

These equations differ significantly from a one-to-one relationship. The present comparisons differ also from those published in Trees et al. (2000a), although care must be used in this comparison since the concentrations were expressed there in ng L^{-1} (which accounts for the factor of 10^{-3} differences in the respective offset coefficients). These results call into question the stability of the fluorometer. It is also evident that the equations provided by the manufacturer must be verified with HPLC data, and that these calibration relationships should be reviewed frequently.

It is interesting and noteworthy that the TD-700 fluorometer did not detect pheopigments in any of the samples analyzed.

REFERENCES

Bianchi, T. S., C. Lambert, and D. C. Biggs. 1995: Distribution of chlorophyll *a* and pheopigments in the northwestern Gulf of Mexico: a comparison between fluorometric and high-performance liquid chromatography measurements. *Bull. Mar. Science,* **56,** 25-32.

Brock, T.D., 1983: *Membrane filtration: a user's guide and reference manual*. Science Tech., Madison, WI, 381 pp.

Campbell, J.W. 1995: The lognormal distribution as a model for bio-optical variability in the sea. J. Geophys Res., **100**, 13237-13254.

Chavez, F., K.R. Buck, R.R. Bidigare, D.M. Karl, D. Hebel, M. Latasa, L. Campbell, and J. Newton, 1995: On the chlorophyll *a* retention properties of glass-fiber GF/F filters. *Limnol. Oceanogr*., **40**, 428-433.

Clesceri, L.S., A.E. Greenberg and A.D. Eaton (eds), 1998a: Part 10000, Biological Examination, Section 10200 H. in Standard Methods for the Examination of Water and Wastewater. 20th ed. Baltimore (MD): American Public Health Association, American Water Works Association, Water Environment Federation.

Clesceri, L.S., A.E. Greenberg and A.D. Eaton (eds), 1998b: Part 10000, Biological Examination, Section 10200 **B**. in Standard Methods for the Examination of Water and Wastewater. 20th ed. Baltimore (MD): American Public Health Association, American Water Works Association, Water Environment Federation.

Dickson, M.-L., and P.A. Weeller, 1993: Chlorophyll *a* concentrations in the North Pacific: Does a latitudinal gradient exist? *Limnol. Oceanogr*., **38**, 1813-1818.

Gordon, H.R., and D.K. Clark, 1980: Remote sensing optical properties of a stratified ocean: an improved interpretation. *Appl. Optics*, **19**, 3,428--3,430.

Hoepffner, N., and S. Sathyendranath. 1992: Bio-optical characteristics of coastal waters: absorption spectra of phytoplankton and pigment distribution in the western North Atlantic. *Limnol. Oceanogr.* **37:** 1660-1679.

Holm-Hansen, O., C.J. Lorenzen, R.W. Holmes, and J.D.H. Strickland, 1965: Fluorometric determination of chlorophyll. *J. du Cons. Intl. Pour l'Expl. de la Mer.*,**30**, 3-15.

Jeffrey, S.W., R.F.C. Mantoura, and S.W. Wright (eds.), 1997: *Phytoplankton Pigments in Oceanography*, Monographs on Oceanographic Methodology, UNESCO, 661 pp.

Lorenzen, C.J. and S.W. Jeffrey. 1980: *Determination of Chlorophyll in Seawater*. UNESCO Technical Papers in Marine Science, Vol. **35**, UNESCO, 20 pp.

Phinney, D.A. and C.S. Yentsch, 1985: A novel phytoplankton chlorophyll technique: Toward automated analysis. *J. Plankton Res*., **7**, 633-642.

Richards, F.A. and T.G. Thompson. 1952: The estimation and characterization of plankton populations by pigment analysis. II. A spectrophotometric method for the estimation of plankton pigments. *J. Mar. Res*., **11**, 156-172.

Saijo, Y. and S. Nishizawa. 1969: Excitation spectra in the fluorometric determination of chlorophyll a and phaeophytin *a*. *Mar Biol*,. **2**, 135-136.

Smith, R. C., and K. S. Baker. 1978: The bio-optical state of ocean waters and remote sensing. *Limnol. Oceanogr*., **23**, 247-259.

Smith, R. C., R. R. Bidigare, B. B. Prezelin, K. S. Baker, and J. M. Brooks. 1987: Optical characterization of primary productivity across a coastal front. *Mar. Biol*. **96:** 575-591.

Strickland, J.D.H., and T.R. Parsons, 1972: *A Practical Handbook of Sea Water Analysis*, Fisheries Research Board of Canada, 310 pp.

Tester, P. A., M. E. Geesey, C. Guo, H. W. Paerl, and D. F. Millie, 1995: Evaluating phytoplankton dynamics in the Newport River estuary (North Caroline, USA) by HPLC-derived pigment profiles. *Mar. Ecol. Prog. Ser*. **124,** 237-245.

Trees, C.C., R.R. Bidigare, D.M. Karl and L. Van Heukelem, 2000a: Fluorometric chlorophyll a: sampling, laboratory methods, and data analysis protocols, Chapter 14 in: Fargion, G.S. and J.L. Mueller (Eds.) *Ocean Optics Protocols for Satellite Ocean Color Sensor Validation*. NASA/TM-2000-209966, NASA Goddard Space Flight Center, Greenbelt, MD. pp 162-169.

Trees, C.C., D.K. Clark, R.R. Bidigare, M.E. Ondrusek, and J.L. Mueller. 2000: Accessory pigments versus chlorophyll *a* concentrations within the euphotic zone: a ubiquitous relationship. Limnol Oceanogr. (in press).

Trees, C.C., M.C. Kennicutt II, and J.M. Brooks, 1985: Errors associated with the standard fluorometric determination of chlorophylls and pheopigments. *Mar. Chem*., **17**, 1-12.

UNESCO, 1994: Protocols for the Joint Global Ocean Flux Study (JGOFS) Core Measurements, Manual and Guides 29, 170pp.

Vernet, M., and C. J. Lorenzen. 1987: The presence of chlorophyll b and the estimation of pheopigments in marine phytoplankton. J. Plankton Re**s., 9**, 255-265.

Yentsch, C.S., and D.W. Menzel, 1963: A method for the determination of phytoplankton, chlorophyll, and phaeophytin by fluorescence. *Deep-Sea Res.*, **10**, 221-231.

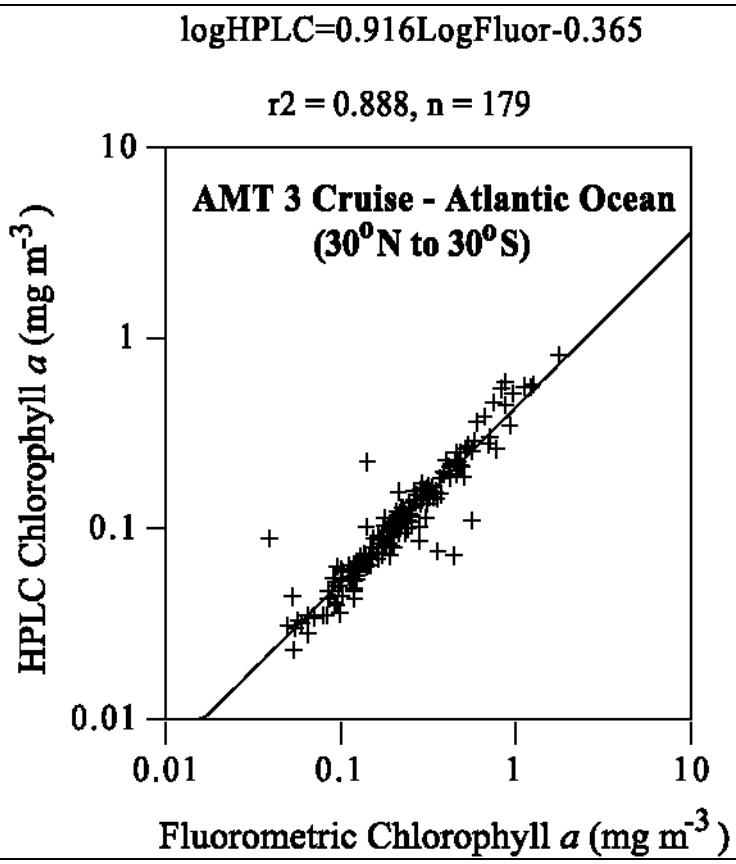

Figure 17.1: Comparisons between fluorometrically determined chlorophyll and HPLC determined total chlorophyll *a* (chlorophyllide *a*, chlorophyll *a* epimer, chlorophyll *a* allomer, monovinyl chlorophyll *a*, and divinyl chlorophyll *a*) from samples collected during Atlantic Meridional Transect 3 cruise (30°N to 30°S, October 1996).

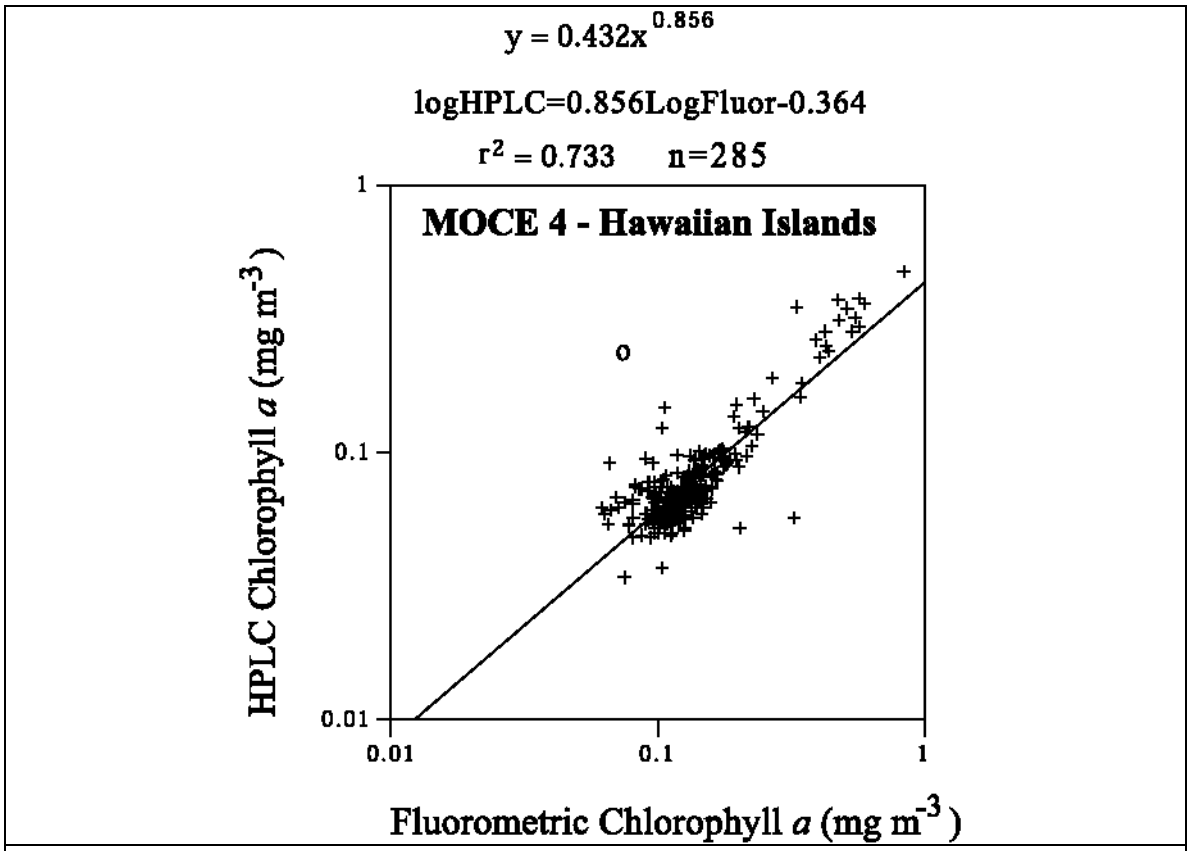

Figure 17.2: Same as Figure 17.1 for data collected during the Marine Optical Characterization Experiment (MOCE) 4 cruise.

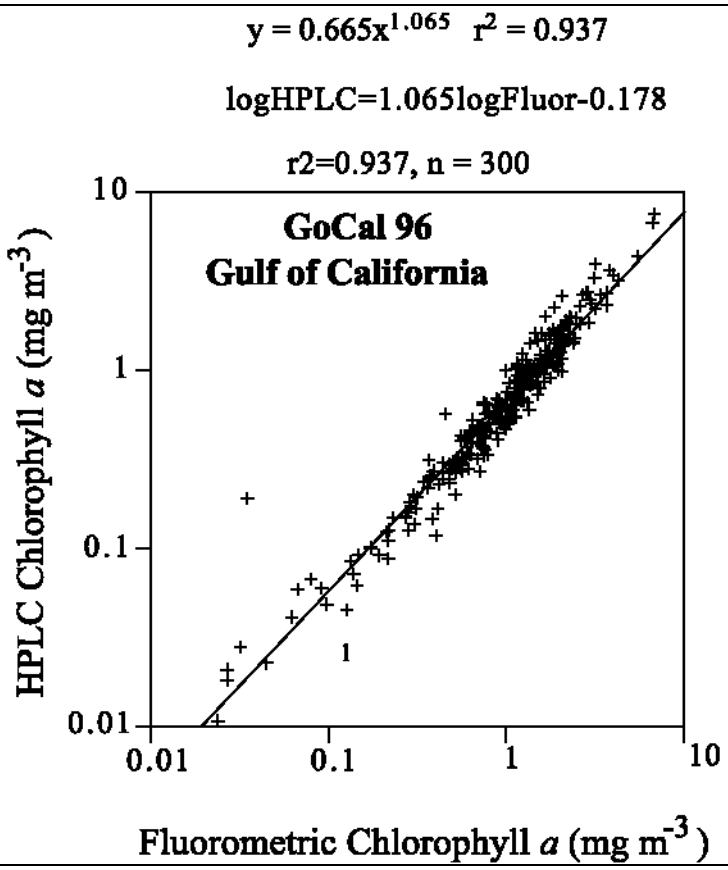

Figure 17.3: Same as Figure 17.1 for data collected during the Gulf of California cruise (Gulf of California, November 1996).

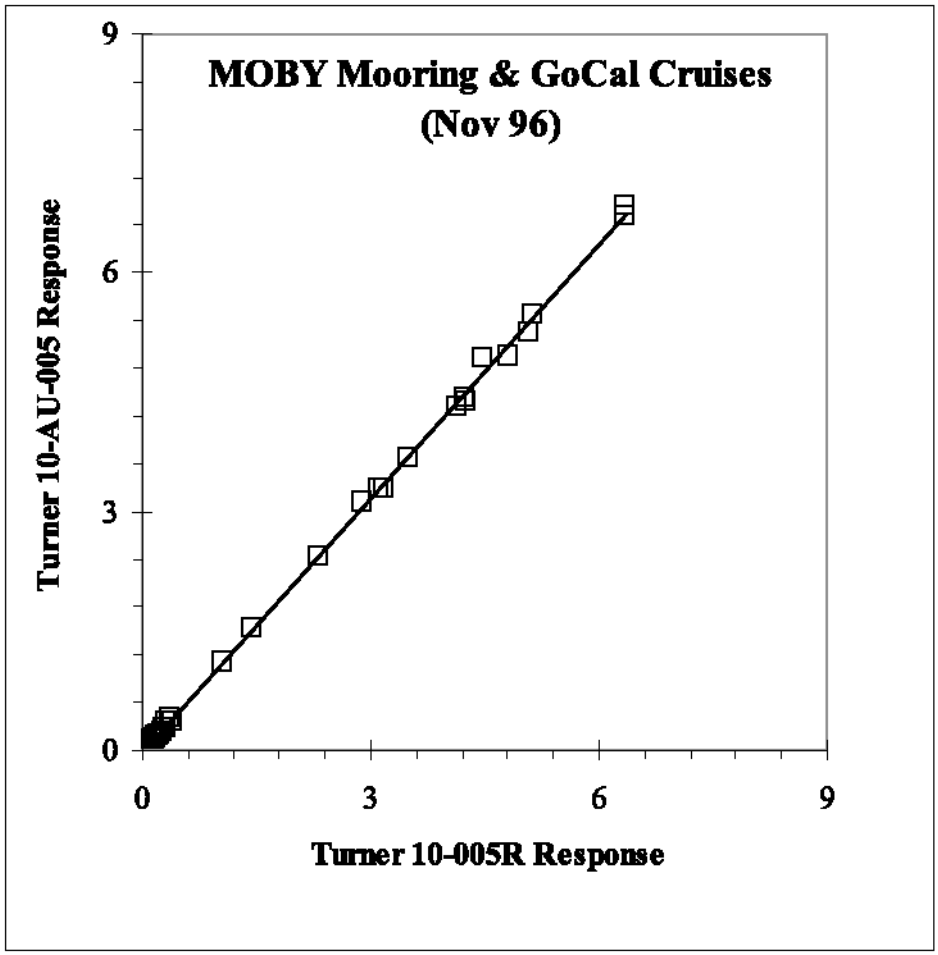

Figure 17.4: Comparison of fluorometrically determined chlorophyll a using the VisLab Turner Fluorometer (10-005R) and the Moss Landing Marine Laboratory Turner Fluorometer (10-AU-005). Samples were analyzed from a MOBY Nov 96 cruise and a Gulf of California cruise (Mueller, Nov 96).

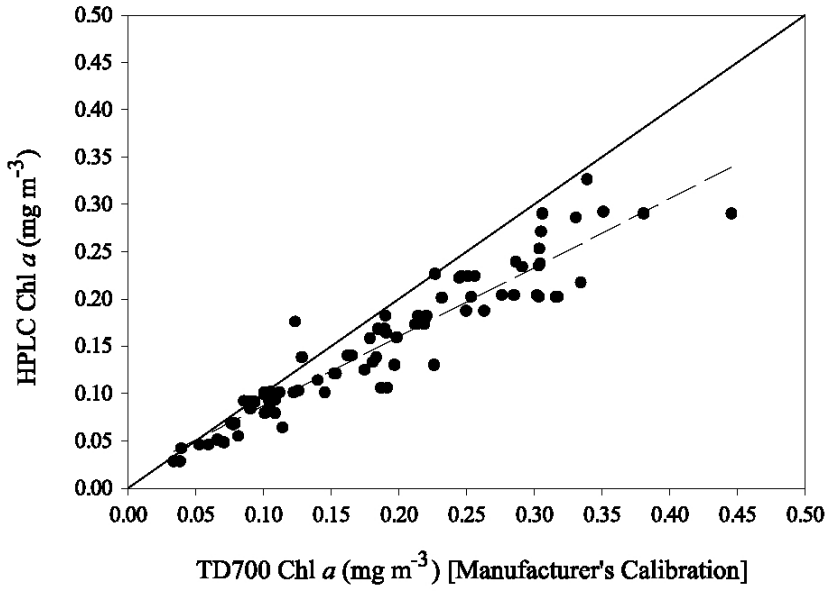

Fig 17.5: Comparison between chlorophyll *a* determined by the TD700 equation supplied by the manufacturer and that measured by HPLC methods.

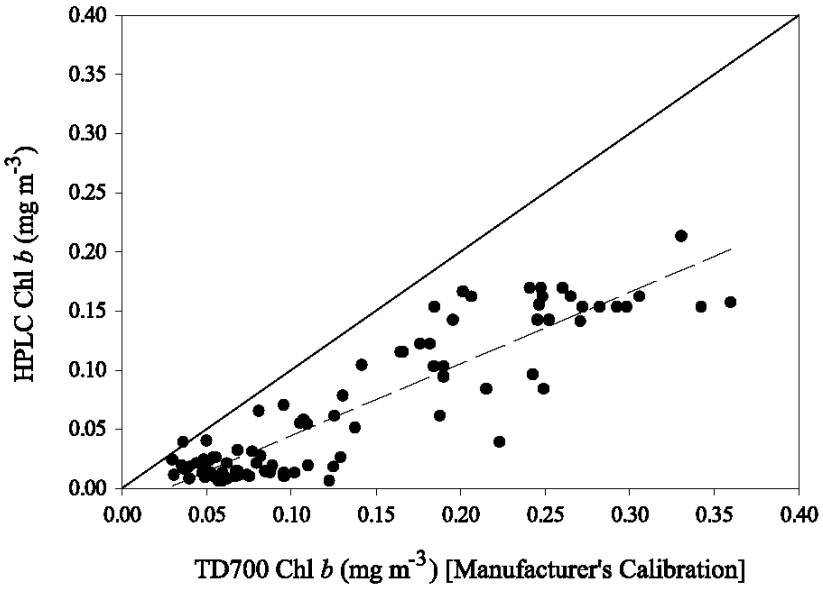

Fig. 17.6: Same as Fig. 17.5 for chlorophyll *b*.

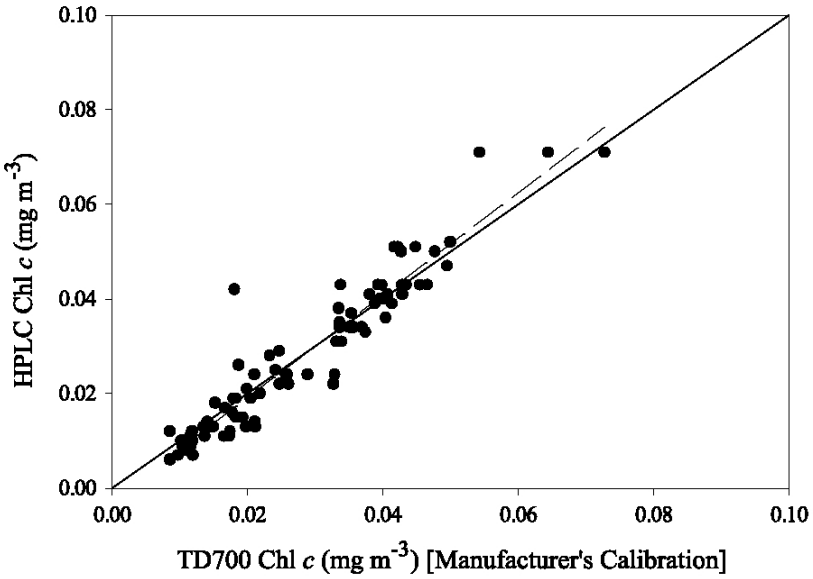

Fig. 17.7: Same as Fig. 17.5 for chlorophyll *c*.

Chapter 18

SeaBASS Data Protocols and Policy

P. Jeremy Werdell[1], Sean Bailey[2], and Giulietta S. Fargion[3]

[1]*Science Systems and Applications Inc., Lanham, Maryland*
[2]*Futuretech Corporation, Greenbelt, Maryland*
[3]*Science Applications International Corporation, Beltsville, Maryland*

18.1 INTRODUCTION

The SeaWiFS Project developed the SeaWiFS Bio-optical Archive and Storage System (SeaBASS) to be a local repository for *in situ* optical and pigment data products regularly used in a variety of scientific analyses. Information on the original SeaBASS design is provided in Hooker et al. (1994), and has since been expanded to contain data sets collected by participants of the SIMBIOS Project. A detailed description of the SeaBASS system is available via the World Wide Web:

<http://seabass.gsfc.nasa.gov>.

Both the SeaWiFS and SIMBIOS Projects use *in situ* bio-optical data for the validation of SeaWiFS and other satellite (e.g., OCTS and POLDER) data products, and for the development of new ocean color algorithms. In addition, SeaBASS supports international protocol workshops, data merger studies, and time-series studies. Archived data include measurements of water-leaving radiance, chlorophyll *a*, and other related optical and pigment parameters. When available, additional oceanographic and atmospheric data (given in Table 2.1) are also archived in SeaBASS. Data are collected by a number of different instrument packages, such as profilers, buoys, and above-water measurement devices, on a variety of platforms, including ships, moorings, and drifters. The contents of SeaBASS are made readily available to the SIMBIOS and MODIS Science Team Members, and to other approved individuals (e.g., members of other ocean color instrument teams, volunteer-contributing researchers, etc.) on a case-by-case basis. Access to the database and data archive is available to authorized users through the SeaBASS Web page.

As SIMBIOS US Science Team members are contractually obligated to provide data to SeaBASS, the volume of archived data is rapidly increasing (McClain and Fargion 1999a and 1999b). With the launch of MODIS, as well as a number of present and upcoming international missions (e.g., GLI, POLDER-2, MERIS, OCI, OCM, etc.), the use of the SeaBASS data archive is expected to increase dramatically as these missions begin to require validation data.

18.2 SeaBASS DATA FORMAT

SeaBASS presently contains over 22,000 bio-optical data files, encompassing more than 650 separate experiments. In addition, its historical pigment database holds over 286,000 records of phytoplankton pigment data. To account for the continuous growth of the data archive, the Project believed it essential to develop efficient data ingestion and storage techniques. Such ingestion procedures and protocols were designed to be as straightforward and effortless as possible on the part of the contributing investigators, while still offering a useful format for internal analysis efforts. The Project considered the following to be the most important in the design of the system:

1. Simple data format, easily read and updated;
2. Global portability across multiple computer platforms; and
3. Web accessible data holdings.

As a result, SeaBASS supports standard, flat (two-dimensional) ASCII text files, which are easily managed from any computer platform and by most programming languages. The architecture of a SeaBASS data file is simple: data are presented in columns (delimited by spaces, tabs, or commas) and preceded by a series of predefined metadata headers. The headers provide descriptive information on the data file, such as date, time, location, investigators, column names and units, and additional ancillary information. Several examples of SeaBASS data files are available both online:

<http://seabass.gsfc.nasa.gov/seabass_submit.html>

and in Appendix B. Appendix B provides a detailed description of the SeaBASS file format.

18.3 SeaBASS ARCHITECTURE

SeaBASS contains two separate but linked entities, a data archive and two relational databases (RDBs), the Historical Pigment RDB and the Bio-Optical RDB. The data archive consists of a directory tree where the physical data files and documentation for the Bio-Optical RDB are stored. Main directories and subdirectories are organized by contributor, affiliation, experiment, and specific cruise. Each cruise has additional subdirectories containing the *in situ* data sets, relevant documentation, and instrument calibration files associated with that cruise. Authorized users may peruse the directory tree via the SeaBASS Web page.

The two RDBs were built using the SQL Server product from Sybase, Inc. The Historical Pigment RDB consists of a single database table with over 286,000 records of phytoplankton pigment data. These data are available to the general public, but are not currently maintained or updated. Access to the holdings of the Historical Pigment RDB is provided via an online search engine:

<http://seabass.gsfc.nasa.gov/cgibin/pigmentquery.cgi>.

Over the past year, the Bio-Optical RDB has been expanded to include 19 database tables for storage of both metadata information and geophysical data values. Half of the tables store general information about each data file (e.g., provided in the headers of each file) and additional information about contributing researchers and standard SeaBASS field names and units. The others are used to store ancillary information about each data record (e.g., date, time, location, measurement depth, and station) and the geophysical data values. Other changes to the Bio-Optical database include:

1. Improved data normalization;
2. A reconfigured system which takes advantage of multiple computer processors and increased physical storage space; and
3. The development of software and applications for internal SIMBIOS Project Office accounting activities.

Several online search engines allow users to access the holdings of the Bio-Optical RDB, either by pointing to files in the data archive or by returning geophysical values. Four are described below, one of which is available to the general public. The General Information Search Engine

<http://seabass.gsfc.nasa.gov/cgi-bin/general_info.cgi>

is available to the public and allows users to retrieve a list of archived cruises and the data types and parameters collected on each. The SeaBASS Bio-Optical Search Engine

<http://seabass.gsfc.nasa.gov/prot/seabass_query.cgi>

permits users to access all of the Bio-Optical data holdings and returns a list of matching files, which are available to view or download. The SeaBASS Pigment Locator:

<http://seabass.gsfc.nasa.gov/prot/pigment_locator.cgi>

provides direct access to the phytoplankton pigment data stored in the Bio-Optical RDB. Likewise, the SeaBASS Aerosol Locator

<http://seabass.gsfc.nasa.gov/prot/aerosol_locator.cgi>

provides direct access to AOT data stored in the Bio-Optical RDB. When using the latter two search engines, queries return a list of geophysical values which are available to view or download. Each search engine allows users to limit searches to particular experiments, cruises, contributors, or parameters (e.g., SPM and AOT) and to apply specific date and location ranges.

The SIMBIOS Project Office regularly develops new and improved Web-based tools for accessing and viewing the holdings of SeaBASS. Links to such resources are always provided at

<http://seabass.gsfc.nasa.gov/dataordering.html>.

18.4 DATA QUALITY

To assist with the standardization of SeaBASS data files, the Project developed feedback software and protocols to evaluate the format of submitted data files. The primary component of the software is known as FCHECK. FCHECK consists of a Practical Extraction and Report Language (PERL) script with connections to several look-up tables and UNIX mail handling utilities.

Data contributors, using any computer platform at their disposal, may test a data file for compatibility with the SeaBASS format by sending the file via electronic mail to fcheck@seabass.gsfc.nasa.gov. Upon receipt of the file, FCHECK parses the data and metadata and compares it to the required SeaBASS format. Results of this analysis are electronically mailed to the contributor and to the SeaBASS administrator. This format analysis requires little-to-no intervention on behalf of the administrator and has proven to reduce considerably the amount of processing time needed for both the administrator and contributor. In late 2000, a file transfer protocol (FTP) version of FCHECK was developed to assist contributors in evaluating (simultaneously) large volumes of data. Additional information on FCHECK is available online:

<http://seabass.gsfc.nasa.gov/fcheck_desc.html>.

Once data are prepared for archiving, the contributor uploads the data and calibration files, and supporting documentation to SeaBASS via FTP. The administrator then collects the files and evaluates the data set. With regards to data format and content, the following requirements must be met:

1. Data files must be organized in the proper SeaBASS format (i.e., FCHECK does not report any errors);
2. Supporting documentation and calibration files must be included in the submission; and
3. The documentation and calibration files must match those listed in the ‘documents’ and ‘calibration_files’ headers in each data file.

The documentation and calibration files are inspected for completeness. At a minimum, the Project requires that documentation include a cruise report or station log (with ancillary information such as date, time, location coordinates, water depth, sea and sky states, observations, and notes) and an instrument report (with information such as instruments used, processing methods, equations, and references). The Project encourages the contributor to include additional documentation, such as digital photographs of sea and sky states. Calibration files must include calibration coefficients and the date each instrument was calibrated. Once the data set has passed visual inspection, the administrator archives the data files and ingests the appropriate information into the database. At this point, the new data become available online to the Science Team.

18.5 ACCESS POLICY AND USERS

The SeaBASS Data Access Policy applies to data submitted to the NASA SIMBIOS Project at GSFC for inclusion in the calibration and validation data collection. An update to the SeaWiFS Data Policy can be found in Firestone and Hooker (2001). The SIMBIOS investigators must, at a minimum, comply with SIMBIOS data policy, although the Project encourages a more open policy.

Ocean color algorithm development is severely observation limited. As such, rapid turnaround and access to field data are essential to advance the state of the art. Data obtained under SIMBIOS NRA-99 contracts must be submitted no later than six months from the date of collection. International SIMBIOS

Science Team and researchers involved in other ocean color missions (i.e., POLDER, GLI, MODIS, MERIS, etc.) are encouraged to provide their data as well, in order to foster collaboration.

For a period of three years following data collection, access to the digital data will be limited to SIMBIOS Science Team members and other approved users as agreed upon by the SIMBIOS Project and data providers. The SIMBIOS Project will grant access to the international science team members on a case-by-case basis according to ongoing collaboration agreements. Other investigators from the ocean color community will be able to query information about the data (i.e., parameters, locations, dates, and investigators), but will not have access to the data itself. Instead, if they are interested in the data, they will be referred to the provider. After the third year anniversary of data collection, the data will change from a "restricted" to an "open" status and will be distributed by National Oceanographic Data Center (NODC). Some special data sets for algorithm development will be made available to the research community without restrictions with the approval of the SIMBIOS Science Team.

Prior to the three-year data collection anniversary, users of data will be required to provide proper credit and acknowledgment of the provider. A citation should also be made of the data archive. The provider(s) shall have the right to be a named as a co-author. Users of data are encouraged to discuss relevant findings with the provider early in the research. The user is required to give all providers of the data being used a copy of any manuscript resulting from the use of the data prior to initial submission for publication, thus providing the data provider an opportunity to comment on the paper. All users and providers are required to report possible data errors or mislabels found in the database to the SeaBASS administration.

A major purpose of the SeaBASS database is to facilitate comparisons between *in situ* observations (regionally, temporally, by technique, by investigator, etc.), as well as between *in situ* and remotely sensed observations. Updates and corrections to submitted data sets are encouraged. Records will be maintained of updates and corrections and a summary of new and updated data will be posted online. It is the provider's responsibility to ensure that the current data in the archive is identical to the data used in the provider's most recent publications or current research. At the end of each SIMBIOS contract, a final data resubmission, or a written certification of data quality, from the provider is mandatory.

After receiving the final data, the SIMBIOS Project will forward the data at the appropriate time to NODC for open distribution. A courtesy citation, naming the provider and the funding agency, will accompany the data. The SIMBIOS Project will not be held responsible for any data errors or misuse.

To afford continued rapid submission of data sets, the SeaBASS Web server is configured as a password protected system. Additionally, the Web server and SeaBASS software log all user activity. This information is available to contributing investigators.

REFERENCES

Firestone, E.R., and S.B. Hooker, 2001: SeaWiFS Postlaunch Technical Report Series Cumulative Index: Volumes 1–11. *NASA Tech. Memo. 2001–206892, Vol. 12,* S.B. Hooker and E.R. Firestone, Eds., NASA Goddard Space Flight Center, Greenbelt, Maryland, 4–5.

Hooker, S.B., C.R. McClain, J.K. Firestone, T.L. Westphal, E-n. Yeh, and Y. Ge, 1994: The SeaWiFS Bio-Optical Archive and Storage System (SeaBASS), Part 1. *NASA Tech. Memo. 104566, Vol. 20,* S.B. Hooker and E.R. Firestone, Eds., NASA Goddard Space Flight Center, Greenbelt, Maryland, 40 pp.

McClain, C.R., and G.S. Fargion, 1999a: SIMBIOS Project 1998 Annual Report, *NASA Tech. Memo. 1999–208645,* NASA Goddard Space Flight Center, Greenbelt, Maryland, 105 pp.

McClain, C.R. and G.S. Fargion, 1999b: SIMBIOS Project 1999 Annual Report, *NASA Tech. Memo. 1999–209486* NASA Goddard Space Flight Center, Greenbelt, Maryland, 128 pp.

Appendix A

Characteristics of Satellite Ocean Color Sensors: Past, Present and Future

Giulietta S. Fargion

Science Applications International Corporation, Beltsville, Maryland.

This appendix summarizes the essential operational characteristics of ocean color sensors of the past, present and future. Table A.1 lists general characteristics of past and presently operating ocean color sensors, including for each the satellite platform, country and agency, operational time period (actual or planned), orbit characteristics, spatial resolution at nadir, swath width, and tilt capabilities. Table A.2 lists the same information for ocean color sensors currently planned for launch and operation in the future. Table A.3 lists the center wavelength, spectral bandwidth (FWHM) and noise equivalent radiance resolution (NEΔL) for the ocean color bands of each of the sensors listed in Tables A.1 and A.2. Many of these sensors have additional bands, not listed here, addressing data requirements in terrestrial or atmospheric sciences. The information in these tables was updated from that published in IOCCG (1998). The sensor band data in Table A.3 should be used to expand Table 4.1 when specifying *in situ* instrument characteristics needed to support algorithm development and validation related to any of the other sensors, in addition to SeaWiFS, which fall within the SIMBIOS purview.

REFERENCES

IOCCG 1998: Minimum Requirements for an Operational, Ocean Colour Sensor for the Open Ocean. *Reports of the International Ocean-Colour Coordinating Group, No. 1.* IOCCG, Dartmouth, Canada, 46pp.

Table A1. Characteristics of past and present ocean-color sensors.

Sensor	**CZCS**	**OCTS**	**POLDER**	**MOS**	**SeaWiFS**	**OCM**	**OCI**	**OSMI**	**MODIS-AM**	**MISR**	**MERIS**
Platform	Nimbus-7	ADEOS-1	ADEOS-1	IRS-P3	OrbView-2	IRS-P4	ROCSAT	KOMPSAT	EOS-AM1	EOS-AM1	Envisat
Agency	NASA	NASDA	CNES	DLR	OSC/NASA	ISRO	Taiwan	KARI	NASA	NASA	ESA
Country	USA	Japan	France	Germany/India	USA	India	Taiwan	Korea	USA	USA	Europe
Operation Start	Oct. 1978	Aug. 1996	Aug. 1996	Mar. 1996	Sep. 1997	Nov. 98	Feb. 1999	Jul. 1999	Dec. 1999	Dec. 1999	Spring 2002
Operation End	Jun. 1986	Jun. 1997	Jun. 1997								
Orbital Inclination	99.3	98.6	98.6	98.7	98.2	98.3	35	98.13	98.2	98.2	98.5
Equatorial Crossing Time (h)	12:00	10:41	10:41	10:30	12:00	12:00	09:00/15:00	10:50	10:30	10:30	10:00
Altitude (km)	955	804.6	804.6	817	705	720	600	685	705	705	800
Resolution at Nadir (km)	0.825	0.7	6 x 7	0.5	1.1	0.36	0.8	0.85	1	0.25	1.2/0.3
Swath (km)	1566	1400	2400	200	2800	1420	704	800	2330	360	1150
Tilt (degrees)	±20	±20	Variable	No	±20	±20	No	No	No	Variable	No
Direct Link	No	UHF/X-band	X-band	S-band	L-band	X-band	S-band	X-band	X-band	No	X-band
Recorded	Yes	X-band	X-band	None	S-band	Yes	None	Yes	X-band	X-band	X-band
Solar Calibration	No	Yes	No	Yes	Yes	Yes	—	Yes	Yes	No	Yes
Lunar Calibration	No	No	No	No	Yes	No	—	No	Yes	Yes	No
Lamp Calibration	Yes	Yes	No	Yes	No	Yes	—	No	Yes	No	No

Table A2. Characteristics of future ocean-color sensors.

	GLI	POLDER-2	MODIS-PM
Platform	ADEOS2	ADEOS–2	EOS–PM1
Agency	NASDA	CNES	NASA
Country	Japan	France	USA
Operation Start	Nov. 2002	Nov. 2002	Spring 2002
Orbital Inclination	98.6	98.6	98.2
Equatorial Crossing Time	10:30	10:30	13:30
Altitude (km)	803	803	705
Resolution at Nadir (km)	1/0.25	6 x 7	1
Swath (km)	1600	2400	2330
Tilt (degrees)	±20	Variable	No
Direct Link	UHF/X-band	X-band	X-band
Recorded	X-band	X-band	X-band
Solar Calibration	Yes	No	Yes
Lunar Calibration	No	No	Yes
Lamp Calibration	Yes	No	Yes

Table A3. Summary of the spectral bands used for ocean-color applications. Center λ (nm), Bandpass (FWHM, nm), NEΔL (W m^{-2} sr^{-1} μm^{-1}).

CZCS			OCTS			POLDER			MOS			SeaWiFS		
Center λ	FWHM	NEΔL	Center λ	FWHM	NEΔL	Center λ	FWHM	NEΔL	Center λ	FWHM	NEΔL	Center λ	FWHM	NEΔL
443	20	0.208	412	20	0.186	443	20	0.138	408	10	0.192	412	20	0.092
520	20	0.173	443	20	0.109	490	20	0.147	443	10	0.124	443	20	0.077
550	20	0.166	490	20	0.089	565	20	0.088	485	10	0.148	490	20	0.056
670	20	0.094	520	20	0.121	670	20	0.063	520	10	0.141	510	20	0.049
750	100	0.040	565	20	0.091	763	10	0.090	570	10	0.150	555	20	0.043
			670	20	0.037	765	40	0.086	615	10	0.105	670	20	0.031
			765	40	0.057	865	40	0.034	650	10	0.141	765	40	0.019
			865	40	0.031	910	20	0.045	685	10	0.088	865	40	0.015
									750	10	0.102			
									815	10	0.034			
									870	10	0.033			

MISR			MODIS			MERIS			OCI			OSMI		
Center λ	FWHM	NEΔL	Center λ	FWHM	NEΔL	Center λ	FWHM	NEΔL	Center λ	FWHM	NEΔL	Center λ	FWHM	NEΔL
446	41	0.063	412	15	0.048	412.5	10	0.026	443	20	–	443	20	–
557	27	0.061	443	10	0.032	442.5	10	0.025	490	20	–	490	20	–
672	20	0.050	488	10	0.025	490	10	0.022	510	20	–	510	20	–
867	39	0.031	531	10	0.018	510	10	0.019	555	20	–	555	20	–
			551	10	0.019	560	10	0.016	670	20	–	670	20	–
			667	10	0.008	620	10	0.014	865	40	–	865	40	–
			678	10	0.007	665	10	0.013						
			748	10	0.009	681	7.5	0.014						
			870	15	0.006	709	9	0.011						
			469 *	20	0.145	779	14	0.008						
			555 *	20	0.127	870	20	0.007						
			645 **	50	0.170	890	10	0.011						
			858 **	35	0.123	900	10	0.010						

GLI			OCM			POLDER-2			S–GLI		
Center λ	FWHM	NEΔL	Center λ	FWHM	NEΔL	Center λ	FWHM	NEΔL	Center λ	FWHM	NEΔL
380	10	0.076	412	20	0.26	443	20	0.138	412	10	0.081
400	10	0.051	443	20	0.22	490	20	0.147	443	10	0.067
412	10	0.045	490	20	0.17	565	20	0.088	490	10	0.054
443	10	0.054	510	20	0.17	670	20	0.063	520	20	0.052
460	10	0.055	555	20	0.15	763	10	0.090	565	20	0.029
490	10	0.027	670	20	0.10	765	40	0.086	625	20	0.021
520	10	0.044	765	40	0.05	865	40	0.034	680	20	0.012
545	10	0.044	865	40	0.08	910	20	0.045	710	20	0.007
565	10	0.018							749	20	0.009
625	10	0.017							865	20	0.006
666	10	0.015									
680	10	0.014									
710	10	0.012									
749	10	0.010									
865	20	0.007									

* Spatial resolution 0.5 km
**Spatial resolution 0.25 km
(others: 1 km)

Appendix B

SeaBASS Data File Format

P. Jeremy Werdell[1], Sean Bailey[2] and Giulietta S. Fargion[3]

[1]*Science Systems and Applications Inc., Lanham, Maryland*
[2]*Futuretech Corporation, Greenbelt, Maryland*
[3]*Science Applications International Corporation, Beltsville, Maryland*

SeaBASS FILE FORMAT

The format of a SeaBASS data file is straightforward: data are presented in columns (delimited by spaces, tabs, or commas) and are preceded by a series of predefined metadata headers (Table B1, see succeeding pages). Every header begins with a forward slash (/) and every data file opens with /begin_header. The headers can then be listed in any order, so long as the list ends with /end_header.

A value of NA ("not available" or "not applicable") is assigned to any header where information cannot be provided. Data files with missing headers will not be accepted for submission to SeaBASS. Commas separate multiple entries; white spaces and apostrophes are invalid entries. A list and description of the SeaBASS metadata headers is available online:

<http://seabass.gsfc.nasa.gov/seabass_header.html>.

This list is updated regularly. Examples of the metadata headers may be found in the example SeaBASS files located at the end of this chapter.

FIELD NAMES AND UNITS

In an effort to ensure compatibility within the SeaBASS data archive, and to facilitate the development of the expanded version of the SeaBASS database, a standard set of case-insensitive field names and units has been adopted (Table B2). An online version of the standard field names list is available:

<http://seabass.gsfc.nasa.gov/cgi-bin/stdfields.cgi>.

While the current list of standardized field names is reasonably comprehensive, it cannot account for all of the possible data types one might wish to provide to the SeaBASS archive. If a data type to be submitted to SeaBASS does not fall under one of the predefined standard field names, the investigator may still include the data. Such non-standard data will be archived, but the geophysical data values will not be ingested into the online database. The data will be retrievable, but only with the original archived file, not as a separate data set. If there are frequent queries for non-standard data types, then the new field names and associated units will be added to the online version of Table B2.

Table B1. SeaBASS metadata headers.

Header	***Description***
`/investigators`	The name of the principal investigator, followed by any associate investigators.
`/affiliations`	A list of affiliations, e.g., university and laboratory, for each investigator.
`/contact`	An electronic mail address for at least one of the investigators or point of contact for the data file.
`/experiment`	The name of the long-term research project, e.g., CalCOFI and CARIACO. An entry of 'SIMBIOS' is not permitted.
`/cruise`	The name of the specific cruise, or subset of the experiment, where the data in the file were collected e.g., cal9802 and car48. An entry of 'SIMBIOS' is not permitted.
`/station`	The name of the station or deployment area where data in the file were collected.
`/data_file_name`	The current name of the data file.
`/documents`	A list of cruise reports, station logs, digital images, and other associated documentation which provide additional information about the experiment and cruise. This documentation must accompany the data file at the time of submission.

/calibration_files	A list of supplementary files containing coefficients and techniques used to calibrate the instruments used in data collection. This documentation must accompany the data files at the time of submission.
/data_type	The general collection method, platform, or type of data found in the file. Acceptable values include: **cast** for vertical profiles, e.g., optical packages and CTD; **flow_thru** for continuous data, e.g., shipboard and underway flow through systems; **above_water** for above surface radiometry data, e.g., ASD, SIMBAD, and Satlantic SAS; **sunphoto** for sun photometry data, e.g., MicroTops and PREDE; **mooring** for moored and buoy data; **drifter** for drifter and drogue data; **scan** for discrete hyperspectral measurements; **lidar** for lidar and other active remote-sensing measurements, e.g., MPL; and **pigment** for laboratory measured pigment data, e.g., fluorometry and HPLC.
/data_status	The condition, or status, of the data file. The value **preliminary** indicates the data are new and the investigator intends to analyze the data further. The value **update** indicates the data are being resubmitted and informs the SIMBIOS Project that a resubmission will occur in the future. The value **final** indicates the investigator has no intention of revisiting the data set.
/start_date	The earliest date data in the file were collected, in the form YYYYMMDD.
/end_date	The latest date data in the file were collected, in the form YYYYMMDD.
/start_time	The earliest time of day data in the file were collected, in the form HH:MM:SS. Values are required to be in Greenwich Mean Time (GMT). This header requires a [GMT] trailer, e.g., /start_time=02:45:30[GMT].
/end_time	The latest time of data in the file were collected, in the form HH:MM:SS. Values are required to be in GMT. This header requires a [GMT] trailer, e.g., /end_time=02:56:20[GMT].
/north_latitude	The farthest north data in the file were collected, in decimal degrees. This header requires a [DEG] trailer, e.g., /north_latitude=45.223[DEG]. Coordinates south of the equator are set negative.
/south_latitude	The farthest south data in the file were collected, in decimal degrees. This header requires a [DEG] trailer (e.g., /south_latitude=31.884[DEG]). Coordinates south of the equator are set negative.
/east_longitude	The farthest east data in the file were collected, in decimal degrees. This header requires a [DEG] trailer (e.g., /east_longitude=-65.225[DEG]). Coordinates set west of the Prime Meridian are set negative.
/west_longitude	The farthest west data in the file were collected, in decimal degrees. This header requires a [DEG] trailer, e.g., /west_longitude=-83.117[DEG]. Coordinates set west of the Prime Meridian are set negative.
/cloud_percent	Percent cloud cover for the entire sky, e.g., 0 for a cloud-free sky and 100 for a completely overcast sky.
/measurement_depth	The discrete depth at which data were collected, in meters. This header is required for bottle samples, shipboard flow-through systems, buoys, and moored radiometers.
/secchi_depth	The secchi depth at the station where the data were collected, in meters.
/water_depth	The water depth at the station where the data were collected, in meters.
/wave_height	The wave height at the station where the data were collected, in meters.
/wind_speed	The wind speed at the station where the data were collected, in meters per second.
! COMMENTS	A space for additional comments. Common comments include additional ancillary information about the data file, sea and sky states, difficulties encountered during data collection, methods of data collection, instruments used, and a description of nonstandard SeaBASS field names included in the data file.
/missing	The null value used as a numeric placeholder for any missing data in the data file. Each row of data must contain the same number of columns as defined in the /fields and /units headers. Only one missing value is allowed per file. It is required that this value be non-zero.
/delimiter	The delimiter of the columns of data. Accepted delimiters include tab, space, and comma. Only a single delimiter is permitted per data file.
/fields	A list of the fields, e.g., CHL, for each column of data included in the data file. Each

	entry describes the data in a single column, and every column must have an entry.
`/units`	A list of the units, e.g., mg m^{-3}, for each column of data included in the data file. Every value in `/fields` must have an appropriate value listed in this header.

Table B2. The SeaBASS standardized parameters, with their appropriate abbreviations, units, and descriptions, as of May 2001. The notation ###.# indicates the parameter is wavelength specific, in nanometers, with the form of, for example, 490.6. The parameter abbreviations shown are mandated by the standard SeaBASS data file format. There are some limitations and restrictions imposed on the format of the unit abbreviations because ASCII text is used. For example, although "per meter" is represented here as "m^{-1}," the format to be input would be "m^{-1}"; "1/m" (i.e., the reciprocal of the unit) can also be used. In addition, the letter "u" is used in the unit abbreviations (e.g., uW cm^{-2} nm^{-1}) instead of the Greek letter μ, again, because Greek letters cannot be used in an ASCII file.

Parameter Abbreviation	Parameter Abbreviation	Unit	Description Parameter
`a###.#`	m^{-1}		Total absorption coefficient
`aaer###.#`	m^{-1}		Absorption coefficient of atmospheric aerosols
`ad###.#`	m^{-1}		Absorption coefficient of detritus
`adg###.#`	m^{-1}		Absorption coefficient of detritus plus Gelbstoff
`ag###.#`	m^{-1}		Absorption coefficient of CDOM
`altitude`	m		Altitude above sea level
`am`	unitless		Air mass
`angstrom`	unitless		Ångström exponent
`AOT###.#`	unitless		Aerosol optical thickness
`ap###.#`	m^{-1}		Absorption coefficient of particles
`aph###.#`	m^{-1}		Absorption coefficient of phytoplankton
`a*ph###.#`	m^{-1}		Chlorophyll *a*-specific absorption coefficient of phytoplankton
`At`	degreesC		Air temperature
`b###.#`	m^{-1}		Total scattering coefficient
`bb###.#`	m^{-1}		Backscatter coefficient
`bincount`	none		Number of records averaged into a bin
`bnw###.#`	m^{-1}		Total scattering coefficient minus the scattering by water
`bp###.#`	m^{-1}		Particle scattering coefficient
`c###.#`	m^{-1}		Beam attenuation coefficient
`cloud`	%		Percent cloud cover
`cnw###.#`	m^{-1}		Beam attenuation coefficient minus the scattering by water
`cond`	mmho cm^{-1} •		Conductivity
`depth`	m^{-1}		Depth of measurement
`Ed###.#`	uW cm^{-2} nm^{-1}		Downwelling irradiance
`EdGND`	volts		Dark current values for E_d sensor
`Epar`	uE cm^{-2} s^{-1} ♦		Profiled PAR
`Es###.#`	uW cm^{-2} nm^{-1}		Downwelling irradiance above the surface
`EsGND`	volts		Dark current values for E_s sensor
`Esky###.#`	uW cm^{-2} nm^{-1}		Downwelling sky irradiance
`Esun###.#`	uW cm^{-2} nm^{-1}		Downwelling direct normal sun irradiance
`Eu###.#`	uW cm^{-2} nm^{-1}		Upwelling irradiance
`EuGND`	volts		Dark current values for E_u sensor

• The unit "mmho" (the so-called "milli-mho") is the traditional unit used in conductivity studies. In SI units, it is equivalent to the reciprocal of the ohm (or the siemens).

♦ The unit E, for Einstein, is the traditional unit used in PAR studies. In SI units, it is equivalent to 1 mole quanta, or 1 mole photons.

F0###.#	uW cm^{-2} nm^{-1}	Extraterrestrial solar irradiance
It	degreesC	Instrument temperature
Kd###.#	m^{-1}	Diffuse attenuation coefficient of downwelling irradiance
Kl###.#	m^{-1}	Diffuse attenuation coefficient of upwelling radiance
Knf###.#	m^{-1}	Diffuse attenuation coefficient of natural fluorescence of chlorophyll *a*
Kpar	m^{-1}	Diffuse attenuation coefficient of PAR
Ku###.#	m^{-1}	Diffuse attenuation coefficient of upwelling irradiance
Lsky###.#	uW cm^{-2} nm^{-1} sr^{-1}	Sky radiance
Lt###.#	uW cm^{-2} nm^{-1} sr^{-1}	Total water radiance
Lu###.#	uW cm^{-2} nm^{-1} sr^{-1}	Upwelling radiance
LuGND	volts	Dark current values for L_u sensor
Lw###.#	uW cm^{-2} nm^{-1} sr^{-1}	Water-leaving radiance
Lwn###.#	uW cm^{-2} nm^{-1} sr^{-1}	Normalized water-leaving radiance ($L_{WN} = L_W F_0 / E_s$)
natf	nE m^{-2} sr^{-1} s^{-1}	Natural fluorescence of chlorophyll *a*
Oz	Dobson units	Column ozone
PAR	uE cm^{-2} s^{-1}	PAR measured at the sea surface
pitch	degrees	Instrument pitch
PP	mg C/mg chla/h♠	Primary productivity
pressure	dbar	Water pressure
pressure_atm	mbar	Atmospheric pressure
Q###.#	sr	E_u / L_u (equal to π in diffuse water)
quality	none	Analyst-defined data quality flag
R###.#	unitless	Irradiance reflectance ($R = E_u / E_d$)
RelAz	degrees	Sensor azimuth angle relative to the solar plane
Rl###.#	sr^{-1}	Radiance reflectance ($R_L = L_u / E_d$)
roll	degrees	Instrument roll
Rpi###.#	unitless	Radiance reflectance with π
Rrs###.#	sr^{-1}	Remote-sensing reflectance ($R_{rs} = L_W / E_d$)
sal	PSU	Salinity
sample	none	Sample number
SenZ	degrees	Sensor zenith angle
sigmaT	kg m^{-3}	Density – 1000 kg m^{-3}
sigma_theta	kg m^{-3}	Potential density – 1000 kg m^{-3}
SN	none	Instrument serial number
SPM	g L^{-1}	Total suspended particulate material
SST	degreesC	Sea surface temperature
stimf	volts	Stimulated fluorescence of chlorophyll *a*
SZ	m	Secchi disk depth
SZA	degrees	Solar zenith angle
tilt	degrees	Instrument tilt
trans	%	Percent transmission
volfilt	L	Volume filtered
wavelength	nm	Wavelength of measurement
windspeed	m s^{-1}	Wind speed
Wt	degreesC	Water temperature
Wvp	mm	Water vapor

♠ This parameter has the units of "milligrams of carbon per milligrams of chlorophyll *a* per hour". The individual units are separated with the solidus (/), instead of the customary reciprocals, to avoid confusion as to how it is to be formatted.

Pigments:		
Allo	mg m^{-3}	HPLC alloxanthin
Anth	mg m^{-3}	HPLC antheraxanthin
Asta	mg m^{-3}	HPLC astaxanthin
At	degreesC	Air temperature
Beta-beta-Car	mg m^{-3}	HPLC ββ-carotene
Beta-epi-Car	mg m^{-3}	HPLC βε-carotene
Beta-psi-Car	mg m^{-3}	HPLC βψ -carotene
But-fuco	mg m^{-3}	HPLC 19′-butaonoyloxyfucoxanthin
Cantha	mg m^{-3}	HPLC canthaxanthin
CHL	mg m^{-3}	Fluorometrically or spectrophotometrically-derived chlorophyll *a*
Chl_a	mg m^{-3}	HPLC chlorophyll *a*
Chl_b	mg m^{-3}	HPLC chlorophyll *b*
Chl_c	mg m^{-3}	HPLC chlorophyll *c*
Chlide_a	mg m^{-3}	HPLC chlorophyllide *a*
Chlide_b	mg m^{-3}	HPLC chlorophyllide *b*
Croco	mg m^{-3}	HPLC crocoxanthin
Diadchr	mg m^{-3}	HPLC diadinochrome
Diadino	mg m^{-3}	HPLC diadinoxanthin
Diato	mg m^{-3}	HPLC diatoxanthin
Dino	mg m^{-3}	HPLC dinoxanthin
DV_Chl_a	mg m^{-3}	HPLC divinyl chlorophyll *a*
DV_Chl_b	mg m^{-3}	HPLC divinyl chlorophyll *b*
Echin	mg m^{-3}	HPLC echinenone
Et-8-carot	mg m^{-3}	HPLC ethyl-apo-8′-carotene
Et-chlide_a	mg m^{-3}	HPLC ethyl chlorophyllide *a*
Et-chlide_b	mg m^{-3}	HPLC ethyl chlorophyllide *b*
Epi-epi-Car	mg m^{-3}	HPLC εε-carotene
Fuco	mg m^{-3}	HPLC fucoxanthin
Hex-fuco	mg m^{-3}	HPLC 19′-hexanoyloxyfucoxanthin
Lut	mg m^{-3}	HPLC lutein
Lyco	mg m^{-3}	HPLC lycopene
Me-chlide_a	mg m^{-3}	HPLC methyl chlorophyllide *a*
Me-chlide_b	mg m^{-3}	HPLC methyl chlorophyllide *b*
Mg_DVP	mg m^{-3}	HPLC Mg 2,4-divinyl phaeoporphyrin a_5 monomethyl ester
Monado	mg m^{-3}	HPLC monadoxanthin
Neo	mg m^{-3}	HPLC neoxanthin
P-457	mg m^{-3}	HPLC P-457
Perid	mg m^{-3}	HPLC peridinin
PHAEO	mg m^{-3}	Total phaeopigment concentration
Phide_a	mg m^{-3}	HPLC phaeophorbide *a*
Phide_b	mg m^{-3}	HPLC phaeophorbide *b*
Phide_c	mg m^{-3}	HPLC phaeophorbide *c*
Phythl-chl_c	mg m^{-3}	HPLC phytylated chlorophyll *c*
Phytin_a	mg m^{-3}	HPLC phaeophytin *a*
Phytin_b	mg m^{-3}	HPLC phaeophytin *b*
Phytin_c	mg m^{-3}	HPLC phaeophytin *c*
Pras	mg m^{-3}	HPLC prasinoxanthin
Pyrophytin_a	mg m^{-3}	HPLC pyrophaeophytin *a*
Pyrophytin_b	mg m^{-3}	HPLC pyrophaeophytin *b*
Pyrophytin_c	mg m^{-3}	HPLC pyropheophytin *c*
Siphn	mg m^{-3}	HPLC siphonein

Siphx	mg m^{-3}	HPLC siphonaxanthin
Tpg	mg m^{-3}	Total pigment concentration
Vauch	mg m^{-3}	HPLC vaucheriaxanthin-ester
Viola	mg m^{-3}	HPLC violaxanthin
Zea	mg m^{-3}	HPLC zeaxanthin

An example of an optical cast data file:

```
/begin_header
/investigators=John_Smith,Mary_Johnson
/affiliations=MBARI,State_University
/contact=jsmith@mbari.org,mary@state.edu
/experiment=TAO_Moorings
/cruise=tao_dec_1997
/station=341
/data_file_name=n97f341b.txt
/documents=README.txt
/calibration_files=ocp14a.cal
/data_type=cast
/data_status=preliminary
/start_date=19971215
/end_date=19971215
/start_time=21:15:39[GMT]
/end_time=21:19:30[GMT]
/north_latitude=-0.016[DEG]
/south_latitude=-0.016[DEG]
/east_longitude=-170.02[DEG]
/west_longitude=-170.02[DEG]
/cloud_percent=10.0
/measurement_depth=NA
/secchi_depth=15
/water_depth=225
/wave_height=0.5
/wind_speed=5
!
!     COMMENTS
!     hazy near horizon, no clouds near solar disk
!     Satlantic OCP profiling radiometer; last calibrated October 1997
!
/missing=-999
/delimiter=space
/fields=depth,Lu412.2,Lu443.4,Lu489.7,Ed412.5,Ed443.1
/units=m,uW/cm^2/nm/sr,uW/cm^2/nm/sr,uW/cm^2/nm/sr,uW/cm^2/nm,uW/cm^2/nm
/end_header@
1.0 1.244184 1.066594 0.852400 65.430025 65.883773
2.0 1.299710 1.113997 0.884608 58.041549 59.823693
3.0 1.298214 1.113140 0.886502 51.693890 51.255351
```

An example of a pigment data file:

```
/begin_header
/investigators=John_Smith,Mary_Johnson
/affiliations=Goddard_Space_Flight_Center,State_University
/contact=jsmith@simbios.gsfc.nasa.gov,mary@state.edu
/experiment=AMT
/cruise=AMT07
/station=14
/data_file_name=A07OD014.SHO
/documents=A7OPSLOG.TXT
/calibration_files=turner_0898.xls
/data_type=pigment
```

```
/data_status=preliminary
/start_date=19981016
/end_date=19981020
/start_time=12:11:08[GMT]
/end_time=15:25:45[GMT]
/north_latitude=36.1234[DEG]
/south_latitude=31.8823[DEG]
/east_longitude=-51.2363[DEG]
/west_longitude=-55.1125[DEG]
/cloud_percent=NA
/measurement_depth=NA
/secchi_depth=NA
/water_depth=NA
/wave_height=NA
/wind_speed=NA
!
!  COMMENTS
!  Turner Designs fluorometer; last calibrated August 1998
!
/missing=-999
/delimiter=space
/fields=date,time,station,lat,lon,depth,CHL
/units=yyyymmdd,hh:mm:ss,none,degrees,degrees,m,mg/m^3
/end_header@
19981016 14:33:22 st001 32.3234 -53.1624 0.5 0.32
19981017 13:01:56 st002 33.1122 -53.1276 0.5 0.33
19981018 15:25:45 st003 36.1234 -51.2363 0.5 0.45
19981019 12:11:08 st004 31.8823 -55.1125 0.5 0.22
19981020 14:13:14 st005 34.2341 -52.3545 0.5 0.11
```

Appendix C

List of Acronyms

James L. Mueller

Center for Hydro-Optics and Remote Sensing, San Diego State University, California

AC9	A commercial device for measurements in situ of $a(\lambda)$ and $c(\lambda)$ at 9 wavelengths.
A/D	Analog-to-Digital
ADEOS	Advanced Earth Observing Satellite (Japanese)
AERONET	Aerosol Robotic Network (see Chapters 7 and 14).
ALSCAT	ALPHA and Scattering Meter (Note: In older conventions, "ALPHA" corresponds to c(λ), the beam attenuation coefficient, in present usage.)
AMT	Atlantic Meridonial Transect, a research cruise series AMT-1, AMT-2, etc..
AOL	Airborne Oceanographic Lidar
AOP	Apparent Optical Properties (Section 2.4)
AOT	Aerosol Optical Thickness
ARGOS	Not an acronym: the name given to the data collection and location system on NOAA Operational Satellites
ASCII	American Standard Code for Information Inter- change
AVHRR	Advanced Very High Resolution Radiometer
AVIRIS	Advanced Visible and Infrared Imaging Spectrometer
BRDF	Bi-directional Reflectance Distribution Function
BSI	BioSpherical Instruments, Inc.
BNL	Brookhaven National Laboratory
CCD	Charge-Coupled Device
CDOM	Colored Dissolved Organic Material
CERT	Calibration Evaluation and Radiometric Testing
CHN	Carbon, Hydrogen, and Nitrogen
CIMEL	Name of a commercial sun photometer equipped with an automated sun tracking mechanism
CTD	Conductivity, Temperature, and Depth
CW	Continuous Wave
CZCS	Coastal Zone Color Scanner
DAS	Data Acquisition Sequence
DIW	Distilled Water
DOC	Dissolved Organic Carbon
DOM	Dissolved Organic Matter
DUT	Device Under Test
DVM	Digital Voltmeter
ECO-VSF	A commercial device for *in situ* determinations of $b_b(\lambda)$.
EOS	Earth Observing System
ER-2	Earth Resources-2, a research aircraft
ESA	European Space Agency
FEL	Not an acronym; a commercial bulb type designator of a lamp used, after suitable modification of its terminals, as a transfer standard of spectral irradiance
FOS	Fiber Optic Spectrometer

FOV	Field-of-View
FRSR	Fast Rotating Shadow-Band Radiometer
FSW	Filtered SeaWater
FWHM	Full-Width at Half-Maximum
GAC	Global Area Coverage
GASM	General Angle Scattering Meter
GF/F	Not an acronym; a specific type of glass fiber filter manufactured by Whatman
GLI	Global Line Imager, a future satellite ocean color sensor (Appendix A)
GMT	Greenwich Mean Time
GOES	Geostationary Operational Environmental Satellite
GPIB	General Purpose Interface Bus
GPS	Global Positioning System
GSFC	Goddard Space Flight Center
HOBILABS	Hydro-Optics, Biology and Instrumentation Laboratories, Inc.
HPCE	High Performance Capillary Electrophoresis, in the present context, a proposed method for determining concentrations of phycobiliproteins.
HPLC	High Performance Liquid Chromatography, in the present context, a chemical method used to separate and measure concentrations of phytoplankton pigments in samples filtered from seawater
HydroScat	Not an acronym. Name of a commercial device for in situ determinations of $b_b(\lambda)$.
IAPSO	International Association for the Physical Sciences of the Ocean
ICES	International Council on Exploration of the Seas
IFOV	Instantaneous field-of-view
IOCCG	International Ocean Color Coordinating Group
IOP	Inherent Optical Properties (Section 2.4)
IR	Infrared
ISS	Integrating Sphere Source
JGOFS	Joint Global Ocean Flux Study
LED	Light Emitting Diode.
LOA	Laboratoire d'Optique Atmosphérique
MDL	Method detection limit.
MER	Marine Environmental Radiometer
MERIS	Marine Environment Research Imaging Spectroradiometer (European Space Agency)
MICROTOPS	Name of a commercially available hand-held sun photometer
MISR	Multi-angle Imaging SpectroRadiometer
MLML	Moss Landing Marine Laboratories
MLO	Mauna Loa Observatory
MOBY	Marine Optical Buoy (Chapter 11)
MOCE	Marine Optical Characterization Experiment
MODIS	Moderate Resolution Imaging Spectroradiometer
MOS	1. Modular Optoelectronic Scanner (German). 2. Marine Optical System, in the MOBY context (Chapter 11 and elsewhere).
MS112	Not an acronym; name of a computer program used for SeaWiFS data processing
NAS	National Academy of Science
NASA	National Aeronautics and Space Administration
NASIC	NASA Aircraft/Satellite Instrument Calibration

NESDIS	National Environmental Satellite Data Information Service
NIMBUS	Not an acronym; name given to a series of NASA weather satellites
NIR	Near-Infrared.
NIST	National Institute of Standards and Technology
NOAA	National Oceanic and Atmospheric Administration
NOARL	Naval Oceanographic and Atmospheric Research Laboratory
NPR	NIST Portable Radiance source.
NRSR	Normalized Remote Sensing Reflectance
OCI	Ocean Color Imager
OCTS	Ocean Color and Temperature Sensor (Japanese)
OCS-5002	Optical Calibration Source (a commercial variant of SQM).
OFFI	Optical Free-Fall Instrument
OL4xx	Series of ISSs manufactured by Optronics Laboratories, Inc.
OMP-8	Not an acronym; a type of marine anti-biofouling compound
OSFI	Optical Surface Floating Instrument
OSMI	Ocean Scanning Multispectral Imager
PAR	Photosynthetically Available Radiation
PE	Phycoerythin
PEB	Phycoerythobilin chromophores
PUB	Phycourobilin chromophores
POC	Particulate Organic Carbon
POLBOX	A devices that transforms natural light to polarized light
POLDER	Polarization and Directionality of the Earth Reflectance (a French satellite radiometer)
PON	Particulate Organic Nitrogen
PREDE	Name of a commercial sun photometer equipped with an automated sun tracking mechanism
PSU	Practical Salinity Units
PTFE	Polytetrafluoroethylene, commonly known by the trade name Teflon
QA	Quality Assurance
QED	Quantum Efficient Detector
ROSIS	Remote Ocean Sensing Imaging Spectrometer, also known as the Reflecting Optics System Imaging Spectrometer (German)
ROV	Remotely Operated Vehicle
ROW	Reverse Osmosis Water
SCOR	Scientific Committee on Oceanographic Research
SeaBASS	SeaWiFS Bio-optical Archive and Storage System.
SeaWiFS	Sea-viewing Wide Field-of-view Sensor
SI	Standard International, as in “SI units”
SIMBAD	Name of a hand-held sun photometer and ocean surface radiance sensor (French)
SIMBIOS	Sensor Intercomparison for Marine Biology and Interdisciplinary Ocean Studies
SIMRIC	SIMBIOS Radiometric Intercalibration, a series SIMRIC-1, -2, of intercomparison experiments.
SIRCUS	Spectral Irradiance and Radiance responsivity Calibrations with Uniform Sources
SIRREX	SeaWiFS Intercalibration Round-Robin Experiment, a series SIRREX-1, -2, etc.
SLM	Standard Lamp Monitor
S/N	Serial Number
SNR	Signal-to-Noise Ratio
SPM	Total Suspended Particulate Material
SPO	SeaWiFS Project Office
SPSWG	SeaWiFS Prelaunch Science Working Group
SQM	SeaWiFS Quality Monitor

SST	Sea Surface Temperature
SXR	SeaWiFS Transfer Radiometer, a series of filter radiometers: SXR, SXR-II, etc.
TIROS	Television Infrared Observation Satellite
TOA	Top of the Atmosphere
TOMS	Total Ozone Mapping Spectrometer
TOVS	Total Ozone Vertical Sounder
T-S	Temperature-Salinity
UNESCO	United Nations Educational, Scientific, and Cultural Organizations
UK	United Kingdom, Great Britain
UPS	Un-interruptable Power Supply
UTC	Universal Time Coordinated
UV	Ultraviolet
UVB	Ultraviolet-B (a sub-range of UV wavelengths)
VSF	Volume Scattering Function
VXR	Visible Transfer Radiometer, an instrument similar in concept to the SXR.
WETLABS	Western Environmental Technology Laboratory, Inc.
WMO	World Meteorological Organization
YES	Yankee Environmental Systems, Inc.

Appendix D

Frequently Used Symbols

James L. Mueller

Center for Hydro-Optics and Remote Sensing, San Diego State University, California

This appendix lists the definition of symbols that are used frequently throughout the ocean optics protocol document. Not included are the SI units (*e.g*. m, cm, nm, Km, mL, L, mg, μg, etc.), or specialized symbols that are defined locally for purposes of discussion in a particular segment of the text, and which do not appear elsewhere in the document. In the convention used throughout the protocols, variables are written in *italics*, with the exception of lower-case Greek symbols.

A or $A(\lambda)$	1. $A(\lambda)$ is spectral absorptance (Sect. 2.4). 2. In HPLC chromatograms, A (with various super- and subscripts) is used to denote peak areas. 3. Altitude. 4. A general coefficient with varied usage as defined locally in the text
a	Area, but only when appearing without parentheses [*e.g*. as in Section 2.3 and Figure (2.3)].
$a(\lambda)$ or $a(z, \lambda)$	Spectral volume absorption coefficient (Section 2.4) in m^{-1}. Frequently used subscripted variants are: • $a_w(\lambda)$ spectral absorption coefficient of pure water • $a_p(z, \lambda)$ spectral absorption coefficient due to suspended particles • $a_g(z, \lambda)$ spectral absorption coefficient of substances dissolved in seawater, *e.g*. CDOM • $a_g(z, \lambda)$ Non-pigmented particle absorption coefficient. • $a_\phi(z, \lambda)$ Phytoplankton pigment spectral absorption coefficient.
$B(\lambda)$	Spectral scatterance, or $B(\lambda,\Psi,\phi)$ directional spectral scatterance (Section 2.4)
$b(\lambda)$ or $b(z, \lambda)$	Spectral volume scattering coefficient in m^{-1} (Section 2.4). Frequently used subscripted variants are: • $b_w(\lambda)$ spectral volume scattering coefficient of pure water • $b_r(\lambda)$ Raman volume scattering coefficient for pure water • $b_p(z, \lambda)$ spectral volume scattering coefficient due to particles • $b_b(z, \lambda)$ spectral volume backscattering coefficient • $\tilde{b}_b(z,\lambda)$ normalized spectral volume backscattering coefficient
C^i_{Sample}	Individual pigment concentration ($\mu g\ L^{-1}$) (Chapters 16 and 17)
C^i_{STD}	Concentration of a pigment standard($\mu g\ L^{-1}$) (Chapters 16 and 17)
Chl	Chlorophyll *a* concentration in mg m^{-3} or $\mu g\ L^{-1}$.
$c(\lambda)$ or $c(z, \lambda)$	Spectral beam attenuation coefficient [equation (2.18)] in m-1. Subscripted variants are the same as for $a(\lambda)$ and/or $b(\lambda)$.

$\hat{\mathbf{D}}$ Unit length vector indicating the direction of a detector, i.e. the reciprocal of the viewing direction for that detector, see *e.g.*, Figs. (2.1) and 2.2).

d 1. Earth-sun distance, where d_o indicates the annual average distance occurring on 3 January. 2. Distance of the lamp source from the collector surface in a radiometric calibration setup.

E Irradiance in μW cm^{-2} (Sect. 2.3).

$E(\lambda)$ or $E(z, \lambda)$ Spectral irradiance in μW cm^{-2} nm^{-1} (Sect. 2.3). Frequently used subscripted variants are:

- $E_d(z, \lambda)$ downward spectral irradiance
- $E_S(\lambda)$ Surface spectral irradiance, a synonym for $E_d(0^+, \lambda)$.
- $E_{sun}(z, \lambda)$ Direct solar spectral irradiance component of $E_S(\lambda)$
- $E_{sky}(z, \lambda)$ Diffuse sky spectral irradiance component of $E_S(\lambda)$
- $E_u(z, \lambda)$ downward spectral irradiance
- $\vec{E}(z,\lambda)$ vector spectral irradiance
- $\overset{o}{E}(z,\lambda)$ scalar spectral irradiance, also $\overset{o}{E}_d(z,\lambda)$ or $\overset{o}{E}_u(z,\lambda)$ Section 2.3)
- $E_N(\lambda, \theta_o)$ direct solar spectral irradiance, normal to the solar beam.

F 1. Radiant flux in, *e.g.*, μW (Sect. 2.3). 2. Used locally with subscripts to denote scale factors associated with various instrument response characteristics (especially in Ch. 6). 3. $F(z)$ is used to denote in situ chlorophyll a fluorescence. 4. Various factors in fluorometric determination of chlorophyll a concentration (Chapter 17).

$\bar{F}_o(\lambda)$ Extraterrestrial solar flux (above the atmosphere) when the earth-sun distance is at its annual mean.

$f(\lambda,...)$ A function relating IOP to irradiance reflectance $R(0^-, \lambda)$, and used together with the factor $Q(\lambda,\ldots)$ to remove the ocean's BRDF effects in determining $L_{WN}^{ex}(\lambda)$ (Chapter 13). The full functional dependence of the function is expressed $f\left[\lambda,(\theta_o,\tau_a,W),a(\lambda),\beta(\lambda,\Psi)\right]$. The symbol $f_o\left[\lambda,\tau_a,a(\lambda),\beta(\lambda,\Psi)\right]$ refers to the simplified case when the sun is at zenith.

$f'(\lambda,\cdots)$ Alternative form of $f(\lambda,\cdots)$, $f'(\lambda,\cdots) = f(\lambda,\cdots)\left[1-\frac{b_b(\lambda)}{a(\lambda)}\right]$ (Chapter 13).

$K(z, \lambda)$ Generic diffuse attenuation coefficient in m^{-1}. Frequently used variants are:

- $K_d(z, \lambda)$ Diffuse attenuation coefficient for $E_d(z, \lambda)$
- $K_u(z, \lambda)$ Diffuse attenuation coefficient for $E_u(z, \lambda)$
- $K_L(z, \lambda)$ Diffuse attenuation coefficient for $L_u(z, \lambda)$

- $K(\lambda)$ Remote sensing diffuse attenuation coefficient, $K_d(z, \lambda)$ for $E_d(z, \lambda)$ averaged over the first diffuse attenuation depth.

$L(\theta, \phi)$ Radiance in μW cm^{-2} sr^{-1} (Sect. 2.3).

$L(\lambda,\theta,\phi)$ or $L(z,\lambda,\theta,\phi)$ Spectral radiance in μW cm^{-2} sr^{-1} nm^{-1} (Sect. 2.3). When expressed without indicating angular dependence, e.g. as $L(\lambda)$, reference is made to nadir-viewing geometry. Frequently used subscripted variants are:

- $L_d(z,\lambda,\theta,\phi)$ downward spectral radiance
- $L_d^t(0^-,\lambda,\theta',\phi)$ downward spectral radiance transmitted across the air-sea interface
- $L_u(z,\lambda,\theta',\phi)$ upwelled spectral radiance
- $L_W(\lambda,\theta,\phi)$ Water-leaving radiance (at z = 0$^+$) transmitted upwards across the air-sea interface.
- $L_{WN}(\lambda)$ Normalized water-leaving radiance (at z = 0$^+$) (Gordon and Clark 1981; see Chapter 13).
- $L_{wN}^{ex}(\lambda)$ Exact normalized water-leaving radiance (at z = 0$^+$) (Morel and Gentili 1996; see Chapter 13).
- $L_{sfc}(\lambda,\theta,\phi,\theta_o,\phi_o)$ Spectral radiance leaving the surface at angles (θ,ϕ) for a given solar position (θ_o,ϕ_o).
- $L_{sky}(\lambda,\theta,\phi,\theta_o,\phi_o)$ Sky spectral radiance incident on the surface at (θ,ϕ) for a given solar position (θ_o,ϕ_o).
- $L_t(\lambda,\theta,\phi)$ Aperture radiance at TOA as measured by a satellite sensor.
- $L_{TOA}(\lambda,\theta,\phi)$ Same as $L_t(\lambda,\theta,\phi)$.

M or $M(\theta)$ Optical air mass.

$m(\lambda)$ Complex index of refraction $m(\lambda)=n(\lambda)+in'(\lambda)$ (Sect. 2.5).

$n(\lambda)$ Real part of the complex refractive index, commonly referred to as simply the "refractive index" (Sect. 2.5). A frequently used variant is $n_w(\lambda)$, the refractive index of water relative to that of air.

OD(λ) Optical density, determined from transmission measurements in a spectrophotometer of a reference sample $V_o(\lambda)$ and a filter or dissolved sample $V(\lambda)$, calculated as $OD(\lambda)=\log_{10}V_o(\lambda)-\log_{10}V(\lambda)$. Used extensively in Chapter 15 with subscripts denoting various types of samples and reference blank artifacts.

P Atmospheric pressure at the sea surface.

$P_a(\lambda, \Psi)$ Aerosol phase function, equivalent to $\tilde{\beta}(\lambda,\psi)$ (Sect. 2.4).

$Q(\lambda,\theta',\phi;...)$	By definition, the ratio of upwelled spectral irradiance to upwelled spectral radiance just beneath the sea surface ($z = 0^-$). The full functional dependence of the quantity Q is expressed as $Q\left[(\lambda,\theta',\phi),(\theta_o,\tau_a,W),a(\lambda),\beta(\lambda,\Psi)\right]$ (Chapter 13), with simplified special cases: • $Q_n\left[\lambda,\theta_o,a(\lambda),\beta(\lambda,\Psi)\right]$ For nadir viewing geometry • $Q_o\left[\lambda,a(\lambda),\beta(\lambda,\Psi)\right]$ For nadir viewing geometry with the sun at zenith.
$R(z,\lambda)$	Irradiance reflectance, *i.e.* the ratio of $E_u(z, \lambda)$ to $E_d(z, \lambda)$ (Section 2.7 and Chapter 13).
$R_{RS}(\lambda,\theta,\phi)$	Remote sensing reflectance, also sometimes denoted $R_{RS}(\lambda,\theta,\phi\in\Omega_{FOV};\theta_o)$ to indicate its dependence on a sensor's solid angle FOV and solar zenith angle (Sect. 2.6 and Chapters 12 and 13). An important variant is exact normalized remote sensing reflectance $R_{RS}^{ex}(\lambda)$ as defined in equation (12.5) (Chapter 12).
R_s	Peak resolution in HPLC protocols (Chapter 16).
r	1. Generic radial distance, or radius of circle or sphere. 2. Earth-sun distance. 3. Instrument radius in the context of instrument self shading.
$\hat{\mathbf{S}}$	Unit length vector defining the direction of a source, e.g. as in Figures 2.1 and 2.2 and related text in Chapter 2.
S or $S(z)$	Salinity.
$\hat{\mathbf{T}}$	Unit length vector defining the direction of radiant flux transmittance from a source, $\hat{\mathbf{T}} = -\hat{\mathbf{S}}$, *e.g.* as in Figures 2.1 and 2.2 and related text in Chapter 2.
$T(\lambda)$	Spectral transmittance (Section 2.4).
T or $T(z)$	Temperature
$t(z)$	Time at which an instrument is located at depth z during a profile.
$t(\lambda,\theta_o)$	Atmospheric transmittance of the direct solar beam.
V	1. Generically, Voltage in (V), e.g. for an instrument's response, as defined locally in the text. 2. In the context of sun photometry, $V(\lambda,\theta_o)$ is a photometer's response for airmass $M(\theta_o)$ and $V_o(\lambda)$ is the sensor's derived response for solar irradiance at TOA, i.e. for $M = 0$, as determined by the Langley-Bouguer method (Chapter 7). 3. Volume, in the context of absorption and pigment measurements from discrete water samples (Chapter 15, 16 and 17).
W	Wind speed in m s^{-1}.

$(\hat{\mathbf{x}}, \hat{\mathbf{y}}, \hat{\mathbf{z}})$ Orthonormal basis vectors defining any local coordinate system, e.g., as in Figures 2.1 and 2.2 and related text of Chapter 2.

z Unless specified otherwise, the vertical coordinate in a local reference frame. Most often used to denote depth in m, but a more general usage is defined in several places in the text (see especially the generalized use of z in the coordinates of Fig. 2.2 and derivation of IOP in Section 2.4). When z is used to indicate depth, $z = 0^+$ and $z=0^-$ refer to z=0 measured above and below the interface, respectively.

0_3 Ozone.

β In the context of spectrophotometric measurements of absorption by particles concentrated on a glass-fiber filter [Chapter 15, equations (15.6a) and (15.6b)], the correction factor for increased pathlength due to scattering within the filter. Also referred to as the "β-factor".

$\beta(\lambda, \psi)$ The spectral volume scattering coefficient (VSF), defined in Sect. 2.4, is also denoted $\beta(z, \lambda, \psi)$ to indicate its variation with depth in the water column. Closely related quantities are $\tilde{\beta}(\lambda, \psi)$, the spectral volume scattering phase function, defined as the ratio of the VSF to the volume scattering coefficient [equation 2.22], and $\tilde{\beta}_w(\lambda, \psi)$, the molecular volume scattering phase function for sea water [equations (2.29) and (2.30)]. Other, more specialized forms of the VSF are defined locally as they occur in the text.

$\varepsilon(\lambda)$ Together with $\varepsilon_{sky}(\lambda)$ and $\varepsilon_{sun}(\lambda)$, model determinations of instrument self-shading errors in measurements of $L_u(0^-, \lambda)$ and $E_u(0^-, \lambda)$, as used in equations (10.16) through (10.30).

ϕ Generic symbol for azimuth angle, measured from the x-axis in the xy-plane (e.g. as in Figs. 2.1 and 2.2). When subscripted as ϕ_o, it denotes solar azimuth angle. A commonly used convention is to rotate the x-axis toward the sun, so that azimuth angles are measured relative to ϕ_o. Other, specialized uses of this symbol are defined locally as they occur in the text.

κ'_{xxx} A family of subscripted coefficients used in instrument self-shading corrections to $L_u(0^-, \lambda)$ and $E_u(0^-, \lambda)$, via equations (10.16) through (10.30).

λ Wavelength, in nm unless specified otherwise.

χ, χ_p, χ_w	Model dependent scale factors used to relate VSF measurements at a single reference scattering angle Ψ^* to $b_b(\lambda)$.
Ψ	Scattering angle (Section 2.2).
θ	Generic symbol for zenith angle measured from the z-axis, as in Figures 2.1 and 2.2. Conventions for frequently used unprimed, primed, or subscripted, symbols are: • θ zenith angle in air • θ' zenith, or nadir, angle in water, related to θ by Snell's Law (Sect. 2.5) • θ_o solar zenith angle (in air), or sometimes that of any source.
$\rho(\lambda, \theta_o, \theta)$	BRDF of a diffuse reflecting surface, for radiant flux incident at zenith angle θ_o and reflected at angle θ, *e.g.*, as in equation (6.4).
$\rho(\theta, \theta')$ and $\rho(\theta', \theta)$	Reflectances for radiances incident from above and below, respectively, on the wave roughened sea surface (Sect. 2.5), where it is noted that $\rho(\theta, \theta') = \rho(\theta', \theta)$. Reflectance is sometimes written as, *e.g.*, $\rho(\theta, \theta', W)$ to explicitly indicate its dependence on wind speed. For a flat plane surface, these quantities converge to the Fresnel Reflectance $\rho_F(\theta, \theta')$ [equations (2.35) and (2.36)].
$\Re(\theta', W)$	Term accounting for all effects of reflection and refraction at the sea surface [equation (13.17)] in determination of exact normalized water-leaving radiance (Chapter 13). The symbol $\Re_o$ denotes the simplified version of this term for nadir viewing geometry.
Ω_{FOV}	Solid angle FOV, in sr, of a particular sensor.
$\sigma_t(z)$	Specific density anomaly of seawater, a function of Temperature and Salinity.
τ	In the context of fluorometric chlorophyll *a* analysis (Chapter 17), used - without functional notation - to quantify a fluorometer's sensitivity to phaeopigment fluorescence.
$\tau(\lambda)$	Total optical thickness of the atmosphere, with primary components: • $\tau_a(\lambda)$ Aerosol optical thickness (AOT). • $\tau_{O_3}(\lambda)$ Ozone optical thickness. • $\tau_R(\lambda)$ Rayleigh optical thickness. • $\tau_g(\lambda)$ Optical thickness of all absorbing gases (including Ozone).
$\varpi(\lambda)$ or $\omega_o(\lambda)$	Single Scattering Albedo (Sect. 2.4).